THÈSE

Pour obtenir le grade de

DOCTEUR DE L'UNIVERSITÉ GRENOBLE ALPES

École doctorale : PHYS - Physique
Spécialité : Physique pour les Sciences du Vivant
Unité de recherche : Grenoble Institut des Neurosciences

Impact de la perméabilisation de la barrière hémato-encéphalique par ultrasons focalisés sur le cerveau : une approche quantitative en IRM

Impact of blood-brain barrier permeabilisation by focused ultrasound on the brain : a quantitative MRI approach

Présentée par :

Sébastien RIGOLLET

Direction de thèse :

Emmanuel BARBIER DIRECTEUR DE RECHERCHE, INSERM - Délégation Auvergne Rhône-Alpes	Directeur de thèse
Chantal PICHON Enseignant-Chercheur, Université d'Orléans	Co-directrice de thèse

Rapporteurs :

CYRIL LAFON
DIRECTEUR DE RECHERCHE, INSERM DELEGATION AUVERGNE-RHONE-ALPES
LORI BRIDAL
DIRECTRICE DE RECHERCHE, CNRS DELEGATION PARIS CENTRE

Thèse soutenue publiquement le **21 novembre 2024**, devant le jury composé de :

MIREILLE ALBRIEUX, PROFESSEURE DES UNIVERSITES, UNIVERSITE GRENOBLE ALPES	Présidente
CYRIL LAFON, DIRECTEUR DE RECHERCHE, INSERM DELEGATION AUVERGNE-RHONE-ALPES	Rapporteur
LORI BRIDAL, DIRECTRICE DE RECHERCHE, CNRS DELEGATION PARIS CENTRE	Rapporteure
MARLENE WIART, DIRECTRICE DE RECHERCHE, CNRS DELEGATION RHONE AUVERGNE	Examinatrice
CLEMENS BOS, ASSOCIATE PROFESSOR, UNIVERSITY MEDICAL CENTER UTRECHT	Examinateur

Invités :

Erik DUMONT
DOCTEUR EN SCIENCES, IMAGE GUIDED THERAPY
Vasile STUPAR
INGENIEUR DE RECHERCHE, INSERM - Délégation Auvergne Rhône-Alpes
Anthony DELALANDE
MAÎTRE DE CONFERENCES, Université d'Orléans

Table Of Contents

Table Of Contents 3
Ethical Statement 7
Abbreviations list 9
General introduction 13
Chapter 1. Introduction to Focused UltraSound for blood-brain barrier permeabilisation 17
1.1. Focused ultrasound in the landscape of medical ultrasound 17
1.2. The neurovascular unit and the blood-brain barrier 18
1.3. Other strategies to cross the blood-brain barrier 23
1.4. Focused ultrasound for blood-brain barrier opening 25
1.5. Cavitation monitoring 37
Chapter 2. Secondary bioeffects of the use of Focused UltraSound and microbubbles to permeabilise the BBB: state of the art 53
2.1. Vascular modifications and cellular extravasation 54
2.2. Neuroinflammation 58
2.3. Metabolism 63
2.4. Behaviour 64
2.5. Clinical parameters evaluated after blood-brain barrier permeabilisation in human 65
2.6. Multiple blood-brain barrier opening 66
Chapter 3. Problems and objectives 71
Chapter 4. General methods and methodological developments 75
4.1. Focused ultrasound transducer characterisation 75
4.2. Microbubble characterisation 77
4.3. Evaluation of magnetic resonance guided focused ultrasound 84
4.4. Focal and Extended blood-brain barrier opening with focused ultrasound 92
4.5. Magnetic resonance image acquisition and processing methods 94
4.6. Histology methods 100
Chapter 5. Study 1: FUS-mediated BBB opening leads to transient perfusion decrease and inflammation without acute or chronic brain lesion 103
5.1. Abstract 104
5.2. Introduction 105
5.3. Method 106
5.1. Results 112

5.2. Discussion 119
5.3. Acknowledgments 121
5.4. Competing interests 121
Chapter 6. Study 2: Longitudinal MR vascular fingerprinting approach tracking physiological changes during repeated MR guided focused ultrasound mediated BBB opening on rats. 123
6.1. Methods 124
6.2. Results 126
6.3. Discussion 135
Chapter 7. Study 3: Median survival time in an F98 rat model is improved by the combination of FUS, carboplatin and radiotherapy 141
7.1. Methods 142
7.2. Results 146
7.3. Discussion and conclusion 151
Chapter 8. Study 4: Whole brain gene delivery in a *Fmr1*^{KO} mice model of fragile X syndrome 155
8.1. Methods 158
8.2. Results 159
8.3. Discussion and conclusion 162
General discussion and conclusion 165
Annexes 169
A.1. *In vitro* cavitation 169
A.2. Overview of multiparametric MRI image processing 171
A.3. Supplementary figures from Study 1 172
A.4. Supplementary figures from Study 2 174
A.5. Supplementary figures from Study 3 175
Curriculum vitae 179
List Of Figures 183
List Of Tables 187
References 189
Résumé français - French Summary 223

Ethical Statement

All animal procedures conformed to French government guidelines (in particular articles R.214-87 to R.214-126), approved by local ethic committee and were authorised by the French Ministry of Education and Research under APAFIS numbers #43777 (Chapter 5, Chapter 6 and Chapter 8), #48225 (Chapter 7) and #47771 and #47394 (Chapter 8). All animal experiment presented in this thesis were performed at the Insitut des Neurosciences de Grenoble, Inserm U1216, headed by Emmanuel L. Barbier with approval number C3851610008 and in compliance with the ARRIVE guidelines (Animal Research: Reporting in Vivo Experiments). Efforts were made to use as less animals as possible to limit this thesis' impact.

Abbreviations list

1,2-dimyristoyl-sn-glycero-3-phosphocholine	DMPC
1,2-dimyristoyl-sn-glycero-3-phospho-ethanolamine	DMPE
1,2-distearoyl-sn-glycero-3-phosphocholine	DSPC
1,2-distearoyl-sn-glycero-3-phospho-ethanolamine	DSPE
^{18}F-2-fluoro-2-deoxy-D-glucose	^{18}F-FDG
4',6-diamidino-2-phenylindole	DAPI
acoustic radiation force imaging	ARFI
acquisition time	T_{acq}
adeno-associated virus	AAV
Alzheimer's disease	AD
amyloid beta	Aβ
apparent diffusion coefficient	ADC
area under the curve	AUC
arterial spin labelling	ASL
Bandwidth	BW
blood-brain barrier	BBB
central nervous system	CNS
cerebral blood flow	CBF
cerebral metabolic rate of oxygen	$CMRO_2$
contrast agent	CA
contrast-enhanced ultrasound	CEUS
deoxyribonucleic acid	DNA
diffusion tensor imaging	DTI
Dulbecco's modified Eagle's medium	DMEM
dynamic contrast enhancement	DCE
echo time	TE
endothelial cells	ECs
fast Fourier transform	FFT
fast low angle shot	FLASH
field of view	FOV
focused ultrasound	FUS
fragile mental retardation 1	*Fmr1*
fragile mental retardation protein	FMRP
full width at half maximum	FWHM
gadolinium	Gd
glial fibrillary acidic protein	GFAP
glioblastoma	GBM
green fluorescent protein	GFP
haematoxylin and eosin	H&E
hydrodynamic diameter	d_H
immunofluorescence	IF
immunoglobulin G/M	IgG/M
indocyanine green	ICG
inertial cavitation detection	ICD
intrapulse harmonic detection	IHD

intrapulse ultra harmonic detection	IUD
ionized calcium-binding adapter molecule 1	Iba1
knock-out	KO
magnetic resonance imaging	MRI
mechanical index	MI
median survival time	MeST
microbubbles	MB
modified neurological severity score	mNSS
motion sensitive gradient	MSG
multi-gradient echo	MGE
NADH:ubiquinone oxidoreductase subunit S4	*Ndufs4*
neurovascular unit	NVU
non-human primates	NHP
nuclear magnetic resonance	NMR
oxygen saturation	SO_2
Parkinson's disease	PD
passive cavitation detector	PCD
peak negative pressure	PNP
percent increase in life span	%ILS
permeability-glycoprotein	P-gp
plasmid DNA	pDNA
polyethylene glycol	PEG
polymerase chain reaction	PCR
positron emission tomography	PET
pseudo-continuous arterial spin labelling	pCASL
pulse repetition frequency	PRF
rapid acquisition with relaxation enhancement	RARE
region of interest	ROI
repetition time	TR
signal to noise ratio	SNR
small animal radiation research platform	SARRP
smooth muscle actin	SMA
stable cavitation detection	SCD
sterile inflammation response	SIR
T1-weighted	T1-w
T2*-weighted	T2*-w
T2-weighted	T2-w
tight junctions	TJs
time to peak	TTP
transforming growth factor beta	TGF-β
tumour necrosis factor	TNF
ultrasmall paramagnetic iron oxide	USPIO
ultrasound	US
vascular endothelial growth factor	VEGF
vascular smooth muscle cells	VSMCs
vessel size index	VSI
zona occludens	ZO

General introduction

In 2021, the central nervous system (CNS) diseases affected more than one in three people, as reported by the esteemed journal The Lancet Neurology. Among these diseases, Parkinson's disease, Alzheimer's disease (AD), and brain tumours represent three of the most prevalent conditions, with respective prevalence increases of 100%, 110%, and 210% since 1990 [Steinmetz *et al.*, 2024]. A multitude of clinical trials have failed to demonstrate improvements in outcomes, despite the fact that numerous therapeutic molecules have shown efficacy *in vitro* or in preclinical models [Angeli *et al.*, 2019; Brahmachari *et al.*, 2017; Rousseau *et al.*, 2007]. One of the main factors contributing to this is the significant barrier that the blood-brain barrier (BBB) represents in facilitating the passage of drugs into the brain. The CNS is effectively protected by the BBB, which serves as a frontier to maintain brain homeostasis and prevent the brain from harmful pathogens. It has been demonstrated that more than 98% of large molecules (with a molecular weight greater than 500 Da) are prevented from entering the CNS by the BBB [Pardridge, 2005].

Consequently, the majority of therapeutic compounds that have been developed, including the antibody aducanumab for AD, carboplatin and other chemotherapeutic compounds for glioblastoma (the most aggressive type of brain tumour with a very poor prognosis) are unable to cross the BBB [Jacobs *et al.*, 2010; Pardridge, 2019]. The combination of focused ultrasound (FUS) with gas microbubbles (MB), approved for clinical use as a contrast agent for ultrasound imaging, has recently demonstrated encouraging outcomes in terms of BBB permeabilisation in patients and, more recently, enhanced aducanumab delivery in AD, trastuzumab in brain metastases from breast cancer and carboplatin in glioblastoma [Carpentier *et al.*, 2024; Lipsman *et al.*, 2018; Meng *et al.*, 2021b; Rezai *et al.*, 2024]. FUS has the capacity to target any brain structure with millimetre precision, thereby enabling the controlled and safe delivery of drugs to the targeted brain regions. However, this technology is still in its infancy, with less than 100 published articles on BBB permeabilisation in patients (PubMed research query: "human" AND ("fus" OR "focused ultrasound") AND "bbb" AND ("opening" OR "permeabilised" OR "delivery"), n = 97, 01/08/2024).

A substantial part of preclinical research has been conducted to assess the efficacy of FUS-mediated BBB opening for the delivery of a range of drugs, including chemotherapeutics and gene therapies [Felix *et al.*, 2021; Wei *et al.*, 2021]. Few articles have evaluated the secondary bioeffects of FUS parameters that were later deemed unsafe, demonstrating significant damage after the procedure [Weng *et al.*, 2011; Yang *et al.*, 2010]. This evidence illustrates the potential adverse effects that can occur if the technique is not fully controlled. Other researchers have reported dysregulation following FUS procedures even in the absence of obvious strong damage, such as haemorrhages [Ji *et al.*, 2021; McMahon and Hynynen, 2017]. In addition, the number of features assessed after BBB opening is still relatively limited, given the recent emergence of interest in this technology. Plus, it is reasonable to assume that FUS in combination with MB has a direct impact on the functioning of the neurovascular unit.

To provide initial answers, different studies have evaluated the cellular effects of FUS-induced BBB opening with MB in the brain [S. Chen *et al.*, 2021], tried to decipher vascular variations and functional alterations using magnetic resonance imaging (MRI) [Todd *et al.*, 2019, 2018], and measured the temporal evolution of these changes using two-photon imaging and MRI [Labriji *et al.*, 2023; Raymond *et al.*, 2007]. MRI is the imaging modality of choice for both fin-scale imaging of brain structures and

measurement of quantitative parameters. Moreover, recent work has been carried out to improve the measurement of cerebral perfusion without contrast agent [Hirschler *et al.*, 2018] and quantitative vascular parameters [Troprès *et al.*, 2015] with novel fast MRI methods as provided by the fingerprint approach [T. Christen *et al.*, 2014; Lemasson *et al.*, 2016; Ma *et al.*, 2013]. There is a lack of knowledge regarding these microvascular parameters following the permeabilisation of the BBB by FUS.

To address this gap, in this thesis, we first investigated the assessment, quantification and dynamics of a range of microvascular parameters, including cerebral perfusion, oxygen levels and vascular properties, utilising innovative quantitative MRI approaches. We also used histological techniques to assess the associated cellular effects. This was done to elucidate the secondary effects and modifications following FUS-induced BBB permeabilisation, which have hitherto remained unclear. Secondly, we applied FUS to animal models of rare diseases, autism and aggressive brain tumours with the aim of improving the delivery of therapeutic agents and thus the outcome in animals.

This thesis was conducted in an interdisciplinary and stimulating environment, which forms part of a tripartite collaborative project involving the company Image Guided Therapy (Pessac, France), the Grenoble Institut des Neurosciences laboratory (Grenoble, France) and the LI²RSO laboratory (Orléans, France).

The present manuscript is organised in eight main chapters.

Chapter 1 introduces the FUS in the broader context of medical ultrasound, presents the primary preclinical studies, highlights the main parameters that influence BBB opening with FUS, and outlines the monitoring and control of BBB opening by imaging techniques and cavitation studies.

Chapter 2 presents a comprehensive and up-to-date review of the major side effects that have been investigated in both preclinical and clinical studies to date. To this end, we have analysed a substantial number of articles with the aim of identifying the gaps in knowledge that would allow a more complete understanding of the underlying mechanisms.

Chapter 3 presents the general problems and objectives of this thesis.

Chapter 4 of this thesis describes the various methods used throughout the research process, including the characterisation of the FUS transducer, the MB and the MR-guided device. It also presents the MRI sequences and image processing pipelines used to characterise the microvascular changes induced by the application of FUS.

Chapter 5 presents a preclinical investigation of the secondary bioeffects of a single FUS-induced BBB opening. This study, published in the peer-reviewed journal *Theranostics*, aims to evaluate the transient perfusion and cellular changes that occur following BBB opening. In this study, we quantified cerebral perfusion, blood volume fraction, water diffusion and several vascular and neuroinflammatory cellular markers in different brain regions.

Chapter 6 presents a preclinical investigation of the secondary bioeffects of multiple MR-guided FUS-induced BBB openings using quantitative MRI. Multiple BBB openings may be required for drug delivery, for example in the context of chemotherapy. This study, performed in small healthy rats, used a novel quantitative MRI approach, called MR vascular fingerprinting [T. Christen *et al.*, 2014; Lemasson *et al.*, 2016; Ma *et al.*, 2013], to monitor a wide range of parameters longitudinally. These included

cerebral perfusion, tissue oxygen saturation, water diffusion, mean vessel radius, blood volume fraction and BBB permeability.

Chapter 7 presents a study using a glioblastoma rat model to assess the biodistribution of carboplatin, a chemotherapeutic agent, after permeabilisation of the BBB. The efficacy of this treatment in combination with a single dose of radiotherapy after FUS was also evaluated.

Finally, Chapter 8 is dedicated to the evaluation of innovative gene delivery strategies using the preclinical experimental setup. We conducted a study in *Fmr1*^{KO} mice, a model of Fragile X syndrome the second most common neurodevelopmental CNS disorder. The aim was to investigate the effect of FUS-mediated adeno-associated virus delivery throughout the brain on the outcome of these mouse models.

Finally, we will conclude with a general discussion and conclusion that summarises the key findings and explores the broader implications of the research presented in this thesis.

Chapter 1. Introduction to Focused UltraSound for blood-brain barrier permeabilisation

1.1. Focused ultrasound in the landscape of medical ultrasound

Ultrasound refers to sound waves with frequencies higher than the upper audible limit of human hearing, typically above 20 kHz. These waves share the same physical properties as audible sound waves but can be used for different applications due to their higher frequency. The shorter wavelengths of ultrasound waves, in comparison to those of audible sound, permit the resolution of smaller structures. The frequency (f) of an ultrasound wave is inversely related to its wavelength (λ) through the speed of sound (c) in the medium:

$$\lambda = \frac{c}{f} \tag{1}$$

In human soft tissues, the speed of sound is approximately 1540 m/s. Ultrasound waves propagate through a medium by compressions (high acoustic pressure) and rarefactions (low acoustic pressure) of the medium. The propagation speed depends on the medium's density and elasticity. When an ultrasound wave encounters a boundary between two different media, part of the wave is reflected back, and part is transmitted through the boundary, potentially changing direction (refraction). As ultrasound waves travel through tissue, they lose energy due to absorption, scattering, and reflection, leading to attenuation. Higher frequency waves attenuate more rapidly. Acoustic impedance (Z) is the resistance of a medium to the propagation of sound and is given by:

$$Z = \rho c \tag{2}$$

where ρ is the density of the medium. Mismatches in impedance at boundaries cause reflections.

The development and use of ultrasound in the medical field have a rich history spanning several decades. In the 1920s, theoretical foundations were established by Paul Langevin and the echo-sounding principles [Langevin, 1924]. Ultrasounds were quickly derived for medical imaging diagnostic purposes and specifically to image the brain. The numerous methodological developments in ultrasound imaging now permit the quantitative imaging of the brain with an unprecedented spatial resolution [Errico *et al.*, 2015] but also change in tissue elasticity and thus diagnose thyroid nodules [Sigrist *et al.*, 2017]. In contrast to ultrasound imaging, which typically employs large, unfocused arrays of ultrasound transducers, the advent of focused ultrasound (FUS) arrays enables the utilisation of multiple ultrasound waves that converge at a designated focal point, thereby achieving a concentration of energy at that point. To focus the ultrasound waves, an array of transducers can be electronically controlled to adjust the phase and amplitude of the ultrasound waves they emit. The aforementioned control enables constructive interference of the waves at the focal point, thereby creating a high-energy spot. This capability enables precise targeting within the body without significantly affecting surrounding tissues in the case of high amplitude ultrasound. FUS has a range of medical applications due to its ability to deliver targeted energy non-invasively: tumour ablation by heating locally the cancerous tissues [Coluccia *et al.*, 2014], create lesions in the ventral intermediate nucleus of the thalamus to treat essential tremor [Elias *et al.*, 2016], activation of thermosensitive

proteins [Rome *et al.*, 2005] and modifying neural activity for therapeutic effects [Beisteiner *et al.*, 2020].

The introduction of ultrasound contrast agents (CA) in the vascular system, first developed for ultrasound imaging in the 80's [Frinking *et al.*, 2020] coupled with low intensity focused ultrasound has emerged as a new therapeutic strategy to overcome biological barriers such as the blood-brain barrier (BBB) or the blood-spinal cord barrier and thus improving the delivery of therapeutic drugs locally [Meng *et al.*, 2021b; Montero *et al.*, 2019].

1.2. The neurovascular unit and the blood-brain barrier

The brain is the most oxygen consuming organ in the human body, accounting for an estimated 20% of total oxygen intake, while it represents only 2% of the body weight. O_2 is carried by red blood cells through the vascular system. From the heart to the brain, the arterial blood is carried first by the aorta, then by the common carotid arteries, which become the internal carotid arteries (4-6 mm diameter in Human), and by the vertebral arteries. Those four arteries converge to feed the circle of Willis, a polygonal-shaped arterial anastomosis at the base of the brain, before being evenly distributed to both hemispheres. From the circle of Willis, the middle cerebral arteries (2-3 mm), one of the largest arteries feeding the brain, is the entrance to a series of increasingly fine vessels, starting for the cortex with the so-called pial arterioles (200-1000 µm), penetrating arterioles (40-50 µm), intraparenchymal arterioles (20-30 µm) and the smallest structure capillaries (6-7 µm) (Figure 1). Arteries and arterioles are composed of an endothelium surrounding the vessel lumen, surrounded by layers of vascular smooth muscle cells (VSMCs), elastic lamina, perivascular nerves, into the subarachnoid space. Small penetrating arterioles have the same structure, but the VSMCs are reinforced by perivascular macrophages and astrocytes [Schaeffer and Iadecola, 2021]. A network of venules and veins, with increasing diameter, drain the blood outside of the brain but will not be described here. In between the arterioles, the venules and the capillaries constitute the richest microvascular network with the largest surface area for blood-brain exchange (120 cm^2/g) [Kisler *et al.*, 2017]. At the level of capillaries, the exchange structure is known as the BBB (Figure 2) and is composed of brain endothelial cells (ECs) maintained by tight junction proteins, pericytes, astrocytic end-feet and neurons [Abbott *et al.*, 2010]. These different structures are part of the neurovascular unit (NVU) and ensure brain homeostasis, proper supply of nutrients to the parenchyma as well as cerebral blood flow (CBF) regulation [Kisler *et al.*, 2017]. CBF is regulated along the NVU via the VSMCs whose structure varies from arteries with multiple layers of VSMCs to arterioles with 1 to 3 layers of VSMCs. In the capillaries, the VSMCs are replaced by the pericytes that ensure the contractile and vasodilation functions of the vessels [Schaeffer and Iadecola, 2021].

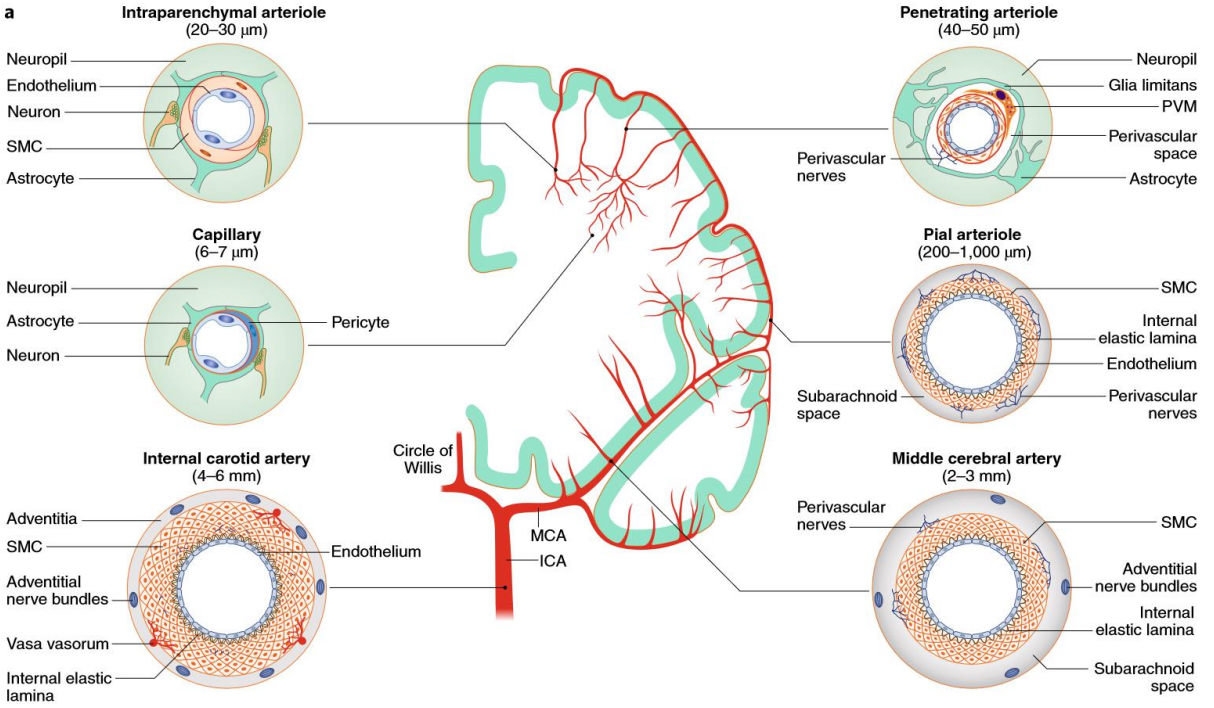


Figure 1. Overview of the brain vascular structure and the neurovascular unit complex for the different vessels supplying blood to the brain [Schaeffer and Iadecola, 2021].

VSMCs regulate intravascular pressure through the myogenic response phenomenon, with increased Ca^{2+} levels leading to an increase in arterial pressure [Lidington *et al.*, 2018]. Connected to the neurons via "boutons", a synaptic-like transmission between neurons and VSMCs, to ensure the passage of neuromediators as well as the regulation of glutamate levels through Glu-NsMJ enable the vasodilation and vasoconstriction actions [Zhang *et al.*, 2024]. Pericytes, which are located within the capillaries, constitute part of the mural cells, along with the VSMCs. They are responsible for maintaining the stability of the vascular wall and regulating the CBF [Kaplan *et al.*, 2020; Sweeney *et al.*, 2016]. The relaxation and contraction of pericytes is mediated respectively through its hyperpolarisation (releasing K^+) and depolarisation (increase in Ca^{2+}) [Kisler *et al.*, 2017]. Other molecules such as nitric oxide, a soluble gas generated by nitric oxide synthase, is involved in pericyte relaxation and capillaries dilation [Yang *et al.*, 2003]. Pericytes are of great importance regarding BBB permeability as pericyte-deficient mice showed an increased BBB permeability to low and high molecular weight tracers and thus play a major role in BBB integrity but also in the development with an attractive role of astrocytic end-feet to form the BBB [Armulik *et al.*, 2010; Daneman *et al.*, 2010; ElAli *et al.*, 2014]. Still, little is known about their spatial transcriptomic profile and the potential existence of different pericytes subtypes that could be the source of explanation of many unknown mechanisms.

ECs are the closest cells to the vessel lumen and its genetic profile evolves through the vasculature cascade, but also depends on the brain regions with a different gene expression profile between hippocampus and cortex for example. The ECs forming the BBB are different in morphology and function from the ECs found in other vessels [Reese and Karnovsky, 1967; Westergaard and Brightman, 1973]. Apparition of these ECs with angiogenesis process begins in mice at embryonic day E9 and ends at day E15 with a decrease in ECs fenestrations and the apparition of TJs and the reduction of transcytosis [Møllgård *et al.*, 2017; Zhao *et al.*, 2015]. The ECs continue to mature under the influence of the pericytes, astrocytes and neurons. Because of a hindered paracellular pathway with the

presence of the TJs, a variety of transcytosis phenomena take place to ensure parenchyma supply (Figure 3): active efflux pumps, carried-mediated transporters, receptor-mediated transporters, adsorption-mediated transporters, ion transporters and cell-mediated transporters [Abbott *et al.*, 2010, 2006; Wu *et al.*, 2023].

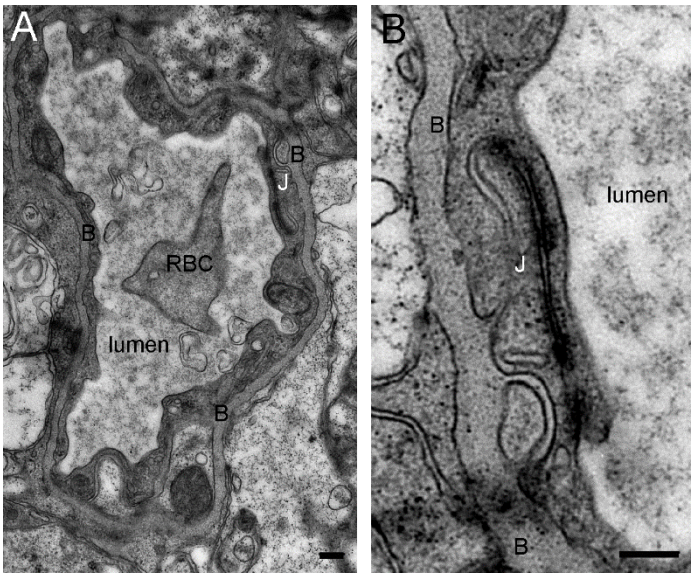


Figure 2. Transmission electron microscopy of the BBB. A) Transverse section of control capillary. The capillary wall is formed by thin endothelial cells that are connected by tight junctions (J), which appear with a higher density. Surrounding the capillary is a basal lamina (B) beyond which is a covering of astrocytic processes. RBC = red blood cell. B) Detail of the tight junction in a healthy capillary. Bar: 200 nm (From [Pernet-Gallay et al.*, 2017]).*

TJs are composed of transmembrane and cytoplasmic proteins including three main families, the claudins, the occludins and the junction adhesion molecules. They provide a dense array impeding most of the paracellular pathway between the ECs, still, some substances can cross the BBB and reach the CNS [Brasnjevic *et al.*, 2009]. These three families are scaffolded by zona-occludens (ZO) proteins at the cytoplasmic surface of the ECs [Bauer *et al.*, 2010]. Actually, very little is known about their role, importance in the level of impermeability and specificity to the BBB. One of the main hypotheses is that the high presence and expression of TJs at the level of ECs forms a dense network. For example, many dysregulations of TJs proteins did not lead to high levels of BBB permeability as occludin [Saitou *et al.*, 2000, 1998], ZO-1, ZO-2, ZO-3 [Katsuno *et al.*, 2008; Umeda *et al.*, 2006; Xu *et al.*, 2008], claudin-3 and claudin-12. The presence of some proteins as claudin-3 and claudin-12 is even still debated [Castro Dias *et al.*, 2019] and did not reveal any role in the function of the BBB [German Mouse Clinic Consortium *et al.*, 2019]. Among claudin's family, claudin-5 has recently attracted attention as numerous studies have evaluated its role at the level of the BBB. The claudin-5 has many regulators as VE-cadherin or glucocorticoid and can be downregulated by growth factors like vascular endothelial growth factor (VEGF) and transforming growth factor β (TGF-β) [Lv *et al.*, 2018]. Claudin-5 dysregulation leads to increase in permeability but only for molecules smaller than 800 Da, maybe due to the impermeability created by the dense network of astrocytic end-feet present around the ECs and TJs. These additional findings suggest the existence of potential compensation mechanisms that would take over from the potential dysregulations and thus maintain the impermeability of the BBB.

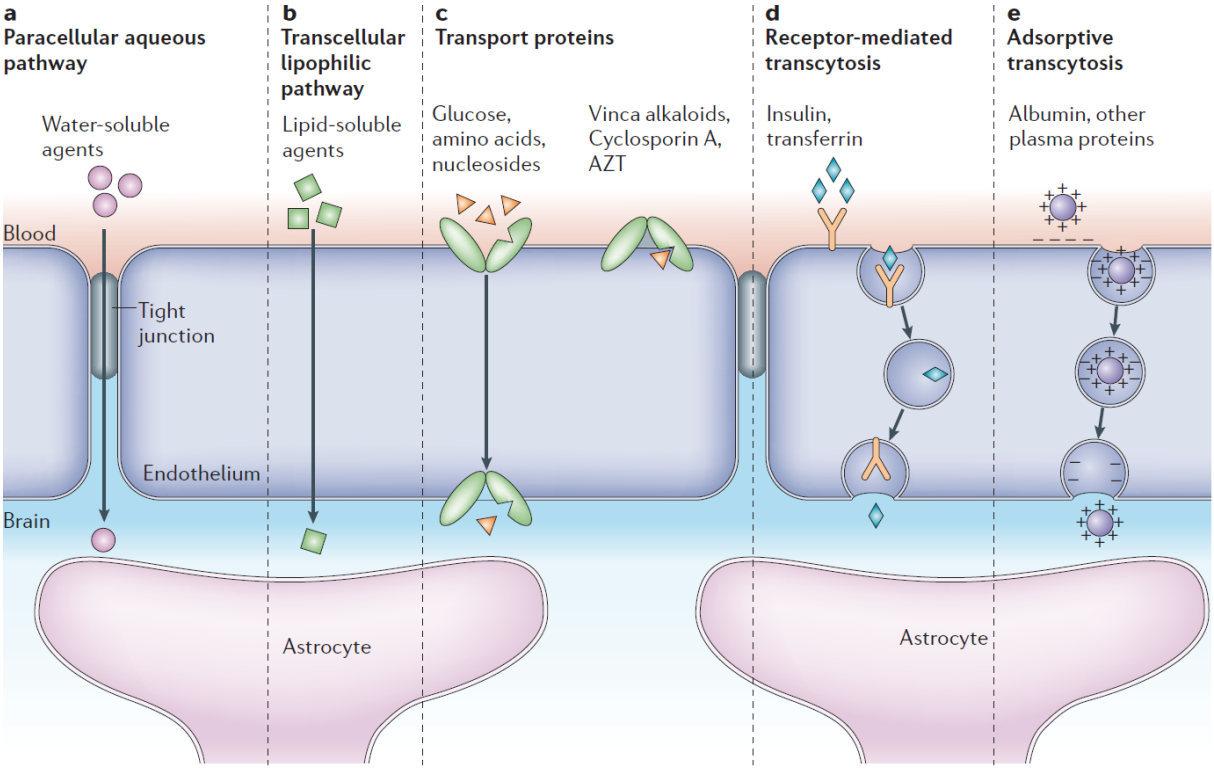


Figure 3. A schematic diagram of the endothelial cells and the perivascular end-feet of astrocytes that form the BBB. The five main routes for molecular traffic across the BBB are shown [Abbott et al.*, 2006].*

Astrocytes are the most abundant cells in the CNS [Kadry *et al.*, 2020] and their role in the NVU and the BBB are not fully understood as various studies lead to opposite conclusions. What is known is the fact that astrocytes widely surround the arterioles and the capillaries in the BBB creating a glia limitans barrier but also a direct interface via astrocytic end feet. The population of astrocytes varies depending on the region of the brain, for example between grey and white matter mediated through the expression of the Aquaporin 4 protein [Mayo *et al.*, 2023; Mazumder *et al.*, 2022; Sofroniew and Vinters, 2010]. Astrocytes play a major role in the BBB integrity during development leading to high coverage of arterioles surface with an increase in discontinuities of the end feet as the arteriole penetrates and again almost no discontinuities in capillaries. It is still debated the fact that astrocytes have an effect on the impermeability of the BBB (space of 20 nm). Two experiments give opposite outcomes with the presence of Ca^{2+} related to vasodilation or vasoconstriction [Takano *et al.*, 2006]. Plus, a recent study showed that astrocytic Ca^{2+} does not regulate arteriolar response [Mishra *et al.*, 2016], reinforcing the controversial implications of astrocytes in the neurovascular coupling at the level of the arteries and the arterioles. The second most abundant type of cell in the brain are immune cells with microglia accounting for 10 to 15% of the cells in the human brain and are the first glial-cell type present during the development of the CNS. The microglia are sentinel cells able to detect first potential CNS aggression and their activation led to repair mechanisms or disruption of the BBB [Shemer *et al.*, 2015]. They upregulate many inflammatory markers such as M1-like that increase inflammation mediators (TNF, IL-1β, ROS) or M2-like to induce repair (IL-10, TGFβ) [Guo *et al.*, 2022]. Completed by mononuclear leukocytes, monocytes and macrophages, they enable a dynamic process through the BBB in order to ensure its integrity and prevent dysregulations.

While most brain regions are protected by the BBB, a few areas - often called the circumventricular organs - are lacking BBB (e.g. the pituitary gland). These regions mostly participate in hormonal control [Byrne, 1997].

Yet, CNS diseases directly impact the NVU and the BBB including multiple sclerosis, hypoxia and ischemia, edema, Parkinson's and Alzheimer's diseases, epilepsy and tumours [Abbott *et al.*, 2010]. This is accompanied with mild to strong neurovascular dysfunctions and a more or less leaky BBB. Indeed alteration of the BBB can take many forms: in cancer the brain vascularisation is remodelled with dysfunctional vasculature, irregular vessels in size, density and permeability [Arvanitis *et al.*, 2020], in stroke (which gather ischemia and/or haemorrhages) the release of MMP9 degrades the TJs complex leading to an increase in BBB permeability (Figure 4.A.iii), which remains opened for several weeks [Neuwelt *et al.*, 2011], in neurodegenerative diseases as AD the amyloid-β plaques are disrupting the major regulatory mechanisms of the cerebral circulation (Figure 4.A.ii) [Iadecola, 2004; Kisler *et al.*, 2017].

MRI is one of the best techniques to finely image the brain structures and detect BBB permeability (Figure 4.B). The utilisation of particular contrast agents that are capable of traversing the BBB enables the visualisation of cerebral regions exhibiting a discernible BBB disruption, as observed in conditions such as amyotrophic lateral sclerosis (Figure 4.C) or brain tumours (Figure 4.D). Damage to the BBB can take several forms, but the principle is that they all lead to an increase in permeability.

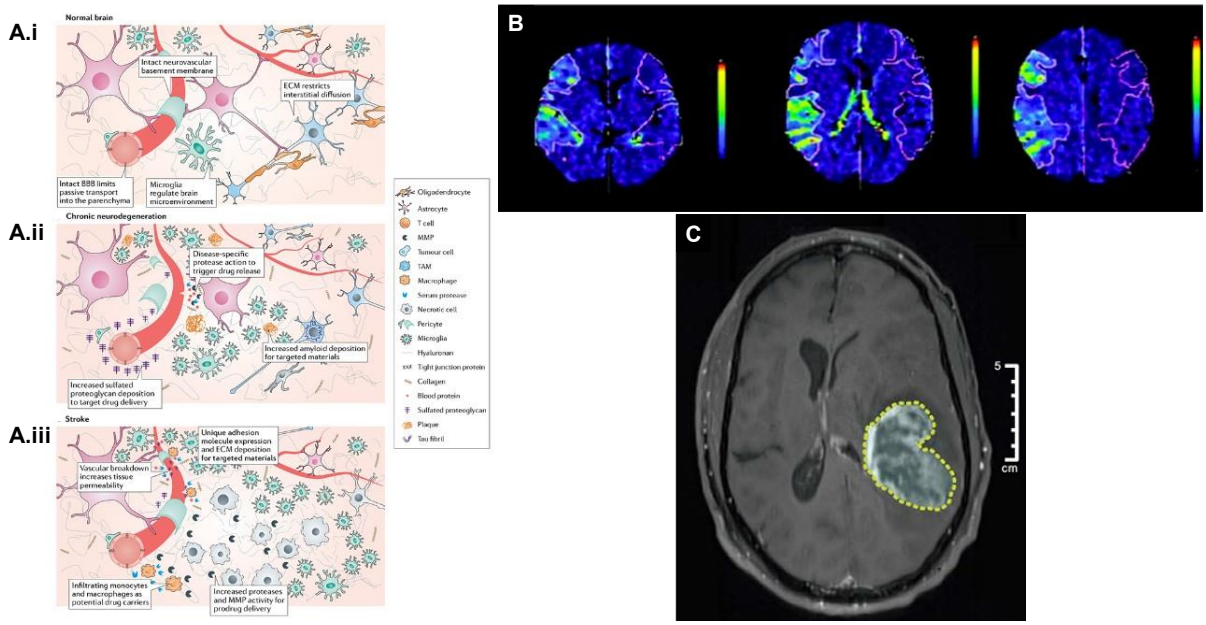


Figure 4. Overview of BBB in pathological conditions. ***A****) Physiological and pathological changes of the central nervous system in chronic neurodegeneration and stroke with the impact of vascular, enzymatic, extracellular, cellular and interstitial barriers on drug delivery is shown in normal brain tissue (****i****), chronic neurodegeneration (****ii****) and stroke (****iii****) [Nance* et al.*, 2022].* ***B****) MRI permeability colour maps showing permeability abnormality in a 75-year-old patient with right middle cerebral artery acute ischemic stroke [Rosenberg, 2012]. C) MRI scan of glioblastoma multiforme (GBM) brain tumour, showing a large mass effect (enhancement within the left temporal lobe, yellow outline) [Nance* et al.*, 2022].*

Compared to other CNS diseases, the BTB poses a genuine challenge to deliver therapeutic agents as it forms its own complex, very different from the BBB, however it is not considered as an autonomous

structure [Steeg, 2021]. The BTB is characterised by a loss of astrocytic end feet, neuronal connections and aberrant pericyte distribution [Dubois *et al.*, 2014]. Brain tumours develop also its proper vascularisation through neoangiogenesis phenomenon facilitated by hypoxia. The newly formed vascularisation network is tortuous with particular branching patterns, it presents large and leaky vessels with a common observation of increased VEGF expression [Quail and Joyce, 2017], a factor known to increase the breakdown of TJs [Argaw *et al.*, 2009]. In addition, the BTB microenvironment, a neuroinflammatory response is triggered, involving astrogliosis and microglia. Together, they form a structure surrounding the tumour to interact with the invading and colonising tumour progression [Steeg, 2021]. Therefore, the BTB is a very heterogeneous frontier with different architecture that rely on the molecular profile of the brain tumour, despite the grey areas regarding the link of the latter mechanisms with this specific heterogeneity [Arvanitis *et al.*, 2020]. In brain tumour metastasis for example, triple-negative have often a disrupted BBB whereas HER2-positive breast cancer metastasis expressing high levels of GLUT1 (glucose transporter 1) and BCRP (breast cancer resistance protein) seems to have an intact BBB [Yonemori *et al.*, 2010]. Numerous animal models have been developed and characterised to better understand the BTB properties as rat tumour models F98, C6 and 9L, providing different insights into the comprehensiveness of the tumour microenvironment. For example, F98 cells are more infiltrative and produce a heterogeneous pattern, whereas 9L or C6 are constricted with a more homogeneous vascularisation pattern [Sahu *et al.*, 2022]. Differences in microvascularisation but also in treatment responses can be characterised with MRI and histological approaches [Lemasson *et al.*, 2016; Valable *et al.*, 2008]. At least as complex as this heterogeneity, the anti-tumour drug cocktail developed in preclinical models includes molecular, cellular and physical approaches.

In conclusion, the increase in BBB permeability observed in pathological conditions permits the passage of a limited number of drugs. However, their distribution remains suboptimal, and the delivery of therapeutic agents is heterogeneous and challenging. The use of FUS coupled with MB represents a promising approach to addressing this challenge.

1.3. Other strategies to cross the blood-brain barrier

The BBB highly protects the brain, therefore finding different ways to cross the BBB is of great interest to deliver therapeutic compounds to the CNS in order to improve patient outcome. Many mechanisms were tested to either permeabilise the BBB on a global or spatially limited basis and a large range of engineered materials to borrow the natural mechanisms of transcellular and paracellular transport through the BBB. Part of these mechanisms is based on the existing mechanisms that enable the passage of ions, polar molecules (glucose, amino acids), macromolecules (peptides, proteins) via transcytosis [Abbott *et al.*, 2010]. Moreover, other delivery routes and external technologies showed enhanced drug delivery to the brain. Additionally, engineering new materials to encapsulate drugs, manage targeting specific ligands, proteins or CNS diseases specific receptors is of great interest to improve the BBB passage and move even closer to personalised medicine. In this paragraph we stressed out the different drug delivery methods to the CNS.

One of the first methods to induce BBB permeabilisation was based on the osmotic phenomenon with carotid infusion of 1.6 molal of arabinose or mannitol solution [Neuwelt *et al.*, 1980; Rapoport and Thompson, 1973]. The proposed mechanism at this time was the dehydration of the ECs, leading to water leaving the brain thus inducing vasodilation. Additionally, the increase in intracellular calcium

induces ECs cytoskeleton contraction. This exerted tension on the TJs mechanically widened ECs gap [Rapoport, 2000]. This method not only implies strong modification at the ECs and TJs level but is not spatially specific. For instance, in brain tumours, it is of great importance to specifically deliver the chemotherapy to the tumour to avoid potential toxic effects.

Other routes and external stimuli-mediated BBB permeabilisation demonstrated enhanced drug delivery to the CNS. Among them, the intranasal administration of therapeutic molecules is very effective. The targeting is rapid due to proximity of this organ to the brain. Two main pathways are taken: the olfactory nerve-olfactory bulb-brain (the shortest and most direct) and the trigeminal nerve-brain (because located in the olfactory and respiratory regions). A third minor and indirect route can be used: the lungs/gastrointestinal tract-blood-brain involving the gastrointestinal and respiratory systems [Wu *et al.*, 2023] (Figure 5.A). External stimuli-mediated BBB disruption can also be achieved using light-based near infra-red devices [M. Choi *et al.*, 2011] or low pulse electric fields [Cooper *et al.*, 2023].

Then, taking advantage of the knowledge on the BBB, down regulating TJs expression with the use of minoxidil sulphate improves BBB permeability by anchoring to potassium channels [Gu *et al.*, 2013]. From this, different derived strategies encapsulated this metabolite in nanoparticles coupled with specific tumour receptors at its surface as CD44 breast cancer receptors in order to enhance the delivery of doxorubicin [Han *et al.*, 2016; Miao *et al.*, 2019]. In addition, the utilisation of specific receptors such as transferrin [Ruan *et al.*, 2018] and insulin [Thorne *et al.*, 2004] conjugated with adapted nanoparticles enable transcytosis using the receptor-mediated transcytosis mechanisms offered at the BBB level (Figure 5.B).

All these compounds need specific carriers, which are mainly nanoparticles. We can decipher three main nanoparticle classes: polymeric nanoparticles with easy surface modification, inorganic nanoparticles (iron, gold or silica based core) with unique electrical and magnetic properties and potential toxic effects, and lipid-based nanoparticles with payload flexibility but low encapsulation efficiency [Mitchell *et al.*, 2021] (Figure 5.C-D).

The field of genetic CNS disorders has placed significant emphasis on gene therapies, with a particular focus on recombinant adeno-associated viruses (AAV). These viruses can be genetically modified to deliver DNA to specific target cells, offering a promising avenue for potential treatments. A novel variant, AAV-PHP.B, has recently been shown to be capable of transferring genes throughout the central nervous system in mice without BBB opening [Deverman *et al.*, 2016]. This novel variant has opened new avenues for the treatment of rare genetic diseases however such variants do not exist for humans. AAV9 seems to be the best variant for CNS transduction even though BBB opening increases its transduction levels [Nonnenmacher *et al.*, 2021; Song *et al.*, 2022]. For instance, Reynaud-Dulaurier *et al*. demonstrated the potential to extend the lifespan of *Ndufs4* KO mice, a model for Leigh syndrome [Reynaud-Dulaurier *et al.*, 2020]. Nevertheless, this approach has not yet been implemented in clinical practice, and further investigations are required to assess its toxicity, immunogenicity, and pattern of expression, in order to fully integrate this gene therapy into clinical protocols [Hordeaux *et al.*, 2018].

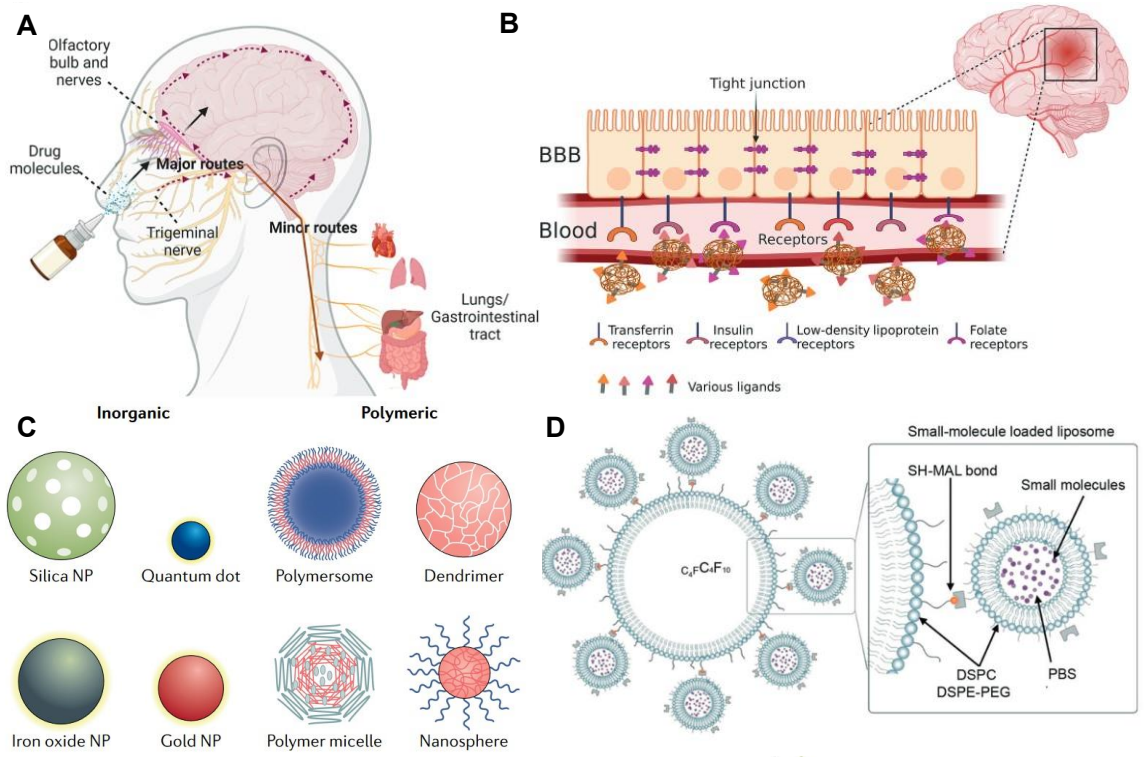


*Figure 5. Overview of BBB drug delivery alternatives with intranasal technique delivery (**A**), ligand-receptor mediated delivery (**B**) and the three main nanoparticle classes: inorganic, polymeric (**C**) and liposome-based nanoparticles (**D**) [Mitchell* et al.*, 2021; Wu* et al.*, 2023].*

1.4. Focused ultrasound for blood-brain barrier opening

Historically employed for medical imaging and rapidly for therapeutic applications such as tissue ablation with high-intensity focused ultrasound, the advent of ultrasound contrast agent marked a pivotal turning point in the field. Apfel *et al*. established the relationship between acoustic cavitation and its utilisation in the biomedical field for the first time. They emphasised the distinction between the utilisation of moderate amplitudes, which induce a slight alteration in bubble size, and high amplitudes, which induce a radical transformation in bubble dynamics, thereby potentially facilitating the exploration of disparate applications [Apfel, 1982]. Miller and Thomas demonstrated the capacity of ultrasound contrast agent to serve as nuclei for inertial cavitation [Miller and Thomas, 1995]. Furthermore, the characterisation of ultrasound contrast agent facilitates a more comprehensive understanding of their cavitation properties, thereby opening avenues for exploring additional biomedical applications beyond imaging [Chen *et al.*, 2000; Krishna *et al.*, 1999].

The concordance of these studies has led to the publication in 2001 of the first reversible non-invasive BBB opening with FUS in rabbits with MRI control and the injection of a gadolinium (Gd) based contrast agent [Hynynen *et al.*, 2001]. This study opened up a new field of FUS application in medicine. Quickly, the search for the best acoustic properties and parameters for safe, efficient BBB opening and therefore enhance drug delivery with the study of histological investigations and cavitation-based correlations [Chen *et al.*, 2003b; Giesecke and Hynynen, 2003; Hwang *et al.*, 2006; McDannold *et al.*, 2005, 2006]. The feasibility of FUS-induced BBB opening was demonstrated in mice [James J. Choi *et al.*, 2007], rats [Treat *et al.*, 2004], ovine [Yoon *et al.*, 2019], NHP [Kamimura *et al.*, 2019; Marquet *et al.*, 2011] and humans [Lipsman *et al.*, 2018; Meng *et al.*, 2021b].

The number of publications utilising this methodology has grown exponentially. This section will delineate the fundamental principles of BBB opening, its characteristics, methods to monitor the FUS-induced BBB permeabilisation, the available systems, and the diverse applications thereof.

Briefly, the BBB opening with FUS principle relies on the injection of gas MB (Figure 6.A). When these MB are injected intravenously, they distribute into the venous system homogeneously. Under the influence of an acoustic field, MB will undergo cavitation at very high frequency (~ MHz) (Figure 6.B). This cavitation induces a mechanical stress on the surrounding environment of the MB and when this mechanism occurs close to biological membranes, it will destabilise the surrounding environment including the TJs, the ECs and the rest of the NVU complex (Figure 6.B-C). Thus, FUS coupled with gas MB can permeabilise biological membranes. When applied to the brain, the cavitation will induce a transient opening of the BBB. Many preclinical studies have evaluated the range of parameters that induce a safe and reversible BBB opening. Yet, the permeabilisation is not fully understood and could take several forms. As highlighted in Figure 6.C the destabilisation of the TJs is one of the consequences of BBB permeabilisation.

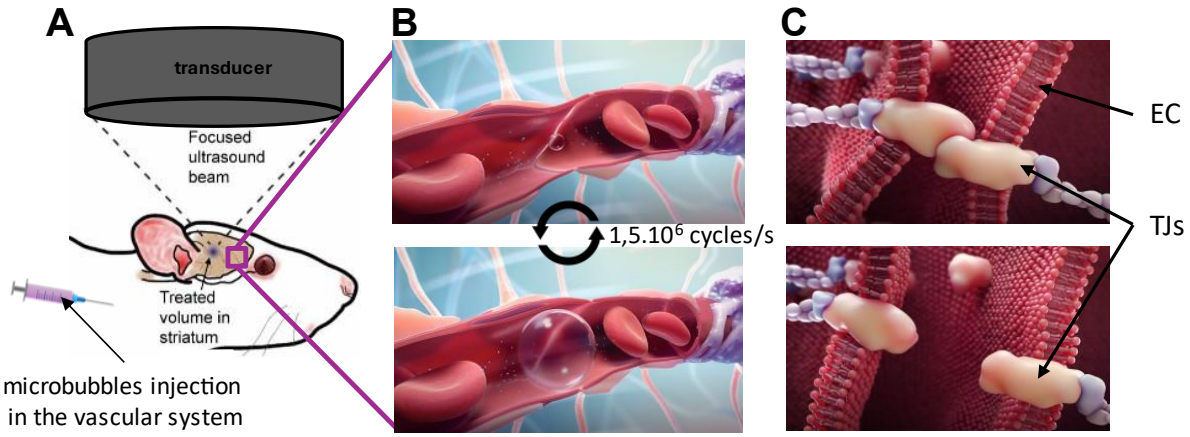


*Figure 6. Principle of the BBB opening with FUS and MB. **A**) the MB are injected in the vascular system and the focalised transducer deliver precisely acoustic energy in the brain. **B**) The MB oscillate at very high frequencies (~ MHz). **C**) The mechanical stress induced by the MB destabilise the TJs. Adapted from https://www.youtube.com/watch?v=r6Sx9y8eytk&ab_channel=HangYuLin.*

1.4.1. Monitoring of the blood-brain barrier opening and closure dynamics

MRI is the preferred method for monitoring the BBB status in many CNS pathologies. This is achieved through the use of gadolinium-based CA, which are small molecules (approximately 1 nm in hydrodynamic diameter) capable of diffusing throughout a compromised BBB. MRI has demonstrated great importance for FUS-induced local drug delivery [Deckers *et al.*, 2008] and has been the gold standard for providing high-resolution and quantitative information following BBB opening. Gadolinium is a paramagnetic contrast agent that shortens the longitudinal relaxation times of nearby hydrogen protons, thus increasing signal intensity in T1-weighted sequences. Different MRI sequences have been used to monitor the BBB opening, spin echo, T1 map [Marty *et al.*, 2012] and dynamic contrast enhancement (DCE) [Vlachos *et al.*, 2010] sequences in combination with Gd-based CA. Superparamagnetic iron oxide contrast agent induce strong local magnetic field inhomogeneities and primarily affect transversal and apparent transverse relaxation times (T2 and T2*) causing a reduction in signal in T2-weighted images. The use of SPIO-contrast agent demonstrated also their ability to

monitor the BBB opening but the acoustic pressures used weren't safe (1.1 to 3.5 MPa at f = 1.5 MHz). Good MRI signal destruction was observed after the injection of the contrast agent and volume of BBB opening was correlated with the acoustic pressure. Long-term persistence of leaky blood vessels could be assessed up to 60 minutes [Liu *et al.*, 2009].

Other MRI sequences specific to FUS applications to the brain were quickly developed as acoustic radiation force imaging (ARFI). This novel strategy to monitor the FUS focal point without the use of MB or contrast agent has been described [McDannold and Maier, 2008] and implemented in MRI compatible FUS devices in order to guide FUS in the brain of rodents [Larrat *et al.*, 2010]. This sequence is acquired along with application of high acoustic pressure and very short ultrasound pulses (around 6 MPa during 3 ms) and synchronised with two motion sensitive gradients (MSG) placed symmetrically from the refocalisation pulse. Information about the acoustic radiation force induced displacement is recovered from the gyromagnetic ratio, the period of the MSG, the gradient magnitude and phase image. This method enables safe and reliable monitoring of the focal point localisation without any contrast agent. In this approach, high acoustic pressures do not induce heating due to the very short ultrasound pulse length.

Other methods have been evaluated to demonstrate BBB opening effectiveness as MRI can be hardly accessible and is expensive [Arnold *et al.*, 2023]. For example, positron emission tomography (PET) imaging [Chevaleyre *et al.*, 2023; Hugon *et al.*, 2021; Porret *et al.*, 2023], ultrasound imaging [Samuel *et al.*, 2009; Singh *et al.*, 2022], or other light-based non-invasive method as bioluminescence were demonstrated to be effective [Sabbagh *et al.*, 2021] or bi-photon imaging coupled with fluorescence dextran dyes [Raymond *et al.*, 2007]. PET imaging remains a method involving the injection of radioactive tracer: it is very sensitive but requires a dedicated environment to safely manipulate radioactivity. Bioluminescence can be very useful in small animals but with poor light penetration through the skin, it has limited efficacy regarding the translation to clinics.

Furthermore, the combination of different MRI sequences and contrast agent facilitates a comprehensive characterisation of the BBB opening, enabling precise measurement of drug delivery concentrations in the brain and the elucidation of the mechanisms of closure.

The gadolinium-enhanced MRI images were compared to histological slices following the intravascular injection of Evans blue dye, the dye involved in the discovery of the BBB by Ehrlich in 1878. Results showed good correlation between normalised MRI signal intensity change and Evans blue extravasation level, suggesting that *in vivo* MRI and gadolinium provide a good metric to evaluate the number of chemotherapeutic agents delivered. This study also demonstrated for the first time that an increasing acoustic pressure enhances the % change in signal intensity (from 15% at 1.43 W to 48% at 4.29 W) and that delaying from 0 to 60 min the injection of Evans blue and MRI contrast agent diminishes the change in signal intensity [Yang *et al.*, 2010]. These results suggested for the first time an initial order of magnitude regarding the BBB closure dynamics. Confirmation by Weng *et al*. with small haemorrhages present that gadolinium enhancement was visible in the region of applied FUS at 0.54 MPa [Weng *et al.*, 2011].

Marty *et al*. characterised the extravasation of different MRI contrast agent from immediately to 24 h after FUS application, using an acoustic pressure of 0.45 MPa (f = 1.5 MHz). The range in diameter of the contrast agent varied from 1 to 150 nm. They demonstrated a relationship between the hydrodynamic diameter (d_H) of the contrast agent and the BBB half closure time. They pointed out that

large molecules shall be injected immediately after FUS to reach a good extravasation into the CNS. The acquisition of T1 maps before and after the injection of the different contrast agent enabled the computation of an apparent contrast agent concentration in the brain. For small contrast agent agents as Gd-DOTA ($d_H \sim 1$ nm), half closure time was estimated to 5.5 h whereas for larger contrast agent as P846 (a larger gadolinium chelates, $d_H \sim 4$ nm) and P904 (SPIO nanoparticle, $d_H \sim 21$ nm) half closure time was estimated respectively to 1.5 h and 3 min [Marty *et al.*, 2012]. Chai *et al*. confirmed these results using a DCE-MRI sequence and extended Kety model fit and the calculation of the k_{trans} parameter. They measured half times of 2.9 h and 5.3 h for FUS induced BBB opening at 0.4 and 0.8 MPa (f = 0.4 MHz) and very similar times for Evans blue extravasation [Chai *et al.*, 2014]. We can see that the dynamics of closure depends on the peak negative pressure (PNP) and the size of delivered particles. For standardisation purposes, the mechanical index (MI) has been introduced as the PNP divided by the root square of the driven acoustic frequency in megahertz. The MI is a parameter used in ultrasound imaging to estimate the likelihood of non-thermal bioeffects, such as cavitation (see 1.5), occurring in tissues exposed to an acoustic wave. A higher MI indicates a higher risk of cavitation due to increased mechanical forces on MB, which are more likely to collapse and cause bioeffects. By incorporating frequency into the MI calculation, it provides a standardised way to assess cavitation risk across different ultrasound systems and settings. Thus, the dynamics closure depends on the MI. The low MI observed by Marty *et al*. (MI = 0.37) contrasts with the high MI reported by Chai *et al*. (MI = 0.63 and 1.27). However, the different quantities of MB used in the two studies make direct comparison of the two studies challenging. It is plausible that the lower quantity of MB used by Chai *et al*. may have compensated for the higher MI.

Confirmations by Chu *et al*. that evaluated a large range of MI (0.41, 0.43, 0.56, 0.83 and 1.12) using DCE-MRI and the same Kety model to estimate k_{trans} measured very good correlation between the MI and the half-closure time, from 2.5 h (MI = 0.41) to 4.5 h (MI = 1.12). The dose of MB (0.2 mL/kg) was 100 times higher than in the Chai *et al*. study (2.4 µL/kg) and 10 times lower than the one used by Marty *et al*. (2 mL/kg), explaining the differences in closure-time dynamics [Chu *et al.*, 2016].

The studies demonstrated an effective method for accessing the pharmacodynamic and pharmacokinetic properties of drugs across the open BBB, providing valuable insights into the essential parameters for delivering drugs of varying sizes, including carboplatin ($d_H \sim$ 1-5 nm), recombinant AAV ($d_H \sim 20$ nm), and plasmid DNA (pDNA) ($d_H \sim 200$ nm), within a specific time window. It is also noteworthy that different types of permeabilisation are induced by FUS and MB. This was highlighted by Raymond *et al*., who employed two-photon imaging to study the extravasation of dextran dyes. Their findings indicated the existence of two distinct modes of extravasation, a slow process occurring over minutes and a rapid process occurring over seconds. This suggests that FUS-induced BBB permeabilisation exerts a significant impact on both the paracellular route and the transcytosis route [Raymond *et al.*, 2007]. Chai *et al*. also evidenced differences in extravasation kinetics with the evaluation of the capillary plasma volume (V_p) and the distribution volume of the contrast agent in the extracellular extravascular space noted Ve. The ratio from both metrics noted K_{ep} described the efflux kinetics, thus the washout rate. Variable K_{ep} showed significantly longer decay than kinetics of k_{trans} and V_e. Spatial variations were also observed, changes in Ve and K_{ep} were larger than k_{trans} changes suggesting also different forms of leakage (fast, sustained and slow) [Chai *et al.*, 2014].

In summary, MRI associated with the use of gadolinium-based CA, is the preferred method for monitoring BBB status, especially in the context of FUS-induced drug delivery. The dynamics of BBB

closure depend on factors like MI and contrast agent size, providing crucial insights into efficacy and mechanisms of drug delivery. Alternative imaging methods are also explored for their practicality and effectiveness.

1.4.2. Parameters that influence the blood-brain barrier opening

Since 2001, a wide range of parameters has been investigated to efficiently permeabilise the BBB. This section will review the parameters that influence the opening of the blood-brain barrier, namely acoustic pressure, pulse length, frequency, frequency, pulse repetition frequency (PRF), ultrasound duration, MB dose and skull heterogeneity.

Hwang *et al.* demonstrated that lowering ultrasound pressure can induce BBB permeabilisation without causing significant damage, as indicated by the absence of hypointense spots on T2*-weighted images [Hwang *et al.*, 2006]. McDannold *et al*. showed that MRI signal enhancement starts at 0.29 MPa PNP without damage, while no enhancement occurs below 0.2 MPa (using 0.05 mL/kg of Optison MB). High pressures correlate with histological damage due to wideband emission, with strong damage observed at 0.57 MPa estimated *in situ* [McDannold *et al.*, 2006].

The skull poses a significant obstacle to effective FUS delivery in the brain. Choi *et al.* found no significant difference in the FUS beam with and without the skull *in vivo* and through numerical simulations based on CT scans. They measured an 18% attenuation due to the skull by targeting the hippocampus in mice [James J. Choi *et al.*, 2007]. Gerstenmayer *et al*. measured the acoustic transmission of degassed rat skulls and found strong inhomogeneities based on target location and transducer frequency. Lower frequencies improved acoustic transmission as well as thinner skulls. These findings suggest that rat body mass, correlated to the mean skull thickness, can be used to adjust acoustic pressure precisely [Gerstenmayer *et al.*, 2018]. O'Reilly *et al*. highlighted that rat skull geometry can lead to standing ultrasound waves, causing nodes of increased pressure and potential damage. Eliminating standing waves by reducing the duty cycle and increasing focal point sharpness was effective in 25% of cases [O'Reilly *et al.*, 2010]. While rodent skulls are relatively simple to overcome with MR-guided FUS, human skulls are thicker and denser, leading to increased attenuation, reflection, and diffraction. Increasing the number of transducer elements and using beam correction simulations can target small, deep brain structures precisely.

Increased pulse length is known to enhance the extravasation of Evans blue dye [Shin *et al.*, 2018] and dextran [James J. Choi *et al.*, 2011] regardless of the pressure [Samiotaki and Konofagou, 2013]. Increased heterogeneity in dextran extravasation with longer pulse length was observed, and O'Reilly *et al*. highlighted a semi-log relationship between pulse length and MRI contrast enhancement [O'Reilly *et al.*, 2011].

Adjusting PRF can modulate the impact of FUS. Tested PRFs from 0.1 to 25 Hz showed that low PRF induced no extravasation of MRI contrast agent or EB, while high PRF values (10, 25 Hz) did not improve results over mild PRFs. A 100% probability of dextran extravasation was observed for PRFs between 5 and 25 Hz, compared to 60% at 1 Hz [James J Choi *et al.*, 2011]. Optimal PRF values between 1 and 5 Hz increase extravasation without raising tissue damage [Shin *et al.*, 2018]. Fletcher *et al.* found that PRF = 0.25 Hz resulted in better dye uptake with reduced damage compared to PRF = 1 Hz, though the mechanism remains unclear [Stecia-Marie P Fletcher *et al.*, 2024]. Broad values of PRF were tested

without finding the best one, yet optimal values seem to be lower than 5 Hz. The potential use of PRF < 1 Hz needs to be furthermore investigated for potentially increasing the safety of the BBB opening.

The total exposure duration significantly impacts contrast agent extravasation, with a plateau effect above 600 seconds [Chopra *et al.*, 2010]. No enhancement was observed between 30 s and 11 min durations [James J. Choi *et al.*, 2011], and sequences exceeding one minute showed increased tissue damage [Shin *et al.*, 2018]. Most single-spot sonication studies use durations of 1 to 2 min [Gattegno *et al.*, 2024; Lim Kee Chang *et al.*, 2023; Shen *et al.*, 2020].

Frequencies ranging from 0.220 MHz, intended for clinical devices, up to few MHz in mice models with diagnostic ultrasound scanner, have demonstrated the feasibility of BBB opening [Bing *et al.*, 2009; Chu *et al.*, 2016; Hynynen *et al.*, 2006; Pouliopoulos *et al.*, 2020]. For preclinical studies frequencies in the range between 0.5 to 1.5 MHz are very appropriate.

MB dosage, formulation, size, injection rate, and timing relative to FUS application are critical for effective BBB permeabilization. We can notice differences among the available MB present on the market. For example, Optison™ and Definity® MB are known to induce different BBB opening patterns when using similar FUS parameters [McDannold *et al.*, 2007] with Optison™ MB more likely to produce haemorrhages for the same MI. In addition, MB diameter has an influence on the BBB opening with MB with larger diameter seem to produce larger and longer BBB opening [Vlachos *et al.*, 2011]. In addition, it is now accepted that increasing the MB concentration increases the risk of haemorrhages due to increased BBB opening intensity [McDannold *et al.*, 2008]. The relationship between cavitation activity and MB is more detailed and discussed in section **Error! Reference source not found.**.

Acoustic pressure	**Pulse length**	**PRF [Hz]**	**FUS duration**	**FUS frequency**
0.2 - 0.6 MPa	1 - 50 ms	1 - 5	30 - 300 s	0.2 - 2 MHz
Species	Mice	Rats	NHP	Humans
Attenuation factor	15% at 1.5 MHz [Felix *et al.*, 2021]	40% at 1.5 MHz [Gerstenmayer *et al.*, 2018] 27% at 558 kHz [O'Reilly *et al.*, 2010]	60% at 600 kHz [Deffieux and Konofagou, 2010]	76% at 600 kHz [Deffieux and Konofagou, 2010]

Table 1. Summary of the safe parameters necessary for efficient drug delivery and skull attenuation factors for mice, rats, NHP and humans based on the analysis of existing literature.

Most FUS-induced BBB opening experiments involving small animals are performed under isoflurane anaesthesia or a mixture of ketamine and xylazine [Chevaleyre *et al.*, 2023; McDannold *et al.*, 2019; Presset *et al.*, 2022; Yang *et al.*, 2014]. McDannold *et al*. investigated the influence of anaesthesia on the BBB opening outcome. They evaluated under two anaesthesia protocols, isoflurane and ketamine/xylazine, and at different acoustic pressures, from 120 to 300 kPa the effect of anaesthesia mixture. Significant difference in MRI contrast enhancement was measured at each tested pressure between the two anaesthesia protocols. Stronger brain damages were visible at a pressure of 250 kPa (MI = 0.34), a pressure known to be safe under isoflurane [McDannold *et al.*, 2011]. The underlying mechanism of these findings was not explained, and many parameters could influence the outcome and must be considered as heart and breath rate, end tidal CO_2, blood pressure and oxygen consumption. Two studies showed that the circulation time of the ultrasound contrast agent was reduced when subjects were breathing 100% oxygen compared to medical air [Itani and Mattrey, 2012;

Mullin *et al.*, 2011]. McDannold *et al*. showed in 2017 that in presence of oxygen, the BBB opening was significantly impeded due to a 1.5-fold increase in the MB clearance rate [McDannold *et al.*, 2017]. In clinics, the delivery of FUS to the brain is performed without anaesthesia and therefore anaesthesia mixture problems will not be encountered, still, the amount of oxygen provided to the patients is of great importance and therefore could impede the safety of the BBB opening and the drug uptake. For further small animal studies, these results are of great importance and must be taken into account as it greatly impacts the quality of the BBB opening, the potential secondary bioeffects and thus the amount of drug delivered.

Numerous parameters such as acoustic pressure, pulse length, frequency, PRF, ultrasound exposure duration, MB dose, and skull thickness heterogeneity have been studied to efficiently permeabilise the BBB. We propose in Table 1 a summary of safe preclinical parameters for opening the BBB using FUS in combination with MB and the corresponding skull attenuation across different species. However, it is crucial to establish a link with the monitoring of acoustic cavitation, as the stability of conditions during treatment is never absolute, and real-time adaptation to the cavitation events is necessary. Currently, this real-time monitoring capability is under development, as cavitation, particularly inertial cavitation of MB, is inherently a stochastic process. As a result, the ability to react promptly to these unpredictable cavitation events is essential to mitigate potential risks and enhance the safety and efficacy of BBB opening procedures.

1.4.3. Therapeutic trials on small animal models

FUS to permeabilise the BBB is of great interest to deliver drugs to the CNS in the past decade, many efforts have been made to study the delivery of therapeutics. Alzheimer's disease, brain tumours and gene delivery for rare brain and spinal-cord diseases have taken most of the attention. Yet, other applications have already been studied in Huntington disease [Lin et al., 2019], traumatic brain injuries [Su et al 2017] and cerebral cavernous malformations [Fisher *et al.*, 2024].

Alzheimer's disease is a progressive neurodegenerative disorder characterised by memory loss, cognitive decline, and behavioural changes. It is the most common cause of dementia, primarily affecting older adults. The disease involves the accumulation of Aβ plaques and Tau neurofibrillary tangles in the brain, leading to neuronal damage and brain atrophy. Numerous studies on mice models (TgCRND8, rTg4510, K3, 3xTg-AD) have evaluated the impact of FUS coupled with MB, without the injection of drugs. Impressive results have been demonstrated with reduction in Aβ plaque load [Jordão *et al.*, 2013; Shen *et al.*, 2020], phosphorylated Tau and Tau phosphorylation [Karakatsani *et al.*, 2019; Shen *et al.*, 2020], and improved both the number of newborn neurons [Burgess *et al.*, 2014], the neuron axonal health [Shen *et al.*, 2020] and hippocampal synaptic plasticity [Kong *et al.*, 2023]. In addition, significant improvement in behaviour, learning and memory have been demonstrated across various mice models [Burgess *et al.*, 2014; Pandit *et al.*, 2019; Shen *et al.*, 2020]. Different explanations have been stressed out with the reduction in Aβ plaque load by its internalisation by microglia [Shen *et al.*, 2020] and the reduction of neuronal Tau by autophagy [Pandit *et al.*, 2019].

Various gene therapies developed *in vitro* for CNS diseases could not be transferred into preclinical trials because of the BBB. Huang *et al*. demonstrated for the first time in 2012 the internalisation of plasmid BDNF (brain derived neurotrophic factor) DNA in neurons that was encapsulated in MB. The expression of the plasmid DNA was observed 48 h after FUS application [Huang *et al.*, 2012]. Type 9 AAV demonstrated efficient gene transfer in neurons, astrocytes and oligodendrocytes after MR-

guided FUS in different regions of the brain [Thévenot *et al.*, 2012] but also whole brain gene delivery with 7.3-fold increase in cortex, striatum and hippocampus after a whole FUS scan of the brain [Felix *et al.*, 2021]. Very recently, Li *et al*. developed new viral vectors specific for FUS applications to improve gene delivery, as natural AAV serotypes have limited efficiency and strong peripheral transduction, which is not desired. They demonstrated an unprecedented 10-fold increase in transduction efficiency in different mice strains and brain regions compared to AAV9 [Li *et al.*, 2024].

Brain tumours can be very aggressive, for example glioblastoma is the most aggressive type of brain tumour and has a very poor prognosis. FUS-induced drug delivery to CNS tumours is the most widely studied application of this technology. Indeed, there is a high clinical relevance to deliver chemotherapy in multiple brain metastasis as surgical resection and drug load are currently very hard to achieve. In addition, the already existing chemotherapies in clinical routine will benefit this technology as some of them can't go through the BBB as the carboplatin. At the preclinical level, a large range of chemotherapies have been delivered in various brain tumour models and are summarised in Table 2**.**

Chemotherapy	**Tumour models**	**Mean survival time (days)**			**References**
		CTRL	Drug	Drug+FUS	
Temozolomide	9L glioma rats	19	20	26 (*)	[Wei *et al.*, 2013]
	U87 human glioma cells xenografted in nude mice	36	40/64 (*)	45/75 (*)	[Liu *et al.*, 2014b]
Doxorubicin	C6 glioma rats	17	22 (*)	27 (*)	[Fan *et al.*, 2013]
	9L glioma rats	18	20	64 (*)	[Aryal *et al.*, 2013]
	GL261 mice	24	26.5	28	[Sun *et al.*, 2023]
Carboplatin	F98 rats	25	27	42 (*)	[McDannold *et al.*, 2019]
	U87, U251 mice	24/32	26.5/35	36/53 (*)	[Dréan *et al.*, 2019]
Irinotecan	F98 rats	25	28	25	[McDannold *et al.*, 2020]
Etoposide	Syngenic glioblastoma model	19	20	26 (*)	[Wei *et al.*, 2021]
Cetuximab	U251 mice	30	35	40 (*)	[Porret *et al.*, 2023]

Table 2. Summary of preclinical studies for different chemotherapies in mice and rat models. Significant increase in mean survival time is depicted with (*).

Among the multitude of chemotherapies that have been previously tested, only carboplatin demonstrated a notable increase in median survival times in disparate glioblastoma models (F98 rats and U87 mice) [Dréan *et al.*, 2019; McDannold *et al.*, 2019]. Consequently, it appears as the most promising chemotherapeutic compound for FUS-induced BBB opening approaches in the near future. Additionally, FUS are not only used to deliver drugs, but also to enhance imaging modalities to follow-up and characterise tumour progression by monitoring PD-L1 expression and the delivery of radioligand for immunoPET imaging [Chevaleyre *et al.*, 2023].

Preclinical studies have yielded promising results, with some of the most efficacious drugs delivered using FUS to open the BBB already undergoing clinical trials and demonstrating encouraging outcomes. The following section will provide an overview of the current therapeutic trials that are in progress or have been completed.

1.4.4. Translation to clinics and clinical trials

Preclinical studies of FUS have demonstrated its potential to safely permeate the BBB, paving the way for its application in clinical settings. These studies have explored various parameters to optimise FUS for effective drug delivery, investigated the efficacy of numerous drugs for the treatment of brain tumours, Alzheimer's and Parkinson's diseases and genetic disorders, and ensured safe translation to human use.



Figure 7. State of research and regulatory approvals for neurobiological and neurological applications (extracted from the annual State of the Field Report 2024 from Focused Ultrasound Foundation: https://www.fusfoundation.org/the-foundation/foundation-reports/state-of-the-field-report-2024/).

Clinical applications of FUS in the brain have been conceived since the inception of this technique with the validation of low frequency FUS for BBB opening [Hynynen *et al.*, 2006]. In addition, many other applications of FUS in the brain not involving BBB opening have been developed, and in particular the FDA approval in 2016 of Insightec's Exablate Neuro platform (InSightec, Israel) to include the treatment of both sides of the body in patients with essential tremor [Elias *et al.*, 2016]. Regarding BBB opening, the feasibility of FUS was quickly demonstrated in non-human primates [Marquet *et al.*, 2014, 2011] despite the challenges of circumventing the thick and inhomogeneous skull. To improve penetration, the transducers have a very low frequency compared to small animal studies, in the range of 200 to 600 kHz and coupled with neuronavigation techniques [Pouliopoulos *et al.*, 2020], CT-based or MRI-based acoustic transmission corrections [Angla *et al.*, 2023; Marsac *et al.*, 2012], MR-guided systems (ExAblate Neuro; InSightec, Israel). Today, there are three devices commercially available and/or approved for clinical FUS: the MR-guided ExAblate Neuro device, the CT-scan based neuronavigated NaviFUS® system and finally the implantable SonoCloud device placed at the location of the tumour resection. As for preclinical studies, extensive forces have been used to study FUS in Alzheimer and brain tumours as well as other minor studies in Parkinson and amyotrophic lateral sclerosis.

The response of different types of brain tumours to different methods and chemotherapies was evaluated. Firstly, **glioblastoma** which is the main brain tumour type studied at this date due to its very poor prognosis. Studies from Idbaih *et al.* and Carpentier *et al.* treated 21 and 38 patients respectively with monthly repeated doses of carboplatin and FUS. Idbaih *et al.* demonstrated a 49% reduction in tumour volume after 10 months with a single implantable SonoCloud-1 device, compared to only a 2% reduction outside the ultrasound field [Idbaih *et al.*, 2019]. Carpentier *et al*. showed that a large BBB opening volume with SonoCloud-9 (9 times the volume of Idbaih *et al.*) was effective with limited side effects despite the carboplatin dose (6/34 patients reported severe pain) [Carpentier *et al.*, 2024]. Sonabend *et al.* used the same device to evaluate different doses of albumin-bound paclitaxel (40 mg/m² to 260 mg/m²) in 17 patients. They performed pharmacokinetic analyses for albumin-bound paclitaxel and carboplatin and measured a 3.7-fold and 5.9-fold increase in the sonicated area, respectively, compared to control [Sonabend *et al.*, 2023]. Park *et al.*, contrary to the 3 last studies performed BBB opening 6 months in a row with MR-guided FUS system ExAblate Neuro in 6 patients along with temozolomide, the most used drug in glioblastoma patients. They observed MRI-CE in 90% of the FUS sessions with limited secondary effects. They did not show any improvement in patient outcome due to the short-term follow-up of the patients [Park *et al.*, 2021]. **Infiltrating glioma** and **brain metastasis** are very challenging brain tumours because of their spatial extension/distribution in the brain. The use of FUS-guided devices, able to deal with highly heterogeneous disease, offers hope for these tumour types. The use of SonoCloud-type devices is therefore very limited in this type of brain tumour, as they are restricted to a very limited field of action, which is the main drawback of the device proposed by Carthera. However, Anastasiadis *et al*. demonstrated feasibility of MR-guided FUS BBB opening in infiltrating glioma and Meng *et al.*, successfully delivered monoclonal antibody trastuzumab in four patients with Her2-positive brain metastasis [Anastasiadis *et al.*, 2021; Meng *et al.*, 2021b].

In **Alzheimer's** patients, Lipsman *et al.* successfully permeabilised the BBB in the prefrontal cortex in 5 patients and Rezai *et al.* achieved BBB opening in the hippocampus in 6 patients with 29% of the total volume of the region [Lipsman *et al.*, 2018; Rezai *et al.*, 2020]. In a study with 30 patients, many interesting results were obtained, in particular the reduction of Aβ plaques in the treated patients; in addition, a very recent study successfully administered the antibody Aducanumab in 3 patients with 1-

year follow-up and showed an increased reduced Aβ plaque load in the treated region [Epelbaum *et al.*, 2022; Rezai *et al.*, 2024, 2022]. Recent study from Bae *et al*. demonstrated also the feasibility of a low-cost neuronavigation-guided FUS device coupled with real-time 2D cavitation mapping in 5 patients out of 6. They showed a slowing increase of the pathology and serum detection of AD proteins [Bae *et al.*, 2024]. The clinical relevance of these studies, as well as others conducted to date, remains to be determined, but these recent findings offer hope for future AD patients.

Parkinson's disease is a neurodegenerative disorder characterised by the loss of dopamine-producing neurons, resulting in tremor, rigidity and movement difficulties. Non-motor symptoms also have a significant impact on patients' quality of life [Poewe *et al.*, 2017]. To date, only three studies have been published demonstrating the feasibility of permeabilising the BBB with MR-guided FUS in the parieto-occipitotemporal junction, putamen and substantia nigra [Gasca-Salas *et al.*, 2024, 2021; Huang *et al.*, 2022]. The 2021 study showed limited cognitive improvements in the 5 patients enrolled, and these results must be seen as a very encouraging first step towards subsequent delivery of therapeutic molecules as AAV. Preclinical study in a non-human primate model of Parkinson's disease delivered AAV to putamen and midbrain regions, providing proof of concept for future applications in Parkinson's patients [Blesa *et al.*, 2023].

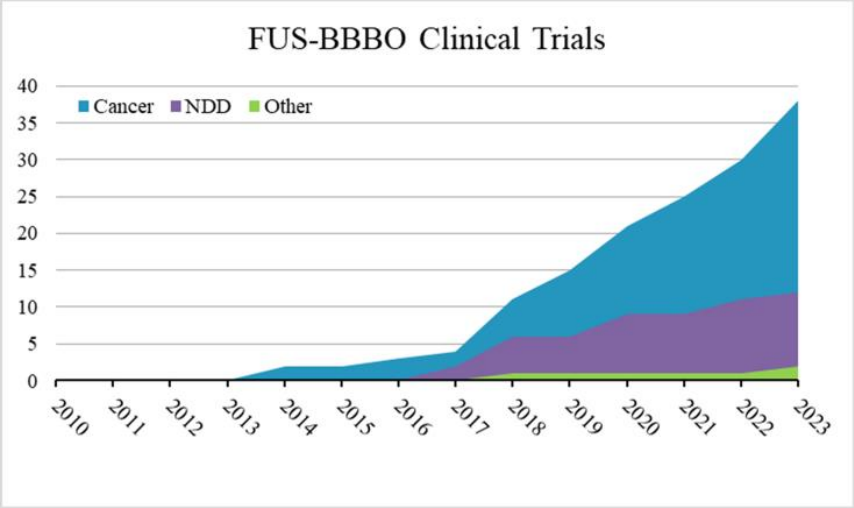


Figure 8. The cumulative number of clinical trials registered on clinicaltrials.gov by year for studies related to ultrasound blood-brain barrier disruption for cancer applications (Cancer), neurodegenerative diseases (NDD), or other applications. Trials found by searching clinicaltrials.gov for the keyword's "ultrasound" and "blood-brain barrier" were included and unrelated trials were removed (from [Durham et al.*, 2024]).*

FUS have demonstrated its potential to permeabilise the BBB and deliver drugs, leading to initial clinical trials that confirm its feasibility for drug delivery in brain tumours, Alzheimer's, and Parkinson's diseases. These promising results highlight the need for larger trials to further evaluate the efficacy and safety of FUS-mediated drug delivery. Feasibility could also be demonstrated in numerous other pathologies of the CNS such as cerebral cavernous malformations [Fisher *et al.*, 2024] and autistic brain disorders to deliver gene therapies for example. A detailed review of the secondary outcomes of these procedures, as well as clinically relevant parameters important to monitor, is provided in 2.5.

The domain of FUS to permeabilise the BBB is very active with a large increase in ongoing clinical trials the last decade (Figure 8). An overview of ongoing clinical trials may be found in Durham *and colleagues*' study [Durham *et al.*, 2024].

1.5. Cavitation monitoring

Despite the trend towards a range of acceptable parameters rated as safe for the permeabilisation of the FUS, there are inherent variations that can potentially lead to unsafe BBB opening. As postulated very early on in this field of study, the main phenomenon responsible for the permeabilisation of the BBB with FUS and microbubbles (MB) is the mechanical stress of these MB on the lumen of the brain vessel. Monitoring this phenomenon of vibration is of great importance to understand the vibration behaviour and thus the effect on the endothelial cells. This phenomenon is called acoustic cavitation, and it describes the behaviour of a MB under the influence of an ultrasonic field. The acoustic cavitation is associated with the formation, growth and collapse of gas-vapour filled bubbles in a liquid [Ashokkumar and Mason, 2007]. For FUS-induced BBB opening, cavitation nuclei are introduced in the vascular system and during a certain period (due to their composition), they will produce acoustic cavitation signal in response to the FUS beam. The first mathematical model describing the evolution of the radius of a gas bubble assuming that the motion of the bubble is symmetric, the wavelength of the incident ultrasound wave is much larger than the bubble radius, no rectified diffusion occurs and the bubble contains gas or vapor which is compressed in a Newtonian liquid behaving like an ideal gas with a constant polytropic exponent was proposed by Rayleigh to which Plesset, Noltingk and Neppiras, and Poritsky [Noltingk and Neppiras, 1950; Plesset, 1949; Poritsky, 1951; Rayleigh, 1917] contributed to propose the so-called RPNNP-bubble model:

$$\rho_0\left(R\ddot{R}+\frac{3}{2}\dot{R}^2\right)=P_g\left(\frac{R_0}{R}\right)^{3\kappa}-\frac{2\sigma}{R}-\delta\omega\rho_0R\dot{R}+P_v-P_0-P_a\cos(\omega t) \quad (3)$$

where R_0 is the ambient bubble radius, ρ_0 is the density of the Newtonian liquid, P_0 is the ambient pressure, P_v is the vapor pressure, σ is the surface tension, κ is the polytropic exponent of the gas, δ is the damping coefficient, P_a is the amplitude of the incident acoustic pressure, ω is the angular frequency of the driving signal, and P_g is the gas pressure inside the bubble.

The introduction of ultrasound contrast agent (UCA) complexified the model as the precedent model did not consider the shell properties, used to increase MB stability. Marmottant *et al.* established a model to investigate the rupture threshold of ultrasound contrast agent with a radius equal to R_{RUPT}, the rupture radius. Thus, surface tension σ is dependent on the radius of the ultrasound contrast agent. This radius of rupture is then dependent on the elastic compression modulus and the surface tension of the fluid within the MB evolves [Marmottant *et al.*, 2005].

Different underlying mechanisms resulting from cavitation regimes are widely described in the literature. When a MB is located close to a biological membrane, five different mechanisms can be distinguished:

- the membrane can be pushed and pulled respectively during the successive expansion and compression phases of the MB in a regime where oscillation amplitude of the MB is controlled, thus leading to membrane destabilisation (Figure 9.A);
- the acoustic radiation force is a mechanical force inducing displacement of the cavitation nuclei, thus displacing the MB against the biological membrane creating a breach. This mechanism could be the source of endothelial transfection when pDNA is complexed at the surface of the MB [Delalande *et al.*, 2017] (Figure 9.B);

- one of the resulting forces driven by the MB oscillation is the microstreaming appearing in the fluid around the MB. Microstreaming can have different patterns and is the source of strong mechanical stress close to the MB, thus disturbing biological membrane stability (Figure 9.C);
- if the amplitude of the oscillation exceeds the elastic limit, the MB can collapse, inducing a shock wave and generating high mechanical pressure on the membrane. The induced temperature and pressure can increase by tens of K and reach a few GPa. These extremes condition can induce irreversible damages as cell death (Figure 9.D);
- when the MB is close to the membrane and the pressure is too high, the MB can collapse asymmetrically. This phenomenon called micro-jetting produces a jet and can puncture the cell membrane creating pores (Figure 9.E).

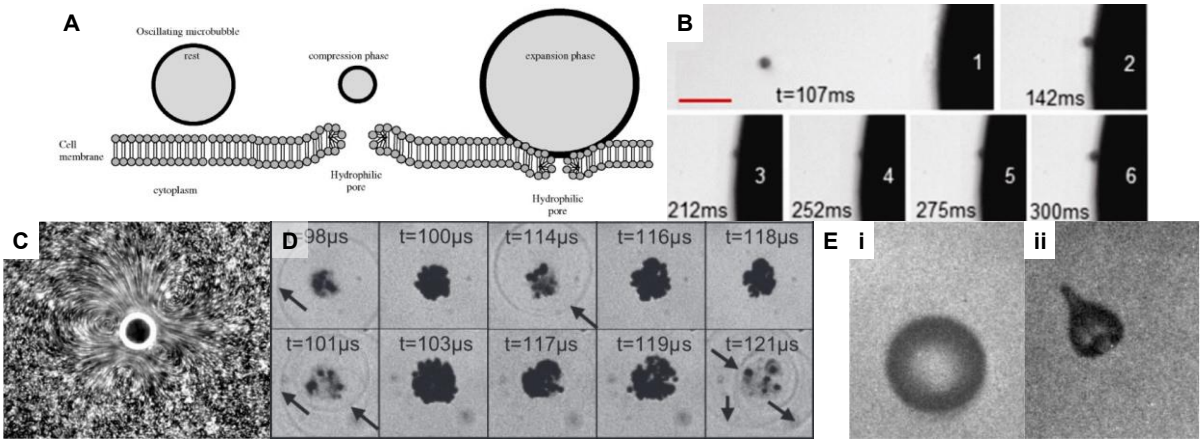


*Figure 9. Overview of the different cavitation mechanisms induced by FUS on a MB. **A**) Model of pore formation by the push/pull mechanism proposed by van Wamel et al. [van Wamel* et al.*, 2006]. **B**) Bubble moving toward the membrane by acoustic radiation force [Zhou* et al.*, 2012]. **C**) fluid streaming around a 136 µm radius MB in a 4 kHz acoustic field [Tho* et al.*, 2007]. **D**) frames of MB clouds at 0.92 (top) and 1.22 MPa (bottom) showing shockwaves (black arrows), increased pressure increases the shock-wave size and recurring period of emission [Johnston* et al.*, 2014]. **E**) Jet development of a MB between frame (**i**) and (**ii**) (MB radius, 8.43 µm; MI, 1.2; inter-frame time, 0.33 µs; estimated created pressure, 60 MPa) [Postema* et al.*, 2004b].*

Detecting the cavitation regime while performing FUS with MB in the context of BBB opening enables the real-time monitoring and the control of the cavitation events listed above. It enables improving the safety of the procedure despite the well-established parameters (model-dependant) appropriate for BBB opening (see 1.4.2). Yet, the variations from one animal to another, as well as the potential increase in MB concentration locally due to abnormalities, highlight the importance of monitoring and controlling MB cavitation as much as possible. It is also important to note that even without considering these variations, the fact that MB form a dynamic system whose population changes over time means that the parameters applied will need to vary between the beginning and the end of the sequence, even if it only lasts a few minutes.

The different types of mechanical stress induced by the MB on the endothelial walls highlighted Figure 9 can be classified in two main regimes: the stable cavitation (SC) and inertial cavitation (IC) (Figure 10). The SC occurs when the MB oscillate in a controllable and stable manner and is associated with reversible BBB opening as in Figure 9.A-B-C and the IC appears above a certain threshold and is associated with tissue damage and irreversible BBB opening with mechanisms in Figure 9.D-E [Ji *et al.*, 2021; McDannold *et al.*, 2006; Sun *et al.*, 2015].

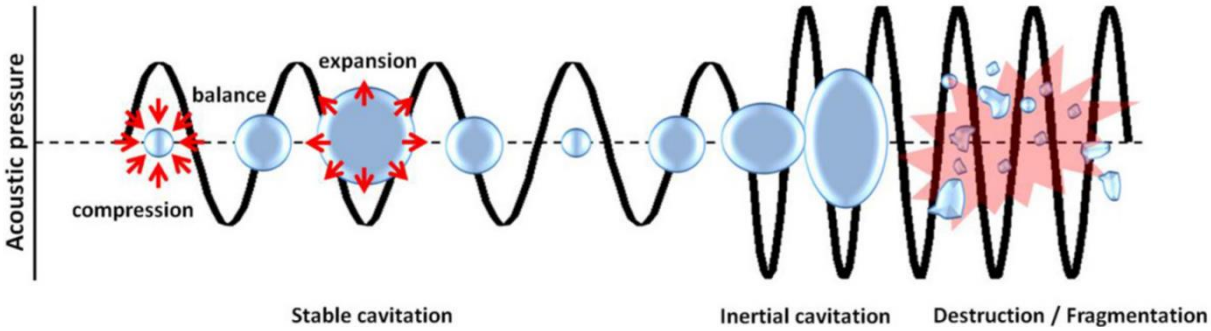


Figure 10. Scheme of the stable and inertial cavitation regimes [Liu et al.*, 2014a].*

In this section, we will review the methods to properly detect, record and process the acoustic signal in order to better understand and control the underlying mechanisms of FUS coupled with MB for BBB permeabilisation.

1.5.1. Origin of the subharmonic and ultra-harmonic frequencies, a journey to inertial cavitation and broadband noise emission

Without any acoustic pressure applied, MB can flow in the bloodstream for several minutes. Some parameters as the percentage of O_2 in the blood can change this persistence time as already explained in 1.4.2. We will describe in this section the three different functioning regimes of cavitation that can be distinguished.

At very low pressures (< 50 kPa), MB undergo gentle, linear periodic compressions and expansions, corresponding to a **linear stable cavitation regime**. In this case, the response to the acoustic field is linear and results in a spectrum containing only the fundamental frequency (f_o). The associated spectrum contains only periodic harmonic of the driven frequency as the oscillation is linear. This state is happening when a large range of conditions are happening as the surface tension of the MB stays below its rupture threshold. This behaviour was modelled by the RPPNP equation. The response to the acoustic field is linear and symmetrical (Figure 11, top panel) and have typical spectrum like in Figure 12.A. In this case, one can assume that the thin shell of the MB is elastic and obeys Hooke's law, which models the behaviour of elastic solids subjected to stress [De Jong *et al.*, 1992].

At moderate pressures (typically 100 to 500 kPa), MB enter a **nonlinear stable cavitation regime** and is referred to as **stable cavitation regime**. In this regime, harmonics ($2 \times f_o$, $3 \times f_o$, …) and sub-/ultra-harmonics ($0.5 \times f_o$, $1.5 \times f_o$, ...) appear, reflecting nonlinear oscillations (Figure 12.B). Although the oscillations are nonlinear, they remain stable over time, meaning no inertial cavitation occurs. To gauge the likelihood of subharmonic emissions due to stable cavitation activity the cavitation index has been settled and is equal to the peak rarefaction pressure amplitude in MPa divided by the frequency in MHz. It was established by Bader and Holland that subharmonic emissions from stable cavitation increase with a cavitation index greater than 0.09 [Bader and Holland, 2013]. This nonlinearity comes from different phenomena happening concurrently. Among them, reversible phenomenon as the excitation at twice the resonant frequency [Katiyar and Sarkar, 2011] and the "compression-only" behaviour (due to the fact that the surface tension is cancelled while the MB is compressed, and the quick expansion induce a rapid increase in MB surface tension) [Marmottant *et al.*, 2005] or non-reversible phenomenon as coalescence, fragmentation, progressive diffusion of the encapsulated gas [Kooiman *et al.*, 2017; Postema *et al.*, 2004a]. In addition, we can distinguish the thermal damping of

the encapsulated gas and the viscous effects of the surrounding fluid [Leighton, 1994], the nonlinear properties of the MB shell [Allen and Rashid, 2004]. The modelling of this phenomenon is very difficult, yet further studies improved the RPPNP model to better fit with experimental data with the introduction of the shell obeying a nonlinear Hooke's law to investigate the nonlinear behaviour of the MB [Allen and Rashid, 2004], the introduction of the "compression-only" behaviour of MB modelled by Marmottant (Figure 11, bottom panel) [Marmottant *et al.*, 2005]. In this range of pressure (100 – 500 kPa), the BBB opening is not likely to happen at low pressures (< 150 – 200 kPa) despite the stable cavitation, yet, for higher pressures, the BBB opening is safe and associated with limited secondary bioeffects [Chu *et al.*, 2016; Kamimura *et al.*, 2019].

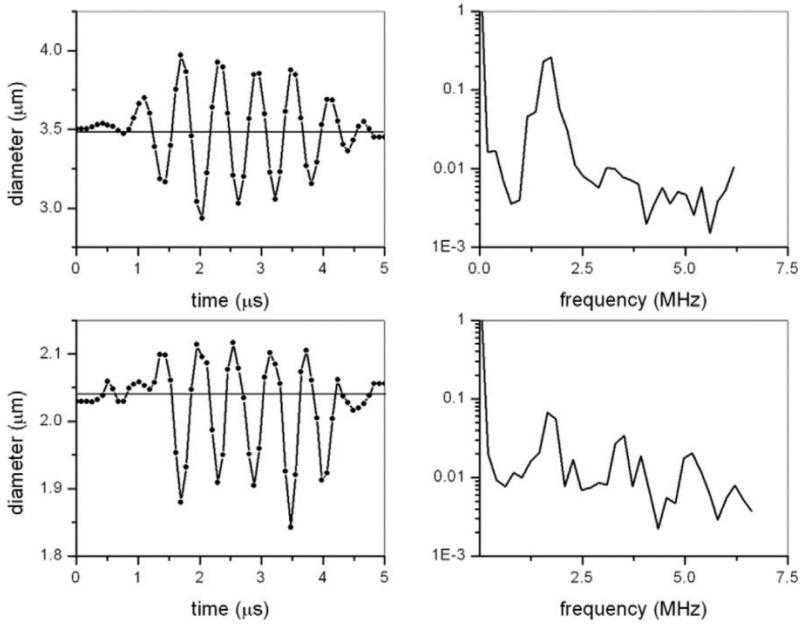


Figure 11. Typical example of regular (top) and "compression-only" oscillations of a SonoVue® MB (diameter equal to 3.5 µm (top) and 2 µm (bottom)) produced from optical high-speed imaging data and the corresponding FFT of the diameter–time curve (right panel). Bubble was insonified with a gated six-cycle sinewave pulse at 1.8-MHz centre frequency at a pressure of 100 kPa [De Jong et al.*, 2007].*

Finally, at higher pressures (> 600 kPa) a **transient nonlinear cavitation regime** is likely to be produced and is referred to as **inertial cavitation regime**. It produces emission of a broadband noise in the cavitation spectrum and is associated with strong biological adverse events. Broadband noise represents the final acoustic spectral signature, with a rapid and pronounced increase in the broadband signal of the cavitation spectrum, indicating the occurrence of significant MB collapse, a phenomenon called Rayleigh collapse [Yasui, 2023, 2018] (Figure 12.C). It exists two primary mechanisms through which the broadband signal may emerge. The first involves the non-periodic and chaotic behaviour of the MB, while the second, more probable mechanism, is associated with acoustic emissions from MB exhibiting temporal fluctuations in the number of MB [Yasui, 2023]. MB are continuously being created, destroyed, or undergoing significant changes in size or behaviour. For example, a MB can disintegrate into a daughter MB or coalescence process can happen by which two or more MB merge to form a single larger MB (Figure 12.D). Broadband pressure peaks modelisation with equation [Marmottant *et al.*, 2005] was validated with *in vitro* measurements and showed that this signal is initiated when the radial oscillation of the MB exceeds the shell break-up threshold and

twice the initial radius [Santin *et al.*, 2010]. Plus, Santin *et al*., showed that the average broadband noise increases with the peak rarefactional pressure to reach a "plateau" (Figure 12.E).

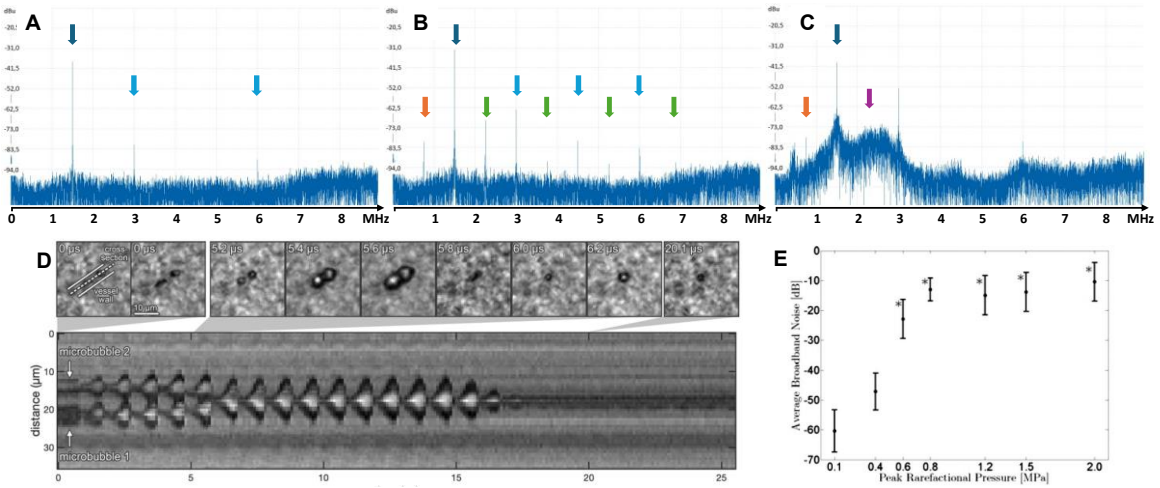


*Figure 12. Different cavitation regimes of the MB according to their spectral signature with stable (**A**), transient destabilisation with the apparition of subharmonics and ultra-harmonics (**B**) and inertial cavitation with broadband noise emission (**C**). Arrows are representing the different characteristic frequencies in the cavitation spectrum: in blue the fundamental frequency, in light blue the harmonics, in orange the subharmonic, in green the ultra-harmonics and in purple the broadband hump. **D**) MB coalescence filmed in an ex vivo capillary model at 1 MHz, PNP = 0.8 MPa and 15 pulses. We can observe the two MB separated after 5.2 µs and the merge MB 5.6 µs after the beginning of the pulse. In the bottom panel the streak of the MB cross-sections [Bezer* et al.*, 2023]. **E**) The average broadband noise as a function of peak rarefactional pressure for a Definity MB (R_0 = 2.14 µm and $R_{break\text{-}up}$ = 1.2 R_0, at 2.8 MHz) [Santin* et al.*, 2010].*

The large complexity of the vascular system in which MB are flowing makes it difficult to simulate and adapt the single shelled MB models. Additionally, the comprehension of the cavitation behaviour of more than 2 MB under the same acoustic field is still not fully understood as the contributions are very difficult to decipher. Bezer *et al*. observed for the first time asymmetric oscillations in small microvessels as well as the range of tissue deformations induced by the cavitation of MB by monitoring the vibration of MB in *ex vivo* samples with high-speed microscopy [Bezer *et al.*, 2023]. It remains to be understood how the bubble-bubble interaction works, from what is originated the large broadband emissions that result from inertial cavitation and if potential in between threshold can be deciphered to increase the safety of the BBB monitoring systems.

1.5.2. Detecting, recording and filtering the acoustic cavitation signal

Cavitation detection can be performed in two distinct ways: actively [Roy *et al.*, 1990] and passively [Arvanitis *et al.*, 2012; Atchley *et al.*, 1988]. Active detection involves the use of transmission/reception devices, whereas passive detection relies on the use of sensors that are not directly involved in the process (passive because it does not transmit any ultrasound waves; it only detects the sounds generated by the cavitation events). In the field of BBB opening, passive cavitation detectors (PCD) are the primary method used to detect the formation of cavitation. Active cavitation detection affects the cavitation process [Madanshetty *et al.*, 1991], may be less sensitive to the presence of bubbles than passive cavitation detection [Roy *et al.*, 1990], and is not specific to collapse cavitation. This is

evidenced by the numerous studies that have employed this approach [Choi *et al.*, 2014; Patel *et al.*, 2019]. A variety of passive acoustic detectors have been developed, utilising different materials: PZT (lead zirconate titanate), PVDF (polyvinylidene fluoride), CMUT (capacitive micromachined ultrasonic transducer) and piezocomposite. These detectors have different properties and costs. The primary characteristics of a PCD are sensitivity and bandwidth. For example, O'Reilly and Hynynen developed a PVDF receiver that is MRI-compatible which exhibited high sensitivity, high signal to noise ratio (SNR), and was capable of functioning at a broad bandwidth (0.1-1 MHz, designed for human application purpose, thus frequencies > 1 MHz are filtered by the skull). Yet, these sensors are more fragile and require regular recalibration. Additionally, it is cost-effective when compared to commercial receivers [O'Reilly and Hynynen, 2010].

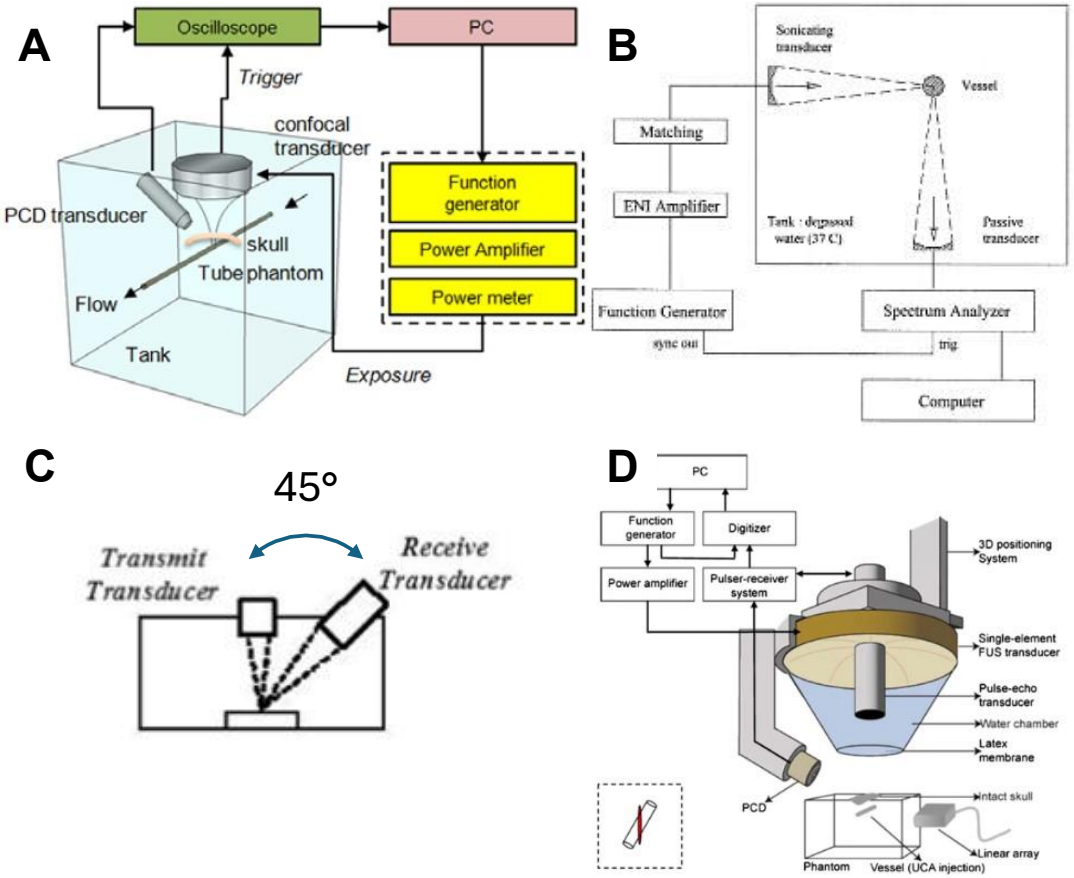


*Figure 13. Different in vitro cavitation monitoring setups containing degassed skulls (**A**) and different PCD positions relatively to the FUS emitter at 60, 90 [Giesecke and Hynynen, 2003] (**B**), 45 [Samuel* et al.*, 2009] (**C**) and 60° [Tung* et al.*, 2010a] (**D**).*

Many studies have evaluated the cavitation of MB in *vitro* to validate their properties before translating them to *in vivo* experiments. To this end, different setups have been constructed (Figure 13), by placing the emitter and receiver transducers at different angles to increase sensitivity, avoid backscatter waves and record more specific signals. The emitter and receiver transducers can be placed between 0° and 90°. Tung *et al*. evaluated the effect of angle on *in vitro* cavitation detection in the presence or absence of the skull. They showed that the attenuation from the skull did not alter the inertial cavitation threshold. As the PCD used in their study has a cylindrical focus, they measured unwanted backscattered signals when placed at 60° with respect to the emitter compared to 90°. It is important to note that for small animal applications, the PCD can only be placed at 0° above the skull as a FUS

emitter. The use of an unfocused PCD will increase the volume of the field of action and is thus sensitive to the whole targeted volume, whereas focused PCD have better specificity but may not be the best suitable due to the use of steered FUS transducer with significant spatial changes in the energy deposition and therefore the resulting cavitation signal.

The cavitation signal is recorded through a simple acquisition chain, possibly with a power amplifier, coupled with an electronic filter and an oscilloscope (Figure 13.A). Not many studies have been done on this acquisition chain as PCDs have good SNR and sensitivity. We can note that a series of filtering methods can be added to enhance the post-processing quality by filtering the fundamental frequency with bad-reject filters, high-pass, low-pass or band-pass filters depending on the frequencies of interest [Arvanitis *et al.*, 2012; Stecia-Marie P Fletcher *et al.*, 2024; Tung *et al.*, 2010b] as well as using windowing to minimise the spectral leakage associated with finite observation intervals by reducing the discontinuity at the boundaries of the periodic extension [Harris, 1978]. Common windowing functions are rectangular, Hann, Hamming and Blackman-Harris. Many studies have applied before the fast Fourier transform on the raw or filtered signal windowing as Hanning window [Stecia-Marie P Fletcher *et al.*, 2024; Khan, 2022].

No consensus has been reached due to the variety of transducers used in the studies and available on the market. As highlighted by Khan [Khan, 2022], several components can falsify the measurements, resulting in severe damage without observing inertial cavitation events. The presence of strong direct current offset components, low SNR, strong fundamental frequency leads to analogue-to-digital converters not working properly. In this sense, the introduction of filtering and amplification elements is of great importance when some of the aforementioned items occur.

1.5.3. Evaluating the cavitation modes

The spectral content and strength of the emissions can be employed to monitor micro-scale perturbations [Arvanitis *et al.*, 2012]. In particular, MB oscillating in an ultrasound field - known as stable cavitation (SC) - can be observed with this approach. The presence of strong harmonic and/or sub- and ultra-harmonic acoustic emissions in the absence of a broadband signal is indicative of the occurrence of stable oscillations [Ilyichev *et al.*, 1989; Leighton, 1994]. The inertial cavitation (IC) activity of MB is known to produce broadband emission [Brennen, 1995; Leighton, 1994]. When both SC and IC occur, the IC activity can be specifically measured as the amount of broadband noise within a given signal between the harmonic components [Chen *et al.*, 2003a].

To quantify these variations and allow the comparison across studies, it was necessary to develop metrics to quantitatively evaluate the cavitation activity and more particularly the stable and inertial cavitation modes. The first indexes are the stable cavitation dose (SCD) and the inertial cavitation dose (ICD). The SCD is defined as the root mean square (RMS) of the area under the fast Fourier transform (FFT) of the harmonics (H), subharmonics (SH), and ultra-harmonics (UH) but the inclusion of both SH and UH is debated in the community due to reversible and non-reversible effects that are likely to happen (see 1.5.1). The ICD is defined as the root mean square of the area under the curve (AUC) of the broadband signal, the frequencies between those used for the SCD. Each of these indexes was defined to specifically determine the cavitation regimes of the MB. In case of transient inertial cavitation, an increase in both the SCD and the ICD should be observed.

All the parameters used to compute these two metrics vary greatly from one study to another, mainly due to variability of equipment developed in-house but also to the variability in the properties of the ultrasonic devices used (emitter, PCD, operating bandwidth, sensitivity detection). Table 3 recapitulates for several studies the parameters used to compute these indexes.

Study	Model	PCD (f_c, BW)	f_0 [MHz]	SCD	ICD
[Wu *et al.*, 2014]	Rhesus macaque	[0.01 – 15 MHz]	0.5	H [3f – 10f] BW=360 kHz, UH [5/2f-19/2f] BW =100khz	Within [1.15-5 MHz]
[Sun *et al.*, 2015]	Fischer rat implanted with F98 cells	10 MHz, [4-12 MHz]	1.5	H [1-6] BW = 300 kHz, UH [7/2-11/2] BW = 100 kHz	400 kHz BW within the frequency range
[Chu *et al.*, 2016]	Sprague-Dawley rats	[0.01 – 10 MHz]	0.4 & 1	UH [0.5, 3/2, 5/2]	Within BW in the frequency range
[Lin *et al.*, 2017]	*In vitro*	7.5 MHz	1	SH + UH [3/2-19/2] BW = 1khz	broadband

Table 3. Different studies using the SCD and ICD indexes to evaluate the cavitation behaviour for BBB opening in rodents and NHP showing the large panels of parameters used for the same metric. Central frequency, f_c; bandwidth at -6 dB, BW; fundamental FUS emitted frequency, f_0.

It is established that the frequencies have different importances and that could result in a more refined control of the cavitation regimes. Wu *et al*. separately quantified the SCD of harmonics (SCD_h) from ultra-harmonics (SCD_u) in macaques and measured the 1st appearance of the SCD_h, ICD and SCD_u at 100 kPa, 250 kPa and 700 kPa, respectively. They concluded that the SCD_u metric was less reliable [Wu *et al.*, 2014], despite that harmonics are not specific to MB activity because they can be induced by the nonlinearities in power amplification or during the wave propagation in water. By contrast, the sub- and ultra-harmonics are specific of MB' response [Leighton, 1994]. Nevertheless, Arvanitis *et al*. found a very good correlation between MRI enhancement and harmonic emission [Arvanitis *et al.*, 2012]. Maimbourg *et al*. investigated the ratio between the 4th and 2nd harmonics and the ratio between different ultra-harmonics and the subharmonic to isolate the cavitation that occurs within the cerebral tissue from the cavitation activity originating from the inside or the outside of the skull. They measured heterogeneities regarding the different frequencies noting a strong attenuation at higher frequencies due to the presence of either a monkey or a human skull, yet the ratio of the 5/2 ultra-harmonic to the subharmonic (1/2) is likely to achieve 100% of sensitivity and specificity for both NHP and human skull. Thus, the harmonic ratio is a very promising approach for BBB opening cavitation monitoring and control [Maimbourg *et al.*, 2018]. Plus, Shekhar *et al*. studied the delayed onset of subharmonic and ultra-harmonic emissions from a phospholipid-shelled MB contrast agent. They found differences of acoustic emissions with drastic increase over a 5 – 10 minutes period of the acoustic emission of the subharmonic and the ultra-harmonic emissions. Plus, the harmonic and fundamental frequency emissions diminished over time, even if the size distribution remained unchanged [Shekhar *et al.*, 2014]. This phenomenon typically comes from the slow and irreversible process of gas fleeing out of the MB shell.

Kamimura *et al*. showed that the sub-harmonic component and the broadband frequencies were present when the FUS treatment resulted in a permanent lesion but not when FUS treatment was safe. As a baseline acquisition, the evaluation of the ratio between harmonics and ultra-harmonics

demonstrated an incorrect coupling between the transducer and the skull of the subject, due to the small air MB trapped in the coupling gel [Kamimura *et al.*, 2019]. Various conclusions appeared from this method of cavitation evaluation. First, according to Sun *et al*., the ICD metrics alone did not allow the detection between BBB opening without lesion and BBB opening with lesions, only the differentiation between non-opened BBB and opened BBB could be detected. In addition, they reported that SCD could allow the distinguishing between the three (i.e. non-opened, opened without and with lesions) with significant measurements between them. The link between the SCD and the increase in BBB opening was also demonstrated. The SCD showed more correlation to BBB opening without lesions compared to ICD. Yet, they found more differences with ICD than SCD at higher pressures and lesional BBB opening [Chu *et al.*, 2016; Lin *et al.*, 2017]. Therefore, a combination of both metrics remains to this day the best solution for safe BBB opening. In addition, these metrics have been widely adopted within the community with at least 51 studies reported in a review by Mondou *et al*. published in 2023 [Mondou *et al.*, 2023]. They reported that, to derive the SCD, most of the studies used either the combination of the harmonics and ultra-harmonics (20/51) or ultra-harmonics only (18/51). A small number of studies computed the SCD with harmonics only (11/21). To derive the ICD, the vast majority of the studies used the broadband noise (45/51) and a few studies computed the ICD with the subharmonic component (4/51) or a combination of the subharmonic component and the broadband frequencies (3/51). In addition, spanning the different articles, they reported that harmonic frequencies number 3 and 4, and ultra-harmonic frequencies 3/2 and 5/2 are the most used, even if some studies go to harmonics 11 and ultra-harmonic 19/2 [Mondou *et al.*, 2023]. For the computation of the SCD, the use of the combination of harmonics and ultra-harmonics and for the ICD the use of the broadband noise are the most consensual approaches, despite the fact that some studies had difficulties monitoring ultra-harmonics [Arvanitis *et al.*, 2012]. Although subharmonics are a fraction of the ultra-harmonics, they are one of the least studied frequencies, despite the fact that they are the frequency that is less filtered by the skull, possibly due to the design of PCDs with a bandwidth that is too far away from this frequency. Still, some studies pointed out the possible importance of its monitoring because of its appearance from the beginning of lesional procedures. Tsai *et al*. demonstrated the feasibility of detecting thresholds that can be utilised to discriminated FUS-induced BBB opening and that it can be implemented to provide excellent control performance both in terms of sensitivity, specificity and prediction rate [Tsai *et al.*, 2016].

No other metrics have been developed as existing metrics suit clinical applications and appear relevant to decipher BBB opening with and without potential lesions. This relies on multiple validations in small animals, NHPs and humans [Kamimura *et al.*, 2019; McDannold *et al.*, 2024; Tung *et al.*, 2010b]. One of the limitations of this approach, however, is the computation of the cavitation indexes based on a single pulse of a few milliseconds (mainly between 10 and 50 ms, as detailed in 1.4.2), which may potentially bypass underlying events that could be harmful. In this context, Novell *et al*. developed and validated in rats and NHPs new cavitation indexes named intrapulse harmonic and ultra-harmonic dose (IHD and IUD). The computation method incorporates the general principles featured previously. Each response to an 10 ms-long ultrasound pulse is divided into small temporal windows of a hundred microseconds (about 128 µs in Novell *et al*.). A fast Fourier transform is computed for every sub-window. After that, the area under the curve over a small frequency range (20 kHz for NHP and 4 kHz for rats) of the first three ultra-harmonic components are summed and normalised by the value computed from the first sub-temporal window. Thus, the IUD is defined, considering the first 3 ultra-harmonic frequencies with n the n^{th} temporal window, as follows:

$$IUD_n = \frac{AUC_{\frac{3f0}{2}}(n) + AUC_{\frac{5f0}{2}}(n) + AUC_{\frac{7f0}{2}}(n)}{AUC_{\frac{3f0}{2}}(1) + AUC_{\frac{5f0}{2}}(1) + AUC_{\frac{7f0}{2}}(1)} \quad (4)$$

IHD can be computed in the same way considering the frequencies $2f_0$, $3f_0$ and $4f_0$, yet this index was found irrelevant as no variations occurred over the application time of ultrasound. These findings reinforce the assumptions that ultra-harmonics are more relevant than harmonics in the assessment of MB cavitation [Novell *et al.*, 2020].

It was observed that harmonics and ultra-harmonics, as well as the subharmonic and the broadband noise, were accepted as reflecting the stable or inertial character of the MB under FUS exposure. Nevertheless, a considerable number of parameters and the contribution of these frequencies remain poorly understood, and debate continues as to whether the optimal frequencies for monitoring to control cavitation with real-time closed loop is the most appropriate approach. The SCD and ICD are effective metrics for predicting the destabilisation of MB. However, new indexes, namely the IHD and IUD, may prove more appropriate as they account for potential variations in the cavitation level of MB within a single pulse of FUS sequences. This increases temporal resolution and, consequently, clinical safety.

1.5.4. Influence of microbubble composition in the detection of cavitation

Cavitation nuclei have great influence on the cavitation behaviour, as well as the environment of vibration. Three main MB are used in BBB opening experiments: SonoVue®, Optison™ and Definity® (Figure 14.A); all clinically approved for diagnostic purposes by the FDA. These three types of MB are very different as well as their cavitation properties. There are many other types of MB with different shells and gas encapsulation (Figure 14.B) used in the literature (Table 4), with mean diameters around 2 µm, but nanobubbles, with mean diameters of a few hundred nm, have also shown increasing interest as they facilitated the permeabilisation of small capillaries [Gattegno *et al.*, 2024].

Type of MB	Gas core	Shell	Mean diameter	Shell surface viscosity κ_s (kg/s)	Surface tension χ (N/m)	IC threshold [MI]	References
Sonovue®	SF_6	Lipidic	1.5 µm	7.20×10^{-9}	0.55	0.6*	[Lin *et al.*, 2017]
Optison™	C_3F_8	Albumin	2 – 4.5 µm	7.65×10^{-8}	0.93	0.12-0.57-0.46	Chen 2003 (in vitro)-McDannold 2006-bing 2018-
Definity®	C_3F_8	Lipidic	1.5 µm	2.40×10^{-9}	0.53	0.36-0.46	[Bing *et al.*, 2018; Tung *et al.*, 2010a]
Sonazoid	C_4F_{10}	Lipidic	2.17 µm	1.2×10^{-8}	0.53	0.14*	[Chen *et al.*, 2003b]
nanobubble	C_4F_{10}	Lipidic	200 nm			0.66-0.56	[Bing *et al.*, 2018; Cheng *et al.*, 2019]

Table 4. Different MB cavitation properties. Shell properties references: [Bader and Holland, 2013; Katiyar and Sarkar, 2011; Santin et al.*, 2010]. Nanobubbles are mostly made from mixtures of phospholipids with carbon chains that are sometimes longer than those used for MB, and they can be separated from the MB by centrifugation. In vitro inertial cavitation thresholds are highlighted with *.*

Surface tension plays a crucial role in the dynamics of small bubbles, when the capillary pressure term is of the order of the static ambient pressure, the coating is expected to strongly influence the dynamics thus, the coating modifies the effective surface tension and cavitation dynamics. In addition

to the classical MB and nanobubbles introduced just before, numerous shells have been developed as cationic shells to turn these MB into drug carriers or even increase the target specificity with antibodies (Figure 14.C).

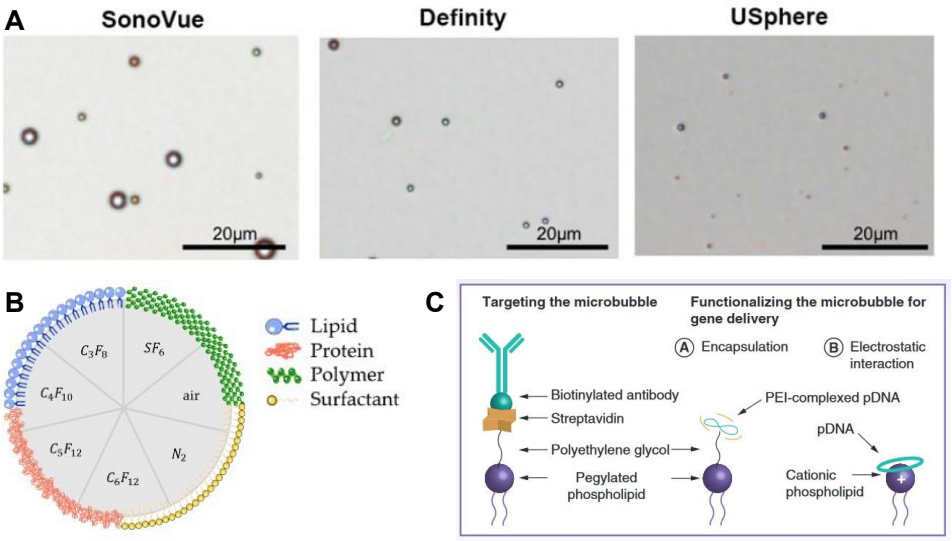


Figure 14. Microscopy images of three different MB (SonoVue, Definity, and USphere). Scale bar =20 µm [Wu et al.*, 2017] (**A**). The large variety of gas cores and shells that can compose a MB [Dauba* et al.*, 2020] (**B**) and two types of functionalising method to improve drug delivery specificity and act as drug carrier [Delalande* et al.*, 2012] (**C**).*

SCD and ICD depend on the different FUS parameters as the PRF, the pulse length but also in MB concentration, size and shell [Bing *et al.*, 2018; Lin *et al.*, 2017; Tung *et al.*, 2011; Wu *et al.*, 2017]. Tung *et al*. Investigated in-house lipidic-shelled MB with different mean diameters, and it appeared that inertial cavitation may be necessary for small MB (1-2 µm) but not at larger diameters (4-8 µm) as the amplitude of the vibrations is reduced and therefore has less of an effect on the vascular system.

Plus, at 0.3 MPa, they did not observe any BBB opening for small-size MB (Figure 15.A) as well as no acoustic signature of BBB opening [Tung *et al.*, 2011]. Bing *et al*. observed the differences between Optison™, Definity and NBs and found that Optison™ and Definity MB were similar in terms of inertial cavitation levels. Which confirms previous results where the probability of BBB opening and the severity of damages were similar while applying the same pressure [McDannold *et al.*, 2007]. Yet, as it is shown in Figure 15.B, a large broadband signal is visible at 0.47 MPa for both MB types but NBs did not show inertial cavitation increase. At 0.91 MPa they observed for the three tested bubble types a strong increase in the broadband signal [Bing *et al.*, 2018]. Similarly, between SonoVue®, Definity® and USphere MB, strong differences in SCD and ICD were measured at low MI (Figure 15.C) [Wu *et al.*, 2017].

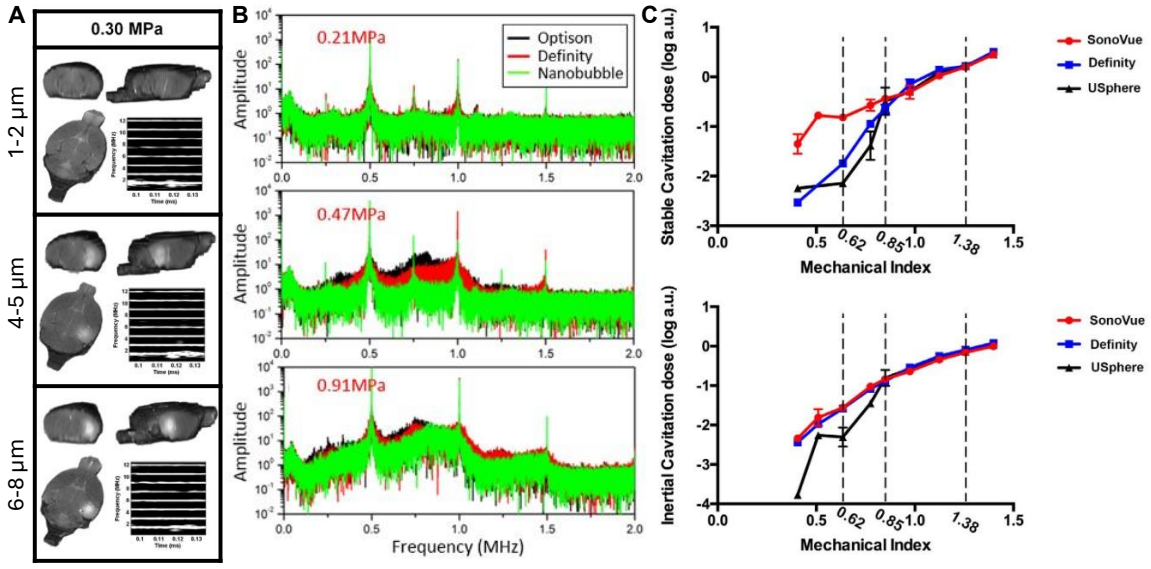


Figure 15. Influence of MB properties on cavitation. ***A****) The BBB opening of three MB diameters is confirmed by 3D MRI images with coronal (top left), sagittal (top right), and horizontal (bottom left) views. The corresponding spectrogram (bottom right) of the first pulse from 95 to 135 µs with MB administration shows the acoustic response [Tung* et al.*, 2011].* ***B****) Acoustic spectrums for Optison (black), Definity (red) and nanobubbles (green) at 0.21, 0.47 and 0.91 MPa [Bing* et al.*, 2018].* ***C****) SCD and ICD in function of the MI for three different types of commercially available MB [Wu* et al.*, 2017].*

1.5.5. Real-time cavitation control and passive acoustic mapping

Real-time control of MB cavitation algorithms may be used to retro-control every given time (the shorter the better) the acoustic pressure delivered at each iteration. Sabraoui *et al*. proposed a close loop that quantifies every 5 ms the cavitation level and modulates in consequence the acoustic level. This method was applied on gas-saturated water and solution placed in wells of culture plate [Sabraoui *et al.*, 2011].

The first *in vivo* control method of acoustic cavitation levels originating from MB was designed by O'Reilly and Hynynen [O'Reilly and Hynynen, 2012] and tested on 27 male rats. It relies on incrementation of the acoustic pressure while monitoring the acoustic cavitation emission until ultra-harmonics are detected. As soon as ultra-harmonics appear, the acoustic pressure is reduced at a certain level. They tested four different level drops: 100%, 75%, 50% and 25% and found that a minimum drop of 50% is necessary to avoid brain damages. A reduction of 100% or 75% of the acoustic level resulted, in several cases, in absence of BBB opening. Five of the six failures that happened took place at these two target levels. This real-time feedback method can be considered as a semi control closed-loop technique as the acoustic pressure isn't evolving over time: once it has been reduced, it remains low until the end of the FUS procedure. To ensure a safe blood-brain barrier opening, published studies used this method to investigate blood-brain barrier closure time [Meaghan A. O'Reilly *et al.*, 2017], the vasculature of rat hippocampal but also microglial activation after BBB disruption [McMahon *et al.*, 2018; Sinharay *et al.*, 2019]. Yet, by drastically reducing the FUS pressure, this method is certainly sub-optimal for drug delivery.

After this pioneering study, more stable, precise and evolving along with the cavitation signal recording has been developed (Figure 16). Firstly, feedback proportional or proportional-integral controllers

[Cornu *et al.*, 2018; Sun *et al.*, 2017], algorithms that increase or decrease step by step the pressure [Bing *et al.*, 2018; Cheng *et al.*, 2019; Kamimura *et al.*, 2019], while more advanced algorithms are described by Çavuşğlu *et al*. [Çavuşoğlu *et al.*, 2019] taking into account a broad history of the previous cavitation signals for the computation of the next pressure.

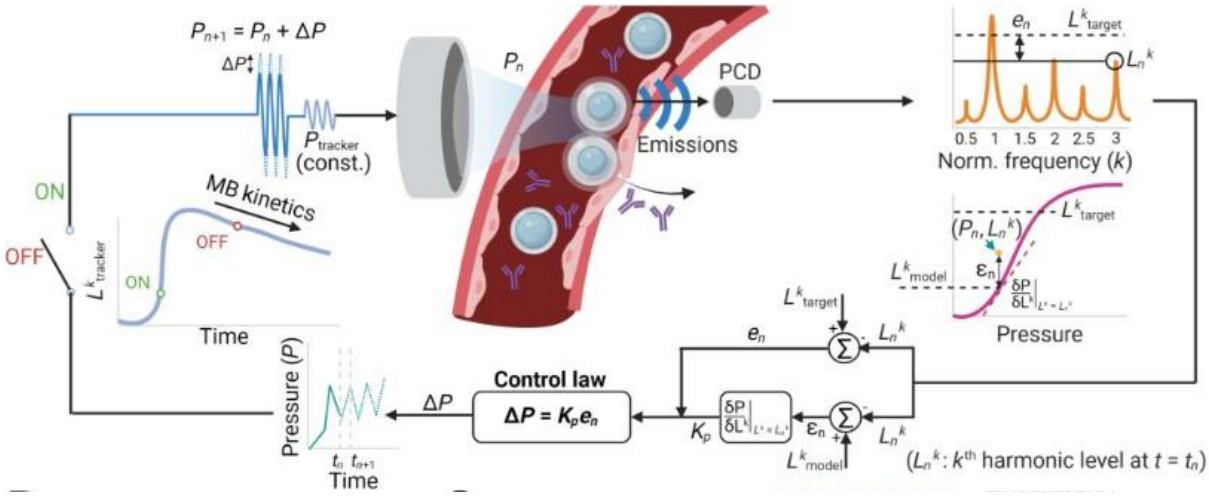


Figure 16. Example of a closed-loop cavitation controller with proportional feedback control law to maintain the targeted acoustic emission level settled (L_{target}). P_{n+1} and P_n the pressures at the current timepoint and the next one, ΔP the pressure increment, L^k_{target} is the acoustic level for harmonic k^{th}, Kp is the gain, e_n the error term [Lee et al.*, 2022].*

Single-detector cavitation monitoring and control methods lack the spatial information of the acoustic energy emitted by MB during FUS. Therefore, passive acoustic mapping (PAM) has been introduced to provide spatial information of the cavitation activity. PAM provides the ability to identify, quantify, and locate cavitation activity simultaneously during sonication by detecting cavitation-generated acoustic emissions using a transducer array [Gyöngy and Coussios, 2010a]. PAM has demonstrated sub-millimetre spatial and millisecond temporal accuracy [Gyöngy and Coussios, 2010b], in particular thanks to new dedicated processing methods that have been developed to allow real-time monitoring and control of the acoustic energy from MB to overcome the issues posed by the considerable computational load for processing data sets and the complex reconstruction algorithms [Kamimura *et al.*, 2021]. One of the biggest challenges comes from the skull heterogeneity and recent developments have been made to correct skull-induced aberration to improve PAM [Schoen *et al.*, 2022]. PAM showed to predict therapeutic outcome *in vivo* [Choi *et al.*, 2014] and efficient BBB opening in Alzheimer's disease patients [Bae *et al.*, 2024]. Further developments will include the implementation of 3D PAM for greater comprehension and safety in BBB opening applications and improvements towards clinical transfer [Schoen *et al.*, 2022].

In conclusion, cavitation monitoring and closed-loop systems for controlling acoustic emission levels enable reliable and safe BBB opening with a broad range of acoustic parameters but also different MB. PCD with single sensing volume are limited and cannot provide information regarding the number or spatial distribution of cavitation events occurring outside this volume. The development of PAM-devices addresses this gap by providing cavitation imaging. In addition, as with single-element cavitation controllers, the association of PAM with a feedback loop controller has been shown to maintain target levels of stable and inertial cavitation levels [Patel *et al.*, 2019]. 3D subharmonic acoustic imaging has also demonstrated the feasibility of calibrating exposure levels for safe FUS-

induced BBB opening [Jones *et al.*, 2018]. For the first time, the use of passive acoustic mapping to deliver FUS was demonstrated in Alzheimer's patients. Patients showed a slowing of disease progression and detection of AD proteins in serum [Bae *et al.*, 2024]. These results pave the way for future low-cost neuronavigation-guided FUS systems to efficiently permeabilise the BBB with FUS for drug delivery or diagnostic applications.

Chapter 2. Secondary bioeffects of the use of Focused UltraSound and microbubbles to permeabilise the BBB: state of the art

The effects of ultrasound therapies on biological tissues have been the subject of considerable interest since the early days of research in this field [Lehmann and Herrick, 1953]. We have seen that the cavitation resulting from the application of FUS in presence of MB can exert high mechanical forces and thus induce pinocytosis in EC, strong haemorrhages and even cellular death. Using monitoring and/or controlling of the cavitation and optimised FUS parameters, transient and reversible BBB opening may be induced, from a macroscopic point of view. Yet, within the safe range of FUS parameters (i.e. without inducing a lesion), different bioeffects have been observed following FUS application such as transient vascular modifications or specific protein and gene expression

To evaluate the resulting effects from the permeabilisation of the BBB with FUS and MB, a variety of techniques have been employed. These different techniques enable a range of complementary approaches to be undertaken at varying levels of observation, from the microscopic to the macroscopic scale. The main techniques used include MRI, positron emission tomography (PET), multi-photon imaging, contrast-enhanced ultrasound (CEUS) imaging, histological analysis with haematoxylin and eosin (H&E) staining and immunofluorescence staining and transcriptomics analysis.

Among imaging techniques, PET enables functional imaging with specific tracers, CEUS involves the use of specific MB to increase the signal in the vascular system, multi-photon imaging is a fluorescence microscope technique that enables real-time imaging of fluorescent-labelled compounds. Main histological techniques include H&E for nucleus and cytoplasmic staining and immunofluorescent ones to target specific cells or proteins with fluorescent dyes. Finally, transcriptomics is the study of the complete set of RNA transcripts that are produced by the genome under specific circumstances or in a specific cell, tissue or organism. This field of study provides insights into gene expression patterns, revealing which genes are active, to what extent, and under what conditions. The techniques most employed in transcriptomics include RNA sequencing, microarrays and quantitative PCR. These techniques permit the measurement of the quantity and sequences of RNA present in each sample.

This chapter will review the extensive range of secondary bioeffects resulting from the permeabilisation of the BBB with FUS, employing the various methods outlined in Figure 17. The major secondary effects encompass neuroinflammation, impact on metabolism, cells and behaviour. We will first review animal studies (2.1 – 2.4). The next section (2.5) will examine the diverse parameters monitored following human BBB permeabilisation. Finally, the last section (2.6) will be dedicated to secondary effects observed after multiple FUS treatments.

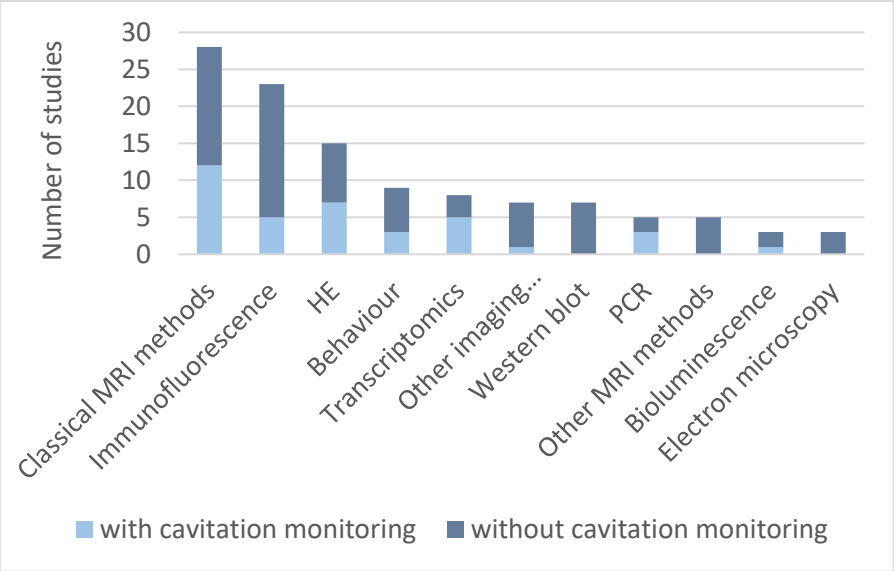


Figure 17. Overview of the techniques used to study the secondary effects of FUS coupled with MB in preclinical models. Other MRI methods include ASL, pCASL, fMRI and ^{13}C MR. Other imaging modalities include bi-photon imaging (3/7), PET (2/7), microscopy and CEUS. These data were pooled among 53 articles from 2004 to 2024.

2.1. Vascular modifications and cellular extravasation

2.1.1. Macroscopic and functional modifications

From a macroscopic perspective, bi-photon fluorescence microscopy studies revealed differences in leakage and transient vessel constrictions. Raymond *et al*. measured a 59.5% constriction in vessel diameter followed by a recovery phase lasting between 21 and 615 s at MI = 0.2. Small arterioles and arteries of up to 50 µm showed constriction, but small capillaries did not constrict, possibly due to the absence or downregulation of SMA [Raymond *et al.*, 2007]. A parallel study showed a linear relationship between the percentage of constriction and the diameter of the vessel: the larger is the vessel, the smaller the constriction is. They also measured vasodilation in few cases (~ 10%). In addition, studies from Ilovitsch's laboratory have also shown which vessels are affected by FUS-mediated BBB opening. They showed that only 10% of small capillaries (2 – 3 µm) were permeabilised compared to 92% of larger capillaries (9 – 10 µm). In addition, nanobubbles appear to improve delivery specifically in the small capillaries compared to MB, but the amount of nanobubbles used seems to be more elevated [Gattegno *et al.*, 2024; Katz *et al.*, 2023]. The latter results are not consistent with observations made by Poon *et al*. They did not find that FUS-induced BBB permeabilisation affect more capillaries than venules or arterioles. The diameter distribution of opened vessels was consistent for diameters between 0 to 50 µm [Poon *et al.*, 2021]. Yet, the small amount of vessel analysed in the study from Poon *et al*. due to the reduced field of view provided by the two-photon microscope may not be representative.

Blood flows through the vessels is regulated by the NVU as explained in section 1.2. Thus, changes in vessel diameter due to FUS and the BBB permeabilisation are likely to modify the cerebral blood flow. Fan *et al*. used contrast-enhanced ultrasound imaging to measure a strong reduction in the CBF 5 seconds post-FUS and a return to baseline 2 h post-FUS with high MI (MI = 1.1) [Fan *et al.*, 2012]. MRI arterial spin labelling measurements showed that FUS-induced BBB opening resulted in a significant

decrease in CBF in the FUS-permeabilised region compared to the contralateral [Todd *et al.*, 2019]. But the MRI methodology used is far from being the most robust and sensitive to such changes. More recently, using a more consistent approach, Labriji *et al*. observed with an unfocused ultrasound transducer a transient decrease in CBF by 30% in the FUS-targeted hemisphere with a lower MI (MI = 0.28) [Labriji *et al.*, 2023].

2.1.2. Transcytosis and paracellular modifications

From a vascular perspective, two main components ensure the permeability of the BBB, the endothelium with specific transcytosis pathways and the TJs preventing most of the paracellular pathway (see section 1.2).

The permeability of ECs in the brain is regulated by several cell signalling pathways, such as the PI3-kinase/Akt pathway, and it has already been shown that hypoxia-induced hyperpermeability is mediated by the activation of PI3-kinase [Fischer *et al.*, 2004]. An increase in the activity of Akt signalling has been measured up to 24 h post-FUS and particularly at the neuronal level, promoting neuronal survival but also increasing BBB permeability as VEGF is known to increase permeability and enhance neuronal protection via PI3-kinase/Akt activity [Jalali *et al.*, 2010; Kilic *et al.*, 2006].

Among these, efflux transporters such as permeability-glycoprotein (P-gp) appeared to be downregulated after safe BBB opening at 0.3 MI *in situ* and without any change in RECA-1 (rat endothelial cell antigen-1) expression [Cho *et al.*, 2016]. This was confirmed by measuring P-gp mRNA expression, which was significantly downregulated at 1, 24 and 48 h post-FUS. Protein expression was significantly reduced at 24 h after FUS BBB opening at 0.5 MI, and immunofluorescence staining also showed a decrease at 24 h, but returned to baseline values at 120 h [Choi *et al.*, 2019]. In that sense, Goutal *et al*. also measured significant changes at 24 and 48 h post-FUS in P-gp expression [Goutal *et al.*, 2023]. These findings suggest that other transporters found in the BBB may be dysregulated such as the BCRP (breast cancer resistance protein), an important efflux transporter of the BBB. McMahon *et al*., by performing transcriptome analyses, measured downregulations by 6 times of ATP-binding cassette and solute carriers' families that returned to baseline 24 h after FUS BBB opening at 0.27 MI. Yet, at 24 h, gene set enrichment analysis revealed that ion transporters of the BBB had significant downregulation (gene ontology descriptions: "calcium ion transmembrane transporter activity", "chloride transmembrane transporter activity", "potassium ion transmembrane transporter activity", "sodium ion transmembrane transporter activity" and "ion transmembrane transporter activity") [McMahon *et al.*, 2017]. If FUS induces a transient downregulation of drug efflux transporter expression in the BBB, this may increase the efficacy of FUS-mediated therapeutic drug delivery. It would also be an important consideration in the development of dosing strategies to avoid toxicity following sonication.

The transporters of the ECs appeared to be affected by the permeabilisation of the BBB with FUS, with an increase in transcytosis [S. Chen *et al.*, 2021; Pandit *et al.*, 2020; Sheikov *et al.*, 2004]. This is partly due to the fact that the rate of transcytosis across cerebral capillary ECs is influenced by proinflammatory cytokines (see 0) [McMahon and Hynynen, 2017; Miller *et al.*, 2005]. Among transcytosis transport pathways, the caveolae are small invaginations present in the plasma membrane of the ECs. They form small vesicular structures (50-100 nm) rich in cholesterol sphingolipids and proteins Caveolins-1, -2 and -3. Pandit *et al*. delivered in caveolin-1 KO mice different molecular weight dextrans (3, 70 and 500 kDa) with FUS. They measured increased levels of caveolin-1 in wild-type mice

and showed that the absence of caveolin-1 dampened significantly the delivery of large-sized 500 kDa dextran. Thus, caveolin must have a role in the transport of large molecules through the BBB open with FUS [Pandit *et al.*, 2020]. Sheikov *et al*. already observed with electron microscopy numerous caveolae attached to the basement membrane as well as caveolae formations present in the cytoplasm of ECs [Sheikov *et al.*, 2004].

It was also shown that several genes related to angiogenesis are upregulated at different time points after FUS. These changes suggest that FUS triggers early angiogenic processes. If FUS can be shown to stimulate angiogenesis in the brain, this could have major implications for patients recovering from stroke or traumatic brain injury by providing a means to promote repair and regeneration of injured brain tissue and promote functional recovery [McMahon *et al.*, 2017]. Additionally, different studies found that blood vessel density and more particularly small vessels (< 5 µm) was increased at 7- and 14-days post-FUS but returned to baseline at 21 days post-FUS. This is associated with different key signalling protein markers of the angiogenic process as VEGFA [McMahon *et al.*, 2018]. This suggests the apparition of newly born vessels through the angiogenic processes. Furthermore, McMahon *et al*. analysed the rat microvascular transcriptome 6 h and 24 h after the cavitation-controlled permeabilisation of the left hippocampus under ketamine/xylazine anaesthesia (mean of PNP were evaluated at 0.19 MPa, f_0 = 0.55 MHz). Among the 19 105 genes included in the analysis, 0.31 % and 0.52% were up-regulated and 0.57% and 0.04% were down-regulated at 6 and 24 h after FUS, respectively. No changes in contralateral tissue and in control rats were found [McMahon *et al.*, 2017].

In addition, FUS-induced BBB opening seems to destabilise the TJs present between the ECs. It is still largely unclear regarding their role in BBB permeability and how their organisation is perturbed by the cavitation of the MB. Electron microscopy observations revealed some clefts between ECs in conjunction with missing zonulae occludentes suggesting altered TJs and an increased paracellular pathway [Sheikov *et al.*, 2004]. The expression of several proteins present at the level of the TJs was assessed. ZO-1 was significantly upregulated at 24 h post-FUS, as were occludin and phosphorylated JNK (c-Jun N-terminal kinases (JNKs) are a family of protein kinases that play a central role in stress signalling pathways) in the targeted region [Choi *et al.*, 2019]. Moreover, the study of claudin-5 in an *in vitro* model of the BBB validated the weakening of TJs by two specific binders of claudin-5 [Chen *et al.*, 2022], thus opening perspectives for a reduced use of FUS energy to achieve the same level of BBB permeabilisation even though this *in vitro* model does not take into account the full complexity of the *in vivo* BBB in the absence of astrocytes and pericytes.

Yet the investigations on the TJs after FUS-induced BBB opening remains clearly under investigated, and the increase in proteins levels from one side may be related to a compensatory mechanism with other TJs proteins that are under-expressed.

2.1.3. Extravasated compounds

Cells, proteins and antibodies present in the vascular system, circulating along with the MB injected to permeabilise the BBB, are the first impacted components. Erythrocytes extravasation can be observed if the MI and/or the MB concentration is too important. Direct relationship has been established between the MI and the number of erythrocyte extravasations [Chu *et al.*, 2016; McDannold *et al.*, 2011]. Albumin, a transport protein present in the blood, was found extravasated 30 min after FUS and its level in tissue increased constantly up to 24 h [Alonso *et al.*, 2011] for high MI = 1.25. For low MI = 0.39 albumin was observed 6 h post-FUS but no longer 24 h after FUS [Kovacs *et al.*, 2017]. In this

study, albumin appeared to be cleared by glial cells rather than by neuronal cells, which is beneficial given the neurotoxic effect of albumin uptake by neurons [Alonso *et al.*, 2011]. IgG and IgM are two different types of antibodies, produced by the immune system to recognise and neutralise pathogens like viruses and bacteria. These antibodies play crucial roles in the body's defence mechanisms. IgG is the most abundant type of antibody in the blood and IgM the first antibody produced by the immune system when a new infection occurs. IgG was found extravasated 1 to 2 h after FUS with immunogold labelling and electron microscopy at MI = 1.26 [Sheikov *et al.*, 2004] and 3 to 6 h with immunofluorescent staining at MI = 0.8 [Raymond *et al.*, 2008]. It was later confirmed that MR-guided FUS facilitated their entry into the parenchyma at lower MI (MI = 0.3). A mean concentration of IgG in the treated cortex of 400 pg/µg of protein 4 days after FUS was measured. Additionally, the presence of IgM (~ 6 times the molecular weight of IgG) in the CNS and found a 200 pg/µg of proteins at 4 days post-FUS [Jordão *et al.*, 2013]. Table 5 summarises the different extravasated compounds.

Type of compound	Molecular weight and size	Function	Extravasation pattern	References
Albumin	69 kDa – 3.8 × 15 nm	Blood transporter protein	6 h post-FUS but not 24 h	[Alonso *et al.*, 2011; Kovacs *et al.*, 2017]
IgG	150 kDa - 14.5 × 8.5 nm	Neutralisation	Still present 4 days post-FUS	[Sheikov *et al.*, 2004; Raymond *et al.*, 2008]
IgM	900 kDa – 30 × 16 nm	Primary immune response	Still present 4 days post-FUS	[Jordão *et al.*, 2013]

Table 5. Summary of extravasated compounds following FUS-induced BBB opening.

2.1.4. Conclusion

Vascular permeability induced by BBB opening is likely to have different forms as we saw that ECs and TJs can be affect very differently. Three studies using two-photon microscopy highlighted the fact that several BBB permeability is occurring after FUS application along with MB. It is very likely that at least two if not three types of leakages happen: fast, slow and sustained [Cho *et al.*, 2011; Poon *et al.*, 2021; Raymond *et al.*, 2007]. According to Poon *et al*., the type of leakage changes from one type of blood vessel to another. For fast leakage, they measured 90% of prevalence for arterioles compared to 70/75% for venules and capillaries. Conversely, for slow leakage, the prevalence was only 10% for arterioles and 25/30% for venules and capillaries [Poon *et al.*, 2021].

The consequences of FUS and MB on the vasculature, whether structural or functional, are still unclear and we do not know how vascular permeability is established. Based on the results of the current literature, it is very probable that several mechanisms occur more or less simultaneously and that the paracellular route is certainly one of the main paths taken by the drugs to reach the CNS.

Only few studies have observed apoptotic behaviours, but it was at high MI. Wang *et al*. designed specific nanoparticles to monitor apoptotic cells after FUS. They confirmed the observation of approximately 20 %, 55% and 70% of apoptotic cells at MI equal to 0.6, 0.8 and 1 respectively despite no red blood cells extravasation was found for MI of 0.6 and 0.8 [Wang *et al.*, 2021].

2.2. Neuroinflammation

Neuroinflammation refers to the inflammatory response occurring within the CNS, involving activation of glial cells and release of inflammatory mediators. It plays a crucial role in the pathology of various neurological disorders, including neurodegenerative diseases and brain injuries. The neuroinflammation as a result of trauma, ischaemia reperfusion injury or chemically induced injury typically occurs in the absence of any microorganisms and has therefore been termed **sterile inflammation**. Similar to microbially induced inflammation, the sterile inflammation response (SIR) is marked by the recruitment of neutrophils, macrophages and the production of proinflammatory cytokines and chemokines, notably tumour necrosis factor (TNF) and interleukin1 (IL1) [Chen and Nuñez, 2010]. Similar inflammation pattern was described in the literature and evidenced for the first time by Kovacs *et al*. after the permeabilisation of the BBB with FUS [Kovacs *et al.*, 2017]. They evaluated longitudinally the expression of various genes related to the NFκB pathway, that plays a central role in the inflammatory response and is crucial for the functioning of the immune system, proteins involved in the injury or damage mechanisms, glial cells (Gfap, Iba1), chemotactic factors (MIP3α), cell adhesion molecules (Icam1, Vcam1) and immune cell trophic factors (Ccl12, Cxcl1, Cxcl3).

Following FUS, a neuroinflammatory response is triggered with immediate effects followed by responses of tissue and cells. After that, the transient SIR, which is modulated by FUS intensity, MB dose and acoustic cavitation intensity release cytokines and trigger protective or potentially risky mechanisms for the CNS.

2.2.1. Microglial modifications

The immediate effect of BBB opening is the release of cytokines and the activation of microglia, which serve as primary responders. Microglia act as sentinels and the expression of the Iba1 protein has been extensively studied in the FUS-induced BBB opening field. Iba1 signals in the brain were found to be significantly increased as early as 1 h post-FUS [Kovacs *et al.*, 2017; Pascal *et al.*, 2020], 4 h [Jordão *et al.*, 2013], 6 h, 24 h and 48 h post-FUS [Choi *et al.*, 2022; Kovacs *et al.*, 2017; Sinharay *et al.*, 2019] and was found dampened at different time points depending on the study: 24 h [Kovacs *et al.*, 2017], 14 days [Jordão *et al.*, 2013] or 13 weeks [Kovacs *et al.*, 2018]. The peak of activation is very difficult to measure due to the wide range of FUS parameters used and was found either at 6 h [Kovacs *et al.*, 2017], 24 h [Gorick *et al.*, 2020] or 4 days [Jordão *et al.*, 2013]. More specific studies on microglial subtypes were performed by Choi *et al*., and for 0.24 and 0.4 MI (with tiletamine/zolazepam and xylazine). They evaluated the activation of pan (*CD68*, *Aif1*, *Ccl12*), M1 (Serpine1, *CD40*, *Gbp4*) and M2 (*Arg1*, *Gpr84*, *Apod*) microglia-specific genes. A significant increase in pan-microglia specific genes was measure by qRT-PCR between 6 and 48 h. No polarisation was found for M1 and M2 subtypes, but slightly more M2 genes were upregulated at 0.4 MI [Choi *et al.*, 2022]. The latter results, although the differences are minimal, suggest that anti-inflammatory microglia types (M2) are more likely to be expressed than pro-inflammatory (M1).

2.2.2. Astrocytes

Activated microglia release cytokines to regulate the astrocytic response and favour neurotoxic or neuroprotective astrocytes known as A1 and A2, respectively [Liddelow *et al.*, 2017; Shinozaki *et al.*, 2017]. In addition, astrocytic end feet are spatially very close to the BBB endothelial cells, the first

mechanically stressed cells during FUS-induced BBB opening. It is very likely that the combination of both afferent pathways induces the astrocytic response observed, by the studies presented below, after BBB permeabilisation. But no studies have been characterised precisely the different contributions. What is currently known from many studies is the fact that GFAP, a protein highly expressed by reactive astrocytes, is significantly expressed as early as 6 h after FUS [Gorick *et al.*, 2020; Kovacs *et al.*, 2017; Pascal *et al.*, 2020] and the expression appears to persist at 24 h [Gorick *et al.*, 2020; Kovacs *et al.*, 2017; Sinharay *et al.*, 2019], 48 h [Choi *et al.*, 2022; McMahon *et al.*, 2020b], 4, 10 and 15 days [Jordão *et al.*, 2013; McMahon *et al.*, 2020b] and even 7 weeks [Kovacs *et al.*, 2018]. None of the studies evaluated GFAP expression dynamically until it returned to baseline levels. At week 13 post-FUS, it was found to be no longer significant in Kovacs *et al*. study [Kovacs *et al.*, 2018], although they surprisingly measured a significant increase at 7 weeks post-FUS. More specifically, Choi *et al*. investigated subtypes A1 and A2 of astrocytes in the brain tissue post-FUS using qRT-PCR measurements. Very few evaluated genes were upregulated at 0.24 MI, but at 0.4 MI there was a significant upregulation of the A2 compared to A1 subtype. The polarisation of A2 subtype astrocytes was increased at 0.4 MI, suggesting that a protective effect is triggered in reaction to FUS-induced BBB opening [Choi *et al.*, 2022].

2.2.3. Neurons

From a neuronal perspective, only a limited number of studies have examined the effects of FUS on cellular processes. Alonso and colleagues observed the ubiquitinylation of neuronal proteins but not glial proteins following FUS at MI = 1.27 [Alonso *et al.*, 2010]. Ubiquitinylation is a post-translational modification mechanism that facilitates proteins degradation via the proteasome. Its appearance suggests neuronal apoptosis. At lower MI (MI = 0.9), a significant increase in the number of anti-doublecortin (newly born or immature neurons marker) positive cells and in the total length of dendrites was measured 8 months after the permeabilisation of both hippocampus [Burgess *et al.*, 2014]. These positive effects are in line with studies that found no widespread neuronal degeneration at 6 h or 4 days at low MI and low MB dose (MI = 0.27; 10 µL of Definity / kg) but not at high MB dose (∼ 10-fold larger, 100 µL of Definity / kg). The presence of microglial nodules in the targeted area suggests a clearance of the neurodegenerative neurons [McMahon and Hynynen, 2017]. Conversely, in another study, TUNEL+ assay and NeuN staining reveal that neurons were damaged 1 h post-FUS (MI = 0.39) [Kovacs *et al.*, 2017]. However, there was no evidence of hyperphosphorylated Tau-positive neurons 7- and 13-weeks post-FUS (MI = 0.4) [Kovacs *et al.*, 2018]. The accumulation of intracellular phosphorylated Tau is associated with the development of Alzheimer's disease [Meng *et al.*, 2017; Querfurth and LaFerla, 2010]. Interestingly, Aβ plaques were found cleared in the AD mice model TgCRND8 with mean plaque size, surface area occupation and number of plaques dampened 4 days post-FUS (MI = 0.4) [Jordão *et al.*, 2010]. Aβ plaques were found in astrocytes and microglia suggesting with increased of both glial cell types an increase in phagocytosed Aβ plaques (MI = 0.42) [Jordão *et al.*, 2013]. Burgess *et al*. confirmed these results 8 months after the procedure (MI = 0.9) [Burgess *et al.*, 2014].

The effects of FUS on the BBB and neuronal processes vary depending on the MI and MB concentration. While lower MIs tend to minimise damage and support neuronal regeneration, higher MI can lead to significant cellular effects, including apoptosis, highlighting the importance of carefully controlling FUS parameters.

2.2.4. Immune system response

The BBB normally prevents most immune cells from entering the CNS, and with FUS coupled to MB, immune cells from the peripheral blood enter the brain. Peripheral immune cells, including macrophages, neutrophils and leukocytes showed that they can infiltrate the CNS after FUS-induced BBB opening [Gorick *et al.*, 2020; Kovacs *et al.*, 2017; Poon *et al.*, 2021].

Poon *et al*. investigated neutrophils after BBB opening which are the most abundant type of granulocytes (innate immune system cells) in humans. They found that FUS-induced BBB opening caused neutrophils recruitment. They found most of the neutrophils inside of blood vessels but some were also present outside [Poon *et al.*, 2021].

Macrophages play an important role in sterile inflammation, particularly in the clearance of cellular debris and in modulating the inflammatory response. Within the CNS, there are also resident macrophage-like cells, particularly perivascular macrophages and meningeal macrophages. These resident macrophages may complement the role of microglia in the inflammatory response by producing cytokines and participating in immune regulation. The innate immune response with peripheral immune cells CD68 was investigated by Kovacs *et al*. with the labelling of systemic macrophages and revealed that a migration occurred to the region of open BBB. Immunofluorescence staining showed that CD68+ cells were significantly increased 6 days post-FUS [Kovacs *et al.*, 2017]. Significant increase was also measured 7- and 13-weeks post-FUS [Kovacs *et al.*, 2018].

Furthermore, gene-set enrichment analyses for selected pathways associated with the innate and the adaptive immunity system were found upregulated 6 h and 24 h post-FUS [Gorick *et al.*, 2020]. Despite BBB closure within a 24 h window, peripheral immune cells have been shown to continue extravasating past the BBB [Marchetti and Engelhardt, 2020; Martinez *et al.*, 2024; Poon *et al.*, 2021].

2.2.5. Associated cytokines

Cytokines are key regulators of neuroinflammation, significantly influencing both the initiation and resolution of the SIR within the CNS. They mediate interactions among microglia, astrocytes, and peripheral immune cells, which are critical for maintaining CNS homeostasis. The dynamic interplay between these cell types, mediated by cytokines, shapes the sterile inflammatory response and influences the progression of neurological disorders. Cytokines such as IL-1β, TNF-α, and IL-6 are crucial for activating microglia and driving their response to injury or infection, while also affecting astrocytic responses that can either support neuronal survival or promote neurodegeneration. By orchestrating these cellular interactions, cytokines not only dictate the nature and extent of the inflammatory response in the CNS but also play a pivotal role in determining the outcomes of various neurological conditions, underscoring their dual roles in neuroprotection and neurodegeneration.

Few studies have evaluated through mRNA and protein quantifications, the production of the pro- and anti-inflammatory cytokines subsequently to the application of FUS and the opening of the BBB. Proinflammatory cytokines such as TNF-α, Il-1β, Il6 and IFNγ showed increased in protein levels between 30 minutes and to 48 h post-FUS [Kovacs *et al.*, 2017; McMahon *et al.*, 2020b] with different kinetics. Anti-inflammatory cytokines such as Timp1, Il4, Il10 and Il13 were also significantly expressed in a short time period after FUS and rather when acoustic pressures were lower than for pro-inflammatory cytokines expression [Ji *et al.*, 2021; Kovacs *et al.*, 2017; McMahon *et al.*, 2020b]. These

cytokines are mediated by different cell types as macrophages (TNF-α, Il6), microglia and astrocytes (*Il10*) or the adaptive immune system (Il4, Il5, Il13). Some of them as IL-1β are very well characterised and is secreted by multiple cell types and mediates a wide range of inflammatory signalling responses [Ji *et al.*, 2021; Turner *et al.*, 2014].

Chemokines, which are a subset of cytokines specifically involved in chemotaxis (the process of directing the movement of immune cells to sites of infection or inflammation) were also recently studied. Different studies measured increased levels of expression of various chemokines with different kinetics of expression, mostly returning to baseline levels 24 to 48 h post-FUS [Choi *et al.*, 2022; Gorick *et al.*, 2020; McMahon *et al.*, 2020a].

2.2.6. Neuroinflammation can be modulated by FUS-induced BBB opening parameters

The BBB can be permeabilised with a wide range of parameters including different acoustic pressures, MB dose and acoustic cavitation dose as outlined in section 1.4.2.

MB dose and formulation have been shown to alter the inflammatory response. Studies by McMahon and Hynynen, McMahon *et al*. and Pascal *et al*. showed significant differences in microglial and astrocytic response [Pascal *et al.*, 2020] and in the relative gene expression of inflammatory mediators (*Tnf*, *Il-1β*, *Ccl2*, *Sele*) [McMahon *et al.*, 2020a; McMahon and Hynynen, 2017].

In addition, a good correlation was found between increasing MI and the number of activated microglia and astrocytes [Pascal *et al.*, 2020]. These results are in line with the recent study by Choi *et al*. who investigated the molecular responses at 0.25 and 0.4 MI after the permeabilisation of the two hippocampi in mice under an anaesthetic mixture of tiletamine/zolazepam (Zoletil®) and xylazine (Rompun®). Tissues were analysed from 1 to 48 h post BBB opening (monitored with cavitation and MRI). A total of 17 403 and 17 570 transcripts were analysed for the 0.25 and the 0.42 MPa groups, respectively. Less differentially expressed genes were measures for the lower acoustic pressure (0.14 vs 1.47%). For the 0.25 MPa group, the expression pattern was mostly downregulation with a maximum at 24 h post-FUS. For the 0.42 MPa group, the expression of genes was upregulated with an exponential increase [Choi *et al.*, 2022]. Recently, the study by Martinez *et al*. demonstrated that the MB volume dose and the MI significantly influence the SIR at 6 h post-FUS. They refined the treatment parameters using cavitation monitoring to propose a therapeutic window relevant for opening the BBB and avoiding the triggering of the NFκB pathway via TNF-α signalling [Martinez *et al.*, 2024].

Acoustic cavitation-controlled systems as highlighted by Ji *et al*., demonstrated efficient control of the relative gene expression of inflammatory cytokines and receptors in mice. The higher cavitation dose groups showed both greater changes in relative expression levels and greater number of significant changes. By 72 h post-FUS, the gene expression levels returned to baseline in all cavitation dose groups, indicating a transient inflammatory response to FUS-induced BBB opening regardless of the cavitation dose level [Ji *et al.*, 2021].

These results are not very surprising, as an increase in the acoustic pressure and the MB dose is associated with a larger and longer BBB opening. Furthermore, characterising the relationship between acoustic cavitation dose and associated neuroinflammatory effects may lead to better control of associated changes following FUS-induced BBB opening. These results suggest that cavitation control during FUS-induced BBB opening can be used to potentially modulate or limit the degree of

neuroinflammation, further emphasising the importance of implementing cavitation controllers as FUS-induced BBB opening is translated into the clinic [Ji *et al.*, 2021].

2.2.7. Conclusion

	Animal model	FUS parameters	Timepoint					References
			hours			days		
			1	4 – 6	24	2 - 4	10 - 15	
Iba1	TgCRND8 & non-Tg	ketamine/xylazine, 0.4 MI		↑		↑*	→	[Jordão *et al.*, 2013]
	SD	isoflurane, 0.39 MI	↑*	↑*	→			[Kovacs *et al.*, 2017]
	SD	isoflurane, 0.4 MI			↑			[Sinharay *et al.*, 2019]
	C57BL/6	ketamine/xylazine/ atropine, 0.38 MI		→	↑			[Gorick *et al.*, 2020]
	mice	Zoletil®/Rompun®, 0.4 MI	→		↑			[Choi *et al.*, 2022]
GFAP	non-Tg	ketamine/xylazine, 0.4 MI		→		↑*	→	[Jordão *et al.*, 2013]
	TgCRND8			→		↑*	↑*	
	SD	isoflurane, 0.39 MI	↑	↑*	↑*			[Kovacs *et al.*, 2017]
	SD	isoflurane, 0.5 MI				↑*	↑*	[McMahon *et al.*, 2020b]
	SD + DEX					→	→	
	SD	isoflurane, 0.4 MI			↑			[Sinharay *et al.*, 2019]
	C57BL/6	ketamine/xylazine/ atropine, 0.38 MI		↑	↑*			[Gorick *et al.*, 2020]
	mice	Zoletil®/Rompun®, 0.4 MI	→	→	→	↑*		[Choi *et al.*, 2022]
CD68	SD rats	isoflurane, 0.39 MI				↑*		[Kovacs *et al.*, 2017]
Cytokines				↑	↑	→		[Choi *et al.*, 2022; Gorick *et al.*, 2020; Ji *et al.*, 2021; McMahon *et al.*, 2020a]
Innate and adaptive immunity	mice	ketamine/xylazine/ atropine, 0.38 MI		↑*	↑*			[Gorick *et al.*, 2020]

*Table 6. Summary of neuroinflammatory response studies for microglial, astrocytic, cytokines, macrophages and immune reactivity responses to FUS-induced BBB opening. Changes include increase (↑) or no increase (→). Arrow with * indicate significant differences compared to a control condition. DEX indicates dexamethasone and SD indicates Sprague-Dawley rats. Studies on mice are highlighted in blue.*

The FUS-induced BBB opening neuroinflammatory response is initially triggered by various cell types such as microglia and astrocytes. At the same time, neutrophils appear to play an important role in signalling BBB opening, as a recent study by Poon *et al*. highlighted neutrophils as the primary reactive cell type in the early stages following application of FUS and MB [Poon *et al.*, 2021]. The release of damage-associated molecular patterns within 5 minutes of BBB opening may be the starting point of the cascade of phenomena presented here [Kovacs *et al.*, 2017]. These patterns are known to influence the local metabolic and physiological pathways that regulate interactions between the vasculature and the NVU [Gadani *et al.*, 2015; Kovacs *et al.*, 2017]. A summary of the different cells and molecules transiently modified is given in Table 6. The pattern, kinetics and intensity of neuroinflammation can

be modulated by the dose of MI and MB and thus controlled by acoustic cavitation closed-loop systems to avoid potential risks but also refine the therapeutic window. This control is also very useful for modulating neuroinflammation for therapeutic purposes for timing considerations to optimise therapeutic benefits while limiting risks. For example, microglial activation is known to internalise Aβ plaques in mouse models of Alzheimer's disease and opens a great perspective for the treatment of Alzheimer's patients [Jordão *et al.*, 2013; Leinenga and Götz, 2015]. In addition to FUS-induced BBB opening, the use of glucocorticoids such as dexamethasone has been shown to reduce the risk of inflammation following BBB opening [McMahon *et al.*, 2020b]. Finally, the neuroinflammatory process associated with repeated BBB opening will be developed in section 2.6, as the result of successive FUS applications may induce more long-term effects.

2.3. Metabolism

Metabolism in the CNS involves the regulation of energy production and the nutrient utilisation. It is critical for neuronal function and survival. Dysregulation of CNS metabolism is linked to various neurological disorders, including neurodegenerative diseases and mental health conditions. Yet, few studies have evaluated the effects of the permeabilisation of the BBB with FUS on the metabolism. Yang *et al*. explored the pharmacodynamic of ^{18}F-FDG uptake with PET imaging followed by western blot analysis of the GLUT1 (glucose transporter 1) protein. They permeabilised the BBB of Sprague-Dawley rats in one hemisphere centred below the right hippocampus at 0.7 MI under 2% isoflurane anaesthesia. PET scan was performed immediately and 24 h post-FUS. No significant differences were observed at either timepoints between sonicated and control regions at both timepoints. Significant decrease in FDG uptake for the whole brain was however measured immediately after FUS, suggesting a lower metabolic rate. 24 h post-FUS, higher ^{18}F-FDG uptake in the whole brain was measured, yet this was not significant [Yang *et al.*, 2014]. One can note that some Evans blue residuals were still visible 24 h post-FUS, suggesting a strong BBB opening. Measures in three primates permeabilised under a mixture of ketamine and xylazine associated with propofol with an implantable device similar to Carthera's device (see 1.4.4) at an MI between 0.6 and 0.8. On average, 1.16 cm^3 of the BBB was disrupted close to the skull in the cortex. ^{18}F-FDG uptake was monitored with PET scans 14 days after BBB permeabilisation and no differences were found between the two hemispheres [Horodyckid *et al.*, 2017], confirming the previous results. We can highlight that very small modifications in glucose uptake at the level of the CNS were observed consequently to FUS application, and this was confirmed by GLUT1 (glucose transporter 1) expression significantly lowered just after BBB opening (0.6-fold change) but returned to baseline 24 h after (0.9-fold) [Yang *et al.*, 2014]. Presset *et al*. evaluated after BBB permeabilisation of Sprague-Dawley rats in different biological tissues (striatum, cerebrospinal fluid, blood serum and urine) at various timepoints (3 h, 2 days and 1 week) using metabolomics performed either with ^{1}H-NMR spectroscopy or mass spectrometry. The BBB opening was performed under anaesthesia with a mix of ketamine and xylazine at 0.6 MI. The FUS focal spot was quite large, and the cortex and striatum were permeabilised. They did not observe differences in the cerebrospinal fluid 3 h post-FUS, but for blood serum, urine and striatum differences persisted up to a week. The striatum samples showed stronger differences at 2 days post-FUS. Regarding glucose metabolism, they did not measure any changes according to Horodyckid *et al*. They reported some dysregulation in various metabolic pathways as arginine [Presset *et al.*, 2022]. Arginine is known to play a major role in the energetic supply and homeostasis by regulating nitrogen levels and immune response. This is in line with studies that previously analysed the immune system responses previously (see 2.2.3). Arginine is

also an immediate precursor to nitric oxide, that is strongly involved in retrograde vasomotor mechanisms (see section 1.2) and thus in line with precedent studies on the vascular flow modifications [Cho *et al.*, 2011; Fan *et al.*, 2012; Labriji *et al.*, 2023; Raymond *et al.*, 2007]. Presset *et al*. measured significant enhancement of metabolites involved in liver-related inflammation due to the stress induced by FUS, neuroinflammation and vascular inflammation and this is supported by precedent studies [Kovacs *et al.*, 2017; McMahon *et al.*, 2017; McMahon and Hynynen, 2017; Sinharay *et al.*, 2019]. Glucose metabolism seemed to be slightly affected by the permeabilisation of the BBB. Peeters *et al*. investigated hyperpolarised pyruvate and lactate metabolism with ^{13}C NMR in mice. These two metabolites are involved in the process of glycolysis. The pyruvate is the end product of glycolysis (the process by which glucose is broken down to generate energy) while the lactate is produced from pyruvate during anaerobic glycolysis. Elevated levels of lactate in tissue or blood are a great indicator of hypoxia (among others). Yet, they did not measure any increase in hyperpolarised pyruvate or lactate related to the FUS procedure [Peeters *et al.*, 2019].

2.4. Behaviour

After FUS-induced BBB opening it has largely been shown that drugs can be delivered efficiently in a safe and spatially controlled manner by analysing the brain tissues with immunohistology or western blot techniques. However, the evaluation of motor behaviour, neurological function and memory is of considerable importance, as it permits the assessment of the efficacy of administered treatments and provides compelling evidence of their potential clinical applicability. A review of the literature reveals a dearth of studies investigating behavioural outcomes following BBB opening, with only 9 studies identified in PubMed summed up in Table 8. One study involved an ovine model, two studies NHPs and 6 studies mice with half concerning Alzheimer's disease models. Tests used in these studies for mice are the classical rotarod, Y-maze, open-field, Morris water maze, step-down and beam walk tests.

Studies	Y-maze	Rotarod	Morris	Other tests
[Burgess *et al.*, 2014]	x			
[Shen *et al.*, 2020]	x		x	step-down
Kong et al 2022	x			
[Kong *et al.*, 2023]	x		x	
[Olumolade *et al.*, 2016]		x		open field
[Su *et al.*, 2017]		x		mNSS, beam walk
[Lin *et al.*, 2019]		x		

Table 7. List of behaviour tests performed on mice after FUS, in grey studies involving Alzheimer's disease models.

The Y-maze enables to test the spatial short-term memory, the rotarod measures balance and motor activity, the Morris water maze assesses the spatial learning and long-term working memory, the beam walk is used to evaluate fine motor coordination and function by measuring the ability of an animal to traverse an elevated beam. The modified neurological severity score (mNSS) is a grid notation score test that rates the neurological functioning on a scale of 0-18 from normal to maximal deficit. The open field chamber consists of observing in an empty isolated room the behaviour of the animals and measuring for example the distance travelled, the number of rearings, the thigmotactic activity (characterising the anxiety), etc... The step-down test is used to measure the memory retention with an electrical shock delivered if the animal steps down from the "safe" platform.

Studies in Alzheimer's disease models showed improvement in cognition with non-significant time spent in the novel arm of the Y-maze compared to non-deficient mice and significantly different from untreated mice [Burgess 2014]. In addition, 3×Tg-AD mice treated with FUS and MB improved their learning and memory capacities, as evidenced by comparable time spent in the novel arm of the Y-maze and a non-significant reduction in latency to escape the water tank in the Morris water maze test, when compared to the control mice. The results of the three independent memory-related behavioural tests provided evidence that the 3xTg-AD mice subjected to repeated FUS treatments exhibited significantly enhanced performance in both short-term and long-term memory, as well as cognition [Shen 2020]. These findings were corroborated in 5xFAD mice, exhibiting comparable outcomes across the assessed parameters in both the Morris and Y-maze tests between the treated transgenic and the control mice [Kong, 2023]. This suggests that FUS coupled with MB treatment effectively rescued the spatial memory deficits in different Alzheimer's disease models, supporting the idea of future success in clinical trials. In a traumatic brain injury (TBI) mice model, it has been demonstrated that the mNSS was markedly reduced in the FUS-treated group in comparison to the control group at days 1 to 28 post-TBI signifying an improvement of the animal outcome. Furthermore, the treated mice exhibited enhanced performance in the rotarod, and beam walk tests, respectively, throughout the observation period and from 14 to 28 days.

The permeabilisation of the BBB with FUS seems to have a positive impact on the memory of treated mice and general behaviour. With very few studies analysing the motor and memory outcome after FUS, it is difficult to draw conclusions, and future work needs to observe behavioural outcomes, especially for brain tumour patients that can already have strong cognitive decline due to the classical procedures currently used clinically.

2.5. Clinical parameters evaluated after blood-brain barrier permeabilisation in human

FUS-induced BBB permeabilisation demonstrated its feasibility in the human brain for diverse applications (see section 1.4.4). These studies, in addition to assess the feasibility, monitored different parameters related to general health. This section will describe the more relevant parameters.

Among the 21 articles that presented the permeabilisation of the BBB in humans, 9 were related to brain tumours, 8 to AD, 3 to PD and 1 to amyotrophic lateral sclerosis.

For brain tumours, FUS in association with MB demonstrated enhanced drug delivery [Meng *et al.*, 2021b], a better control in tumour growth [Carpentier *et al.*, 2024] and enhanced circulating brain-derived biomarkers to improve liquid biopsy diagnostic [Meng *et al.*, 2021a]. Most studies presented reversible BBB opening without tissue damage. Regarding brain tumours, the main purpose is to deliver chemotherapies that are known to have a high toxicity and are recurrently not well tolerated by patients. BBB opening did not seem to increase drastically the level of toxicity. For example, Sonabend et al. permeabilized the BBB using a large implantable ultrasound device (Sonocloud-9, 9 × Sonocloud-1) to deliver albumin-bound paclitaxel, a common chemotherapy used for metastatic breast cancer. They administered a standard dose and observed encephalopathy, a rare side effect of albumin-bound paclitaxel, which was reversible, allowing the treatment to continue. Additionally, the study showed that FUS and MB increased the brain/plasma ratio of carboplatin by 5.8 times, demonstrating enhanced delivery of both albumin-bound paclitaxel and carboplatin across the BBB

[Sonabend *et al.*, 2023]. These results are supported by Idbaih *et al*. study, that repeatedly permeabilised the BBB monthly over 10 months with injection of carboplatin, observed no cumulative toxicity with the treatment repetition [Idbaih *et al.*, 2019]. In addition, the combination of temozolomide and FUS did not show new temozolomide-related toxicity [Park *et al.*, 2021], yet this therapeutic strategy did not prove to efficiently increase the overall mean survival in patients with glioblastoma. Some adverse events were reported within 1 month following the FUS procedure with fatigue, nausea and headaches [Carpentier *et al.*, 2024; K.-T. Chen *et al.*, 2021; Idbaih *et al.*, 2019; Sonabend *et al.*, 2023] but was not correlated to the MB and FUS procedure. In addition, haematological disorder was found with neutropenia (decrease of neutrophils) and leukopenia [Idbaih *et al.*, 2019; Sonabend *et al.*, 2023]. Yet, Chen *et al*. did not measure immunological response 7 days post-FUS. They mainly found macrophages in normal, peritumoral and tumour tissues but there were no statistically significant differences between control and treated samples [K.-T. Chen *et al.*, 2021].

Regarding AD clinical studies, almost all patients presented no cognitive declines, neurological and neuropsychological adverse effects [Bae *et al.*, 2024; Epelbaum *et al.*, 2022; Lipsman *et al.*, 2018; Mehta *et al.*, 2023, 2021; Rezai *et al.*, 2024, 2022, 2020]. Long-term follow-up demonstrated also no differences between 15 to 19 months after the BBB opening [Mehta *et al.*, 2021; Rezai *et al.*, 2020]. Few exceptions may happen as In Rezai *et al*. study, a single patient presented a small cognitive decline according to the RBANS score (a brief cognitive assessment tool evaluating immediate memory, visuospatial awareness, language, attention and the delayed memory). But according to ALDI score (a test that evaluate speech fluency, lexical richness, syntactic complexity and acoustic features) these patients did not show differences [Rezai *et al.*, 2024]. Different adverse events were stressed out after BBB opening in AD patients that received intracranial FUS therapy with Sonocloud-1 (Carthera, Paris, France) device: fatigue, back and abdominal pain or headaches [Epelbaum *et al.*, 2022]. All patients presented among these studies showed transient BBB opening. Some studies observed hypointense or hyperintense voxels with MRI that were resolved by 48 h [Mehta *et al.*, 2023] or 72 h [Rezai *et al.*, 2022], respectively. Repeated treatment demonstrated no important adverse effects [Epelbaum *et al.*, 2022] and the treatment of AD combined with Aducanumab led to the reduction of Aβ levels [Rezai *et al.*, 2024].

In conclusion, very few adverse events seem to be related to the combination of FUS and MB. The actual number of patients involved in these studies are not high enough to stress out conclusions and more studies should focus on the potential adverse effects. In addition, the patients enrolled in these studies, especially regarding brain tumours, are very often patients with recurrences and thus are in a very advanced stage of disease progression. Using FUS and MB in patients at an early stage of disease progression remains a challenge but to bridge this gap preclinical studies are increasingly more interested in biological effects and understanding the underlying mechanisms than in survival outcomes to refine the therapeutic window and strategies.

2.6. Multiple blood-brain barrier opening

Single FUS session has been demonstrated to facilitate effective enhancement of drug delivery in the treatment of brain tumours and other central nervous system (CNS) diseases. It was observed that the occurrence of secondary bioeffects and more particularly the neuroinflammation was reduced and/or controlled when the FUS parameters were meticulously regulated through the utilisation of cavitation monitoring and control (see 2.2, for cavitation refers to section 1.5). In the context of brain tumour

diseases, it is common practice to prescribe a range of chemotherapy doses in conjunction with other potential treatments, including radiotherapy and tumour-treating fields. To illustrate, the current gold standard for treating glioblastoma is the Stupp protocol, which involves five administrations of temozolomide in conjunction with 30 × 2 Gy fractions of radiotherapy over a six-week period [Stupp *et al.*, 2005].

As previously observed, a single FUS treatment can induce secondary effects. It may therefore be hypothesised that repeated treatment could result in increased neuroinflammation or cellular damage. This section will review the studies that have evaluated the secondary bioeffects of multiple FUS sessions and the potential enhancement of this method as a treatment for the brain.

Most of the attention has been centred in preclinical mice models of AD regarding the use of repeated FUS treatments. It has been shown in different studies of preclinical models of AD that the repetition of FUS treatments led to behavioural improvements, reduction of Tau protein and Aβ-plaque load [Kong *et al.*, 2022; Leinenga and Götz, 2015; Pandit *et al.*, 2019; Shen *et al.*, 2020]. Treatment plannings were very different across studies from 3 biweekly (one treatment every two weeks) [Kong *et al.*, 2022] to 15 weekly FUS sessions [Pandit *et al.*, 2019]. By controlling the FUS energy deposition, no significant secondary bioeffects were highlighted by the different studies. Surprisingly, Leinenga and Götz did not see any neuroinflammation after 5 or 8 biweekly treatments in APP23 mice [Leinenga and Götz, 2015]. They permeabilised the BBB with a higher MI (0.7 vs 0.42) and with a 10-fold MB dose than previous study by Jordão *et al*. that found increased in GFAP and Iba1 expression [Jordão *et al.*, 2013]. The animal model was different (APP23 vs TgCRND8) but the outcome was similar with the reduction in size and number of Aβ plaques, and their internalisation by microglia. Other studies have showed increased levels of Iba1 and CD68 at the site of the FUS application [Kong *et al.*, 2022] and with confocal microscopy a significant change in the shape of the microglia with significantly reduced endpoint and process length [Shen *et al.*, 2020]. In addition, proteomics analysis revealed the upregulation of several proteins related to synapse, microtubule and mitochondria [Shen *et al.*, 2020].

All in all, these results did not appear to differ from a single FUS application to the brain. Also, their purpose was not to study the impact of repeated treatment compared to single FUS application, thus finding control is difficult. To bridge this gap, specific studies were interested in the effects of repeated FUS treatments to permeabilise the BBB investigating the immunohistological, MRI and PET modifications.

Several studies have shown that the repeated application of FUS led to significant changes in T2*-weighted images with a decrease in mean T2* values in both hippocampus and cortex after 2 weekly FUS sessions and 6 weekly FUS sessions compared to a single FUS session [Sinharay *et al.*, 2019]. MRI imaging revealed also a ventricular enlargement, large hypointense regions with persistent BBB opening 1 week after 6 weekly treatments [Kovacs *et al.*, 2018]. These results suggest that the FUS induced BBB opening was not safe. Also, large regions were permeabilised compared to studies presented earlier. Furthermore, histological evaluation with H&E staining did not show large haemorrhages but found a significant number of Prussian blue-positive metallophagocytic cells that had phagocytosed extravasated red blood cells from microhaemorrhages previously visible with MRI [Kovacs *et al.*, 2018].

PET analysis with [^{18}F]DPA-714, a biomarker of translocator protein to assess for neuroinflammatory changes, revealed that the repetition of FUS treatments did not show significant changes compared to

single and twice application of FUS in the cortex and the hippocampus [Sinharay *et al.*, 2019]. This was confirmed by the histological analysis of Iba1 and GFAP. Although ratios were > 1, they did not measured differences across the three groups. But comparing a group with a single application 24 h post-FUS and a group with two treatments 13 days post-FUS and a group with 6 FUS treatments 7 days post-FUS is not very possible. They should have paid more attention to the timing of brain harvesting for histology because the results presented as they stand do not allow us to draw any conclusions.

Kovacs *et al*. study did not show significant differences 7 weeks post-FUS between single and 6 FUS treatments in GFAP and Iba1 expression in the cortex. Regarding the hippocampus, the difference was not significant in GFAP, but Iba1 was increasingly expressed for the 6-FUS group. Finally, changes in CD68+ were similar between the two treatments planning. Western blot analysis of phosphorylated Tau protein revealed a significant increase in the 6-FUS treated cortex but not in the hippocampus. Phosphorylated Tau was found collocated with neurons on immunohistological analysis [Kovacs *et al.*, 2018]. Results from this study suggest that the SIR started after a single FUS session continued and increased slightly, inducing an increased expression of phosphorylated Tau after the 6 weekly treatments. The accumulation of phosphorylated Tau in neurons have been associated with AD [Noble *et al.*, 2013] and it is known that the SIR contributes to neurodegenerative processes [Bellucci *et al.*, 2011]. As the MRI image evidenced, BBB opening was not reversible after 6 weekly treatments, and it suggests that lowering the acoustic pressure or using a cavitation controller system will avoid such secondary bioeffects.

Translation studies in NHP have evaluated the feasibility of repeated FUS with the evaluation of cognitive tasks [Downs *et al.*, 2015; McDannold *et al.*, 2012], electrophysiology, ^{18}FDG-PET and histological analysis [Horodyckid *et al.*, 2017]. No significant changes were found between the control group and the group that received successive treatments across all studies. Even in NHP that presented hyperintense voxels on MRI, suggesting oedema, Downs *et al*. did not observed variations in the reaction time or touch errors during the cognitive tasks [Downs *et al.*, 2015]. These important results, suggest that repeated FUS planning can be transferred to clinics.

Clinical trials have already evaluated the successive application of FUS in the brain of recurrent glioblastoma patients [Idbaih *et al.*, 2019] and AD patients [Epelbaum *et al.*, 2022].

In conclusion, the repetition of FUS treatments, despite the fact that it showed impressive results in the outcome of AD mouse models, should require special attention for the treatment parameters, as it can induce damage at the level of the BBB, strong neuroinflammation that leads to the production of neurodegenerative-like pathways with the presence of phosphorylated Tau. Studies using controlled acoustic parameters inducing safe and reproducible repeated BBB opening should focus on the repetition duration and propose standardise procedures for successive BBB opening treatments.

Chapter 3. Problems and objectives

This thesis involved three different partners, the company Image Guided Therapy (IGT, Pessac, France) owned by Erik Dumont, that develops and commercialises MR-guided FUS solutions to perform BBB opening of thermal ablation, the LIR²SO laboratory (Orléans, France) headed by Pr Chantal Pichon in which Dr Anthony Delalande conducts his research, and finally the Grenoble Institut des Neurosciences (GIN, Grenoble, France) led by Dr Emmanuel L. Barbier in which Dr Vasile Stupar is research engineer. This project was funded partly by Image Guided Therapy (CIFRE) and the FRC Neurodon foundation with the support of the Autun Rotary association. This is the first project about the permeabilisation of the BBB with FUS that is conducted in this lab and even in Grenoble's scientific area.

The vast majority of the experiments presented in this thesis were conducted on the preclinical part of the IRMaGe facility. It includes two preclinical MRI (4.7 and 9.4 T, Bruker, Ettlingen, Germany), an MR-guided FUS system (IGT, Pessac, France), a stereotaxic radiotherapy platform for small animal irradiation (XStrahl, Suwanee, GA, USA) and various surgical rooms dedicated to animal experimentation. All MB used in this study were produced by the LIR²SO (Anthony Delalande; see 4.2 for their characterisation).

As previously outlined, the utilisation of FUS in the brain, in conjunction with MB, to facilitate the delivery of therapeutic compounds has recently been discovered and proven to be one of the best solutions to permeabilise the BBB thanks to the reversibility, safety and precision reached. A substantial body of research has been conducted to elucidate the principal factors influencing the outcome of drug delivery, including concentration and biodistribution. This technology is still in its infancy in terms of clinical trials, with only a limited number of studies conducted to date and many more yet to come. Nevertheless, a considerable number of underlying mechanisms remain to be investigated, particularly those pertaining to the vascular system, where MB exert a direct influence due to their cavitation behaviour in response to the FUS beam.

This thesis proposes an evaluation of various vascular parameters using quantitative MRI methods to address the question of whether vascular dysregulation may occur following the permeabilisation of the BBB with FUS. This approach will facilitate a more detailed characterisation of the secondary bioeffects of this treatment, thereby enabling the refinement of treatment parameters to ensure optimal translation to clinical settings. After a careful characterisation of the experimental set-up and some methodological developments (**Chapter 4**), we evaluated in a first study the vascular modifications following a single application of FUS in the brain of healthy rats (**Chapter 5**). For this project, I learn to manipulate animals and perform surgery (anaesthesia), to work with the MRI scanner and the FUS system, and to process data. I received support to install catheters for MB injections. I had the opportunity to present the results at the annual meeting of the International Society for Therapeutic Ultrasound (ISTU) and to publish in Theranostics [Rigollet *et al.*, 2024c].

With the intensification of studies using multiple FUS treatments, we explored the impact on the brain of repeated FUS treatments assuming that there is a threshold beyond which it becomes too damaging to repeat the FUS treatments (**Chapter 6**). For this, I learned MR vascular fingerprinting with the support of Aurélien Delphin, Thomas Christen and Benjamin Lemasson. I then performed all the experiments in autonomy and had the opportunity to present the results orally at the 2024 annual

European Molecular Imaging Meeting in Porto and the 2024 International Society for Magnetic Resonance in Medicine in Singapore. A manuscript is in preparation.

Furthermore, with the recent installation of a preclinical stereotaxic irradiator platform in the IRMaGe facility, we aimed at combining MR-guided FUS and radiotherapy to treat brain tumours. Patients diagnosed with brain tumours, and in particular glioblastoma, have an extremely poor prognosis. The conventional treatments employed in clinical settings are unable to deliver chemotherapies effectively and accurately at the tumour core and peritumoral regions due to the presence of the BBB. The arrival of the FUS, with the aid of MRI, enables reaching deep brain structures and the treatment of complex tumour shapes as well as metastasis. In collaboration with the Synchrotron Radiation For Biomedicine laboratory (STROBE, Grenoble, France) and the Dr Hélène Elleaume, we delivered carboplatin in an F98 rat glioblastoma model with FUS followed one day after by a single stereotactic radiotherapy session. We evaluated the biodistribution of this chemotherapy in the brain at 1 hour and 24 hours post-FUS as well as the survival outcome of the animals with an MRI longitudinal follow-up (**Chapter 7**). For the latter experiments, I had the opportunity to mentor a M2 student.

Finally, the project encompasses the utilisation of FUS in knock-out mice models. Gene therapy has emerged as a highly promising strategy, offering the potential to provide novel therapeutic solutions for genetic diseases affecting the CNS that currently lack effective treatments. In this context, two studies were conducted. First, in collaboration with Dr Michael Decressac and his team at GIN with the specific aim of delivering recombinant AAV type 9 to the entire brain of *Ndufs4*^{KO} mice to restore gene expression. This study will not be presented here due to the confidentiality of the results. I performed all the FUS-related experiments as well as MRI acquisitions (about 100 animals and 15 to 20 days of experiment). Then, a study was conducted in collaboration with Thomas Ador, a PhD student supervised by Pr Chantal Pichon and Dr Anthony Delalande, with the objective of evaluating different gene therapy strategies in a *Fmr1*^{KO} mice model of the Fragile X syndrome. Consequently, in **Chapter 8** we will present the results of this gene therapy protocol delivered with FUS with the evaluation of its effectiveness using biological techniques and behavioural tests. The preliminary results of this study were presented at the 2024 ISTU meeting.

Chapter 4. General methods and methodological developments

In this section, we will describe the general methods used during the experiments and the characterisation of aspects of the general context.

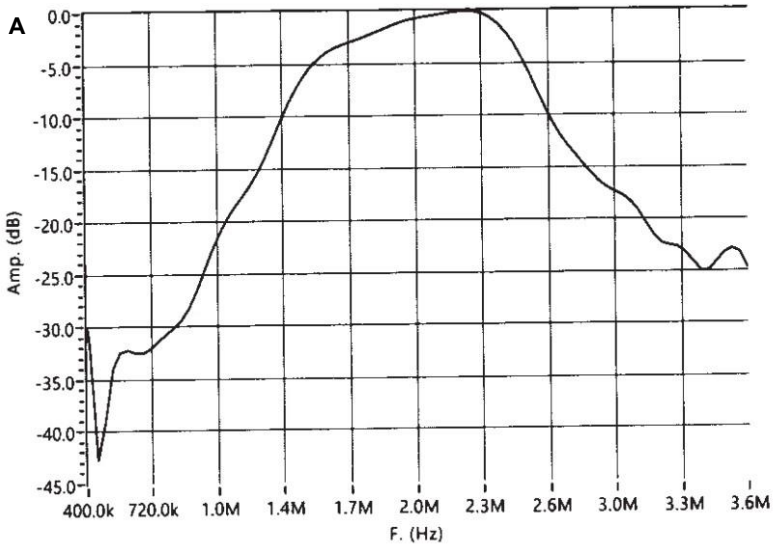
In particular we evaluated: the focused transducer, the microbubbles (MB), the MR-guided FUS system, the BBB opening with the kinetics of the permeabilisation, the cavitation monitoring method and finally the MRI sequences and processing applied along this thesis. Each evaluation step includes a description of its specific methods.

4.1. Focused ultrasound transducer characterisation

Transducer characterisation was a necessary step to perform controlled and reproducible BBB opening as transducer characteristics directly impact the outcome of the procedure (see 1.4.2). Thus, we characterised the focal task and calibrated the pressure of the FUS transducer.

The ultrasound transducer used in all the studies reported in this manuscript has seven annular concentric elements made of piezoelectric material. Elements have the same area to keep the impedance constant. It is commercialised by Imasonic (Voray-sur-l'Ognon, France). The average radius of curvature is equal to 20.01 mm and with a F-number equal to 0.8. Additional data are presented in Figure 18.

A



B

Characteristics at -6 dB	
Central frequency	2.01 MHz
Ratio Bw/Fc	54 %
Bandwidth	1.08 MHz
Lower Cutoff Frequency	1.47 MHz
Upper Cutoff Frequency	2.55 MHz

Figure 18. Focused ultrasound transducer pulse echo transfer function. Data provided by Imasonic.

We mounted an HGL-0200 Onda bullet hydrophone (Sunnyvale, CA, USA) on a 3-axis motorised system driven by an in-house LabVIEW program to finely map the focal task. The hydrophone was plugged to a pre-amplifier Onda AG 2010 and a Picoscope. The transducer and the hydrophone were placed in a degassed water tank (Figure 19.A) and measurements were taken at frequencies of 1, 1.1, 1.2, 1.3, 1.5, 1.75 and 2 MHz and for steering from 0 to -15 mm. The focal spot was mapped with a resolution of 0.1 × 0.1 × 0.2 mm^3 (Figure 19.B). Results of the calibration at the native focal spot and of the focal spot are displayed in Figure 19.C-D. We measured correlation between the amplitude of the emitted

acoustic signal and the PNP as well as correlation between the steering depth and the length of the focal task. We can also observe that when the frequency of the transducer increases, the slope of the curve steepens (Figure 20.A). The results of the focal task size measurements for the different steering are displayed in Figure 19.

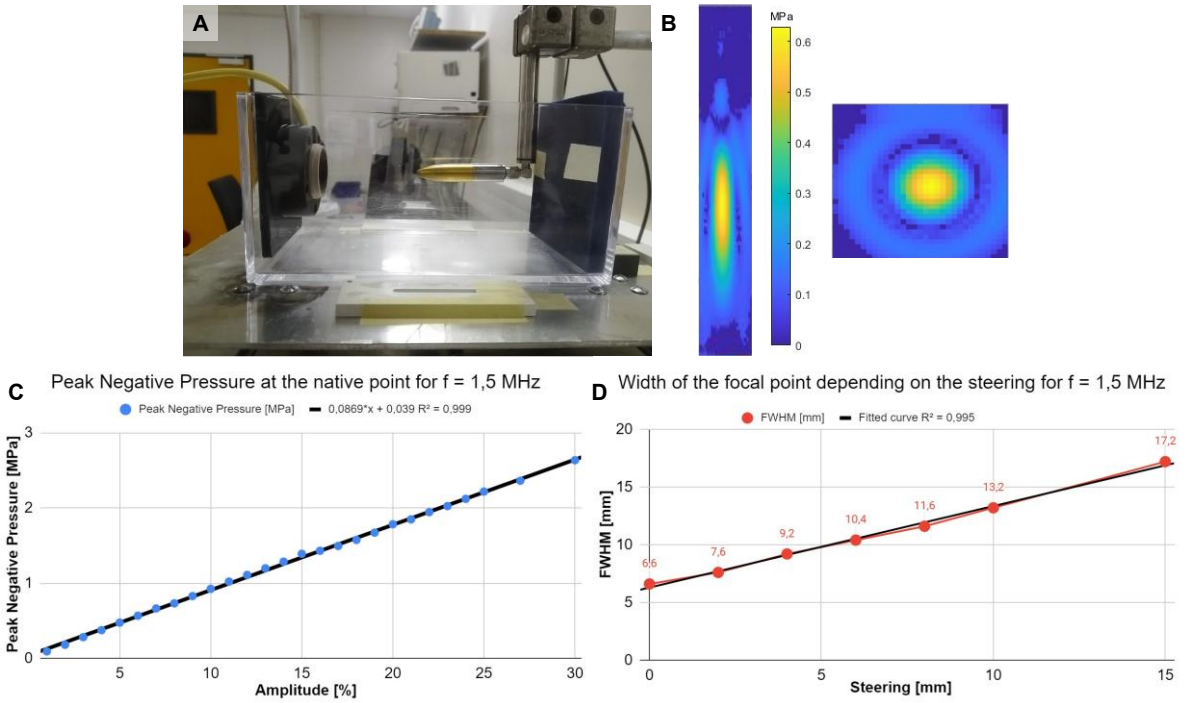
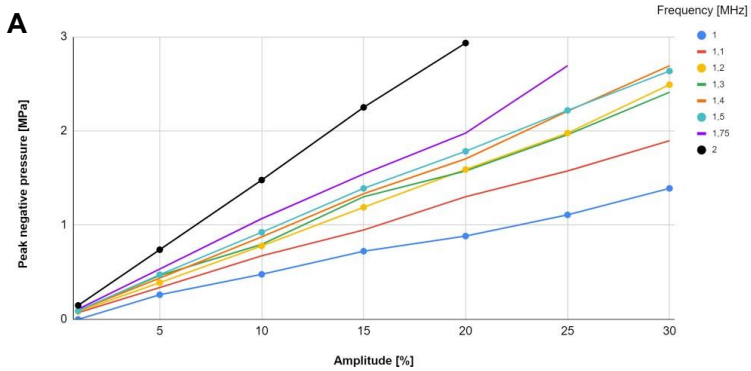


*Figure 19. Transducer characterisation system and calibration curves. **A**) The transducer and hydrophone with pre-amplifier in the degassed water tank. **B**) Coronal and axial sections of the measured focal task ($FOV_{coronal}$ = 3 × 25 mm^2 and FOV_{axial} = 3 × 3 mm^2, resolution 0.1 × 0.1 × 0.2 mm^3). **C**) Calibration curve of the PNP for f = 1.5 MHz and zero steering. **D**) Evolution of the FWHM of the focal task length depending on the steering.*



B

Steering [mm]	FWHM [mm^3]
0	1.1 × 1.2 × 6.6
2	1.15 × 1.5 × 7.6
4	1.2 × 1.3 × 9.2
6	1.25 × 1.3 × 10.4
8	1.35 × 1.4 × 11.6
10	1.45 × 1.5 × 13.2
15	1.65 × 1.7 × 17.2

*Figure 20. Transducer characteristics as a function of frequency and steering. **A**) Evolution of the PNP for different frequencies of the transducer [1-2 MHz]. **B**) FWHM of the focal task of the transducer for different steering depth.*

To further investigate our measurements, MATLAB simulations were made with the k-wave toolbox [Treeby and Cox, 2010], by modelling a transducer with comparable properties. Two transducers were modelled, the first without considering the different elements (“mono”) and a transducer considering the 7-concentric annular elements (“multi”). With the numerical simulations we could verify, as depicted in Figure 21 that by increasing the frequency we can reduce the size of the focal spot. This is

in line with the measurements made (see Table 8) and according to the equations governing the acoustics.

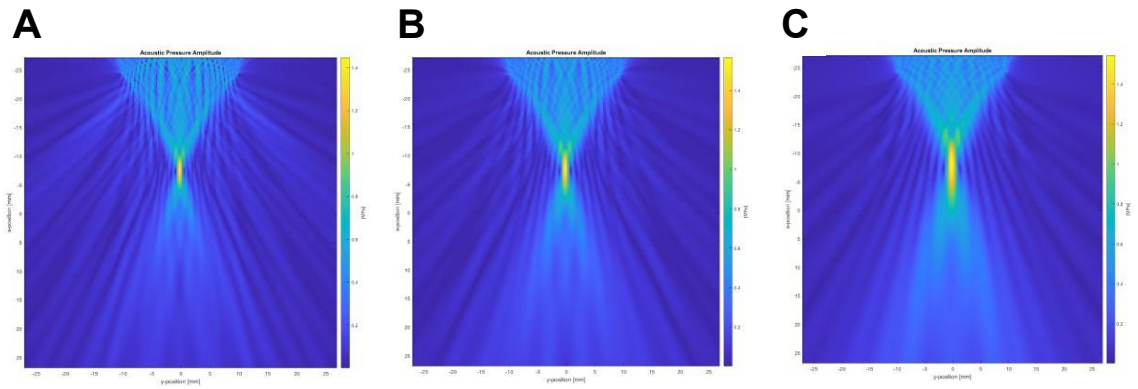


*Figure 21. Results of the simulation of the focal spot at 2 (**A**), 1.5 (**B**) and 1 MHz (**C**).*

Frequency [MHz]	**1**	**1.5**	**2**
Measured FWHM [mm^3]	1.6 × 1.65 × 9.6	1.1 × 1.2 × 6.6	1.4 × 1.6 × 5.2
Simulated FWHM mono [mm^3]	1.75 × 1.75 × 12.75	1 × 1 × 8.5	1 × 1 × 6.25
Simulated FWHM multi [mm^3]	1.5 × 1.5 × 11.5	1 × 1 × 7.5	1 × 1 × 5.75

Table 8. Presentation of the full width at half maximum (FWHM) of the focal spot for the measurements with the hydrophone, the simulated transducer with same diameter and a mono-element and the simulated transducer with the 7-concentric annular elements.

Results from this calibration were compiled in an excel file to facilitate its use and were used to deliver properly the right pressure *in situ*. The values of transmission through the rat skull from Gerstenmayer *et al*. were also added to improve the accuracy of the *in vivo* estimated pressure [Gerstenmayer *et al.*, 2018].

We characterised both the acoustic pressure and focal task size for a large range of frequencies and confirmed our results with simulations in order to perform the more accurate BBB opening with this FUS transducer. It exists a large variety of transducers in the literature, thus this is a necessary step to be as reproducible as possible. This transducer was the only one used during this thesis.

4.2. Microbubble characterisation

The MB are the other compound that greatly influences both BBB opening outcome through its cavitation properties (see 1.4.2, 1.5.4). In this section we will describe the characteristics of the MB used during this thesis. Most of the experiments presented in this part were performed by Lucas Tachen, a master 2 intern I supervised with Dr Vasile Stupar. The most important results will be presented in this section.

MB were manufactured and lyophilised at Orléans. Different types of MB were used in this thesis. The main MB used are neutral and have a shell composed of 1,2-distearoyl-sn-glycero-3-phosphocholine (DSPC) and 1,2-dimyristoyl-sn-glycero-3phospho- ethanolamine-N-[methoxy(polyethyleneglycol)-2000] (DSPE-PEG2000), 88:12 molar ratio. Lipids were obtained from Avanti Polar lipids (Alabaster, Alabama, USA). The gas core is composed of perfluorobutane (F2 Chemicals, Preston, United Kingdom).

MB have on average a mean diameter of 1. 4 µm 99% of events below 5 µm, and concentration of 2.2 × 10^{10} MB/mL. These MB were used in the Chapter 5, Chapter 6, Chapter 7 and Chapter 8 of this thesis.

And finally, we used cationic MB composed of a shell of 1,2-dimyristoyl-sn-glycero-3-phosphocholine (DMPC), 1,2-dimyristoyl-sn-glycero-3-phospho-ethanolamine-N-[methoxy(polyethyleneglycol)-2000] (DMPE-PEG2000), KLN27 C14-lipophosphoramidate cationic lipid and MM30 fusogenic C14-lipophosphoramidate lipid. Lipophosphoramidates have previously shown their ability in gene delivery [Berchel *et al*., 2016; Gonçalves *et al*., 2014]. Due to their cationic shell properties, these MB can complex anionic compounds such as plasmid DNA (pDNA) and thereby behave as a gene therapy carrier agent. The cationic MB complexed with pDNA were characterised *in vitro*. pDNA with cationic MB was used *in vivo* in the *Fmr1*^{KO} mice model and the results are part of the study presented in Chapter 8. For the sake of clarity, the *in vitro* and *in vivo* results will not be presented here and will be presented in detail in Thomas Ador's PhD thesis.

Type of MB	Composition	Mean diameter	Zeta potential
Neutral	DSPC:DSPE-PEG2000 (88:12)	1.37 ± 0.5 µm	-20 mV
Biotin functionalised	DSPC:DSPE-PEG2000:DSPE-PEG2000-biotin (88:11.5:0.5)	1.54 ± 0.1 µm	-20 mV
Cationic	DMPC:DMPE-PEG2000:KLN27:MM30 (45:3:43:9)	1.21 ± 0.5 µm	+19.1 ± 0.5 mV

Table 9. Microbubble formulations.

The properties of the MBs were characterised *in vitro* in Orléans. MB size and concentration were characterised by optical microscopy and image analysis. Zeta potential was measured by dynamic light scattering using SZ100 (Horiba) or Zetasizer Ultra (Malvern). The lipids formulations were optimised for the best MB concentration and stability. All MB were activated in a 500µL of 10 mM HEPES buffer (pH = 7.4) through 45 s of mechanical agitation using a VialMix® shaker (4000-4500 rpm, Lantheus Medical Imaging). We developed an *in vitro* cavitation system to measure the different acoustic properties of the MB under various FUS parameters. Cavitation indexes SCD and ICD were used to determine the different cavitation thresholds of these MB. In addition, a cavitation monitoring algorithm was used to determine the acoustic cavitation doses for large BBB opening protocols (see 4.4).

4.2.1. Methods

This setup consisted in a 20 mL-circuit with circulating MB. The MB flowed in a polythene PE200 tubing (internal diameter, 1.40 mm; outer diameter, 1.90 mm) and was held by a custom-made 3D plastic printed piece that also maintained the transducer (Figure 22.A). MB were flowing with a peristaltic pump at a 3 mL/min flow rate. A beaker was set as the reservoir and a magnetic stirrer was inserted to prevent MB from rising to the surface. The system is depicted in Figure 22.B-C.

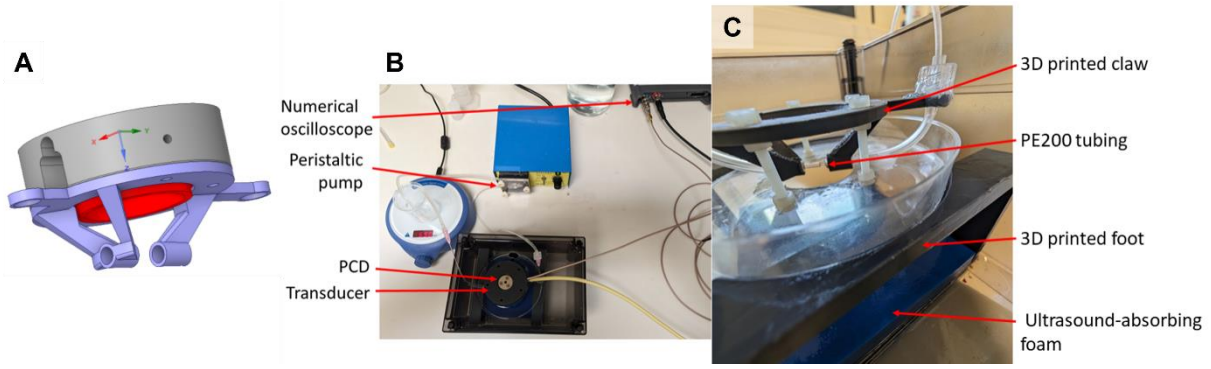


*Figure 22. In vitro cavitation experimental setup. 3D design of the transducer and tube holder (in blue) (**A**). Overview of the whole setup with the peristaltic pump, the PCD and FUS transducer, the numerical oscilloscope and stirrer (**B**). More detailed view of the system with the 3D printed claw, the PE200 tube and the ultrasound absorbing foam to avoid refraction of the ultrasound waves (**C**).*

FUS pulses were controlled through the application programming interface (API) of IGT in Python (version 3.8, Python Software Foundation). Pulses of 50 ms every 1000 ms were generated for every measurement. Data was recorded by a digital oscilloscope (Picoscope 5244D, Pico Technology Ltd, England) and were visualised with Picoscope 7 T&M (Pico Technology Ltd, England). Signal was sampled over 16 bits at 17.9 MS/s for 1.84 ms. Home-made software recorded and performed a fast Fourier transform on the raw signal and a Blackman windowing was applied. Spectrums were analysed to compute the SCD and ICD. As mentioned in section 1.5.3, no consensus has been reached on how to calculate SCD and ICD. We have opted to calculate these indexes by calculating the area between the curve and a reference test without ultrasound to limit the influence of ambient noise [Novell *et al.*, 2020]. For SCD, we used a 2 kHz bandwidth around $\frac{f_0}{2}$, $\frac{3f_0}{2}$ and $\frac{5f_0}{2}$ frequencies (where f_0 is the ultrasound frequency). The ICD was calculated using $\frac{3f_0}{4}$, $\frac{5f_0}{4}$ and $\frac{7f_0}{4}$ frequencies and a bandwidth of 200 kHz to measure the importance of broadband characteristics of inertial cavitation. The unit for these two indicators is therefore expressed in dBu.Hz in our study (Figure 23).

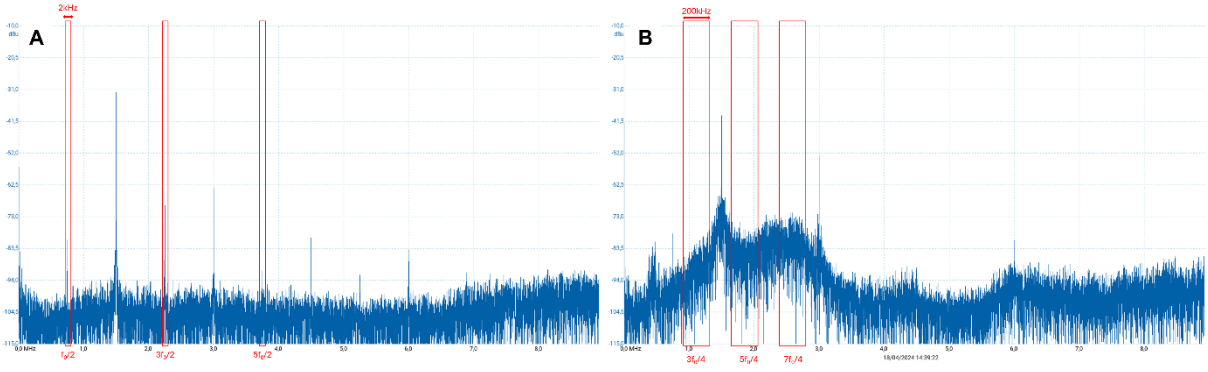


*Figure 23. Cavitation spectrum for SCD (**A**) and ICD (**B**) calculation with respective bandwidth of interest.*

4.2.2. Results

4.2.2.1. Influence of the concentration, excitation frequency and microbubble composition on the stable and inertial cavitation doses

SCD and ICD were measured for the three different types of MB at different frequencies spanning from 2 to 30% of the amplitude. The PNP was retrieved from the transducer calibration measurements (see 4.1). As previously reported in the literature, an increase in MB concentration led to an increase in the inertial cavitation dose (Figure 24).

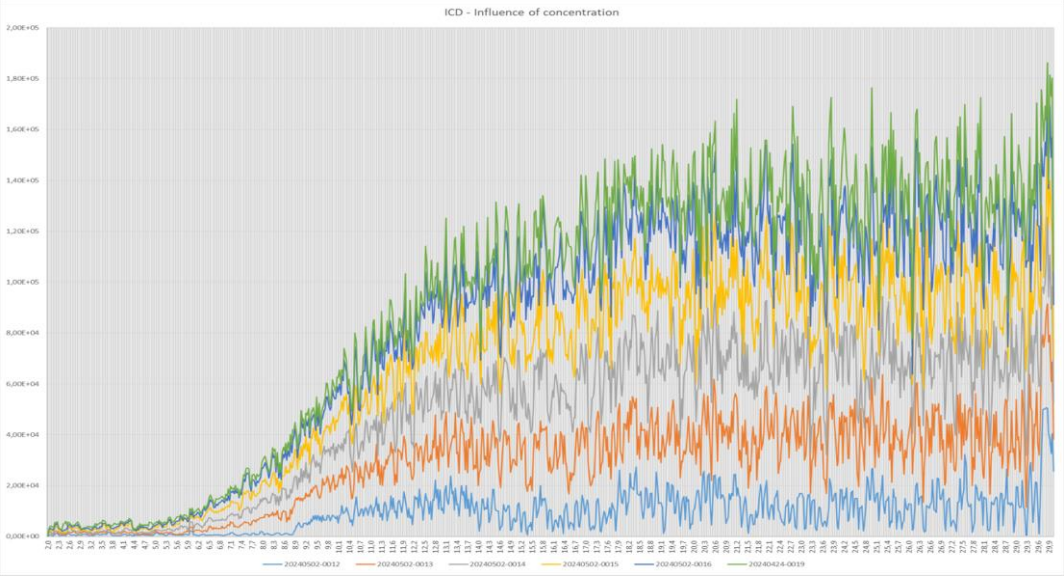


Figure 24. Evolution of ICD depending on the PNP for increasing MB concentrations and for a 1.5 MHz excitation frequency.

SCD and ICD were measured for the three different types of MB at different frequencies spanning from 2 to 30% of the amplitude. The PNP was retrieved from the transducer calibration measurements (see 4.1). As previously reported in the literature, an increase in MB concentration led to an increase in the inertial cavitation dose (Figure 24).

SCD values increased rapidly at low pressures to reach a plateau followed by a second increase to reach a second plateau. This was visible for the three types of MB (see Figure 25, and Figure 79 and Figure 80 in annexe A.1). No important differences were identified across the different excitation frequencies. For ICD, we can see that the values remained low until higher pressures are reached and finally reach a plateau for strong pressures. We can see differences between the 1.3 MHz frequency compared to other frequencies for all types of MB. Also, for the cationic MB, the ICD increased much less than the other types of MB.

We tested the influence of the shell properties on the SCD and ICD. As we can see in Figure 26, the neutral and biotin-functionalised MB behave similarly but cationic MB have a very different ICD. The strong increase in ICD values is approximately seen for 1.78 MPa PNP acoustic pressure compared to 1 MPa for the two other MB type. In addition, the rising part for neutral and biotin-functionalised MB

have a more linear shape, signifying a potential better control of acoustic cavitation without potential sudden hump.

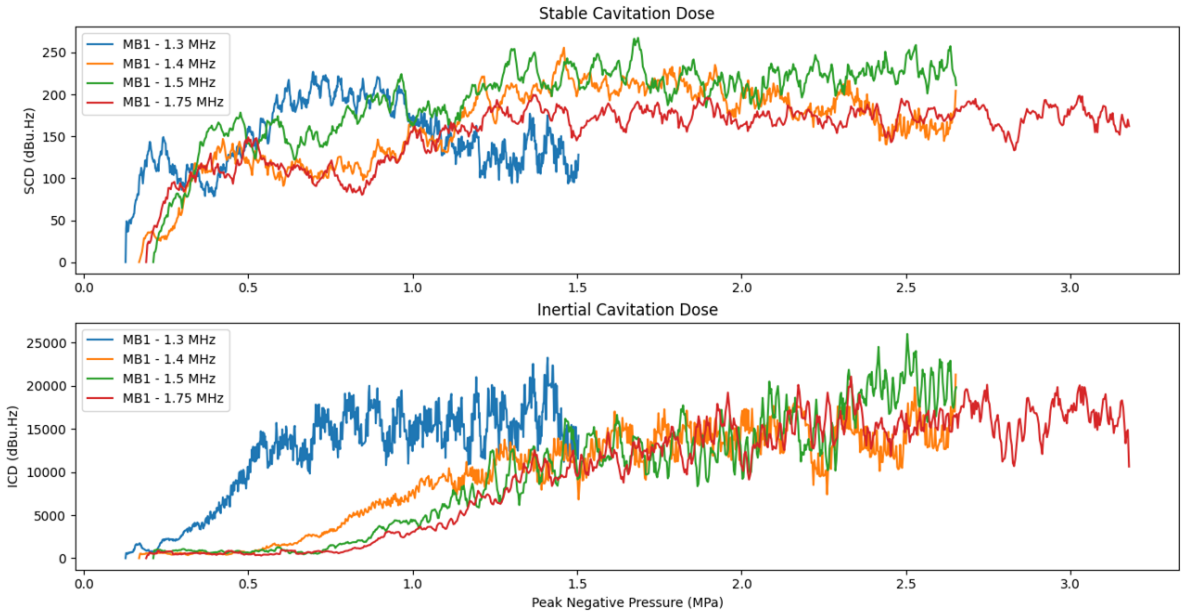


Figure 25. Evolution of the SCD (top) and ICD (bottom) in function of the PNP for the neutral DSPC-DSPE-PEG2000 MB. Each data point was averaged from three measurements. Frequencies evaluated are 1.3, 1.4, 1.5 and 1.75 MHz.

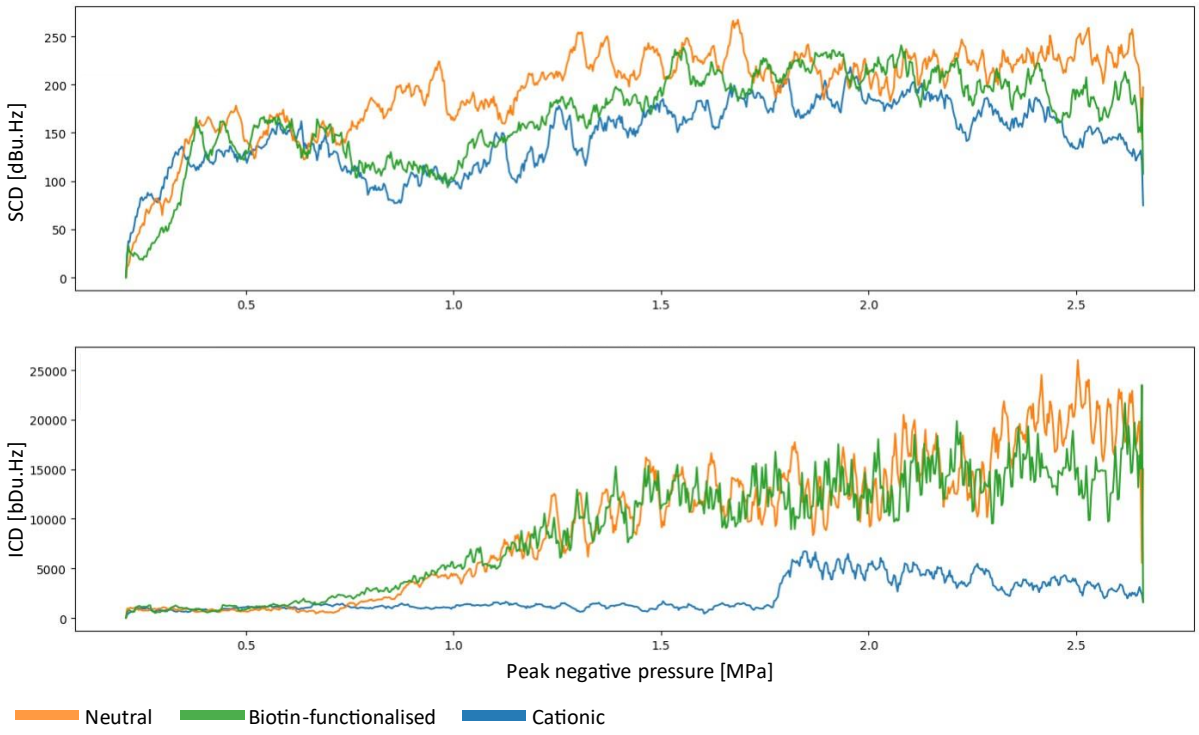


Figure 26. Evolution of the SCD (top) and ICD (bottom) at 1.5 MHz for the three types of MB, the neutral in orange, biotin functionalised in green and cationic in blue.

4.2.2.2. In vivo cavitation monitoring

In vivo cavitation monitoring was performed for the study presented in the Chapter 5, the protocol is detailed in section 5.3.4. As we used raster scans for large BBB opening in the studies presented in the Chapter 6, Chapter 7 and Chapter 8, we did not monitored the acoustic cavitation. Yet, for a few numbers of subjects, we acquired data to implement a new cavitation monitoring algorithm to be able to improve the safety in large BBB opening protocols. To date, no protocol for this type of FUS sequence pattern has been studied.

In Figure 27, we can see the raster scan pattern (Figure 27.A) and the resulting SCD and ICD (Figure 27.C-D). The values of the SCD and ICD were quite constant along the whole trajectory and does not seem to correlate with the signal intensity of the T1-w image after the injection of a gadolinium contrast agent (Figure 27.B). In the top right part of the raster scan, we can see an increase in the ICD values, possibly due to the fact that the FUS beam was the most normal to the skull surface, and therefore more reflections were present.

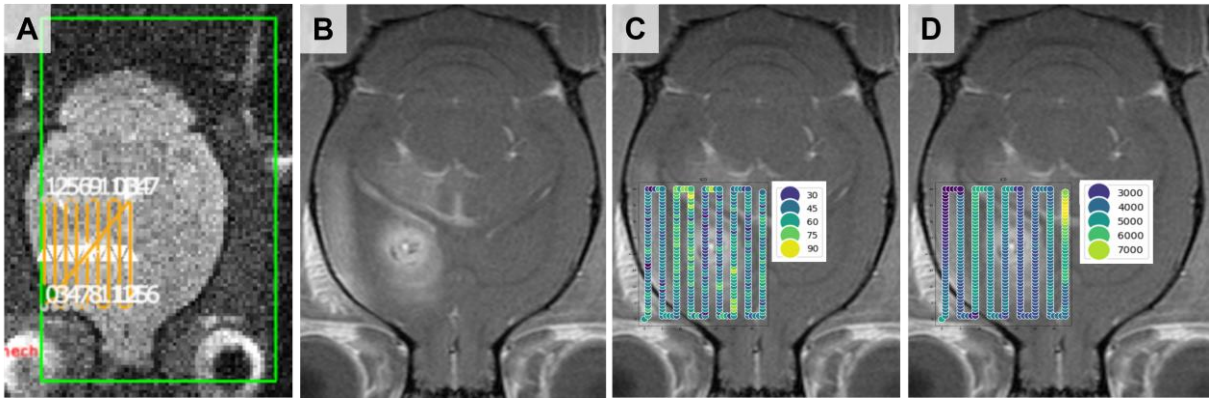


*Figure 27. In vivo cavitation monitoring. **A**) Screenshot from Thermoguide® with T2-w image of a rat brain and the FUS raster scan. **B**) T1-w image after FUS and Gd-DOTA injection, one can see the tumour with enhanced signal around. **C**) SCD dose painted over the T1-w image. **D**) ICD dose painted over the T1-w image. SCD and ICD are expressed in dBu.Hz.*

4.2.3. Discussion

We monitored the acoustic cavitation of three types of MB: neutral, very similar to commercialised SonoVue® MB, with a biotin shell to perform functionalisation with magnetic nanoparticles for example and cationic to complex anionic compounds as pDNA. The two first type of MB have a very similar shape, and we did not see differences in the acoustic cavitation properties. The cationic MB are very different and did not produce strong cavitation signal. Two main reasons can come from this, first their behaviour is very dependant from the solution they are flowing in due to ionic interactions, then their shell is much more rigid and stronger FUS amplitude is needed to reach similar cavitation levels.

The development of cavitation monitoring algorithms is of great importance to ensure the safety of the BBB opening (see 1.5) as well as closed-loop control systems. We first implemented a monitoring algorithm to be able to acquire and observe cavitation signals from a moving trajectory. The signals acquired have a poor SNR due to the displacement of the transducer, thus inducing vibrations. The transducer delivered continuous pulses, then the PCD is recoding signal non-specific signal. If we consider the speed of sound to 1500 m/s and the distance between the PCD and the focal task equal

to 25 mm, we can assume that the transducer travels 0.3 mm between the moment it emits the signal and it receives the reverberated signal. From the focal task scale, with approximately a 1.5 mm width the signal recorded from the PCD must be quite representative from the acoustic cavitation phenomenon produced. This work is still in its early stages and further a more in-depth study will be necessary to validate this protocol.

4.3. Evaluation of magnetic resonance guided focused ultrasound

MRI is the method of choice to precisely guide the FUS energy deposition. Different methods have been developed: specific MR sequences as ARFI and MR thermometry or software-based methods aiming at providing a theoretical localisation of the energy deposition. During this thesis project, we implemented ARFI and MR thermometry methods to validate the guidance of the FUS system and its ability to precisely target structures.

4.3.1. Device and software

The FUS device is constituted of an MR-compatible bed with anaesthesia mask, an MRI saddle coil used for both transmission and reception of MR signals (Figure 28.A). First, the position of the transducer within the MRI coordinate system was established. For this aim, an axial and a coronal, T1-weighted (T1-w), fast low angle shot (FLASH) images were acquired (TR/TE = 200/2 ms; 25 slices; field of view (FOV), 50 × 50 mm^2; matrix, 128 × 128; voxel size, 391 × 391 × 1000 μm^3; number of averages (NA), 2; acquisition time T_{acq} = 51 s). The location of the transducer was then computed offline using dedicated ThermoGuide® software from Image Guided Therapy. An additional T2 TurboRARE sequence (TR/TE = 2500/33 ms; RARE-factor, 8; 15 coronal slices; FOV = 37 × 37 mm^2; matrix, 256 × 256; voxel size, 145 × 145 × 1000 μm^3; NA, 4; T_{acq} = 5 min) was used to precisely localise the target (Figure 28.E and Figure 29).

The software ThermoGuide® (IGT) provides an environment to import data acquired with Paravision (Bruker, Ettlingen, Germany) and enables the colocalisation on MR images of the transducer (Figure 28.D-E). Once the co-localisation is made, the transducer can be moved in a 2-axis plane and the focal depth can be changed due to the electronic steering of the 7-elements transducer.

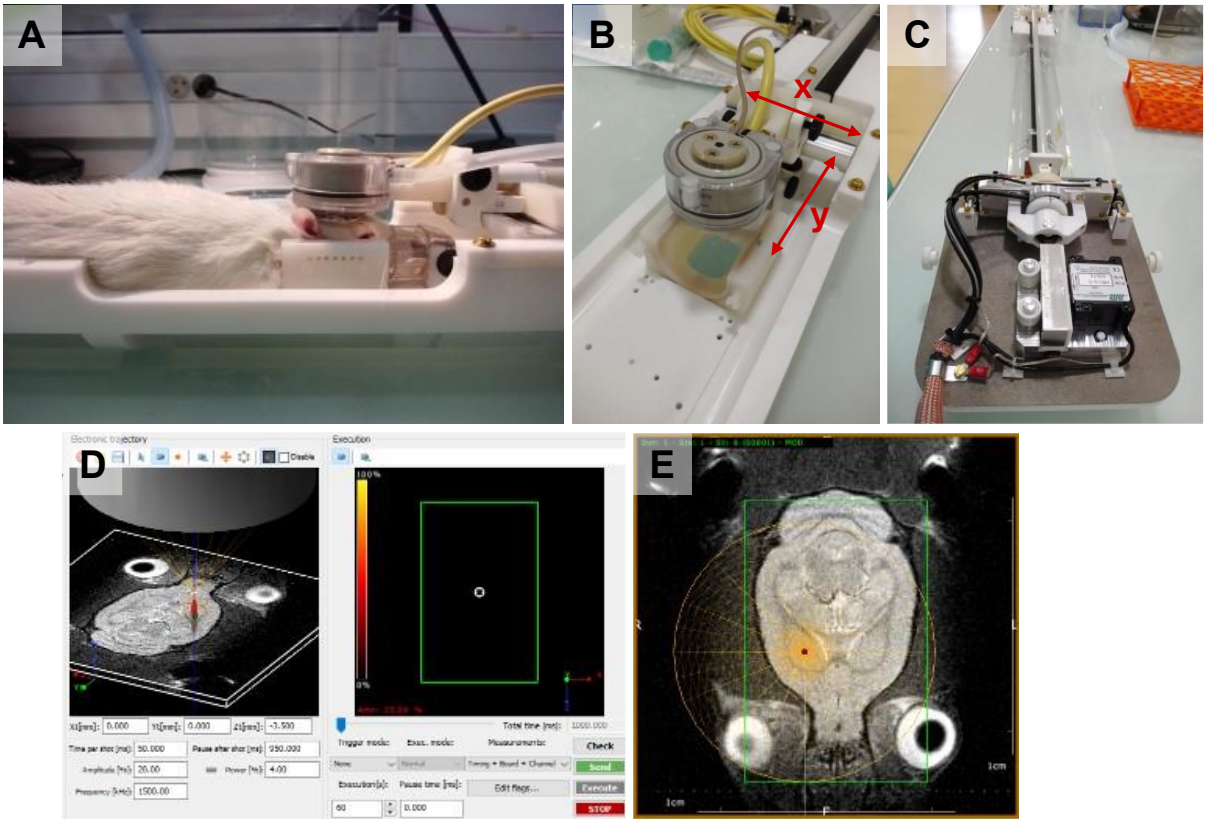


*Figure 28. The MR-guided FUS system with the inverted MRI saddle coil that covers the cheeks of the rat and on top of its head the FUS transducer (**A**). Another view of the saddle coil and the FUS transducer (**B**) that can be displaced by the motors (**C**) in the coronal plane. Thermoguide® (IGT) view with an MRI image to target brain structures, the different parameters to control the FUS sequence (**D**). View of the theoretical focal point of the transducer superimposed with MRI (**E**).*

In Figure 29, we can see that the localisation of the BBB opening is in good accordance with the target location made with the software.

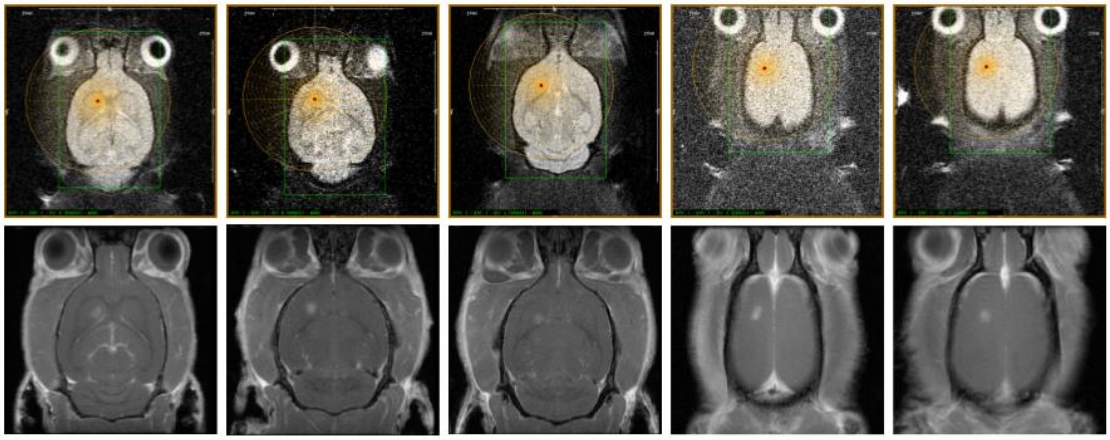


Figure 29. Thermoguide® screenshots of target location for 5 rats (upper panel) and the corresponding MR-guided FUS BBB opening visualisation with T1-w image after Gd-DOTA injection (lower panel).

In the next two paragraphs, we will validate the precision of localisation with two MR methods: the thermometry and the ARFI, as the skull can induce modifications from the theoretical FUS focal point provided in the software.

4.3.2. Magnetic resonance thermometry

We aimed at validating the precision of the FUS energy deposition *in vitro* and of the electronic steering with the MR-guided FUS system. It is now well known that the resonance frequency of water hydrogens depends on the tissue temperature [Ishihara *et al.*, 1995]. Temperature-dependent changes in PRF measurements have good precision, it is fast and there is a linear relationship between the temperature and the PRF. When using an echo time T_E in gradient echo MRI, the phase ϕ of the MR signals depends on the temperature-dependant magnetic shielding σ:

$$\phi(T) = \gamma\sigma(T)T_E B_0 \tag{5}$$

where γ is the gyromagnetic ratio of the observed nucleus (42.58 × 10^6 Hz.T^{-1} for protons) and B_0 the magnetic field strength. The temperature-dependant magnetic shielding σ is proportional to the temperature:

$$\sigma(T) = \alpha T \tag{6}$$

where α is the temperature-dependant chemical shift coefficient in ppm.°C^{-1} [Blackwell *et al.*, 2022]. By subtracting the field distribution at a reference temperature from the field at a temperature T, we can obtain the following equation [Rome *et al.*, 2005]:

$$\Delta T = T - T_{ref} = \frac{\phi(T) - \phi(T_{ref})}{\alpha\gamma T_E B_0} \tag{7}$$

Based on this, we placed inside the MR-guided FUS bed a chicken breast sample and inserted it in a 4.7 T Bruker scanner (Figure 30.A). A gradient echo sequence (TR/TE, 100/13 ms; repetition, 10; alpha, 5°; FOV, 50 × 50 mm^2; matrix size, 92x92; slice thickness, 1 mm; T_{acq} = 5 min) was used during the FUS sequence. We placed a single MRI slice -6 mm down below the natural focal distance of the transducer. We applied a 3.2 MPa PNP for 30 seconds. One image was acquired every 3 seconds. We targeted different depths with the transducer: 0 (the natural focal distance), -3, -6, -9 and -12 mm. For a shooting depth at 0 mm, we can see a small rise in temperature. When increasing the target depth, the temperature increases and reaches a maximum for a shooting depth of -6 mm. It then decreases for -9- and -12-mm depth (Figure 30.B).

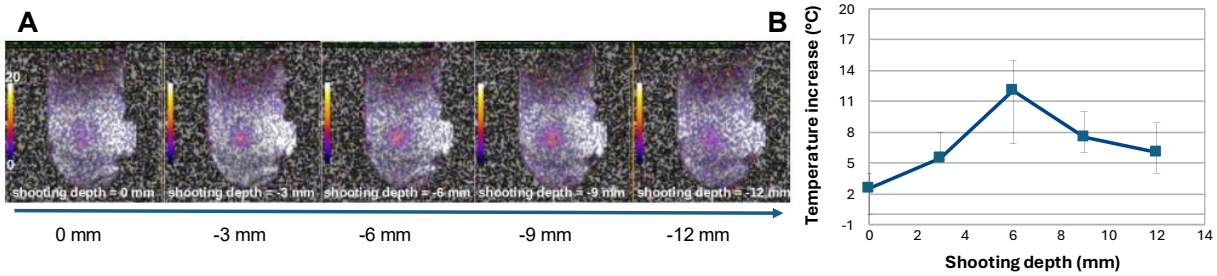


*Figure 30. Thermometry results. **A**) Thermometry maps 30 s after the beginning of the FUS sequence for different shooting depth. **B**) Temperature elevation depending on the shooting depth.*

We validated *in vitro*, using MR thermometry, the ability of the focal spot to be steered electronically. This method was not validated *in vivo* due to the temperature rise necessary to perform this experiment which would induce irreversible secondary bioeffects in the tissues [Vykhodtseva *et al.*, 2000]. This method can however be used to monitor the delivery of high intensity focused ultrasound

(HIFU) to trigger thermosensitive compounds (gels, proteins) or for instance to ablate tumours and control this energy deposition with closed-loop controlled algorithms (with proportional, integral and derivative principles). Altogether, the electronic steering of the focal spot appeared accurate.

4.3.3. Acoustic Radiation Force Imaging

To observe the focal spot of the focused ultrasound, an alternative to MR thermometry is a method known as acoustic radiation force imaging (ARFI). This method is based on the measurement of the displacement induced by the acoustic radiation force induced by the ultrasound beam in soft tissues, and thereby provides the location of the FUS energy deposition with less ultrasound energy than the one required for HIFU methods. This MRI sequence uses motion encoding gradients (MSG) to acquire information about the ultrasound-induced displacement in the phase maps (Figure 31). At the focal point, the phase variation is greater, which translates into a greater displacement of the tissue, and thereby enables the *in vivo* detection of the position of the ultrasound focal spot.

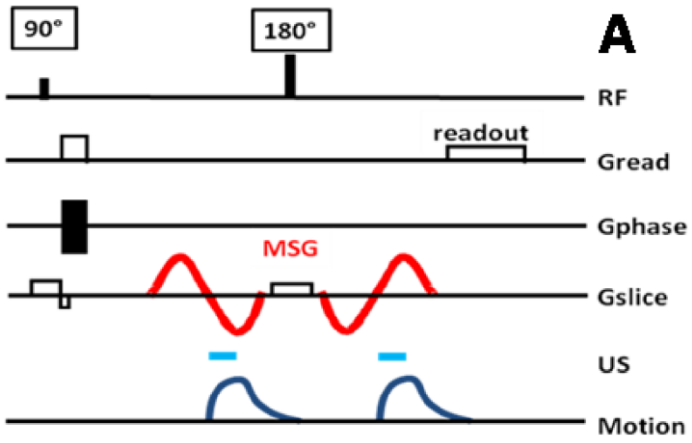


Figure 31. Time sequence diagram of the ARFI sequence. The sequence is based on a standard spin-echo sequence, represented in black. In red, the motion encoding gradients. In blue, the position in time of the ultrasound emission [Larrat et al.*, 2010].*

We acquired an ARFI sequence (TE/TR, 2000/20 ms; t_{MSG}, 6.4 ms; FOV, 58 × 58 mm²; matrix size, 64 x 64; slice thickness, 2 mm; T_{acq} = 2 min 08 s) and FUS pulses were triggered (t_{pulses} = 3 ms, PNP = 6.6 MPa). A processing pipeline has been implemented in MP3 [Brossard *et al.*, 2020]. The raw phase maps must first be unfolded to remove phase jumps from -π to +π. This was done using Goldstein's branch cuts method [Spottiswoode, 2022]. The unfolded image acquired during the ultrasound shots is then subtracted from a reference image acquired without ultrasound shots. Using this map, known as the residual map, we calculated the displacements induced by the shots using the following formula:

$$d = \frac{\Delta\Phi}{\gamma G T} \tag{8}$$

where Δϕ represents the phase difference between the image acquired using the MSG while the FUS is working and the reference image without the FUS, T the MSG period, G the amplitude of the motion-encoding gradients and δ the duration of the gradients [Ilovitsh *et al.*, 2019].

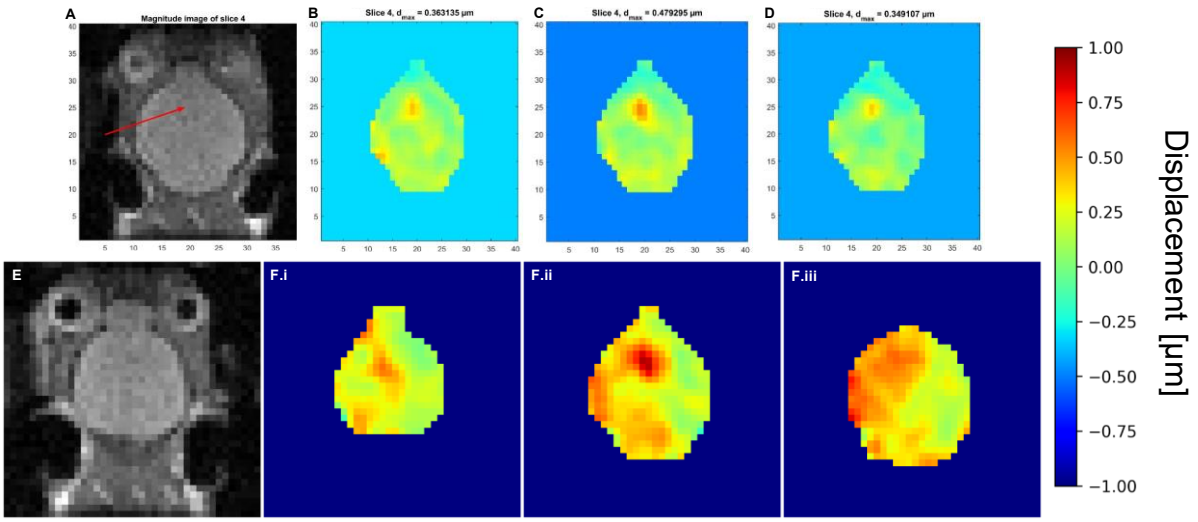


*Figure 32. Validation of Acoustic Radiation Force Imaging. Magnitude image of mice brain with FUS application location highlighted with red arrow (**A**) and corresponding displacement maps for different application times of FUS: 2.5 (**B**), 3 (**C**) and 3.5 ms (**D**). Magnitude image of mice brain (E) and corresponding three adjacent slices of the displacement map on top (**F.i**), middle (**F.ii**) and bottom (**F.iii**).*

We tested different FUS application times as the sensitivity of the ARFI sequence depends on it. In Figure 32.B-D we can see the different displacement maps for FUS duration of 2.5, 3 and 3.5 ms. The maximum displacement measured were respectively 0.36, 0.48 and 0.35 µm. Thus, we validated a duration of 3 ms. Figure 32.E shows the displacement maps calculated for an adult C57BL/6 mouse. We applied a 6.6 MPa PNP during 3 ms. This was the first *in vivo* proof of concept. The displacement maps reconstructed from images acquired with the transmit/receive antenna embedded in the IGT setup did not have the expected resolution and sensitivity. Although the total ultrasound application time compared with the acquisition time does not exceed 5%, thus no thermal elevation is produced *in situ*. Reducing the pressure to limit the potential deleterious effects on the body with the presence of cavitation nuclei trapped in the FUS beam would be of great interest. An antenna was purchased to alleviate this problem (RAPID Biomedical GmbH, Germany). The apparatus is a surface antenna comprising a loop through which ultrasound can be transmitted. Tests to evaluate the SNR were carried out to assess the gain provided by this new antenna and can be found in Figure 33. We measured a 227% increase in SNR. This antenna arrived in the middle of the 3rd year of my thesis project and could not be used daily. It will be of great interest to embed this new coil in the MR-guided FUS system to increase sensitivity and therefore reduce acquisition time for the targeting phase and pursue high resolution image acquisition after FUS application to monitor BBB opening or other quantitative parameters.

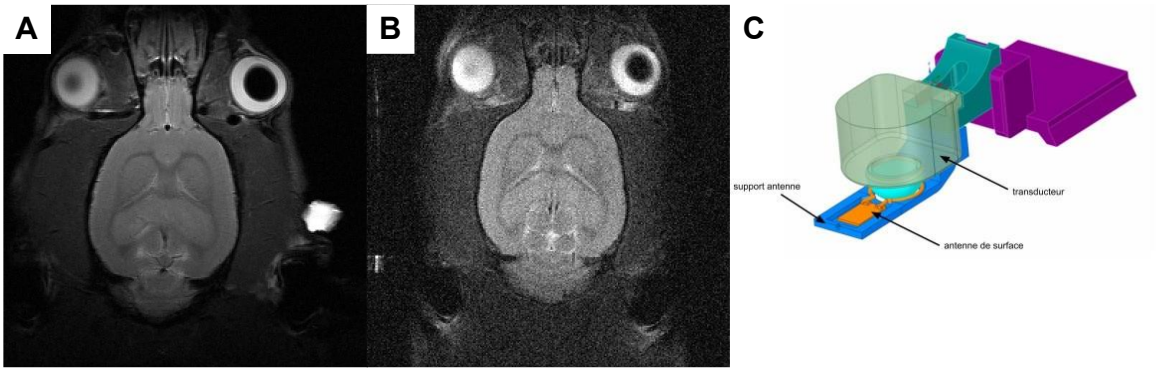


*Figure 33. T2-w TurboRARE coronal images (TR/TE, 2500/36; RARE factor, 8; 15 slices; T_{acq} = 6 min 40 s) for Rapid Biomed coil (**A**) and IGT coil (**B**) and 3D modelisation view of the coil integration in the actual MRI system (**C**).*

It is evident that the IGT coil lacks sensitivity, and the FUS-targeted precision results were comparable to those obtained using the software-based target location method of section 4.3.1.

However, the theoretical focal point available in the software does not account for potential diffraction and deviation induced by the skull of the rodents. This was an unsurprising outcome, given the findings of previous work by Choi *et al*., which measured the impact of the mice skull on the focal spot using CT-scan images and simulations. The simulation method and ex vivo skull experiments [J. J. Choi *et al.*, 2007] yielded 0.038 mm and 0.046 mm changes, respectively. The impact of the rat skull is certainly more important, but this will not result in a drastically increase of the FUS beam deviation. The technique was not employed for targeting brain regions in the remainder of the thesis.

4.3.4. Blood-brain barrier opening characteristics

As previously outlined (see section 1.4.2), the time-closure dynamics of the BBB exhibit variability across studies, due to the variability in FUS and in MB parameters. The validation of the closure dynamics of the BBB was conducted for three principal reasons: first, to facilitate a comparison between the BBB opening observed in our studies and previous studies, thereby validating the range of parameters of this novel system; second, to validate the use of a novel BBB opening photoacoustic and bioluminescence CA, namely indocyanine green (ICG); and finally, to validate this contrast agent with MRI with Gd-DOTA, the gold-standard method of BBB opening. This experiment was conducted in collaboration with Thomas Ador, a PhD student at the CBM in Orléans, with the objective of characterising this novel BBB opening CA.

4.3.4.1. Method

18 Balb/cJR mice (6 weeks old, m = 18 g), anaesthetised in a mixture of air and oxygen with 2% isoflurane, were used. A catheter was placed in the tail vein for injection of MB, MRI and ICG CAs. Care was taken to shave the heads of the mice to remove any hair and ensure the best possible coupling between ultrasound and the brain. In addition, ultrasound gel was applied on the scalp before the transducer was placed. We performed this experiment without MRI guidance to save time but based on anatomical landmarks. Before applying the ultrasound sequence lasting 1 minute and alternating 50 ms of ultrasound pulses and 950 ms of pause, a bolus of 100 µL of MB was injected into the vascular system, corresponding to 1.5×10^7 MB. After the ultrasound sequence, the animal was placed in the

MRI scanner and we acquired an anatomical T2 TurboRARE sequence (TR/TE, 2200/36 ms; RARE-factor, 8; 13 axial slices; FOV, 20 × 20 mm^2; matrix size, 256 × 256; voxel size, 78 × 78 × 1000 μm^3; NA, 3; T_{acq} = 3 min 31 s), then two T1 map RARE VTR sequences (TR, 3000 to 18 ms; TE, 6.6 ms; RARE factor, 4; FOV, 20 × 20 mm^2; matrix size, 128 × 128; voxel size, 156 × 156 × 1000 μm^3; T_{acq} = 12 min 39 s) before and after the injection of a bolus of Gd-DOTA (200 µmol/kg). The injection of this contrast agent followed by the second T1 map acquisition were performed at various times after the BBB opening: 0, 30 and 120 minutes. At the same time as the Gd-DOTA injection, a 50 µL dose of ICG (10 mg/mL) was injected. The brains were harvested 24 hours after the FUS sequence and directly frozen dry in liquid nitrogen, a timing corresponding to the peak intensity of the ICG, to perform *ex vivo* bioluminescence measurements (IVIS Lumina LT; λ_{ex} = 730 - 760 nm; λ_{em} = 810 - 875 nm) to quantify BBB opening. T1 maps were reconstructed using a Paravision macro, then all MRI data were processed using MP3. Concentration maps were derived from T1 maps acquired before ($T_{1,0}$) and at t = [0, 30, 60, 120 min] after ($T_{1,t}$) the injection of Gd-DOTA using the following equation:

$$C = \frac{1}{r_1}\left(\frac{1}{T_{1,t}} - \frac{1}{T_{1,0}}\right) \quad (9)$$

r_1 value was set to 3.4 $mM^{-1} \times s^{-1}$ [Swift and Connick, 1962]. Region of interests were drawn in the contralateral region and in the muscle as depicted in Figure 34.A to normalise the concentration of Gd-DOTA extravasated with following equation [Marty *et al.*, 2012]:

$$C^{\Delta} = \frac{C_{ROI,ipsi} - C_{ROI,contra}}{C_{ROI,muscle} \times IP_{ac}} \quad (10)$$

IP_{ac} was set to 1 as we did not retrieve this parameter with acoustic radiation force imaging sequence. A one-phase decay exponential fit was calculated through GraphPad and was used to calculate the time to divide by two the apparent concentration of Gd-DOTA and fluorescence intensity at t = 0 min ($T_{1/2}$), using the trend line's equation as follows:

$$T_{1/2} = \frac{1}{b}\left(\ln\left(\frac{y_0}{2}\right) - \ln(a)\right) \quad (11)$$

4.3.4.2. Results

MRI with gadolinium as a contrast agent is the standard technique for assessing BBB permeability. A comparison was made between MRI and fluorescence imaging in the same animals. BBB was successfully opened in the left hemisphere of 14 mice with sixty 1.5 MHz pulses at 300 kPa *in situ* using the MR-guided FUS device (n = 5 for 0 and 30 min; n = 4 for 120 min). Gd-DOTA and ICG extravasations were evaluated *in vivo* by MRI and *ex vivo* by fluorescence (Figure 34.A-B). As in the experiment to assess BBB closure kinetics, Gd-DOTA and ICG were injected into the same animal immediately, 30 or 120 min after FUS-induced BBB opening. MRI was performed following FUS treatment and the injection of Gd-DOTA and ICG's fluorescence was measured *ex vivo* in brains collected 24 h after FUS and the injection of ICG. All data were normalised to the average signal obtained at 0 min to observe and compare the decay of both techniques. We observed that the contrast of Gd-DOTA and the fluorescence of ICG both follow an exponential decay, and we were able to perform a one-phase decay exponential fit. For Gd-DOTA, the decay follows the equation y = 0,7995 × $e^{-0,02110x}$ + 0,2007 (R^2 = 0,99999) while for ICG, it follows the equation y = 0,9716 × $e^{-0,02120x}$ + 0,02859 (R^2 = 0,999). The percentage of signal remaining at 2h is 25% and 10% for Gd-DOTA and ICG respectively. GraphPad's

exponential fits also calculates a half-time of 32.85 and 32.70 min for Gd-DOTA and ICG respectively, corresponding to the time to divide by two the apparent concentration C^{Δ} of Gd-DOTA and the fluorescence intensity of the 0 min timepoint. We also showed, using an F-test, that the data from Gd-DOTA and ICG significantly follow the same distribution (p-value = 0.9357).

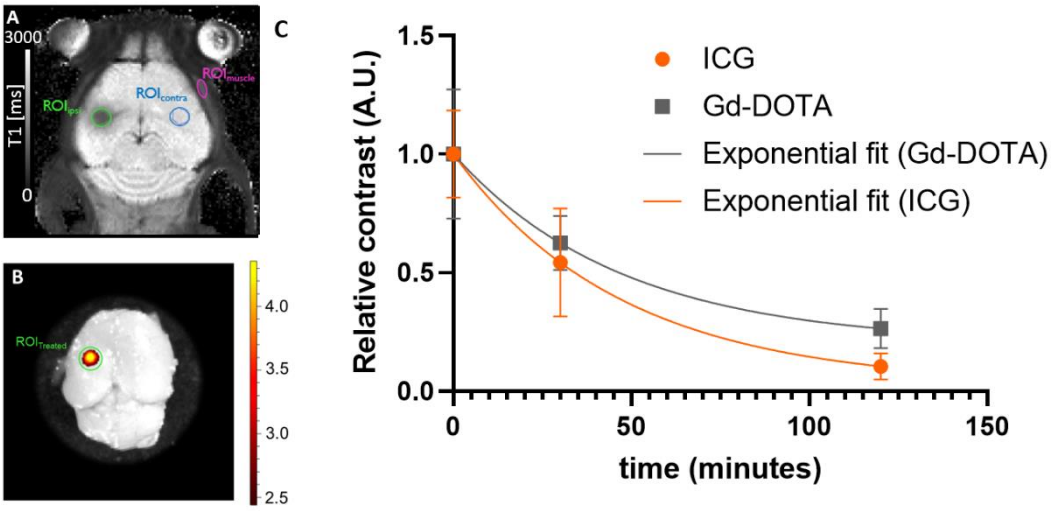


*Figure 34. BBB closure dynamics. (**A**, **B**) T1 map and ex vivo ICG fluorescence of mice following BBB opening and co-injection of 40 µL of Gd-DOTA diluted 5 times and 0.5 mg of ICG, with ROI used for measure. **C**) Kinetics of ICG and Gd-DOTA extravasation decrease normalised at T_0, measured with in vivo MRI and ex vivo fluorescence respectively. Contrast agents were co-injected directly after the FUS procedure or with a delay of 30 to 120 minutes. Ex vivo fluorescence was performed on frozen brains collected 24 h after FUS. Data are expressed as mean +/- SEM. One phase decay exponential fit (GraphPad).*

4.3.4.3. Discussion and conclusion

The results we obtained using ICG are comparable to those obtained with Gd-DOTA and can be explained as they both exhibit a similar hydrodynamic diameter (d_H ~ 1.2 nm [Porcu *et al.*, 2016]). Our results are somewhat different from previous studies from Marty *et al*. or Chai *et* al. mainly due to the MI of 0.37 and 0.63, respectively. It is known that the BBB closure dynamics highly depends on the pressure (see 1.4.2). In our study the MI was estimated to 0.24 *in situ* (PNP = 0.36 calibrated in water with a 21% attenuation due to the skull [Felix *et al.*, 2021]). Chai *et al*. measured half-closure time of 2.9 h for Gd-DOTA [Chai *et al.*, 2014]. In comparison, Marty *et al.* measured a half-closure time of 5 h (almost twice Chai and colleagues' study) for Gd-DOTA in rats. We can point out that a single individual was used per time point, making the measurement not reliable [Marty *et al.*, 2012] (in comparison, we used 5 individuals per time point) and the number of timepoints was different: from 5 minutes to 24 hours, whereas we concentrated on shorter periods (up to 120 minutes). In addition, Marty *et al*. delivered large compounds as P792 (d_H ~ 5 nm [H. S. Park *et al.*, 2015]) and P904 (d_H ~ 25-30 nm, source: https://www.chematech-mdt.com/produit/p904-uspio/) where high pressure *in situ* is needed to observe any changes in MRI signal.

In conclusion, the measurement of BBB closure kinetics in mice is comparable to that in rats. ICG and Gd-DOTA behaved similarly after BBB opening. The ICG is a suitable candidate for *in vivo* monitoring of BBB opening with equipment that is less expensive and easier to set up than MRI. One of the

disadvantages of using the ICG is that the maximum signal occurs 24 hours after FUS application, whereas with the Gd-DOTA the response is 'immediate'. This is due to the large amount of background noise present just after injection and the homogeneous distribution of ICG in the brain. 24 h later, only the ICG molecules that had extravasated following the opening of the BBB remained present, making it possible to discriminate the area of opening.

This section is part of an article submitted to the peer-reviewed journal *iScience*.

4.4. Focal and Extended blood-brain barrier opening with focused ultrasound

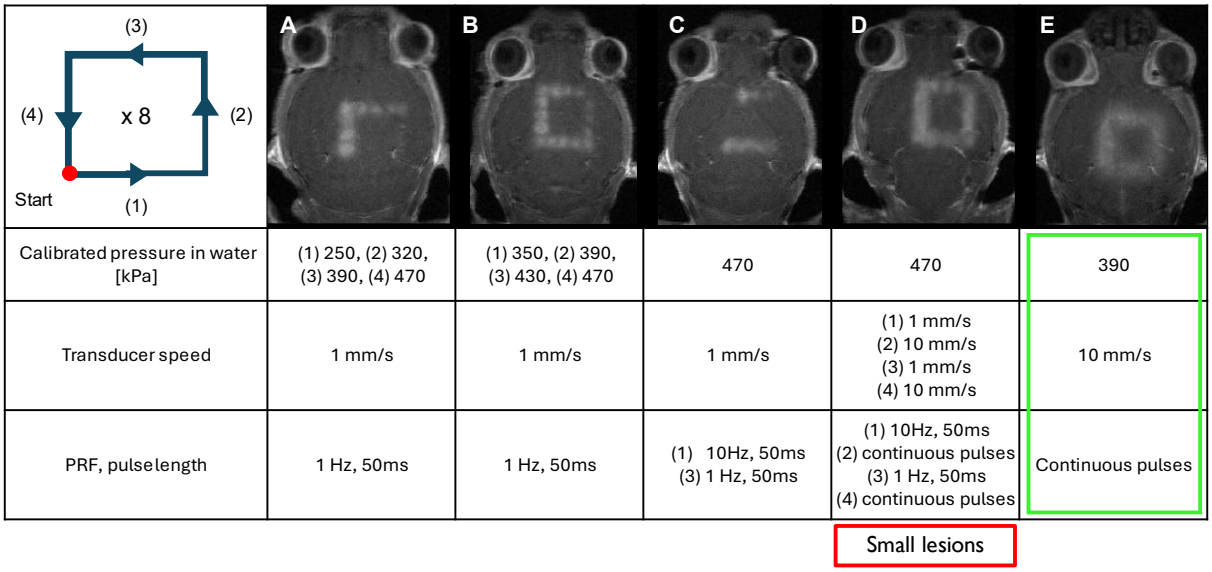
In this thesis, we used different strategies to permeabilise the blood-brain barrier: single-spot and raster scan FUS sequences. The first one enables the precise targeting of brain regions and the second one enables the covering of large brain regions and even the whole brain. In this section we describe the protocol used to permeabilise the BBB using either technique and present the validation made for large BBB opening.

After shaving the animal above the head and applying depilatory cream to remove any potential hair on the scalp, the animal is placed in the MR-guided FUS cradle. Echographic gel is added to the top of the scalp to ensure the best coupling between the FUS transducer membrane and the brain.

The application of FUS begins 15 s after the injection of MB in the vascular system of the rodent. 100µL of MB are injected as a bolus over a 10 s period with a total of 4×10^8 MB for rats and half of the dose for mice. MB are diluted in HEPES buffer (10 mM, pH = 7.4) and an additional 5 µL of 50% sucrose is mixed for mice to improve blood circulation due to viscosity changes after the injection. For single-spot BBB opening, the FUS sequence consists of 1.5 MHz pulses of 50 ms applied every second during 60 s. For large BBB opening, the sequence is prepared in advance in the Thermoguide® software as depicted in Figure 36.A. A raster scan with 50 ms pauses at the direction changes is drawn, the transducer is moving at 10 mm/s and continuous FUS pulses of 1.5 MHz are delivered along the moving trajectory. We varied the size of the raster scan depending on the application. The parameters were validated during an experiment to ensure the efficiency of the delivery but also the safety of the procedure. The validation is described in the next section.

4.4.1. Validation of whole brain permeabilisation in mice

Firstly, we tested different pressures, different moving speed of the transducer and different ultrasound pressures to ensure the best BBB opening outcome: without lesions and homogeneous. In the Figure 35, we can see in panel A by increasing the pressure we increase the amount and size of positive contrast, in panel B that pressures suitable for BBB opening are between 350 and 470 kPa, in panel C the difference between two PRF (1 and 10 Hz) with increased homogeneity for the higher PRF at the same transducer speed, in panel D the test of continuous pulses that resulted in lesions at 470 kPa but very good homogeneity, and finally, in panel E the best parameters with high contrast and very good homogeneity without any lesions. The parameters defined to permeabilise the BBB in large areas were set at 390 kPa, with continuous pulses and a transducer moving at 10 mm/s. These parameters are in accordance with previous studies [Chevaleyre *et al.*, 2023; Felix *et al.*, 2021].



Calibrated pressure in water [kPa]	(1) 250, (2) 320, (3) 390, (4) 470	(1) 350, (2) 390, (3) 430, (4) 470	470	470	390
Transducer speed	1 mm/s	1 mm/s	1 mm/s	(1) 1 mm/s (2) 10 mm/s (3) 1 mm/s (4) 10 mm/s	10 mm/s
PRF, pulselength	1 Hz, 50ms	1 Hz, 50ms	(1) 10Hz, 50ms (3) 1 Hz, 50ms	(1) 10Hz, 50ms (2) continuous pulses (3) 1 Hz, 50ms (4) continuous pulses	Continuous pulses
				Small lesions	

Figure 35. Optimisation parameters for whole brain BBB permeabilisation. In the upper panel, the FUS trajectory used, and T1-w images obtained after Gd-DOTA injection. In the bottom panels, the different tested parameters [Rigollet et al.*, 2023].*

We thus tested these parameters in 5 mice and injected right after the BBB opening recombinant AAV type 9 viruses expressing the GFP protein to validate drug delivery. H&E staining, iba1, podocalyxin and GFP expression were analysed in brains harvested 3 weeks after FUS application (Figure 36). In T1-w images, we contoured the area with BBB opened. As a result, 52.8 ± 6.4% of the brain volume exhibited BBB permeability. We did not see any visible lesions in T2-w images and H&E staining after visual inspections. Levels of iba1 and podocalyxin expression were very low or non-existent suggesting a resorbed neuroinflammation. Finally, we can see a very good expression in the whole brain of GFP signifying a large and effective transduction with recombinant AAV type 9. Plus, we can see that there is a very good colocalisation between the raster scan, the T1-w image after Gd-DOTA injection and the GFP expression.

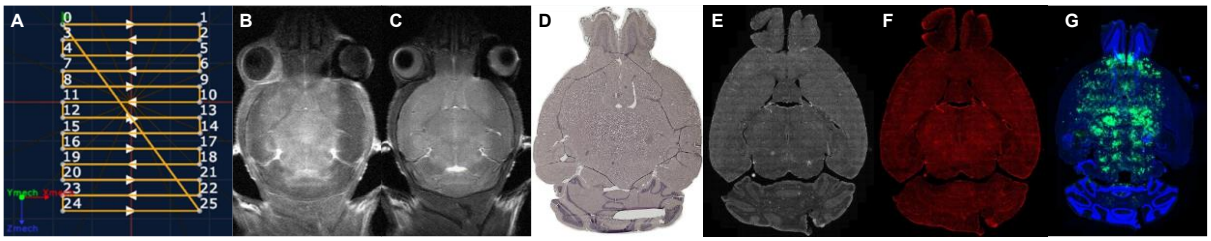


*Figure 36. Validation of whole brain BBB permeabilisation. Example for one mice with the raster scan. Raster scan trajectory (**A**). Associated T1-w post-DOTA (**B**), T2-w (**C**), H&E (**D**), Iba1 (**E**), podocalyxin (**F**) and GFP expression (**G**) images in representative mice 3 weeks after FUS application. Histological images were provided by Dr Michael Decressac, Romain Clément and Cassandra Cresson [Rigollet* et al.*, 2023].*

To conclude, we validated the large BBB opening protocol with a moving FUS transducer along a raster scan and it resulted in effective drug delivery, limited neuroinflammation and without lesions. This FUS sequence will be largely used during the thesis with small adaptations due to the specificity of the experiments.

4.5. Magnetic resonance image acquisition and processing methods

All MRI acquisitions of this thesis were performed on a 4.7 T magnet (BioSpec 47/40) drive with Avance III electronics (Bruker, Ettlingen, Germany) MRI available at the IRMaGe facility. The scanner embeds a 120 mm internal diameter gradient sleeve with 660 mT/m maximal intensity and 114 µs rise time. For acquisitions without the MR-guided FUS system, the scanner was equipped with a volume transmit coil and a single-element surface receive coil (Figure 37). Most of the image processing was done with the in-house MP3 software [Brossard *et al.*, 2020] specifically developed to facilitate large database management and enable multiparametric quantitative image processing. The general processing steps for each session involved extracting the brain mask from the raw T2-w images using pulse-coupled neural networks [Chou *et al.*, 2011] and registering it to a rat brain template [Valdés-Hernández, 2011] using *FLIRT* algorithm from FSL software [Jenkinson *et al.*, 2002]. The resulting transformation was then applied to each scan acquired during the session. This step facilitated the rapid and robust extraction of brain structures for subsequent analysis.



*Figure 37. Preclinical 4.7 T MRI (**A**) with linear volume transmit coil (**B**) and receiver coil (**C**). All equipment are Bruker devices.*

4.5.1. Anatomical images

Anatomical image was acquired with T2 rapid imaging with refocused echoes (TurboRARE) (TR/TE = 2500/33 ms; 23 axial slices; FOV = 30 × 30 mm^2; matrix, 256 × 256; voxel size, 117 × 117 × 1000 μm^3; RARE-factor = 8; T_{acq} = 2 min 40 s) sequence. This sequence enables rapid imaging of the brain and can be used to decipher any small haemorrhages, oedema and brain structures as well as tumour implantation for example. Different T2-w images are presented in Figure 38.

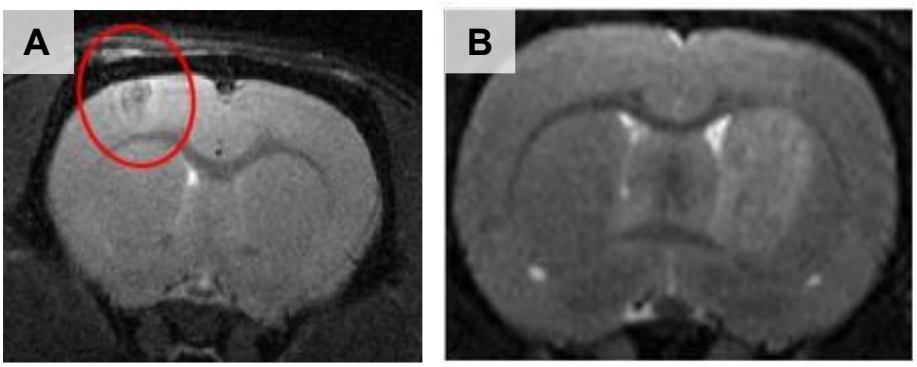


*Figure 38. T2-w images with an example of a too intense BBB opening resulting in a small haemorrhage (**A**), and a rat brain with F98 tumour cells 14 days after the implantation of 1000 cells (**B**).*

4.5.2. Evaluation of blood-brain barrier permeability

Different methods were used to quantify BBB permeability, and the common denominator was the use of gadolinium-based contrast agent at a concentration of 200 µmol/kg (DOTAREM®, Guerbet, Villepinte, France) intravenously.

3 types of images were used:

- T1 FLASH axial and coronal image (TR/TE = 300/3.5 ms; FOV = 30 × 30 mm²; matrix, 256 × 256; voxel size = 117 × 117 × 1000 µm^3; flip angle = 40°; T_{acq} = 1 min 43 s) were acquired before and after a bolus of Gd-DOTA;
- T1 map RARE variable time repetition (VTR) sequence (TR, 3000 to 18 ms; TE = 6.6 ms; FOV = 20 × 20 mm²; matrix 128 × 128; voxel size, 156 × 156 × 1000 µm^3, RARE-factor, 4; T_{acq} = 12 min 39 s) was acquired before and after the injection of the gadolinium contrast agent Gd-DOTA;
- Dynamic contrast enhanced sequence (TR/TE = 800/4 ms; FOV = 30 × 30 mm²; matrix, 128 × 128; voxel size = 234 × 234 × 1000 µm^3; RARE-factor = 4; echo spacing = 4 ms; 20 repetitions; T_{acq} = 5 min 04 s) with a bolus of Gd-DOTA injected 1 min after the beginning of the acquisition, equivalent to 4 consecutive baseline images. From this sequence, we can extract different metrics: the percentage of contrast enhancement (CE, [%]) between the last and first acquired images, the maximum of intensity (Max, [a.u.]), the time to peak (TTP, [s]) as the time to reach the maximum intensity and the area under the curve (AUC, [a.u.]) (Figure 39).

These methods enable the characterisation of the BBB opening with a small MR contrast agent in various ways. T1-weighted images facilitate rapid semi-quantitative analysis and allow for the computation of contrast enhancement in the permeabilised zone. The DCE sequence permits the longitudinal observation of Gd-DOTA in the brain, thereby offering dynamic insight into vascular permeability. While a T1 map represents a quantitative method, its main disadvantage is the duration of the acquisition time.

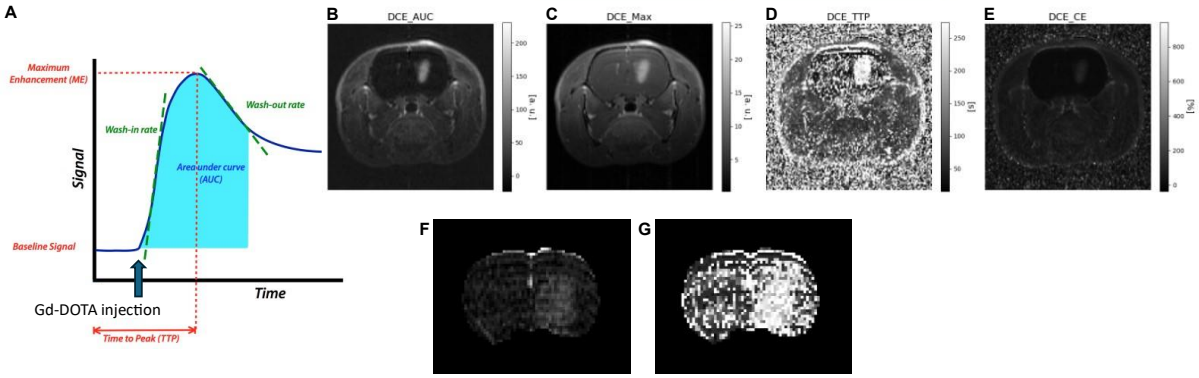


*Figure 39. Principle of DCE-MRI and example of DCE-computed images with AUC (**B**), maximum enhancement (**C**), time to peak (**D**) and contrast enhancement (**D**) of a rat brain implanted with F98 tumour cells and an example of contrast enhancement (**F**) and time to peak (**G**) after FUS-induced BBB opening. The principle of DCE-MRI was found in mriquestions.com.*

4.5.3. Perfusion acquisition and processing

Information about capillary microcirculation is very important for the diagnosis and follow-up of several brain pathologies. An important parameter of the brain hemodynamic is the cerebral blood flow (CBF). It is defined as the net blood flow through the voxel divided by the mass of the voxel and is expressed in mL/min/100g of tissue [Barbier *et al.*, 2001]. We used a method based on the blood arterial spin labelling (ASL) that enables to repeat non-invasively CBF measurements. Plus, for clinical applications, it is recommended to use pseudo-continuous arterial spin labelling (pCASL) methods [Alsop *et al.*, 2015]. pCASL enables efficient perfusion mapping *in vivo* without injection of contrast agent or use of multiple coils [Buck *et al.*, 2018]. The pCASL method used during this thesis was developed by Hirschler *et al*. and implemented in the Bruker scanner and Paravision console [Hirschler *et al.*, 2020, 2018].

CBF was quantified as described by Hirschler *et al*. [Hirschler *et al.*, 2018] and using:

- An inversion efficiency map obtained from a 1 mm-thick slice located 5 mm downstream of the pseudo-continuous arterial spin labelling (pCASL) plane and acquired with a flow-compensated gradient-echo sequence (TR/TE = 225/3.6 ms; FOV = 30 × 30 mm²; matrix, 256 × 256; voxel size = 117 × 117 × 1000 µm^3; T_{acq} = 3 min 30 s) (Figure 40.A);
- A T1 map of the brain tissue derived from a nonselective inversion recovery sequence (TR/TE = 10000/19 ms; 18 inversion times (TIs) between 30 and 10000 ms; FOV = 30 × 30 mm²; matrix, 128 × 128; voxel size, 234 × 234 × 1000 µm^3; T_{acq} = 4 min) (Figure 40.B);
- A perfusion-weighted signal obtained with a pCASL-encoded echo-planar imaging (EPI) sequence (TR/TE = 4000/21 ms; eight axial slices; FOV = 30 × 30 mm²; matrix, 128 × 128; voxel size, 234 × 234 × 1500 mm^3; number of repetitions, 30; label duration, 3000 ms; post labelling delay, 300 ms; T_{acq} = 4 min) (Figure 40.C).

From these images, with M_C and M_L the complex signals from the control and the label experiments, the inversion efficacy (IE) was derived as follows:

$$IE = \left| \frac{M_C - M_L}{2 \times M_C} \right| \tag{12}$$

In the IE image, a ROI was delineated manually in the carotids to obtain the mean IE across both carotids. To compute the CBF maps (Figure 40.D), it is assumed that the arterial transit time (i.e. the time taken for the blood to travel from large arteries in the neck to the cerebral tissue) is equal to the post-labelling delay (PLD = 300 ms), and that the magnetisation of arterial blood at thermal equilibrium, may be approximated by the magnetisation of tissue at thermal equilibrium divided by the blood-brain partition coefficient. The CBF was quantified pixel-by-pixel with the following equation:

$$CBF = \frac{6000 \times \lambda \times \Delta M \times \exp\left(\frac{\omega}{T_1^b}\right)}{2 \times IE \times T_1^t \times M_0^t \times 1 - \exp\left(-\frac{\tau}{T_1^t}\right)} \tag{13}$$

where λ is the blood-brain partition coefficient of water equal to 0.9 mL/g [Herscovitch and Raichle, 1985], ΔM the signal difference between the control and label acquisitions averaged over repetitions, T_1^t the apparent T_1 of tissue from the T1 map, T_1^b is the longitudinal relaxation time of blood equal to

1833 ms at 4.7 T [Dobre *et al.*, 2007], M_0^t is the control image intensity of the ASL experiment multiplied by $\left|1 - \exp\left(-\frac{TR}{T_1^t}\right)\right|^{-1}$ to correct for incomplete T_1 relaxation during the 4-s TR [Hirschler *et al.*, 2018].

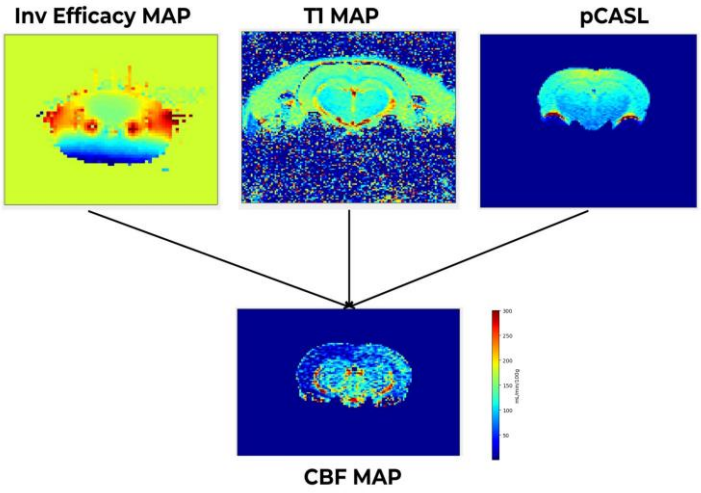


Figure 40. Cerebral blood flow image processing pipeline. Example of inversion efficacy map, T1 map and pCASL raw image necessary to compute the CBF map.

4.5.4. Multiparametric MRI protocol

The multiparametric MRI protocol aims to quantify a large range of parameters quantitatively. This protocol involve the acquisition of 10 MRI sequences (parameters of acquisition described in Table 10) after which the following derived maps were computed: T2-w, T1 and T2 maps, vascular density, vessel size index (VSI), blood volume fraction (BVf), CBF, cerebral metabolic rate of oxygen ($CMRO_2$), oxygen tissue saturation (SO_2) and the derived DCE parameters. This protocol was first developed by Lemasson *et al*. and further completed along the years already validated by many studies [Boux *et al.*, 2021b; Clément *et al.*, 2021; Lemasson *et al.*, 2010, 2013].

The ADC is calculated from the average of the ADCs in the three orthogonal directions. The variations in transversal relaxation speed were obtained from gradient echo and spin echo before and after the injection of ultrasmall paramagnetic iron oxide (USPIO) nanoparticles (referred as *pre* and *post* in the following equations) in the vascular system with the multi-gradient field induction decay spin echo (MGEFIDSE) sequence. The transverse relaxation rates T_2^* were obtained pixel-by-pixel by nonlinear least-squares fitting in the signal intensity SI to the exponential function:

$$SI(T_E) = S(0)exp\left(\frac{T_E}{T_2^*}\right) \tag{14}$$

Then, the ΔR_2^* map was computed according to $\Delta R_2^* = \frac{1}{T_{2,post}^*} - \frac{1}{T_{2,pre}^*}$, while transverse relaxation rates ΔR_2 were derived from the signal intensity:

$$\Delta R_2 = \frac{1}{T_E} ln\left(\frac{SI_{pre}}{SI_{post}}\right) \tag{15}$$

The increase in magnetic susceptibility $\Delta\chi$ between the tissue and the blood following the USPIO injection was fixed to 0.28 in GCS (gram – centimetre – second) system for 4.7 T measurements. The total BVf in a voxel is directly proportional to ΔR_2^* :

$$BVf = \frac{3}{4\pi \times \gamma \times \Delta\chi \times B_0} \times \Delta R_2^* \quad (16)$$

from [Troprès *et al.*, 2001].

The vessel size index can be estimated from $\left(\frac{\Delta R_2^*}{\Delta R_2}\right)^{3/2}$ ratio according to [Troprès *et al.*, 2001]:

$$VSI = 0.425\left(\frac{ADC}{\gamma \times \Delta\chi \times B_0}\right)^{1/2}\left(\frac{\Delta R_2^*}{\Delta R_2}\right)^{3/2} \quad (17)$$

SO2 maps were estimated using a quantitative BOLD approach [Christen *et al.*, 2010] and by using T_2 and BVf from the corresponding map. The MR signal decay was fitted to the following equation, beyond 10 ms of the volume-averaged multiple gradient-echo:

$$s = Cte \times exp\left(-\frac{1}{T_2}t - BVf \times \gamma \times \frac{4}{3} \times \pi \times \Delta\chi_0 \times Hct \times (1 - SO_2) \times B_0 \times t\right) \quad (18)$$

The mean vessel density is derived from the following relationship [Troprès *et al.*, 2015]:

$$mean\ vessel\ density = \frac{\Delta R_2}{(\Delta R_2^*)^{2/3}} \quad (19)$$

From the measurements of CBF and SO_2, one can derive the expression of $CMRO_2$:

$$CMRO_2 = CaO_2 \times CBF \times (SaO_2 - SO_2) \quad (20)$$

where SaO_2 the arterial oxygen saturation settled to 100% and CaO_2 to 19 mL O_2/100mL [An *et al.*, 2001; Bouvier *et al.*, 2015; West, 2007].

The different maps are displayed in Figure 41 and an overview of the processing pipeline is included in annexe A.2 (Figure 81).

Sequence name	TR/TE [ms]	n_{slices}	FOV [mm²]	Matrix size	Voxel size [µm³]	Other	T_{acq}
T2 TurboRARE	See section 4.5.1						
CBF	See section 4.5.3						
T1 map	See section 4.5.3						
DTI-EPI	2200/33	19	30 × 30	128 × 128	234 × 234× 1000		3 min 31 s
T2 map MSME	2350	7	30 × 30	128 × 128	234 × 234× 1000		3 min 45 s
MGE3D		/	30 × 30	256 × 256	117 × 117 × 239		8 min 57 s
MGEFIDSE	4000	7	30 × 30	128 × 128	234 × 234× 1000		6 min 24 s
DCE	See section 4.5.2						

Table 10. Acquisition parameters for the multiparametric MRI protocol.

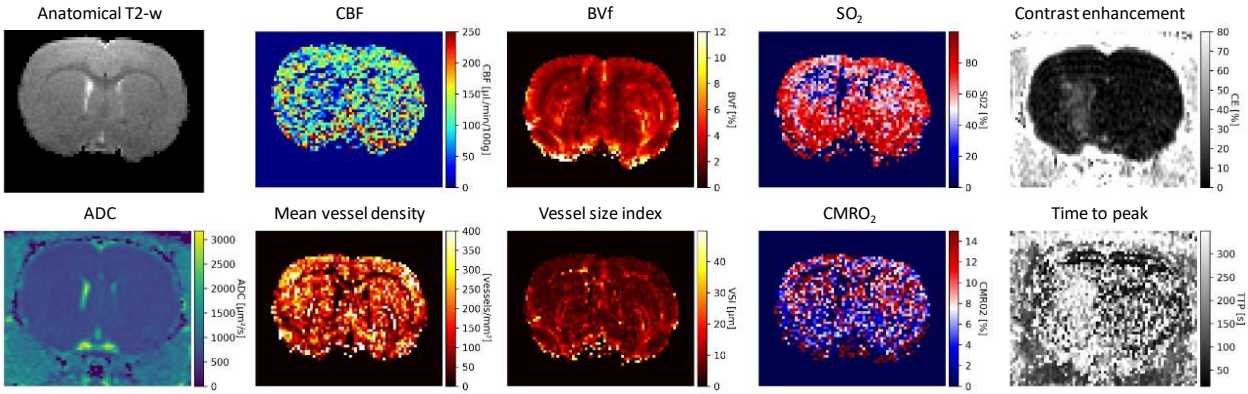


Figure 41. Overview of computed MRI maps with the multiparametric MRI protocol.

4.5.5. MR vascular fingerprint reconstruction

MRI fingerprinting was introduced in 2013 [Ma *et al.*, 2013] and enables to capture unique tissue properties by comparing acquired signal evolutions to a precomputed database of possible evolutions. Unlike conventional MRI, which measures single parameters with dedicated sequences, MR fingerprinting provides multiple quantitative tissue properties with a single acquisition. Recent developments in the team provided accurate and reliable measurements of the oxygen saturation in the tissue (SO_2), the mean vessel radius (R), the blood volume fraction (Vf) and the T2 parameter in the brain [Boux *et al.*, 2021a; T. Christen *et al.*, 2014; Lemasson *et al.*, 2016]. Fingerprints are extracted from simulations based on virtual voxels. The use of straight isotropic cylinders as vessels enabled to compute high spatial resolution brain maps of SO_2 [T. Christen *et al.*, 2014; Thomas Christen *et al.*, 2014; Lemasson *et al.*, 2016]. This simple representation was recently improved using 3D voxels segmented from datasets of whole brain in healthy mice [Delphin *et al.*, 2024]. We propose to use the latter improvements to compute quantitative MRI maps of SO_2, R and Vf.

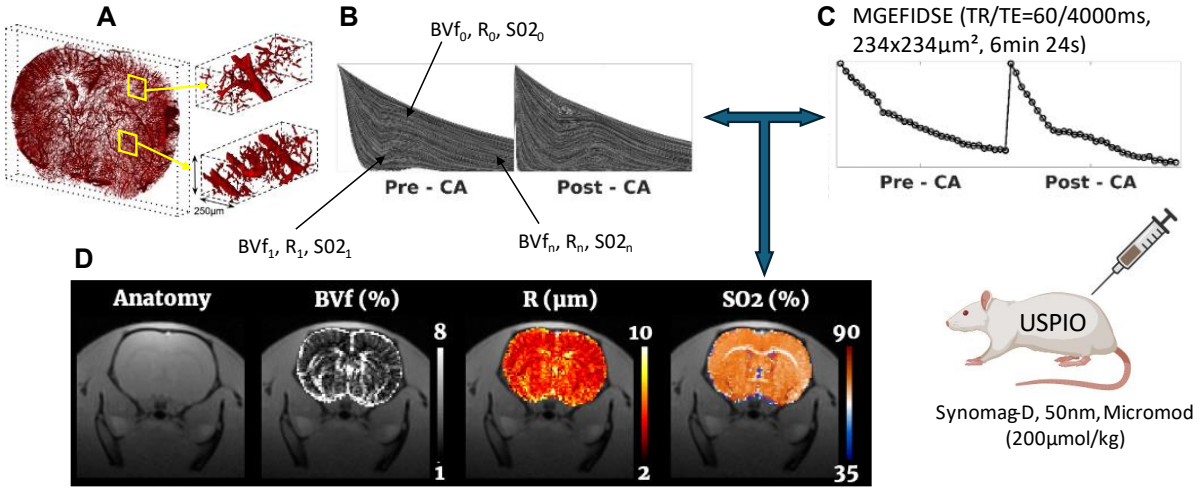


*Figure 42. Principle of the MRI fingerprint approach with realistic voxel based numerical simulations of MR signal. **A**) example of a single 744 µm thick slice of a mouse brain vascular network. **B**) Dictionary of MR signals from numerical simulations of a MGEFIDSE sequence without and with the presence of USPIO CA. **C**) MR signals from in vivo acquisition before and after the injection of the USPIO contrast agent in the vascular system. **D**) Example of resulting MRI maps after the acquired MR signals are matched to the simulated signals in the dictionary. Adapted from [Delphin* et al.*, 2024].*

A dictionary of 28,000 MRI signals was simulated based on as many MRI-sized voxels of 248 × 248 × 744 µm^3. MR simulations were performed with an in-house Matlab software [Pannetier *et al.*, 2013]. Real MR signals were acquired before and after the injection of USPIO (200 µmol iron/kg, Synomag-D 50 nm, Micromod, Rostock, Germany) with two MGEFIDSE sequences (for the acquisition parameters, see section 4.5.4). Image processing was performed on MP3 and a dictionary-based matching approach was performed to match the acquired signal in the dictionary.

4.5.6. Magnetic susceptibility maps

Quantitative susceptibility mapping (QSM) was achieved based on the phase signal of the MGE acquisition (see 4.5.4). Complex non-linear fitting followed by Laplacian operation provided temporal and spatial phase unwrapping, respectively [Liu *et al.*, 2013; Wang and Liu, 2015]. Background field extraction was performed with V-SHARP as it was recommended by the QSM Consensus Organization Committee [QSM Consensus Organization Committee *et al.*, 2024] and was the best-performing method after different tests. Then, magnetic susceptibility maps were reconstructed with star-QSM [Wei *et al.*, 2015; Wu *et al.*, 2012]. Star-QSM compensates for streaking artefacts that may originate from regions of strong magnetic susceptibility changes as in sinuses, potentially compensating for the chosen phase unwrapping method chosen.

Magnetic susceptibility sources separation relied on the χ-separation implementation [Shin *et al.*, 2021]. The algorithm was initialised with tissue maps after V-SHARP background field extraction, star-QSM reconstructed maps provided an initial estimate of total magnetic susceptibility, and R2' relaxation rate was obtained with R_2*-based ARLO fitting and a nominal R_2 value of 13 Hz [Pei *et al.*, 2015] even if this may lead to overestimations in the separated maps. This choice was made to avoid unreliable R_2, leading to negative R_2'. It was already implemented in the original algorithm, and it was more stable than using calculated R_2.

4.6. Histology methods

One of the main objectives of this project was to quantify various vascular and neuroinflammatory markers longitudinally after opening the BBB. These investigations at the cellular level are complementary to MRI measurements.

Brains were quickly removed, frozen in -40°C isopentane and stored at -80°C. Coronal slices (10 µm) at various points along the antero-posterior axis were obtained with a cryotome operating at -20°C. Haematoxylin and eosin (H&E) staining and immunohistochemistry for vascular and neuroinflammation markers were performed.

For immunohistochemistry, sections were fixed in paraformaldehyde (Fluka Chemie AG, Buchs, Switzerland). Brain sections were then incubated overnight at 4°C in primary antibody and in secondary antibody after rinsing with PBS. After rinsing in PBS-Tween 0.1%, coverslips were applied on slides with the nuclear marker DAPI (Thermofisher). A list of combinations between primary and secondary antibodies is available in Table 11.

Primary antibody	C [µg/mL]	Secondary antibody	C [µg/mL]	
rabbit anti-GFAP (DAKO, 70334)	1/1000	goat anti-rabbit (Invitrogen, A11008)	1/1000	Chapter 5 Chapter 6
mouse anti-SMI 71 (Biolegend Cat., No. 836803)	1/1000	donkey anti-mouse (Thermofisher, A31540)	1/1000	Chapter 5 Chapter 6
rabbit anti-Iba1 (1:500, Abcam, ab108539)	1/500	goat anti-rabbit (Invitrogen, A11008)	1/1000	Chapter 5

Table 11. List of combinations of primary and secondary antibodies with adapted concentrations.

Images were digitised using the Axioscan scanner (Zeiss, Oberkochen, Germany) and analysed using ZEN 3.6 software (Zeiss, Oberkochen, Germany), QuPath [Bankhead *et al.*, 2017] and Python 3.10.0. On H&E images, the entire section was visually inspected, with a special attention to regions where the FUS was applied, to look for potential haemorrhages. Red blood cells extravasations were analysed by counting the number of sites with at least 5 red blood cells. For immunofluorescence images, regions of interest (ROI) were manually drawn to extract the treated and control regions using ZEN software. Adjacent ROI were also drawn to analyse the surrounding area of the BBB opening. Different image processing pipelines were used for the different markers and adapted to ensure the best extraction. We quantified the mean intensity, the fraction of the field of view occupied by marked objects (area occupation); for vessel staining we also analysed the mean vessel diameter, length and tortuosity.

Chapter 5. Study 1: FUS-mediated BBB opening leads to transient perfusion decrease and inflammation without acute or chronic brain lesion

The following section includes an article published in *Theranostics*. The aim of this study was to monitor and characterise the transient perfusion and inflammatory process after a single application of FUS in the brain. We evaluated the consequences of permeabilising the BBB in the rat cortex and striatum.

This study was initiated by Dr Vasile Stupar, Dr Claire Rome and Dr Emmanuel L. Barbier. The first results were presented at the ISMRM in 2018 [Stupar *et al.*, 2018]. One of the drawbacks of the study was the use of a FUS transducer with a very large focal task, thus opening the BBB in a very large area. In addition, the BBB opening wasn't safe, which led to results that potentially wouldn't occur in a safe and reversible BBB opening. During my Master's internship, I started to complete the study by comparing the perfusion changes with a more focused transducer and a more reliable FUS setup. I completed the study during the first year of my thesis. I performed the BBB opening in rats, acquired the MRI sequences, analysed the MRI data, prepared the immunohistological sections, stained the tissues and analysed the micrographs. Some of the microtome sectioning and immunohistological staining was done by Qendresa Arifi during her internship, which I supervised. I wrote the first draft of the manuscript, and it was revised by all the co-authors.

Sébastien Rigollet[1, 2], Claire Rome[2], Thomas Ador[3, 4, 5], Erik Dumont[1], Chantal Pichon[3, 4, 6], Anthony Delalande[3, 4], Emmanuel L. Barbier[2, 7#], Vasile Stupar[2, 7]

1. Image Guided Therapy, Pessac, France
2. Univ. Grenoble Alpes, Inserm, U1216, Grenoble Institut Neurosciences, Grenoble, France
3. Université d'Orléans, LI²RSO, Orléans, France
4. ART ARNm, Inserm US55, Orléans, France
5. Laboratory of Experimental and Molecular Immunology and Neuromodulation (INEM), UMR 7355 CNRS-University of Orleans, Orleans, France
6. Institut Universitaire de France, Paris, France
7. Univ. Grenoble Alpes, Inserm, CHU Grenoble Alpes, CNRS, IRMaGe, Grenoble, France

5.1. Abstract

Impact: The permeabilization of the BBB to deliver therapeutics with MR-guided FUS redefines therapeutic strategies as it improves patient outcomes. To ensure the best translation towards clinical treatment, the evaluation of hemodynamic modifications in the CNS is necessary to refine treatment parameters.

Methods: MR-guided FUS was applied at 1.5 MHz with a 50 ms pulse every 1 s to open the BBB. CBF, BVf and ADC parameters were monitored with MRI. Cavitation was monitored with a PCD during the FUS sequence and classified with the IUD index into three cavitation levels. We distinctly applied the FUS in the cortex or the striatum. After the BBB permeabilisation, neuroinflammation markers were quantified longitudinally.

Results: The BBB was successfully opened in all animals in this study and only one animal was classified as "hard" and excluded from the rest of the study. 30 min after FUS-induced BBB opening in the cortex, we measured a 54% drop in CBF and a 13% drop in BVf compared to the contralateral side. After permeabilisation of the striatum, a 38% drop in CBF and a 15% drop in BVf were measured. CBF values rapidly returned to baseline, and 90 min after BBB opening, no significant differences were observed. We quantified the subsequent neuroinflammation, noting a significant increase in astrocytic recruitment at 2 days and microglial activation at 1 day after FUS. After 7 days, no more inflammation was visible in the brain.

Conclusion: FUS-induced BBB opening transiently modifies hemodynamic parameters such as CBF and BVf, suggesting limited nutrients and oxygen supply to the CNS in the hour following the procedure.

Keywords: focused ultrasound, MRI, neuroinflammation, secondary bioeffects, MR guidance

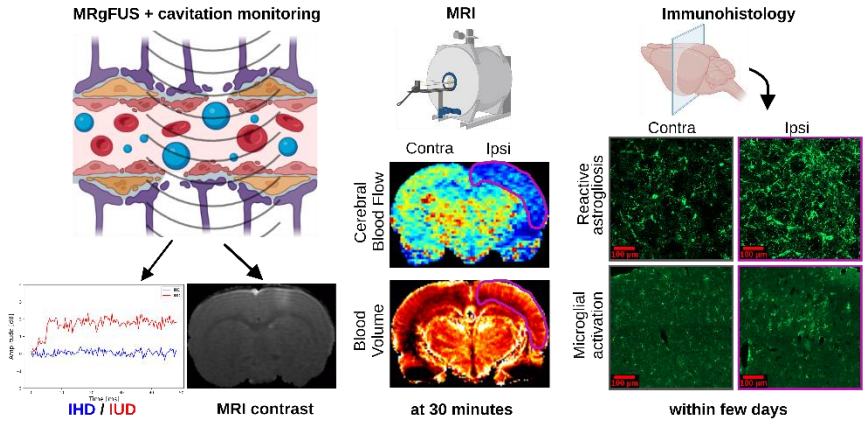


Figure 43. Abstract caption

5.2. Introduction

To perform local drug delivery in the brain, the combination of focused ultrasound (FUS) with gas microbubbles (MB) to permeabilise the blood-brain barrier (BBB) has gained interest since the pioneering demonstration by McDannold *et al*. in 2001 of the first extravasation of a gadolinium contrast agent (CA) in the central nervous system (CNS) [Hynynen *et al.*, 2001]. Prior to this, molecules such as hyperosmotic mannitol were used as agents to increase BBB permeability [Chu *et al.*, 2022], albeit with non-specific effects on blood vessels, limited spatial control, and changes in permeability that were not robustly predictable. Conversely, the combination of FUS and MB, guided by magnetic resonance imaging (MRI) and commonly referred to as MR-guided FUS, offers a non-invasive and precisely controllable method to transiently permeabilise the BBB [Chu *et al.*, 2022]. Moreover, monitoring or even controlling cavitation can enhance the safety of the procedure [Chu *et al.*, 2016; Kamimura *et al.*, 2019; Novell *et al.*, 2020]. This method also enables the use of functionalised MB for therapeutic applications. For example, MB loaded with chemotherapy such as doxorubicin [Aryal *et al.*, 2015; Tinkov *et al.*, 2010], paclitaxel [Zhu *et al.*, 2016], gemcitabine [Delaney *et al.*, 2021] or cationic MB for nucleic acid delivery [Delalande *et al.*, 2017; Sirsi *et al.*, 2012] have been developed, opening a new field of application.

However, the precise effects on brain tissue and vascularisation after FUS-mediated BBB permeabilisation with MB have not been fully explored, which hinders its safe clinical translation. Early investigations by Hynynen *et al*. [Hynynen *et al.*, 1996] in the late 1990s demonstrated that high-power FUS (6000 to 7000 W/cm²) without MB substantially constricted the femoral artery, reducing blood flow by 50%. A return to the original state occurred within a week, although sometimes accompanied by localised haemorrhages. Gao *et al*. investigated the vascular effects of MB coupled with 4.6 MPa high-intensity FUS on the liver with contrast-enhanced ultrasound. They concluded that it can temporarily block or reduce liver perfusion in rabbits, with a return to normal perfusion within one hour [Gao *et al.*, 2012]. Cho *et al*. monitored cerebrovascular dynamics in the cortex using intravital microscopy after BBB permeabilisation with pressures ranging from 0.071 MPa to 0.25 MPa, revealing vasoconstriction or vasodilation in a small number of cases [Cho *et al.*, 2011]. In summary, these results suggest that FUS-mediated BBB permeabilisation may affect cerebral blood flow (CBF).

Further reports corroborate this hypothesis. Following hind paw stimulation and BBB permeabilisation using MB and FUS in the right S1 cortex, arterial spin labelling (ASL) MRI measurements revealed a significant decrease in CBF changes within the right S1 cortex compared to the left [Todd *et al.*, 2019]. More recently, Stupar *et al.* [Stupar *et al.*, 2018] and Labriji *et al.* [Labriji *et al.*, 2023] reported a decrease in CBF following, respectively, FUS and non-focused US-mediated BBB permeabilisation using MB at about 0.38 MPa. It is therefore pertinent to inquire whether the reduction in CBF also occurs when BBB permeabilisation is performed for drug delivery to the brain.

Several dysregulations of the CNS following FUS-mediated BBB opening have been reported. Kovacs *et al*. demonstrated that sterile inflammation was triggered in cases of BBB permeability at 0.3 MPa PNP and noted an immediate damage-associated molecular pattern with IL-1, IL-18, and TNF-alpha transitory upregulation [Kovacs *et al.*, 2017]. Furthermore, angiogenic characteristics such as increased endothelial cell density and frequency of small blood vessel segments were observed several days after BBB opening. Additionally, blood vessel density exhibited a slight increase in the targeted area between 7- and 14-days following FUS treatment. These changes were followed by a return to baseline

after three weeks [McMahon *et al.*, 2018]. However, these cellular evaluations were not associated with an *in vivo* evaluation of brain perfusion.

We hypothesised that FUS-mediated BBB opening could lead to significant modifications in brain perfusion, thereby triggering cellular mechanisms to repair the BBB.

The primary objective of this study was to measure and compare changes in brain perfusion at various time points following FUS-mediated BBB permeabilisation. Cavitation was monitored to assess the safety of the procedure and evaluate the deposited energy in the brain. MRI was used to quantify the CBF and the blood volume fraction (BVf) in the targeted brain regions at 30, 60, 90 min, and 24 h post-FUS. Histological changes in the brain tissue were examined with a focus on neuroinflammation markers, vessel integrity and signs of haemorrhages or oedema. This analysis was performed to detect any structural or cellular alterations resulting from BBB permeabilisation.

5.3. Method

5.3.1. Animal care and preparation

All animal procedures were conducted in compliance with ethical guidelines and were approved by both the Ethics Committee and the French Ministry of Research and Education (Authorisation n° APAFIS#43777). Thirty-five male Wistar Han rats (age = 7 weeks) weighing between 270 and 350 grams were selected as experimental subjects and divided into three distinct groups. Anaesthesia was induced using 4% isoflurane in a mixture of oxygen and air (20/80%). Throughout the experimental protocol, anaesthesia was maintained at a consistent level between 1.5% and 2.5% isoflurane using the same oxygen and air mixture administered using an anaesthesia compact module (Minerve, Esternay, France). Respiratory rate and body temperature were maintained respectively around 60 breaths per min and 37 °C with care. Prior to the experiment, the hair on the top of the head was entirely removed using a trimmer followed by the application of a depilatory cream to optimise ultrasound transmission coupling. A 24 G catheter was carefully inserted into the tail vein to perform intravenous (IV) injections of saline, MB, and MRI contrast agents (CA) (Figure 45.A). At the end of the experimental procedures, the rats were closely observed until they fully regained consciousness, ensuring their well-being and recovery.

5.3.2. Microbubbles

For this study, we used a solution of homemade lipidic-shelled MB. The shell is composed of 1,2-distearoyl-sn-glycero-3-phosphocholine (DSPC) and 1,2-dimyristoyl-sn-glycero-3-phosphoethanolamine-N-[methoxy(polyethyleneglycol)-2000] (DSPE-PEG2000), 88:12 molar ratio. Lipids were obtained from Avanti Polar lipids. The gas core is composed of perfluorobutane (F2 Chemicals, UK). MB have a mean diameter of 1.5 µm ranging between 1 and 5 µm, and concentration of 2×10^{10} MB/mL (Figure 45.B). MB were activated in a 10 mM HEPES buffer (pH = 7.4) through 45 s of mechanical agitation using a VialMix® shaker (Lantheus Medical Imaging).

5.3.3. MR-guided FUS

BBB permeabilisation was performed using a dedicated MR-guided FUS system (Image Guided Therapy, Pessac, France) described by Magnin *et al*. [Magnin *et al.*, 2015]. This setup includes a seven-concentric-elements transducer (Imasonic, Voray-sur-l'Ognon, France), which enables a control of the ultrasound focus length by steering (center frequency: 1.5 MHz, radius of curvature: 20.01 mm, focal length: 20 mm). The focal spot was characterised with a bullet hydrophone (HGL-0200, ±3 dB frequency range of 0.25–40 MHz; Onda Corporation, Sunnyvale, CA, USA) in a degassed separate water tank with a 3-axis LabVIEW controlled homemade system to position the hydrophone and measure the focal spot with a resolution of 0.1 × 0.1 × 0.2 mm^3. The radial and axial lengths of the full width at half maximum (FWHM) were 1.1 mm and 6.6 mm, respectively (Figure 19.B). The MR-guided FUS system includes an MRI saddle coil used for both transmission and reception. First, the position of the transducer within the MRI coordinate system was established. For this aim, an axial and a coronal, T1-weighted (T1-w), fast low angle shot (FLASH) images were acquired (TR/TE = 200/2 ms; 25 slices; field of view (FOV), 50 × 50 mm^2; matrix, 128 × 128; voxel size = 391 × 391 × 1000 μm^3; acquisition time (T_{acq}), 51 s). The location of the transducer was then computed offline using dedicated software from Image Guided Therapy (ThermoGuide®). An additional T2 TurboRARE sequence (TR/TE = 2500/33 ms; 15 coronal slices; FOV = 37 × 37 mm^2; matrix, 256 × 256; voxel size, 145 × 145 × 1000 μm^3; T_{acq} = 5 min) was used to precisely localise the target (Figure 45.C).

Animals were placed under the ultrasound transducer with ultrasound gel to ensure proper coupling. A dose of 4 × 10^8 MB diluted in 100 µl HEPES buffer (10 mM, pH = 7.4) was injected over 10 seconds and flushed with 150 µL of saline. The ultrasound sequence started 15 s after the saline injection. Ultrasound stimulation consisted of 50 ms pulses with a pulse repetition frequency of 1 Hz (duty cycle = 5%) applied for 60 s. This duty cycle was not exceeded to avoid thermal elevation [Larrat *et al.*, 2010]. We aimed to deliver an acoustic amplitude of 0.6 MPa PNP in the targeted brain region. Using the calibration of the ultrasound transducer (Figure 20.A-B), the amplitude was adjusted for each animal depending on its weight and based on the attenuation of the brain (5 Np/m/MHz) and of the skull, according to Gerstenmayer *et al*. [Gerstenmayer *et al.*, 2018].

5.3.4. Cavitation monitoring and analysis

Cavitation monitoring plays a crucial role in controlling the safety and in optimising the efficacy of BBB opening. In our study, we monitored cavitation with an unfocused passive cavitation detector (PCD) integrated at the centre of the transducer (central frequency: 2 MHz, frequency bandwidth: 54% diameter: 20 mm; Imasonic, Voray-sur-l'Ognon, France). The PCD was connected to a digital oscilloscope (Picoscope 5242D, Pico Technology, UK) and signal acquisition was triggered by the ultrasound system (sampling frequency, 15.625 MHz). Data were analysed offline to assess the safety of the BBB opening with a Python script (version 3.10.12, Python Software Foundation, USA). Recently, Novell *et al*. [Novell *et al.*, 2020] proposed a new cavitation monitoring method that does not require the acquisition of a baseline signal prior to the MB injection. This method has the advantage of allowing the characterisation of inertial cavitation events using a shorter time range, thereby facilitating a more accurate estimation of the acoustic energy deposition. Stable cavitation is characterised by oscillating MB that do not collapse, typically driven by a low amplitude acoustic field. In contrast, inertial cavitation involves the collapse of MB, producing broadband acoustic emissions. In this context, the appearance of ultra-harmonic frequencies serves as a common marker for the onset of inertial

cavitation [Tung *et al.*, 2010a]. The monitoring of this phenomenon involves the calculation of the intrapulse ultra-harmonic dose (IUD) and intrapulse harmonic dose (IHD) [Novell *et al.*, 2020]. These were calculated considering respectively 1.5 × f_0, 2.5 × f_0, 3.5 × f_0 and 2 × f_0, 3 × f_0, 4 × f_0 frequencies with a 50 kHz bandwidth. Each 50 ms pulse was analysed as follows: an initial pulse cut of 200 µs was set to get rid of non-linear oscillations of the transducer, followed by 247 windows of 200 µs taken into account for further calculations of IUD and IHD, and the final 400 µs were not analysed to also avoid distortions. A separate fast Fourier transform was performed on the 247 windows before calculating IUD and IHD. It is important to note that a risk of inertial cavitation events can occur if the IUD index increases rapidly. The cavitation signal was computed for the n^{th} temporal window as follows:

$$IUD_n = \frac{AUC_{\frac{3f0}{2}}(n) + AUC_{\frac{5f0}{2}}(n) + AUC_{\frac{7f0}{2}}(n)}{AUC_{\frac{3f0}{2}}(1) + AUC_{\frac{5f0}{2}}(1) + AUC_{\frac{7f0}{2}}(1)} \quad (21)$$

We defined a threshold likely to represent a strong destabilisation of the MB and therefore induce harmful effects on the brain tissue. We set this threshold to $1.5 \times IUD_0$. When the value of IUD_n exceeded $1.5 \times IUD_0$, we classified the cavitation signal as inertial. We then evaluated the number of consecutive events exceeding $1.5 \times IUD_0$ (the black dashed line in Figure 45.E). Previous studies have evaluated different levels of BBB opening as the acoustic energy strongly influences the outcome of BBB opening [Chopra *et al.*, 2010; Chu *et al.*, 2016; Ji *et al.*, 2021]. We classified the animals in our study into three different levels of cavitation dose: soft, mild, and hard. The soft case was considered when no event exceeded the settled cavitation threshold (Figure 48.A.5), the mild case when most events were between the noise threshold and some events exceeded the threshold (Figure 48.B.5), and the hard case when events exceeded the threshold and many of them were consecutive (Figure 48.C.5) and associated with many red blood cell extravasation (Figure 48.C.3).

5.3.5. Study design

This section describes the groups of animals, and the MRI measurements performed after MR-guided FUS BBB opening (Figure 44). A detailed description of each MRI sequence is provided in section 5.3.6.1. Histological analyses were performed at the end of the procedure (see 5.3.7). As the evaluation of CBF and ADC requires that subjects are free of contrast agents, measurements of BVf, which require USPIO contrast agents, cannot be performed at the same time points.

5.3.5.1. Group 1: CBF and ADC evaluation

Group 1 (n = 14) was used to evaluate the effects of BBB opening localisation on CBF and ADC 30 min after FUS. A second imaging session was performed 24 h after FUS to measure these parameters prior to analysis. Half of the animals underwent FUS in the cortex, while the other half underwent FUS in the striatum. Electronic steering of the transducer was used to modify the position of the focal point, thereby adjusting the target location (see 5.3.3). This allowed assessment of whether changes in CBF or ADC were dependent on the target location.

5.3.5.2. Group 2: CBF over time

Group 2 (n = 14) was designed to measure the evolution of CBF at 30, 60, 90 min, and 24 h after BBB opening. To avoid any bias in our CBF data, no Gd-DOTA injection was performed in group 2 and therefore BBB opening could not be evaluated.

5.3.5.1. Group 3: BVf evaluation

Group 3 (n = 9) was used to study the BVf 30 min after BBB opening. An anatomical T2-weighted (T2-w) image and multi-gradient echo images were acquired before and after injection of USPIO nanoparticles (200 µmol iron/kg, Synomag-D 50 nm, Micromod, Rostock, Germany) to measure BVf. To assess BBB opening, a T1-w image was acquired before and after injection of Gd-DOTA (200 µmol/kg, DOTAREM®, Guerbet, Villepinte, France). A second imaging session was performed one week after FUS to assess the presence of brain haemorrhage using multi-gradient echo images and the integrity of the BBB using T1-w images and an injection of Gd-DOTA. In this group, 6 animals received FUS treatment in the cortex and the last 3 in the striatum.

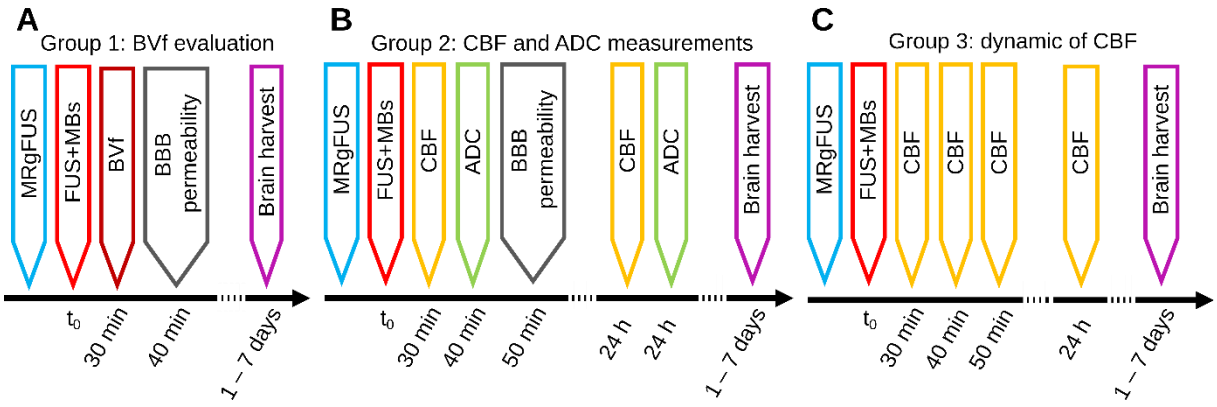


Figure 44. Workflow of the study, with the timeline for each group.

5.3.6. Magnetic resonance imaging (MRI) data and analysis

5.3.6.1. CBF, ADC, BVf and BBB opening area measurements

MRI was performed at 4.7 T (Avance III, Bruker, Germany) at IRMaGe MRI facility (Grenoble, France). The scanner was equipped with a volume transmit coil and a single-element surface receive coil. An overview of the different MRI images acquired in this study is presented in Figure 45.F. Anatomical T2-w images were acquired using a TurboRARE sequence (TR/TE = 2500/33 ms; 23 axial slices; FOV = 30 × 30 mm^2; matrix, 256 × 256; voxel size, 117 × 117 × 1000 μm^3; RARE-factor = 8; T_{acq} = 2 min 40 s). CBF was quantified as described by Hirschler *et al*. [Hirschler *et al.*, 2018] and using:

- An inversion efficiency map obtained from a 1 mm-thick slice located 5 mm downstream of the pseudo-continuous arterial spin labelling (pCASL) plane and acquired with a flow-compensated gradient-echo sequence (TR/TE = 225/3.6 ms; FOV = 30 × 30 mm^2; matrix, 256 × 256; voxel size = 117 × 117 × 1000 μm^3; T_{acq} = 3 min 30 s);
- A T1 map of the brain tissue derived from a nonselective inversion recovery sequence (TR/TE = 10000/19 ms; 18 inversion times (TIs) between 30 and 10000 ms; FOV = 30 × 30 mm^2; matrix, 128 × 128; voxel size, 234 × 234×1000 μm^3; T_{acq} = 4 min);
- A perfusion-weighted signal obtained with a pCASL-encoded echo-planar imaging (EPI) sequence (TR/TE = 4000/21 ms; eight axial slices; FOV = 30 × 30 mm^2; matrix, 128 × 128; voxel size, 234 × 234 × 1500 μm^3; number of repetitions, 30; label duration, 3000 ms; post labelling delay, 300 ms; T_{acq} = 4 min).

To detect oedema in the brain, diffusion tensor imaging (DTI) EPI scans were acquired, and ADC maps were computed (TR/TE = 2300/21 ms; b-values = 0 and 1000 $s.mm^{-2}$; 30 directions; 23 axial slices; FOV = 30 × 30 mm^2; matrix, 128 × 128; voxel size, 234 × 234 × 1000 μm^3; T_{acq} = 10 min 44 s). BVf was derived from multi gradient echo (MGE) images acquired before and after the injection of USPIO (TR = 920 ms; TE1 = 3.5 ms, ΔTE = 5 ms; number of echoes, 8; 19 axial slices; FOV = 30 × 30 mm^2; matrix, 256 × 256; voxel size, 137 × 137 × 1000 μm^3; T_{acq} = 5 min 53 s).

5.3.6.2. MRI processing

ADC maps were reconstructed using ParaVision 6.0.1 (Bruker, Ettlingen, Germany). All MRI data were processed and analysed using MP3 [Brossard *et al.*, 2020]. Raw T2-w images of the brains were masked using pulse-coupled neural networks [Chou *et al.*, 2011] and registered to a rat brain template [Valdés-Hernández, 2011] using *flirt* from FSL software [Jenkinson *et al.*, 2002]. The resulting transformation was then applied to each scan acquired during the session. BVf maps were calculated from the change in transverse relaxation rate due to USPIO as described by Troprès *et al*. [Troprès *et al.*, 2015]. Data from the ipsilateral (i.e., the hemisphere that underwent FUS) and contralateral cortex and striatum were extracted using the SIGMA rat brain atlas [Barrière *et al.*, 2019] (https://www.nitrc.org/projects/sigma_template). We calculated the difference between T1-w images obtained before and after Gd-DOTA injection and manually delineated the BBB-open area.

5.3.7. Histological analysis

5.3.7.1. Immunohistochemistry staining protocols

Brains were quickly removed, frozen in -40°C isopentane and stored at -80°C. Coronal slices (10 µm) at various points along the anteroposterior axis were obtained with a cryotome operating at -20°C. Haematoxylin and eosin (H&E) staining and immunohistochemistry for vascular and neuroinflammation markers were performed.

For immunohistochemistry, sections were fixed in paraformaldehyde (Fluka Chemie AG, Buchs, Switzerland). Brain sections were then incubated overnight at 4°C in rabbit anti-GFAP (1:1000, DAKO, 70334), rabbit anti-Iba1 (1:500, Abcam, ab108539) or mouse anti-SMI 71 (1:1000, Biolegend Cat., No. 836803). Sections were then incubated with goat anti-rabbit (1:1000, Invitrogen, A11008) or donkey anti-mouse (1:1000, Thermofisher, A31540) secondary antibody. After rinsing in PBS-Tween 0.1%, coverslips were applied on slides with the nuclear marker DAPI (Thermofisher).

5.3.7.1. Image acquisition and analysis

Images were digitised using the Axioscan scanner (Zeiss, Oberkochen, Germany) and analysed using ZEN 3.6 software (Zeiss, Oberkochen, Germany), QuPath [Bankhead *et al.*, 2017] and Python 3.10.0. On H&E images, the entire section was visually inspected, with a special attention to the application of FUS, to look for changes. Red blood cells extravasations were analysed by counting the number of sites with at least 5 red blood cells. For immunofluorescence images, regions of interest (ROI) were manually drawn to extract the treated and control regions using ZEN software. Iba1 quantification was performed using QuPath with microglial cell segmentation by pixel classification and mean fluorescence intensity extracted for quantification. Astrocytes were quantified using a Python script by retrieving the fluorescent fraction of the surface area and mean fluorescence intensity. Similarly, vessel

quantification was performed using a Python script that retrieved the mean vessel diameter, length and tortuosity in the contralateral, ipsilateral and two adjacent areas of the ipsilateral region.

5.3.1. Statistical analysis

Statistical analysis was performed using GraphPad Prism 9.0 software (GraphPad Software Inc., La Jolla, CA, USA). Blood volume, flow and water diffusion data are presented as mean ± standard deviation (S.D.). Histological quantifications are expressed as a percentage of area (%) and mean fluorescence intensity (arbitrary unit (a.u.)). A non-parametric two-tailed paired t-test was used for pairwise comparisons (α level was set at 0.05).

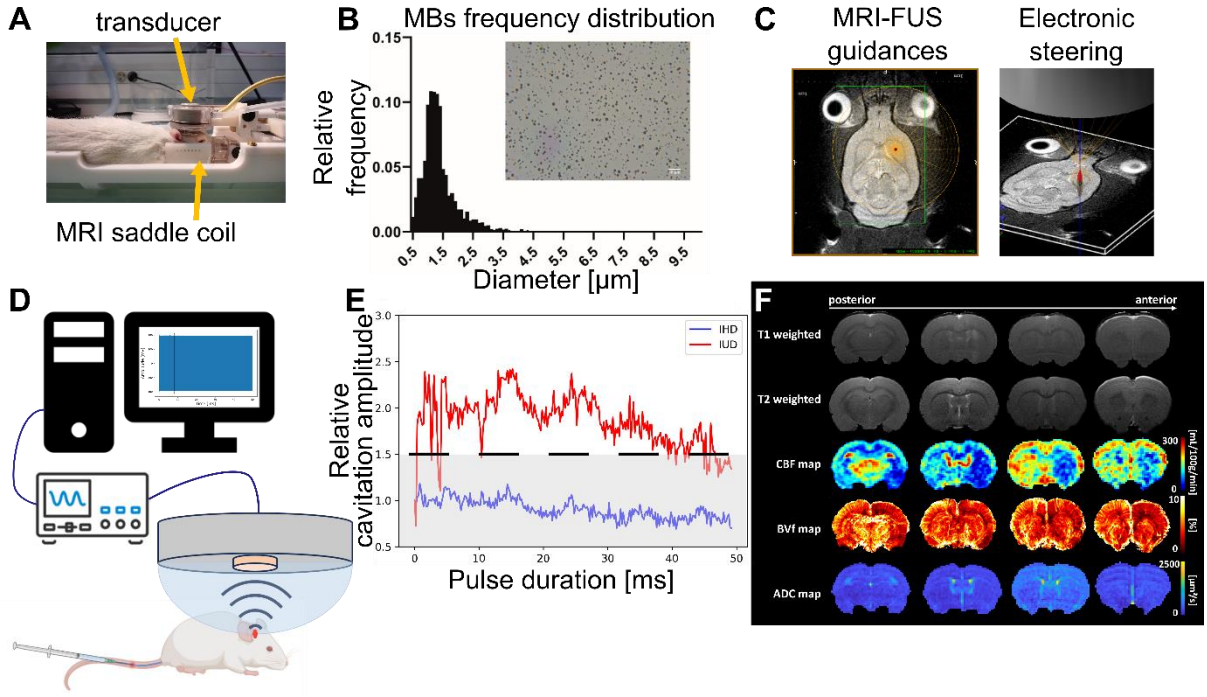


*Figure 45. Outline of the different steps of the study. The animal is placed in the MR-guided FUS bed, which includes an MRI saddle coil with the transducer placed over the animal's head (**A**). the region of interest is targeted using Thermoguide® software and focal steering (**B**). Micrograph showing MB and histogram of MB diameter distributions (**C**). Cavitation monitoring setup with the PCD in the centre of the transducer, an oscilloscope and signals processed by a computer (**D**) to calculate IHD and IUD for each pulse duration. An example of the IHD and IUD evolution over a single pulse duration is shown, with the IUD evolution in red, the IHD evolution in blue, the black dashed line representing the inertial threshold, and the grey dashed area indicating the noise level (**E**). Representative MRI images and parametric maps obtained from one animal in this study (**F**).*

5.1. Results

5.1.1. MR-guided FUS BBB opening effectiveness

The MR-guided FUS system was integrated with the MRI to precisely guide the focal point to the region of interest. We targeted two different brain regions: the cortex (located 0.5 mm posterior and 3 mm lateral to the bregma on the right side of the skull and at a depth of 1.5 mm from the brain surface) and the striatum (0.5 mm posterior and 3 mm lateral to the bregma on the right side of the skull and at a depth of 5 mm from the brain surface) (Figure 46.A-B). The BBB was successfully opened in all animals, with an average enhancement of 18.66% following IV injection of Gd-DOTA (Figure 46.C). We compared the volume of Gd-DOTA extravasation with the volume of the targeted brain regions (Figure 46.D). Altogether, 5% of the cortex volume and 30% of the striatum were permeabilised.

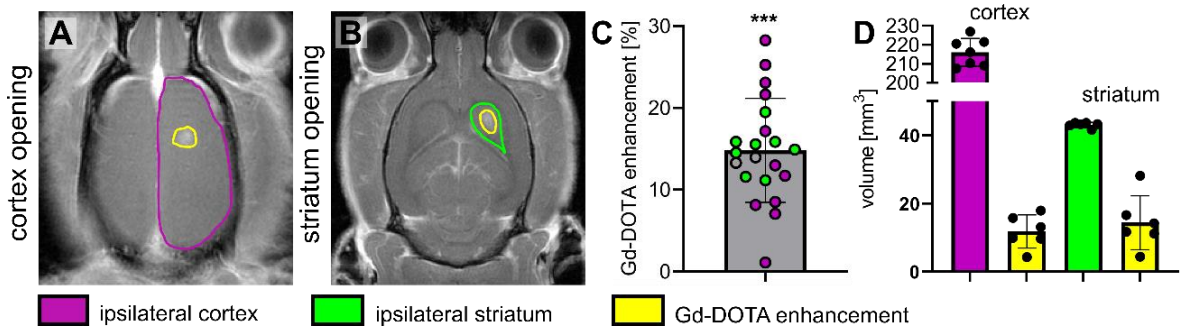


*Figure 46. Representative T1-w images of the brain after the BBB has been opened at the level of the cortex (outlined in purple) (**A**) and the striatum (outlined in green) (**B**) and Gd-DOTA injection, the opened BBB is outlined in yellow. (**C**) Relative Gd-DOTA enhancement of the ipsilateral region after Gd-DOTA injection. In purple, the subjects targeted in the cortex and in green the ones targeted in the striatum. A two-tailed non-parametric paired t-test (***p < 0.001) was performed on the ipsilateral region between images acquired before and after Gd-DOTA injection. (**D**) The volume of the ipsilateral cortex (purple), ipsilateral striatum (green) and the corresponding volume of the BBB opening for subjects targeted in the cortex and striatum. The results are expressed as mean ± S.D.*

5.1.2. Safety of the procedure: passive cavitation monitoring, MRI images, and HE analysis

Cavitation was closely monitored during the application of the FUS sequence. IUD and IHD indices were calculated to provide insight into the mechanical aspects of BBB opening. Subjects were categorised into three levels of cavitation intensity - soft, mild, and hard - based on the IUD level and the inertial threshold equal to $1.5 \times IUD_0$. The IHD parameter did not vary enough to discriminate between the subjects in this study. This categorisation process allowed us to exclude animals that received excessively intense energy deposition. Twenty-three animals from groups 1 and 3 were monitored with the PCD and only twenty were analysed due to technical issues. We quantified both the number of cavitation events that exceeded the inertial threshold and the number of consecutive inertial events. We saw an increase in the number of inertial events and the number of consecutive inertial events that did not correlate with the contrast enhancement measured in MRI (Figure 47.A and Figure 47.B) suggesting that MRI-based quantification has limitations. A linear fit between the consecutive and total inertial events showed a good correlation (R^2 = 0.91) and seems to discriminate two main groups.

Fourteen animals (70%) were classified as soft and 6 as mild or hard (30%). We performed H&E analysis to validate the correlations.

In the soft cases, the relative cavitation signal values did not show any significant humps (Figure 48.A.4), and the IUD remained within the noise level, as shown in Figure 48.A.5. No erythrocytes were visible on H&E images (Figure 48.A.2-3). Inertial and consecutive inertial events did not exceed 1.4% and 0.3%, respectively, as shown in Figure 47.A and Figure 47.B.

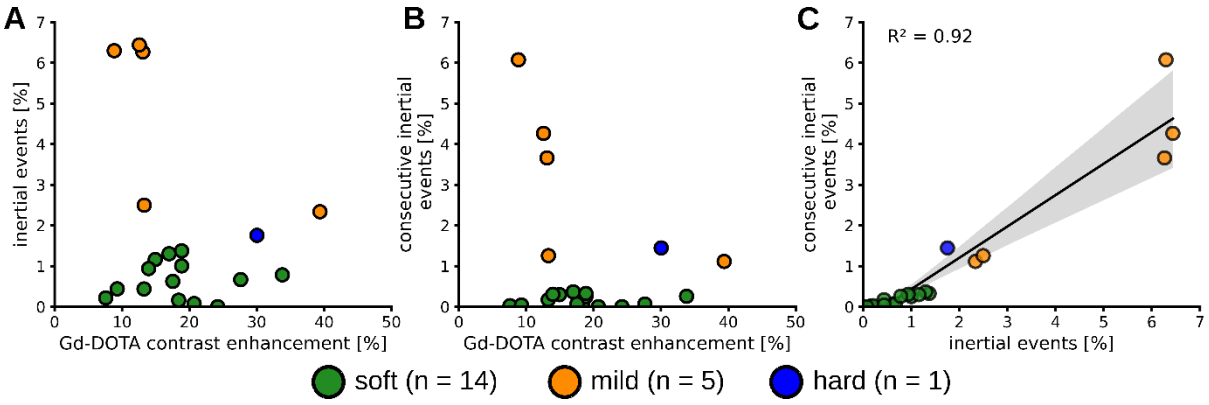


*Figure 47. Number of events above the $1.5 \times IUD_0$ threshold (i.e. inertial events) (**A**). Number of consecutive inertial events (**B**). Evolution of the consecutive inertial events depending on the total number of inertial events and linear regression (**C**). The values are expressed as a percentage of the total number of IUD_n measured.*

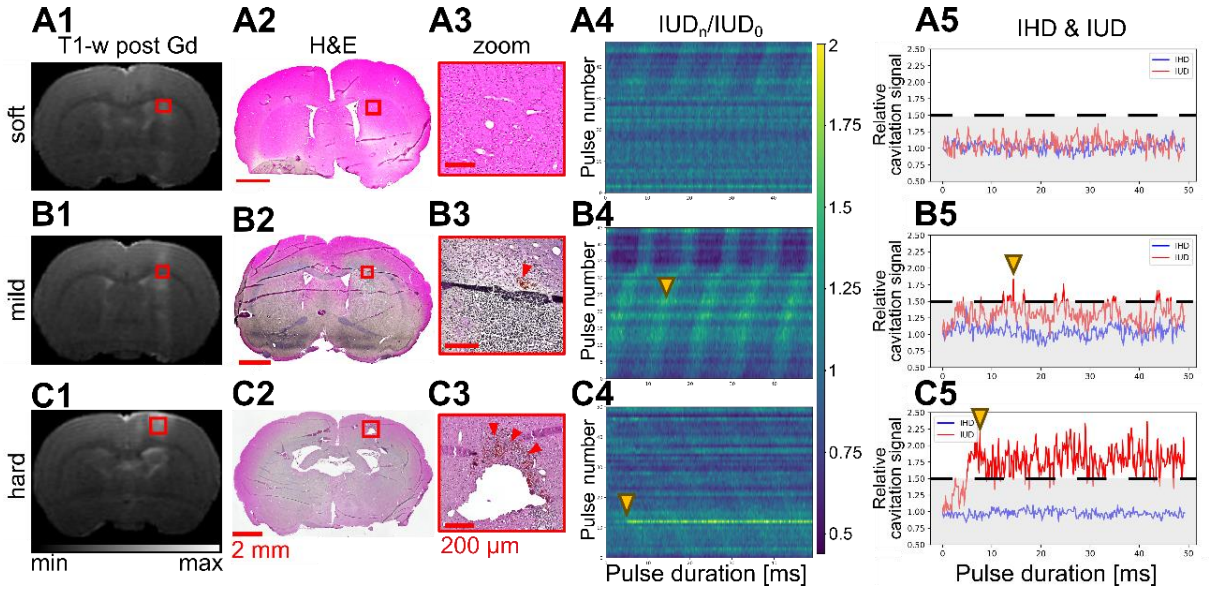


*Figure 48. Representative examples of soft (row **A**), mild (row **B**), and hard (row **C**) BBB opening with the MRI T2-w image (**A1**-**C1**), micrograph of H&E staining (**A2**-**C2**), and a zoom on the treated area (**A3**-**C3**). Associated evolution of relative IUD over the 50 ms ultrasound pulses for each pulse of the sequence (**A4**-**C4**) and the evolution of IUD and IHD for a single pulse (**A5**-**C5**) extracted from column 4.*

When analysing the other subjects, we observed more events exceeding the inertial threshold (Figure 48.B.4-5). This increase was associated with an increase in the number of total and consecutive inertial events, reaching respectively almost 6.3% and 6%. In the permeabilised BBB region (Figure 48.B.1), a few erythrocyte extravasations were visible on H&E (Figure 48.B.2-3). We noted that for the soft and

mild cases the average cavitation signal did not exceed the inertial threshold (in annexe A.3, Figure 82).

Only one animal was excluded from the mild group because of too many erythrocytes present on the H&E staining (Figure 48.C.2-3). We classified this subject as hard and it was excluded from the rest of the study. It was characterised by a sudden bump at the beginning of the FUS sequence (Figure 48.C.4-5) that exceeded the inertial threshold (beginning highlighted with yellow arrow in Figure 48.C.4-5) and remained above the threshold until the end of the pulse. On average, for the whole duration of the pulse, the cavitation signal remained above the threshold (in annexe A.3, Figure 82.C2). Note that this behaviour was measured in one subject only, as our study did not aim to evaluate critical cavitation situation. This observation implies the beginning of a haemorrhage and therefore a change in the concentration of the MB, as evidenced by the decrease in cavitation signal for the following pulses. The T1-w image (Figure 48.C.1) showed a large extravasation of Gd-DOTA as well as several red blood cells (Figure 48.C.2-3). We counted more than 100 red blood cells sites (in annexe A.3, Figure 83).

5.1.3. Characterisation of hypoperfusion after BBB opening in the striatum and in the cortex

To determine the effect of FUS combined with MB on CBF, pCASL datasets were acquired 30 min after delivering the treatment. FUS targeted the striatum in one group and the cortex in the other, with precise targeting achieved through MRI guidance.

When the right cortex was targeted (Figure 49.A), we observed a large decrease in perfusion in the treated cortex. FUS-induced BBB opening led to a decrease in perfusion that extended beyond the treated area. After 30 min, the CBF in the treated cortex decreased by 54%. An average CBF of 42.24 ± 13.8 mL/min/100g (n = 7) was measured in the ipsilateral cortex compared to 93.57 ± 30.5 mL/min/100g in the contralateral one (Figure 49.B), showing a significant difference between both regions (p = 0.0156). After 24 hours, there was no significant difference in CBF between the ipsilateral and contralateral cortices.

When targeting the striatum (Figure 49.C), we observed a decrease in CBF values at the targeted location and even beyond, according to the anterior CBF maps shown. The quantifications in Figure 49.D show a 38% reduction in perfusion in the targeted striatum compared to the contralateral striatum 30 min after BBB opening. The difference between the two striatum is significant (p = 0.0313), with a mean CBF of 50.68 ± 10.8 mL/min/100g in the ipsilateral striatum and 81.21 ± 27.5 mL/min/100g in the contralateral striatum. In this case, the decrease in perfusion seems to be limited to the single target region, as no decrease in perfusion was observed in the cortex. After 24 h, the difference between the two striatum is no longer significant.

Figure 50 shows the time course of CBF. There is a significant difference between the two cortices at 30 min (p = 0.0010) and 60 min (p = 0.0273) after FUS. At 90 min post-FUS, the difference is no longer significant (p = 0.0547, CBF_{ipsi} = 117.2 ± 44.9 and CBF_{contra} = 164.2 ± 36.2 mL/min/100g). After 24 h, CBF returns to baseline values, showing no significant differences between the two cortices, consistent with observations 24 h post-FUS in group 1. For comparison, values from the literature ([Debacker, 2014; Esparza-Coss *et al.*, 2010; Ewing *et al.*, 2003; Kim and Kim, 2005; Tanaka *et al.*, 2011; Wegener *et al.*, 2007]) obtained in the brains of rats anaesthetised with isoflurane (n = 8) are shown in Figure 50. There is no significant difference between our data and those from the literature at 24 h. The

reduction in CBF in the targeted cortex is transient, as it takes 90 min after BBB opening for differences between the two cortices to become non-significant following the initial significant decrease.

ADC maps acquired 30 min and 24 h after BBB opening could provide insight into a possible oedema resulting from the FUS procedure (in annexe A.3, Figure 84). No significant difference was measured in either the cortex or the striatum at either time point. The slight increase measured at 24 h is related to the repeatability measurement, as the increase is global and not attributable to the spread of oedema throughout the brain.

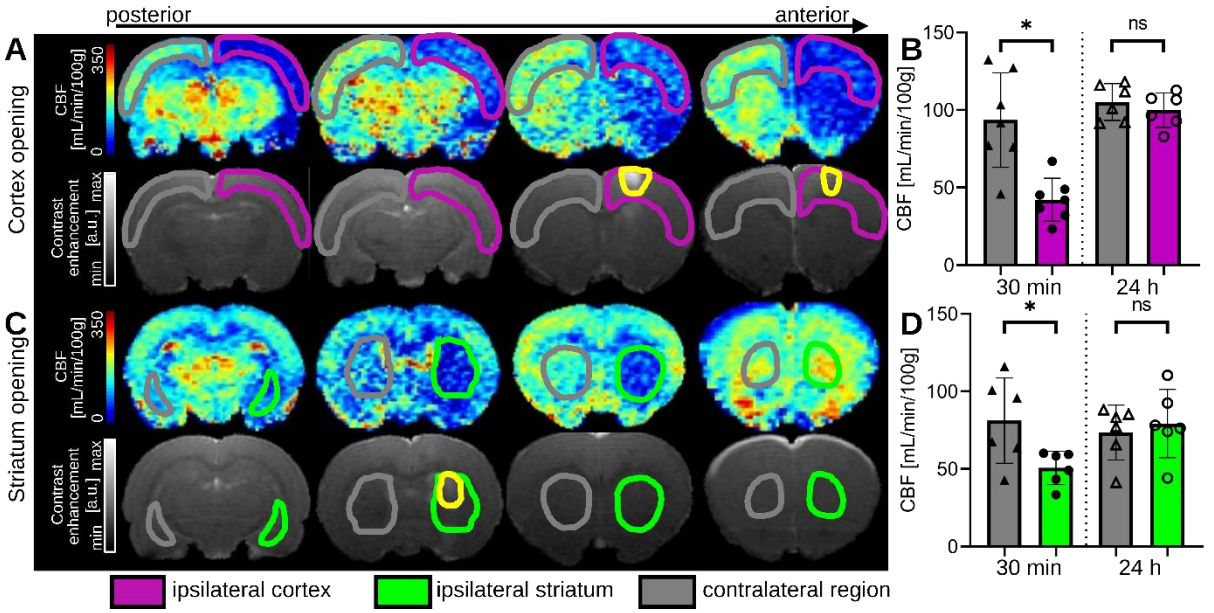


*Figure 49. Examples of CBF maps 30 min after BBB opening and corresponding T1-w images after Gd-DOTA injection for cortex (**A**) and striatum (**C**) permeabilisation. The area with opened BBB is outlined in yellow. CBF 30 min and 24 hours after FUS in cortex (**B**) and striatum (**D**). The data were analysed using a two-tailed non-parametric test (Wilcoxon) (*p < 0.05; **p < 0.01; ***p < 0.001; ns, non-significant). The results are expressed as mean ± S.D.*

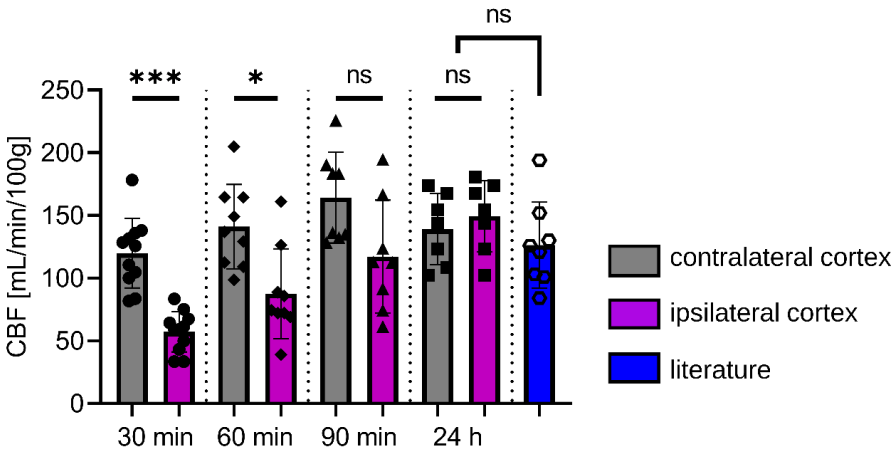


*Figure 50. CBF in ipsi- and contralateral cortices as a function of time following the opening of the BBB. Values from the literature, obtained under experimental conditions similar to ours but without FUS, represent the normal CBF values (blue). The data were analysed using a two-tailed non-parametric test (*p < 0.05; **p < 0.01; ***p < 0.001; ns, non-significant). The results are expressed as mean ± S.D.*

5.1.4. Assessment of BVf 30 minutes after BBB disruption

The measurements of BVf in the cortex targeted by FUS (ipsilateral) and in the contralateral cortex were calculated from MGE images acquired before and after injection of USPIO nanoparticles [Troprès *et al.*, 2015]. The results, expressed as a percentage of blood occupying the voxel, are shown in Figure 51. Figure 51.A illustrates the reduction in BVf values in the targeted cortex extending beyond the open area (highlighted in yellow on the T1-w after Gd-DOTA injection). It should be noted that Gd-DOTA was injected after USPIO, and this does not prevent the observation of contrast enhancement of Gd-DOTA on T1-w images [Beaumont *et al.*, 2009]. A significant reduction in BVf was measured ($p = 0.0313$). The average reduction in BVf was 13% (3.9 ± 1.3% in the contralateral cortex and 3.4 ± 1.2% in the ipsilateral cortex) (Figure 51.B). To evaluate the response in the striatum, a further set of three animals was employed (Figure 51.C). No significant difference was observed when the BBB was opened in the striatum, with an average BVf of 3.18 ± 0.2% in the ipsilateral striatum and 3.73 ± 0.2 % in the contralateral striatum (Figure 51.D). Consequently, the BVf was found to be reduced by 15% in the ipsilateral region, thereby confirming vasoconstriction across the entire area.

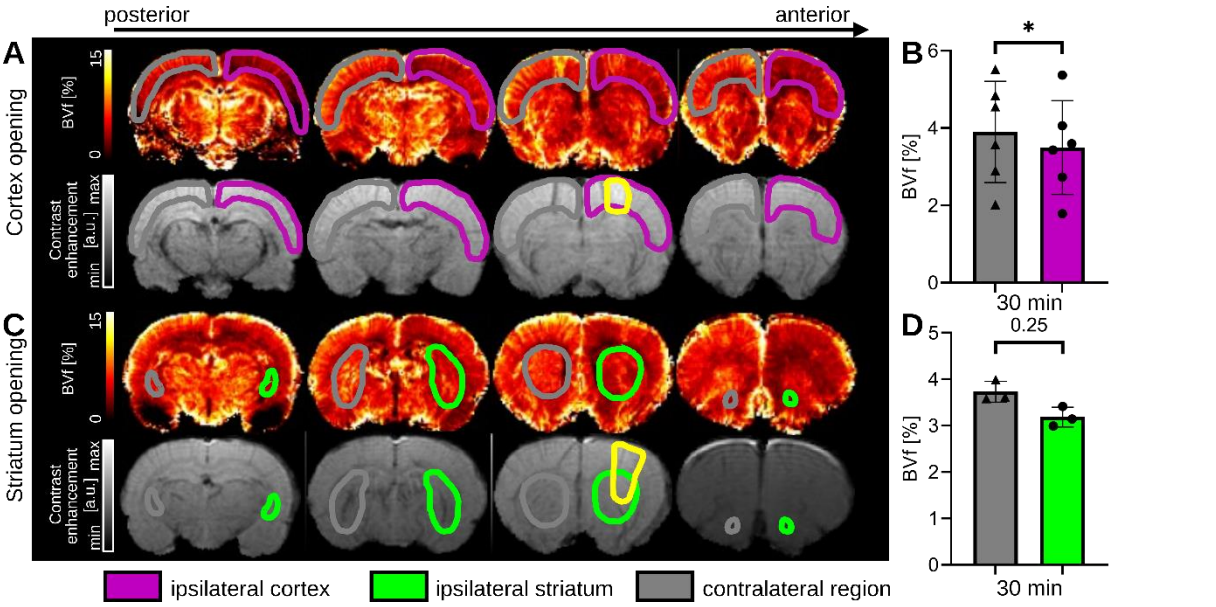


*Figure 51. Examples of BVf maps 30 min after BBB opening in the cortex (**A**) and in the striatum (**C**), together with associated T1-w images following Gd-DOTA injection. The BBB-opened area is delineated in yellow. BVf was quantified 30 min after FUS in the cortex (**B**) and in the striatum (**D**). The data were analysed using a two-tailed non-parametric test (Wilcoxon) (*p < 0.05). The results are expressed as mean ± S.D.*

5.1.5. Cellular impact of the procedure: evaluation of neuroinflammation markers

The expression of two neuroinflammation markers, GFAP and Iba1, was analysed to evaluate the brain tissue response to the FUS procedure and to investigate potential correlations with the measured haemodynamic changes. Additionally, vessels were stained with the SMI71 marker, and no differences were found 5 days after the FUS treatment. This suggests that 30 min following the measured vasoconstriction, the blood vessels returned to their original shape (in annexe A.3, Figure 85).

Figure 52, panel A, presents the evolution of the GFAP marker following BBB opening, while panel B presents the evolution of the Iba1 marker. ROIs were drawn at the location of the BBB opening, and measurements of the Iba1 and GFAP markers were pooled together, regardless of whether the cortex or the striatum were permeabilised. Additionally, the inflammation does not appear to depend on the location of the deposited FUS energy.

Following the FUS treatment, a large astrocytic activation was observed in the ipsilateral region (Figure 52.A.3) compared to the control region (Figure 52.A.2). This astrocytic activation was observed in the BBB-opened area, but not in the area with reduced CBF (not shown). The mean fluorescence intensity was not significantly different between the contralateral and the ipsilateral regions (Figure 52.A.4). However, the relative area occupation was significantly increased in the ipsilateral region two days ($p<0.001$) and three days ($p<0.05$) after the treatment (Figure 52.A.5). Astrocytic activation tends to return to baseline levels one week after the FUS-induced BBB opening.

Figure 52.B.2 and B.3 illustrate a change in microglia shape between the ipsilateral and contralateral regions. In Figure 52.B.2, the microglia exhibit a ramified shape indicated by the blue arrows. In contrast, the ipsilateral region displays a rounded shape, as highlighted by the red arrows in Figure 52.B.3. The mean fluorescence intensity and relative area occupation of segmented pixels were quantified by image processing in the ipsilateral region compared to the contralateral. A significant increase in the ipsilateral region was observed one day after the BBB opening, with a subsequent decrease on the second- and third-days post-treatment (Figure 52.B.4). Similarly, an increase in the relative area occupation of microglia was significant on the first day after the BBB opening, with a subsequent decrease in the following days (Figure 52.B.5).

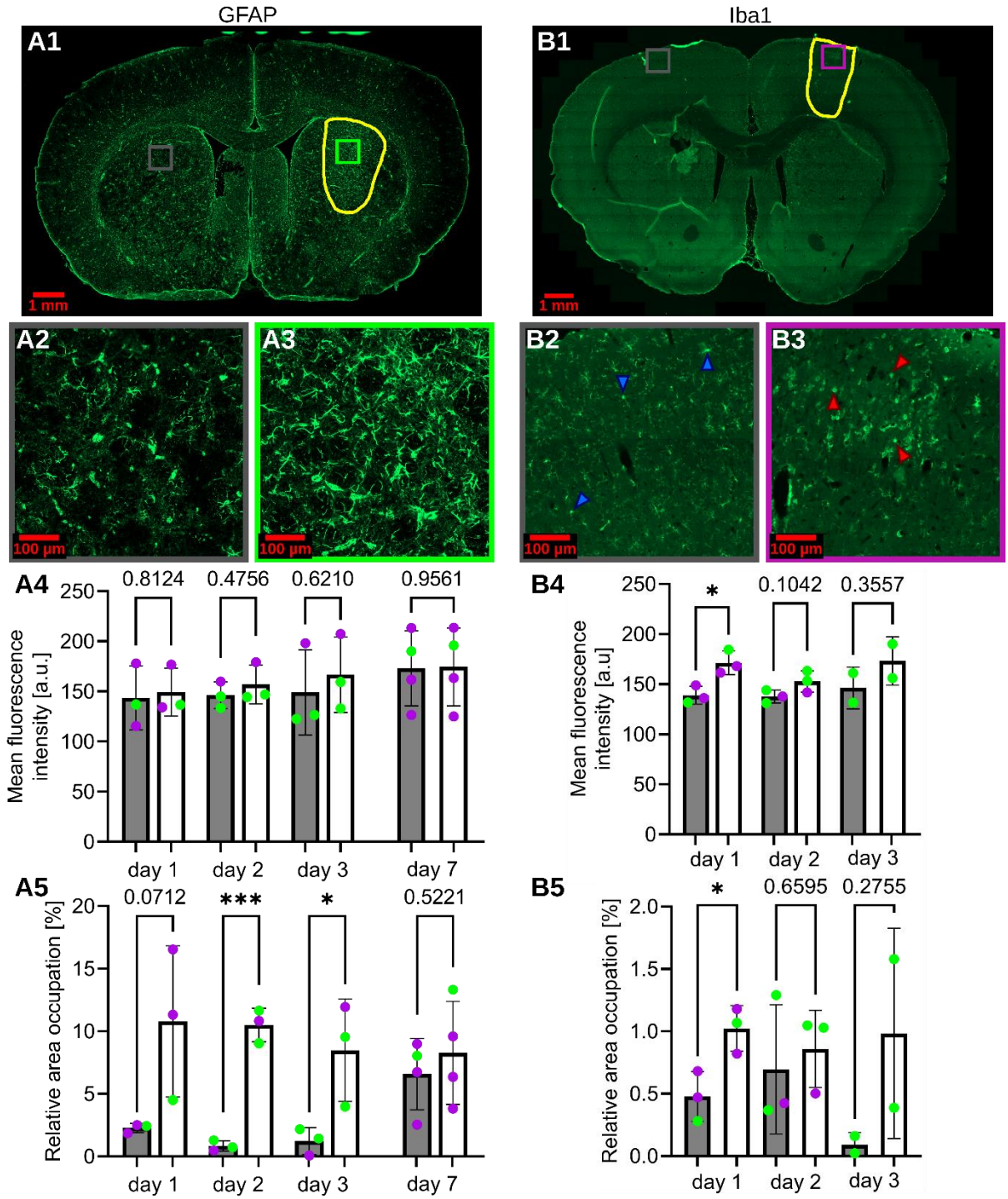


*Figure 52. Activation of astrocytes (**A1**) and microglia (**B1**), respectively, 3 days and 1 day after FUS-induced BBB opening. The BBB-opened area is delineated in yellow. Amplified images of the contralateral (grey square) and ipsilateral (purple for cortex, green for striatum) regions (**A2-3**, **B2-3**) are also shown. The blue (**B2**) and red (**B3**) arrows highlight microglia cells in their typical basal state (**B2**) and in an activated state (**B3**). The evolution over days after BBB opening of the mean fluorescence intensity of GFAP (**A4**) and Iba1 (**B4**) and of the relative area occupation of GFAP (**A5**) and Iba1 (**B5**) is also shown. For every bar plot, each point represents the value averaged on at least three slices per subject. The green dots represent animals that received the treatment in the striatum, while the purple dots represent those who received a cortical treatment. A two-tailed unpaired test was performed on the data (*p < 0.05, **p < 0.01, ***p < 0.001). The results are expressed as mean ± S.D.*

5.2. Discussion

Understanding the side effects associated with FUS-mediated BBB opening is crucial for developing effective therapeutic strategies that rely on localised drug delivery to the brain. In our study, we observed that, despite the absence of tissue damage, both blood flow and the blood volume were significantly reduced for at least one hour in an extended region surrounding the BBB opening area. While perfusion normalised within 24 h post-FUS, transient inflammation persisted for several days in the targeted tissue. Additionally, we introduced a method for monitoring the MB cavitation status during FUS treatment, enhancing the robustness of our experiments.

The BBB opening was performed with real-time cavitation monitoring and homemade lipidic MB. We chose an experimental setup with MB and a mechanical index similar to those used in previous studies [Chu *et al.*, 2016; Wu *et al.*, 2018], and all procedures resulted in BBB opening. The mechanical index (PNP divided by the square root of the acoustic frequency) was 0.5 in this study. According to Chu *et al*. [Chu *et al.*, 2016], this confirmed the safety of the FUS procedure. Indeed, with this setup, 95% of the BBB opening procedures resulted in neither oedema nor bleeding, as assessed by MRI. It is noteworthy that the quantification of inertial cavitation events using IUD enabled the differentiation between animals that underwent excessive FUS treatment and developed lesions and those that did not. While this was not the primary objective of the study, these findings are encouraging and warrant further investigation, particularly with a larger number of animals to demonstrate the full potential of this approach. A specific study of critical cavitation situations could confirm and improve the control of this behaviour as well as our understanding. Additionally, future developments should include closed-loop cavitation control to prevent lesions. Consequently, the safety of the BBB opening procedure could be enhanced, thereby improving animal outcomes [Kamimura *et al.*, 2019].

Brain perfusion was measured between 30 min and 24 h after FUS treatment. While the CBF in the contralateral hemisphere was normal and comparable to previous literature reports [Debacker, 2014; Esparza-Coss *et al.*, 2010; Ewing *et al.*, 2003; Kim and Kim, 2005; Tanaka *et al.*, 2011; Wegener *et al.*, 2007], the CBF in the hemisphere exposed to FUS experienced a 38% reduction within 30 min after FUS treatment. This reduction was lower than that observed in a stroke model, where a reduction of approximately 70% has been reported [Boisserand *et al.*, 2017]. The magnitude of the CBF reduction observed after FUS treatment is consistent with the observation that no change in ADC was observed, which typically occurs in stroke models with larger CBF reduction [Boisserand *et al.*, 2017]. Such a reduction has previously been reported by Todd *et al*. [Todd *et al.*, 2019] between one and two hours after FUS treatment. Over time, CBF in our study recovered. At 90 min after FUS treatment, the difference was no longer significant, possibly due to a small number of animals. At 24 h, no difference could be observed.

To further understand the origin of this CBF reduction, we also measured BVf 30 min after FUS. BVf was reduced by only 15% compared to 50% in the stroke model. A reduction in vessel diameter after FUS, in line with a reduction in BVf, has previously been observed using intravital microscopy [Raymond *et al.*, 2007]. A larger reduction in blood flow than in blood volume may be explained by a reduction in the flow entering the observed area. Interestingly, the reduction in CBF and BVf maps were spatially homogeneous, suggesting that all vessels in the area underwent vasoconstriction, which might have been more pronounced at the level of larger feeding arteries. Moreover, the area in which perfusion parameters were reduced extended beyond the FUS target, as evidenced by the extravasation of the

contrast agent. This occurred when the target was in the cortex (the entire cortex exhibited reduced perfusion) and when it was in the striatum (the entire striatum became hypoperfused). This spatial mismatch between the extension of the ultrasound target and that of the perfusion reduction has been previously reported in the literature, without the use of a focused transducer or cavitation monitoring [Labriji *et al.*, 2023].

The origin of this discrepancy could be attributed to retroactive vasoconstriction, based on the retroactive vasodilation mechanism described by Schaeffer and Iadecola [Schaeffer and Iadecola, 2021]. An alternative mechanism could be the slow propagating cortical spreading depressions described by Leaõ [Leao, 1944], which have been reported after traumatic brain injury (TBI) [Strong *et al.*, 2002] and stroke [Hartings *et al.*, 2011; Hossmann, 1996]. Altogether, it can be stated that, even in the absence of MB cavitation and the use of a focused transducer, a transient reduction in perfusion occurs and extends beyond the FUS target. This reduction does not lead to tissue oedema, as monitored using ADC. Further experiments, such as transcranial ultrasound localisation microscopy [Errico *et al.*, 2015] or cortical electrical activity recording [Masvidal-Codina *et al.*, 2019] could be performed to further characterise the reduction in brain perfusion that occurs after FUS.

At the cellular level, some changes occurred during the first three days after FUS. We quantified the peak of astrocytic activation at day three post-BBB opening, a result very similar to that reported by Jordão *et al*. [Jordão *et al.*, 2013]. Moreover, a significant increase in microglia recruitment was observed, suggesting that the neuroprotective role of the CNS was triggered. The activation peak was observed at day one after FUS. In contrast, several studies reviewed by Todd *et al*. [Todd *et al.*, 2020] reported activations at 1, 6 and 24 h post-BBB opening. Both astrocytes and microglia returned to normal levels one week after FUS. It is noteworthy that this neuroinflammation was observed only in the FUS target and was not observed in the extended area where perfusion was reduced. This suggests that inflammation is triggered by the BBB opening. However, it cannot be excluded that the perfusion reduction also contributes to this effect.

When extrapolating our findings to humans, a key difference lies in the fact that our study was conducted under anaesthesia, which reduces the cerebral metabolic rate of oxygen [Schoknecht *et al.*, 2023]. Moreover, isoflurane anaesthesia tends to elevate CBF. Considering that a decrease in oxygen demand and an increase in oxygen supply may confer some degree of protection against reduced perfusion, our study might underestimate the consequences of the FUS-induced perfusion reduction. Conversely, it has been reported that FUS-mediated BBB opening transiently impedes axonal conduction, thereby lowering neuronal activity and potentially protecting the tissue against a perfusion decrease [Chu *et al.*, 2015]. Further investigations could involve awake animal studies or employ anaesthesia protocols that yield CBF values akin to those observed in the awakened state. Given the reduction in blood flow and the absence of blood vessel alteration (see annexe A.3, Figure 85), it would also be of interest to explore whether angiogenic processes are triggered, as suggested by Kovacs *et al*. [Kovacs *et al.*, 2017]. This could also imply an assessment of the expression of HIF-1a or VEGF, shortly after FUS.

In summary, FUS-mediated BBB opening induces diffuse vasoconstriction beyond the targeted area, resulting in a transient reduction in both CBF and BVf. However, this reduction is insufficient to cause tissue lesions in our experimental setup. While transient markers of tissue inflammation may be observed at the FUS-targeted area, they are not observed outside this area. These findings emphasise

the need of caution regarding tissue perfusion when considering the translation of FUS-mediated BBB opening to human applications.

5.3. Acknowledgments

We thank Nora Collomb for her assistance during the in vivo experiments and Qendresa Arifi for realising part of the histological staining. Grenoble MRI facility IRMaGe is partly funded by the French program Investissement d'avenir run by the Agence Nationale de la Recherche (grants ANR-11-INBS-0006 and ANR21-CE18-0019), C-VALO (FUSBRAIN project). Part of the FUS equipment was sponsored by the Fédération pour la Recherche sur le Cerveau (FRC) and the Autun Rotary.

5.4. Competing interests

E. D. owns Image Guided Therapy and S. R. is an employee of Image Guided Therapy (CIFRE stipend to S.R.). No potential conflicts of interest were disclosed by the other authors.

Chapter 6. Study 2: Longitudinal MR vascular fingerprinting approach tracking physiological changes during repeated MR guided focused ultrasound mediated BBB opening on rats.

This study was designed by Dr Vasile Stupar and Dr Emmanuel L. Barbier. The MRI protocol was kindly provided by Dr Benjamin Lemasson and Dr Thomas Christen, which is a protocol developed in the laboratory through the years and parts were already used in various published studies [Boux *et al.*, 2021b; Clément *et al.*, 2021]. I performed the experiments during the 2nd year and the beginning of the 3rd year of my thesis. For MRI data analysis, I performed the analysis, Dr Aurélien Delphin provided to me the algorithm to reconstruct with the fingerprint approach the quantitative maps and Lucie Chalet processed the data to extract the QSM maps as well as the different magnetic contribution maps. I prepared the immunohistological sections, stained the tissues and analysed the micrographs. Some of the microtome sectioning and immunohistological staining was done by two interns I supervised: Qendresa Arifi and Thaïs La Rocca. The first results of this study were presented at the EMIM [Rigollet *et al.*, 2024b] and at the ISMRM 2024 [Rigollet *et al.*, 2024a].

In the study presented in the **Error! Reference source not found.**, we showed that single FUS treatment r esulted in transient and significant perfusion changes with a transient neuroinflammatory process involving activation of astrocytes and microglia. These transient changes did not show any secondary adverse effects in the brain or in the general behaviour of the animals. More recently, repeated application of FUS to the brain have shown promising results in preclinical and clinical studies. For example, Aryal *et al*. demonstrated improved therapeutic outcomes in a 9L rat tumour model through the enhanced delivery of liposomal doxorubicin following multiple FUS treatments [Aryal *et al*., 2013]. In addition, McDannold *et al*. demonstrated improved mean survival time and reduced tumour progression in an F98 rat glioma model after two successive applications of MR-guided FUS and the delivery of carboplatin intravenously [McDannold *et al*., 2019]. These studies highlighted the potential of repeated BBB opening to improve efficacy treatments in brain tumours. Plus, different studies demonstrated the feasibility of the procedure in Alzheimer's disease (AD) mice models [Karakatsani *et al*., 2019; Leinenga and Götz, 2015; Shen *et al*., 2020] with improve in memory and clearance of amyloid-β plaques. These studies enabled the transfer to clinics of these repeated FUS treatment schedules in AD patients [Epelbaum *et al*., 2022; Sonabend *et al*., 2023] and in glioblastoma patients [Carpentier *et al*., 2024; Idbaih *et al*., 2019]. Outcome from latter studies have reporting noting improvements in drug delivery and tumour response with a reduction in tumour growth.

However, as a single application of FUS, the repeated use of FUS to disrupt the BBB is associated with secondary mechanisms and potential side effects. The mechanical stress and subsequent BBB disruption can trigger a cascade of biological responses within the NVU, including reparative mechanisms, inflammation and vascular modifications and were developed in the section 2.6 of Chapter 2.

Recent studies have begun to delve deeper into these bioeffects by investigating the cumulative effects on brain tissue and neurovascular health [Kovacs *et al*., 2018; Sinharay *et al*., 2019], with the

investigation of neuroinflammation associated with the treatment schedule of weekly FUS sessions. In addition, Olumolade *et al*. analysed the potential behavioural changes that could occur in relation to the repetition of the BBB and found no adverse effects on the locomotor activity of the treated animals [Olumolade *et al*., 2016]. These recent studies were limited in three main ways: firstly, the pressures used in the studies by Kovacs *et al*. and Sinharay *et al*. studies do not seem to be very suitable for treatment planning due to the large area of hypointensities visible on MRI images; secondly, the time point at which histological staining and imaging were performed provides little explanation and the comparisons are complicated, making it difficult to compare with other studies; and finally, Olumolade *et al*. administered FUS on a bi-weekly or monthly basis, which seems to be the right timing for clinical applications [Carpentier *et al*., 2024; Epelbaum *et al*., 2022; Idbaih *et al*., 2019; Sonabend *et al*., 2023], but in terms of preclinical models, it may be too long given the spread of certain disease models (for example, median survival in the F98 rat glioblastoma model is around 20 to 30 days after implantation, compared to 15 months in humans), so we need to investigate the use of more condensed schedules.

Thus, the underlying mechanisms of repeated BBB opening are not fully understood, as there is very little literature on the subject, and the long-term effects of this new therapy remain a subject of ongoing research, particularly with regard to the microvasculature of the brain, which has not yet been studied.

Based on this literature, we hypothesised that repeated FUS-mediated BBB opening could lead to significant changes in different systems, such as the microvascular system and the mild neuroinflammation repair system.

To address these gaps, in this study we propose to longitudinally evaluate the effects of repeated FUS-induced BBB opening on the brain vasculature of healthy rats. BBB permeabilisation was performed using FUS parameters known to be safe [Chu *et al*., 2016] and to efficiently deliver therapeutic agents as aducanumab, carboplatin or flexibility-tunable polymers encapsulating camptothecin and doxorubicin [Kong *et al*., 2022; McDannold *et al*., 2019; Sun *et al*., 2023]. FUS treatments were administered either once, once weekly or twice weekly for four weeks. Two different pressures were used to assess the effects of increasing acoustic pressure on the microvascular system. We used MRI to measure brain perfusion, water diffusion with the ADC parameter, BBB permeability and an MRI fingerprinting approach to quantitatively assess mean vessel radius, oxygen saturation and volume fraction in the rat brain. After the final MR-guided FUS treatment, brains were analysed to assess cellular effects with markers of the blood-brain barrier and surrounding cells.

6.1. Methods

6.1.1. Animal care and preparation

71 male Wistar Han rats (6 weeks old and a mean across all animals of 305 ± 35 g at the beginning of the experiments) were used in this study. Every procedure was validated by the local ethics committee and the French ministry of Education and Research with the APAFIS number #43777. Animals were induced with a mixture of air, oxygen (80% / 20%) and isoflurane (4%) and maintained for the rest of the procedure between 1.5 - 2.5% of isoflurane. Hair on the head was removed with a razor and depilatory cream to ensure proper coupling of the ultrasound beam. A catheter was inserted into the tail vein to collect blood samples before the first FUS treatment and left for the subsequent injections of MB and MRI CA. After each FUS treatment and MRI session, animals were closely monitored until

they regained full consciousness. Animals were monitored for weight and general behaviour throughout the entire duration of the experiments. We distinguished 3 main groups, the first receiving a single FUS treatment, the second 4 FUS treatments over 4 weeks and the third 8 FUS treatments over 4 weeks. A recapitulation of the groups is displayed in Table 12.

Group	*in situ* PNP	histology time point	number of animals	Weight [g]
1-FUS	440 kPa	3 h post-FUS	4	387 ± 17
	440 kPa	24 h post-FUS	4	405 ± 13
	440 kPa	1-week post-FUS	4	227 ± 13
	390 kPa	4 weeks post-FUS	6	342 ± 9
	440 kPa	4 weeks post-FUS	4	328 ± 5
4-FUS	390 kPa	1-week post-FUS	7	286 ± 49
	440 kPa	1-week post-FUS	7	299 ± 30
8-FUS	390 kPa	1-week post-FUS	7	318 ± 14
	440 kPa	1-week post-FUS	7	273 ± 22
		Total	50	

Table 12. Summary of the number of animals per group with the different histological analysis timepoints. Average weights are expressed as mean ± S.D.

6.1.2. Experimental protocol

BBB opening was achieved using the MR-guided FUS system described in 4.3 and the transducer described in 4.1 and lipidic MB composed of DSPC:DSPE-PEG2000 MB (see 4.2) and the protocol was similar to that described in section 4.4. Continuous ultrasound waves were delivered during the displacement of the transducer that followed a raster scan of 4 by 3.2 mm targeting the striatum and the hippocampus, two subcortical regions as in Figure 53. We permeabilised the BBB at two different pressures known to be safe and able to deliver therapeutic molecules [Chevaleyre *et al.*, 2023; Dréan *et al.*, 2019; McDannold *et al.*, 2019]: 390 kPa and 440 kPa *in situ*, equivalent to mechanical index (MI) of 0.32 and 0.36. The pressure was adapted for each treatment according to the positioning of the animal and its body weight to deliver the pressure targeted.

After the application of FUS, the MR-guided FUS device was removed from the MRI tunnel and classical MRI coils were installed. The animal was re-placed into the MRI approximately 5 min post-FUS. The multiparametric MRI protocol described in 4.5.4 was acquired with injections of USPIO and Gd-DOTA, using the preclinical 4.7 T scanner at the IRMaGe facility. This multiparametric MRI protocol was acquired for the 1-FUS group in 14 animals at 1- and 4-weeks timepoints. For the 4-FUS group, it was acquired after each FUS treatment. For the 8-FUS group it was acquired after FUS treatments 2, 4, 6 and 8, a shorter protocol with acquisition of anatomical T2-w, DTI and the DCE sequences was acquired to reduce as much as possible the effects of anaesthesia and to limit the number of USPIO.

After the different FUS treatments and MRI sessions, brains were harvested, frozen, sliced and stained with H&E, GFAP, SMA and SMI71 antibodies. Then slices were digitised and analysed to quantify the differences across groups and brain regions. The complete description of the protocol used is in section 4.6.

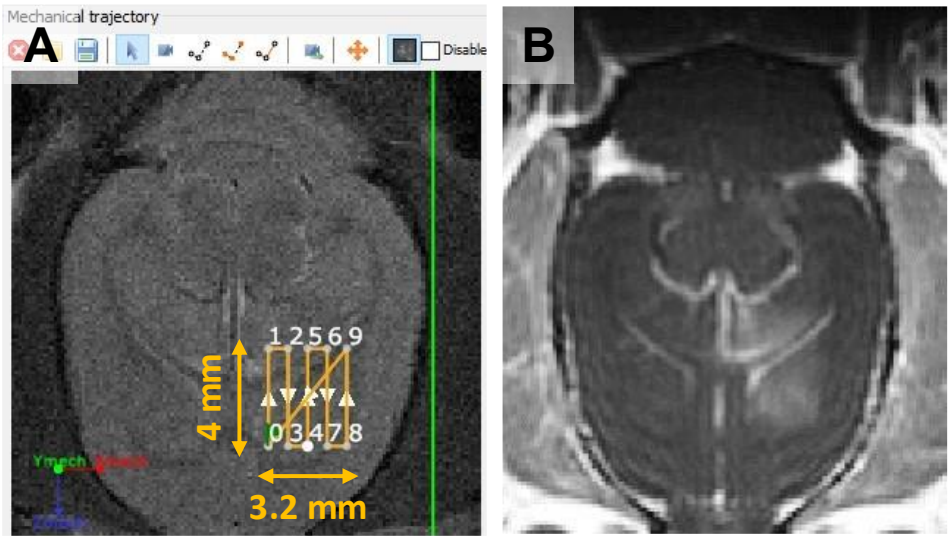


*Figure 53. Raster scan planned on the T2-w MRI in Thermoguide® software (**A**) and resulting T1-w image obtained at 4.7 T 2 min after Gd-DOTA injection and 70 min after FUS (**B**). One can notice the good agreement between the targeted and the BBB opened area.*

6.1.3. Image processing

All MRI images were analysed and processed using MP3 and Python (see 4.5). In case of multiple MRI sessions, images of each session were registered to the first MRI session to perform longitudinal analysis. The ipsilateral ROI was delineated manually based on the derived maps from DCE sequence that showed contrast enhancement, that is to say correspond to the permeabilised BBB. A contralateral ROI was delineated manually in the contralateral hemisphere with the aim of having the same shape and volume as much as possible. The aim of this study was to evaluate the impact on the BBB that was repeatedly permeabilised, to this purpose we extracted from the sessions the ipsilateral and contralateral ROI and intersectionned them. The intersection of all ROI in ipsilateral and contralateral regions is the one analysed in the whole study and referred to as ipsilateral and contralateral.

6.2. Results

6.2.1. General observations

During the whole procedure, animals were monitored weekly for any behaviour that may suggest suffering. We did not see any change in food intake, general behaviour and weight gain. Animal behaviour and weight was followed weekly using a behaviour score grid approved by the local ethical committee to detect potential behaviour degradation. No visible harmful effects were noted during the whole experiment and every group gained weight normally (Figure 54). Animals that received a single treatment gained weight more rapidly compared to groups that received 4 or 8 treatments, still no significant difference could be observed between groups. Regarding the brain anatomy, we did not notice any evident changes except ventricular enlargements. These ventricular enlargements did not occur for all animals, and we did not see any significant differences across groups. The results are displayed in Figure 86.

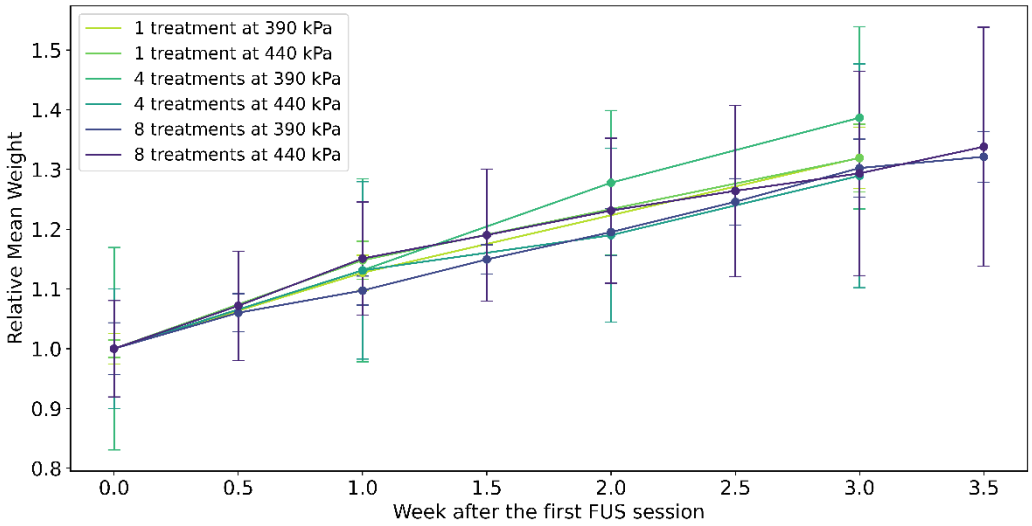


Figure 54. Relative mean weight evolutions of the different groups after the first FUS treatment. Results are expressed as the normalised to maximum mean ± S.D.

6.2.2. Repeatability and safety of the BBB opening

The BBB was successfully and repeatedly opened in all animals. We can see in Figure 55 that the procedure of MR-guided FUS was repeatable and enabled the permeabilisation of the BBB in the same tissue region. For the 4-FUS groups, the volume of the BBB permeabilised 4-times opening was 21 ± 17 mm^3 at 390 kPa and 30 ± 16 mm^3 at 440 kPa. For the 8-FUS groups, volumes permeabilised 8-times were equal to 23 ± 12 mm^3 at 390 kPa and 29 ± 12 mm^3 at 440 kPa. We did not measure any significant difference across groups and pressures (Figure 55). Figure 56 shows the CE and the TTP values derived from the DCE-MRI data. We can see that the CE was at least 1.5-fold between ipsilateral and contralateral regions, and we did not measure any significant differences between FUS treatments. Regarding TTP, we did not measure significant differences between the first and last treatment in 4-FUS groups, yet significant differences between the 1^{st} and 4^{th}, and between the 1^{st} and 8^{th} treatment were measured for the 8-FUS groups, suggesting a more permeable BBB when FUS are repeated more often. Indeed, a decrease in the TTP corresponds to a reduced time to reach the maximum CE intensity. Such reduction occurs with the blood flow increases and/or when the permeability of the vessel wall increases. As we have previously seen in Chapter 5 that FUS induces a transient reduction in blood flow, the increase in permeability appears as the most probable way to explain the observed reduction in TTP.

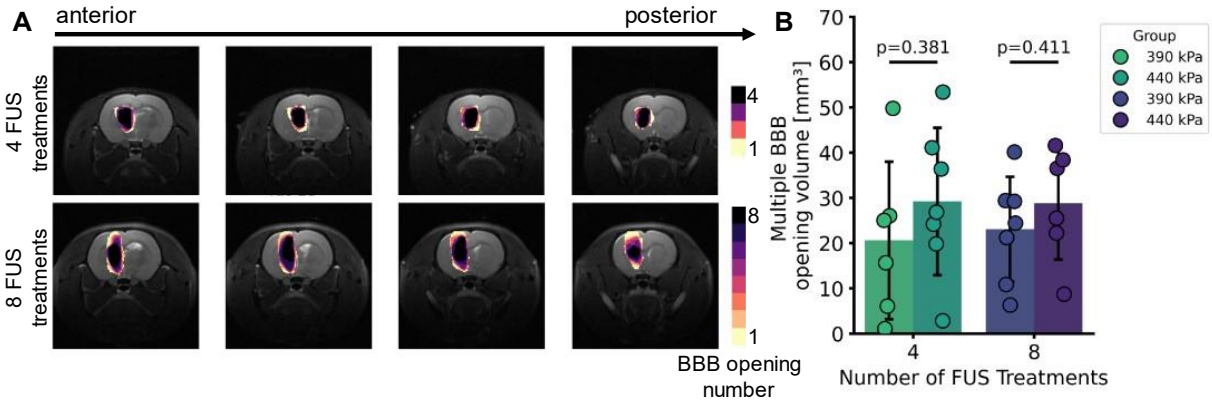


*Figure 55. **A**) Representative T2-w images covering the treated brain volume. The number of BBB openings of each pixel was colour coded: 1 to 4 for the 4-FUS group (top panel) and 1 to 8 for the 8-FUS group (bottom panel). For both groups, the black area corresponds to a BBB successfully open at each session. **B**) Volume of permeabilisation for 4-FUs and 8-FUS groups. The data were analysed using a two-sample t-test. The results are expressed as mean ± S.D.*

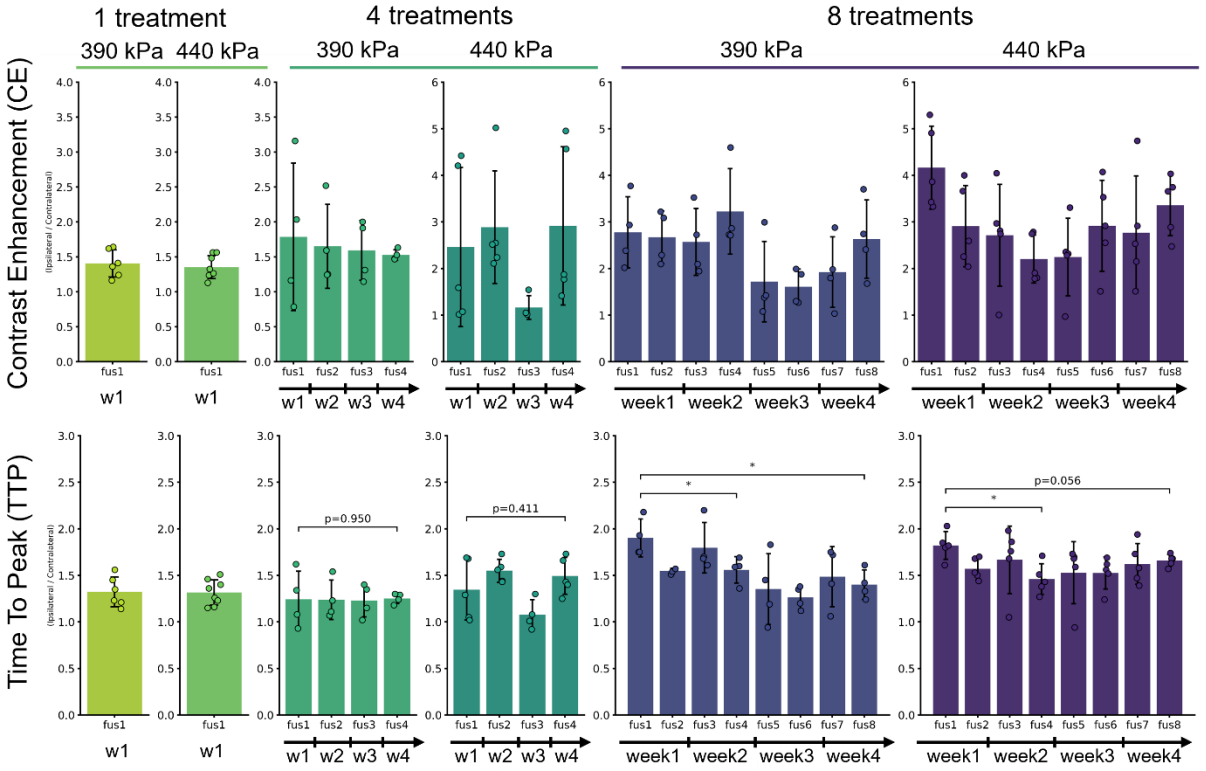


*Figure 56. Relative contrast enhancement (top panel) and time to peak (bottom panel) values for the different groups after the different FUS treatments. Paired t-test was performed between first and fourth treatment as well as first and 8th treatment. The data were analysed using a two-tailed parametric test (*p < 0.05). The results are expressed as the ratio between the ipsilateral and the contralateral regions (mean ± S.D.).*

Despite these modifications in BBB permeability, we did not see any hyper- or hypointense spots on T2-w images and T2* maps signifying we did not see any microhaemorrhages (Figure 57.A-B) or oedema (Figure 57.C). In addition, we did not observe oedema during the whole procedure and no significant difference was found between ipsilateral and contralateral regions in ADC maps (Figure 57.D).

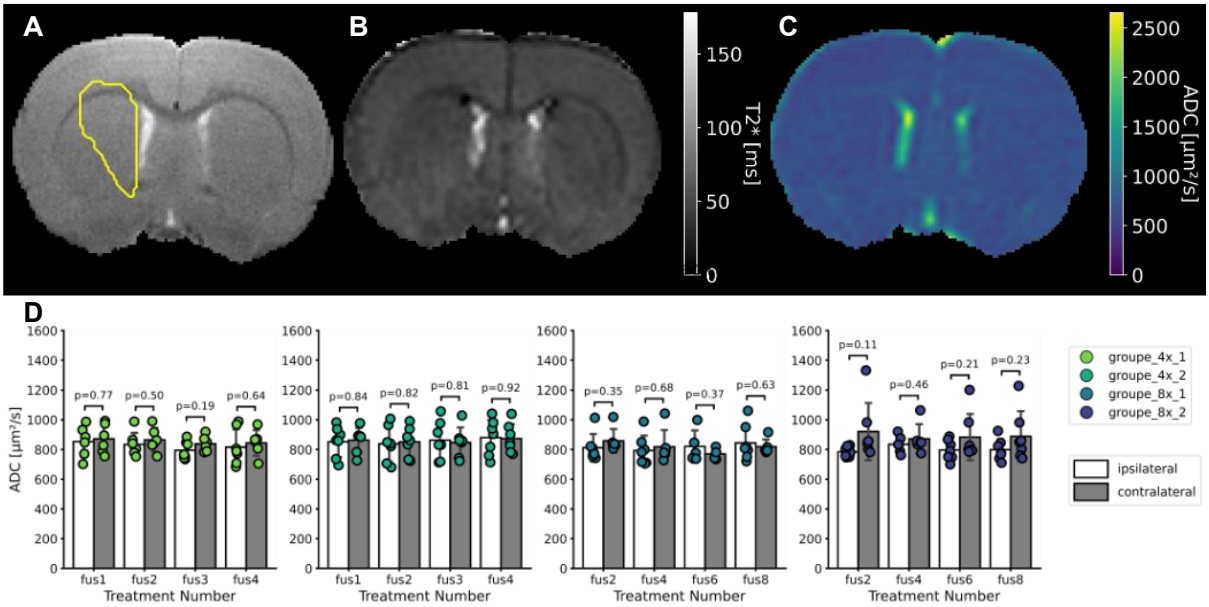


*Figure 57. Representative MRI T2-w (**A**), T2* (**B**) and ADC maps (**C**) images of an 8-FUS animal at 440 kPa after the last treatment, in yellow the BBB opening region opened 8 times. (**D**) ADC measured in the ipsilateral and contralateral regions for the 4 groups that received multiple treatments. The data were analysed using a two-sample t-test. The results are expressed as mean ± S.D.*

We stained the brains with H&E to seek for any potential microhaemorrhages, with particular attention at the level of the BBB permeabilisation. 3 h post-FUS for the highest pressure, we did not see any microhaemorrhages at the localisation of the opened BBB (Figure 58.D). The analysis of the H&E sections performed 1 week after the last treatment for the groups that received multiple treatments did not reveal any extravascular red blood cells at the site of the FUS deposition or in adjacent regions (Figure 59).

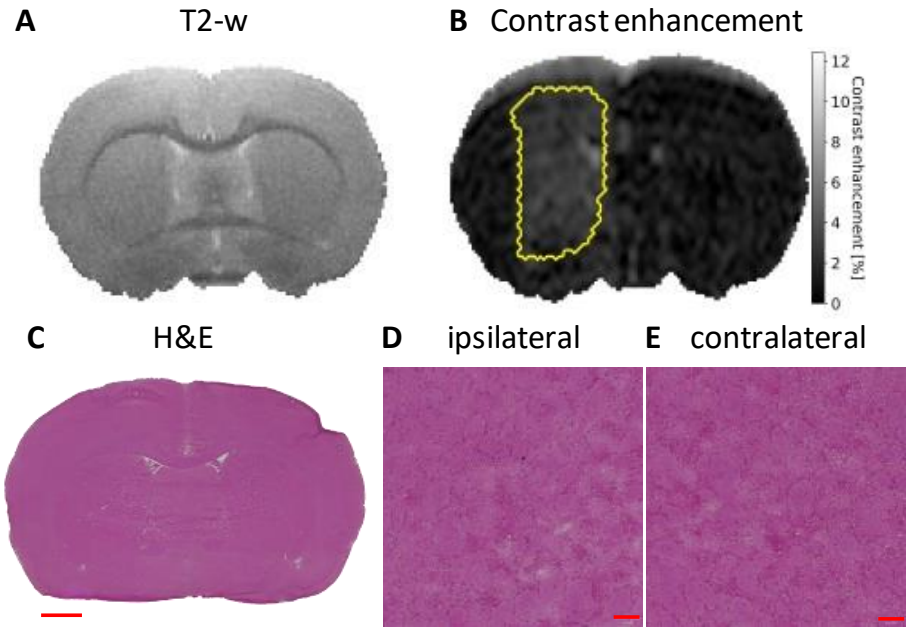


*Figure 58. Representative T2-w (**A**) and contrast enhancement (**B**) MRI images and H&E staining (**C, D, E**) from the brain harvested 3 h post-FUS for a rat sonicated at 440 kPa. The BBB opening region is highlighted in yellow. Bar sizes are equal to 800 µm (**C**) and 100 µm (**D, E**).*

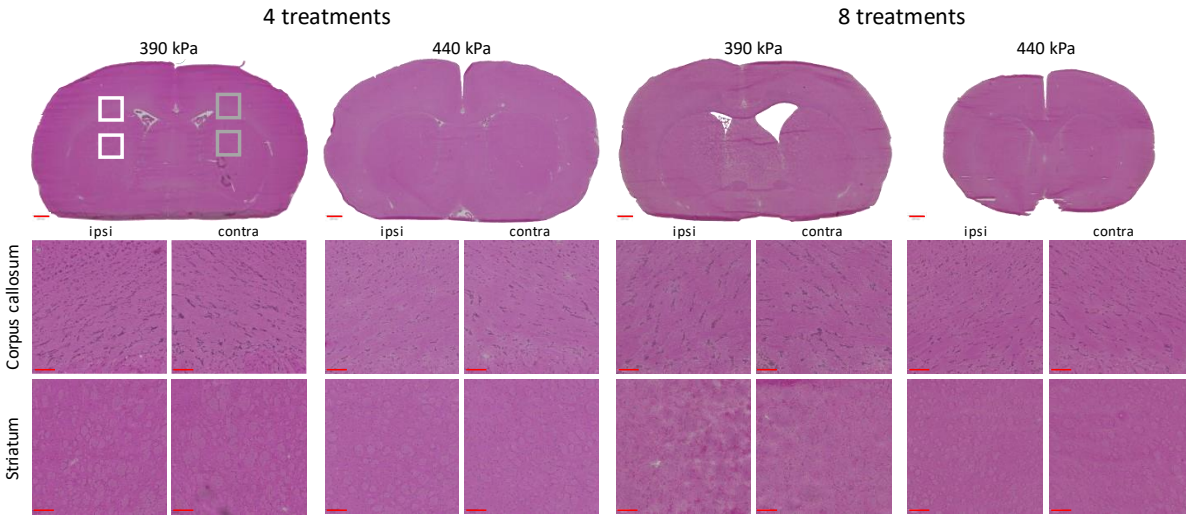


Figure 59. Representative micrographs of H&E for 4-FUS and 8-FUS groups in the top panel. Zooms in ipsilateral and contralateral regions at the level of the corpus callosum are displayed in the middle panel and striatum in the bottom panel)

6.2.3. Cerebral blood flow modifications

We measured a significant drop of perfusion in the ipsilateral region compared to the contralateral after a single BBB opening (Figure 60.A-B). A summary of mean CBF values is displayed in Table 13. We can see that no more difference is observed 4 weeks post-FUS.

	390 kPa		**440 kPa**	
	ipsilateral	contralateral	ipsilateral	contralateral
30 min post-FUS	64 ± 12	88 ± 18	65 ± 20	90 ± 21
4 weeks post-FUS	131 ± 25	130 ± 21	105 ± 5	100 ± 14

Table 13. CBF values after a single FUS treatment measured 30 min and 4 weeks post-FUS. CBF values are expressed as mean ± S.D. in mL/min/100g.

For the groups that received multiple FUS treatments, a significant drop in the ipsilateral region compared to contralateral was measured 30 min after the last FUS treatment in all groups. In 8-FUS groups, a significant drop was also measured after the 6th treatment. A significant drop was measured in 4-FUS groups after a single FUS session (Figure 60.C). We did not measure any longitudinal changes throughout the FUS treatments in the ipsilateral and contralateral regions.

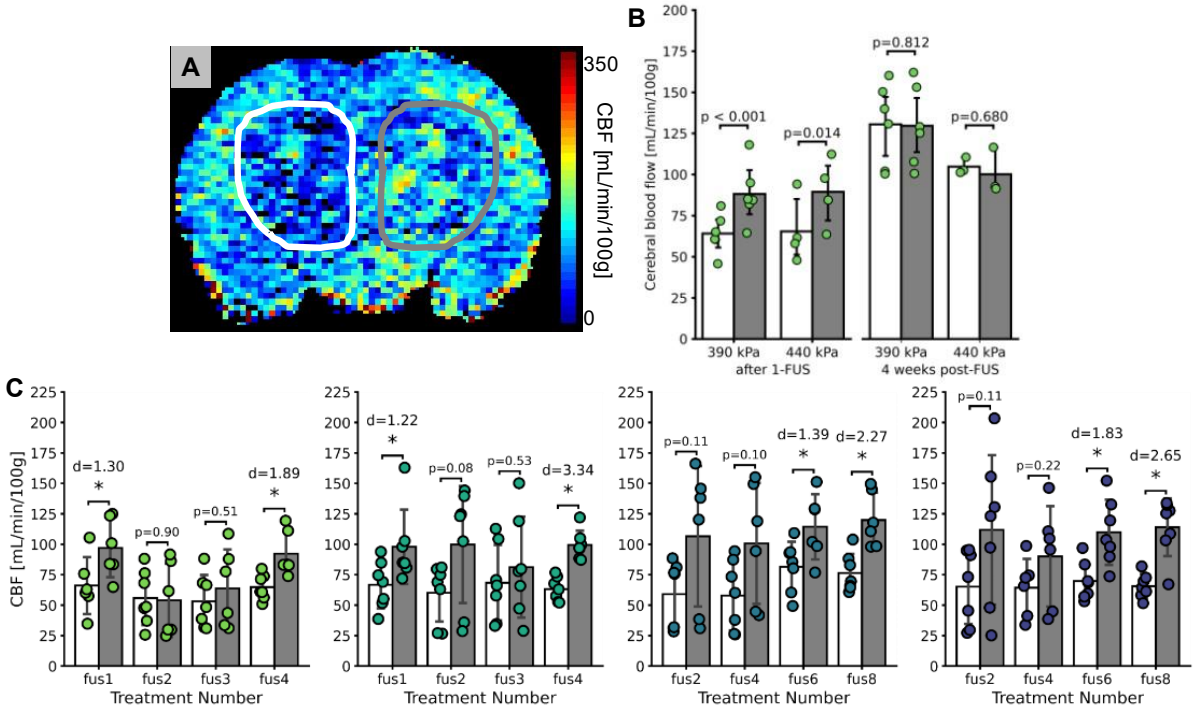


*Figure 60. Cerebral blood flow after repeated FUS. **A**) Representative example of a CBF map 30 min post-FUS with ipsilateral and contralateral regions drawn respectively in white and grey. **B**) Mean CBF 30 min and 4 weeks after single application of FUS. **C**) Mean CBF 30 min after successive applications of FUS. The data were analysed with a two-sample t-test between ipsilateral and contralateral regions (*p < 0.05). Effect size was computed with Cohen's d criteria. The results are expressed as mean ± S.D.*

6.2.4. MR vascular fingerprint maps

To estimate the mean vessel radius (R), the blood volume fraction (Vf) and the oxygen saturation of the tissues (SO_2), we matched the signals acquired before and after the injection of USPIOs with realistic simulated MR signals [Delphin *et al.*, 2024]. We observed significant increase in R in the ipsilateral region compared to contralateral after 1-FUS at 390 kPa and 2 and 6 FUS treatments at 440 kPa (Figure 61.A). We did not measure any significant differences of BVf between both hemispheres for all the groups and measured a significant decrease in SO_2 after 6 and 8 FUS treatments at 390 kPa (Figure 61.B-C). A summary of relative differences is available in Table 14. We can note that for R and Vf, the tendency is towards higher values in the ipsilateral regions. We can see the higher enhancement for the groups that received the strongest treatment (8-FUS at 440 kPa) and the smallest differences for the group that received 4-FUS treatments at 390 kPa. For the estimated SO_2, we can see a decrease in the ipsilateral region. Overall, small modifications were measured with two main effects perturbing the treated regions: the intensity of the acoustic energy deposited and the number of FUS treatments. The more intense is the treatment, the stronger are the modifications.

		4-FUS treatments		8-FUS treatments	
		390 kPa	440 kPa	390 kPa	440 kPa
Ipsi vs contra differences in R [%]	1-week post-FUS	**3.9**	4.8	2.6	**6.9**
	2 weeks post-FUS	-0.1	1.6	3.6	5.9
	3 weeks post-FUS	-1.2	-0.5	2.7	**9.0**
	4 weeks post-FUS	2.7	7	2.7	8.8
Ipsi vs contra differences in Vf [%]	1-week post-FUS	2.8	5.0	-5.8	18.3
	2 weeks post-FUS	9.3	-6.0	1.1	11.6
	3 weeks post-FUS	-1.6	-5.2	-0.9	24.0
	4 weeks post-FUS	8.2	17.5	-6.3	19.8
Ipsi vs contra differences in SO_2 [%]	1-week post-FUS	-2.4	-3.6	-2.8	2
	2 weeks post-FUS	0.0	-4.5	-4.1	-2.3
	3 weeks post-FUS	1.5	-4.9	**-5.0**	-1.1
	4 weeks post-FUS	-2.8	-5.9	**-8**	-1.9

Table 14. Summary of relative differences (in %) between ipsilateral and contralateral regions 1 h post-FUS for R, Vf and SO_2 estimated values. Significant differences are highlighted in bold.

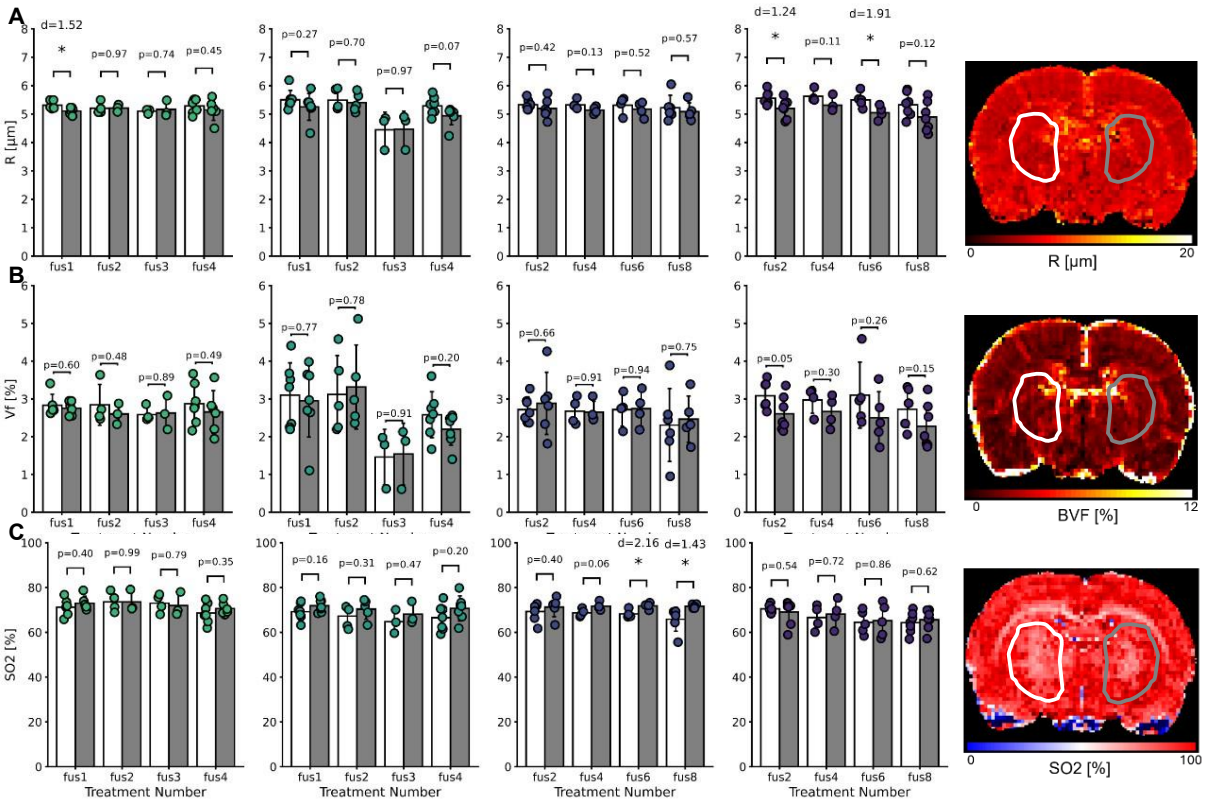


*Figure 61. Ipsilateral (white) and contralateral (grey) values of R (**A**), Vf (**B**) and SO2 (**C**) with a representative example of the MR fingerprint map for each parameter. In white is highlighted the ipsilateral ROI and in grey the contralateral ROI. The data were analysed with a two-sample t-test (*p < 0.05). Effect size was computed with Cohen's d criteria. The results are expressed as mean ± S.D.*

6.2.5. Iron deposition

The repetition of the BBB opening accompanied with the injection of USPIO within the hour following the FUS application can potentially impact the MRI measurements. Liu *et al*. demonstrated the monitoring of the BBB opening using SPIO as a contras agent as well as Marty *et al*. who monitored BBB closure dynamics with USPIO (see 1.4.1) [Liu *et al.*, 2011; Marty *et al.*, 2012]. As SPIO may extravasate and thereby alter the MRI signal, we reconstructed quantitative susceptibility maps (QSM) to assess the potential modifications of this parameter (Figure 62). The mean across timepoints and regions did not show any significant differences. The paramagnetic and diamagnetic contributions were extracted from the QSM maps in ipsilateral and contralateral regions, accounting for positive and negative QSM. We did not measure any significant differences between regions. There is a tendency of increased susceptibility in the brains with higher values in the contralateral than in the ipsilateral ROI according to Figure 63.A. Yet, the positive and negative contributions seem to be equal (Figure 63.B-C). We extracted the volumes of different levels of susceptibility from the ipsilateral and contralateral ROI respecting the following criteria: $0.05 < \chi^+ < 0.1$ and $\chi^+ > 0.1$. Significant increase for $\chi^+ > 0.1$ volume was measured in the ipsilateral region after 2-FUS treatments. We did not see any significant differences in the volumes of low and high magnetic susceptibility contributions. Yet, it seems that there are more voxels with a high magnetic susceptibility in the ipsilateral ROI than contralateral ROI (Figure 63.D-E). Altogether, this suggests that a very small amount of USPIO may extravasate but not enough to alter our measurements.

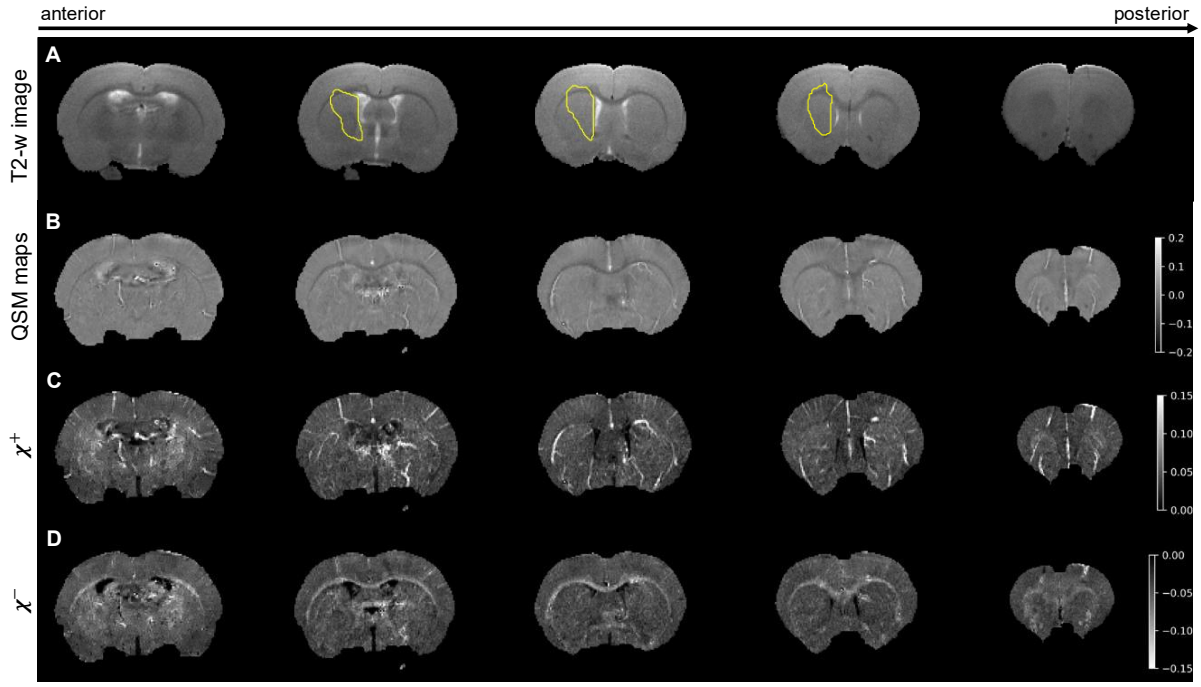


*Figure 62. Representative T2-w images (**A**), QSM maps (**B**), the paramagnetic contribution (**C**) and diamagnetic contribution (**D**) of a rat that followed 8-FUS treatments at 440 kPa. The region in which the BBB has been opened 8 times is highlighted in yellow.*

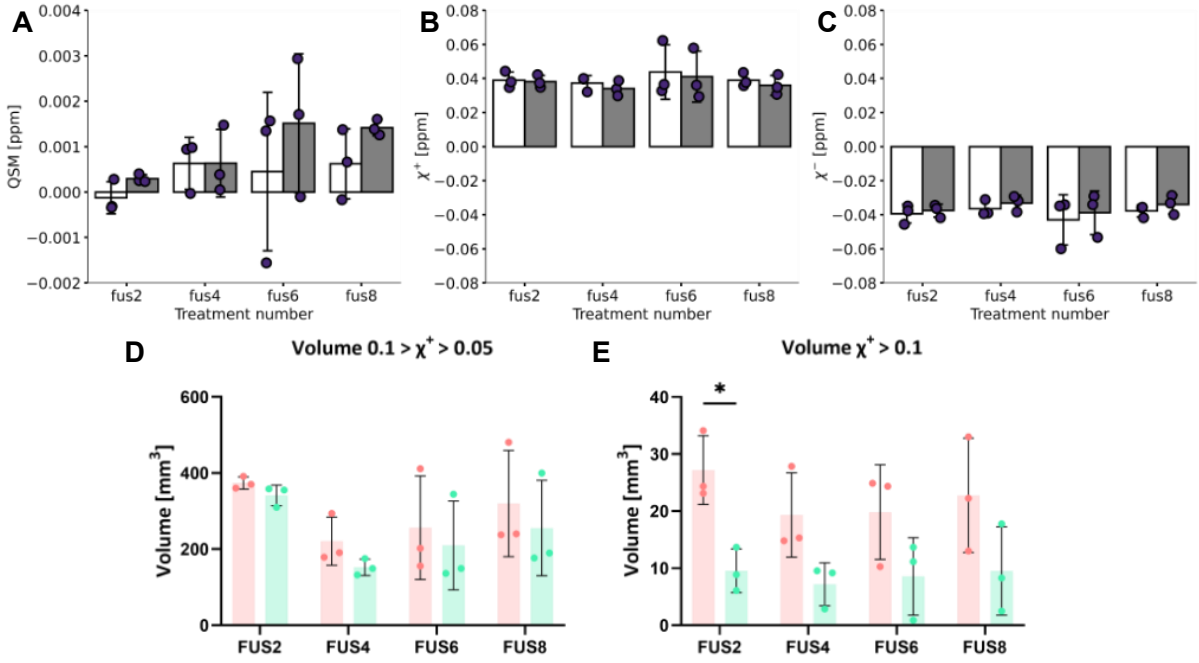


*Figure 63. Ipsilateral (white) and contralateral (grey) QSM (**A**), paramagnetic (**B**) and diamagnetic (**C**) contributions for the 8-FUS at 440 kPa group. Volumes of moderate paramagnetic ($0.05 < \chi^{+} < 0.1$) (**C**) and high paramagnetic ($\chi^{+} > 0.1$) (**D**) contributions in ipsilateral (red) and contralateral (green) ROI. The data were analysed using two-sample t-test (*$p < 0.05$). The results are expressed as mean ± S.D.*

6.2.6. Immunohistology

The brains of animals from groups that received multiple FUS treatments were harvested 1 week after the last treatment. We stained the BBB with the SMI71 marker, specific for a rat endothelial protein found in areas with BBB, and the astrocytes with GFAP (cf 4.6 for methodological details). For the 4-FUS group at 440 kPa, we did not measure any differences in area occupation of the BBB, GFAP and any increase in fluorescence intensity in the ipsilateral ROI. For the 8-FUS group at 440 kPa, we can see in Figure 64.B an increased vessel diameter for the ipsilateral ROI, compared to the contralateral one. We also observe a strong astrocytic activation (Figure 64.C) in the ROI targeted by FUS. It resulted in a significant increase in both area occupation and mean fluorescence intensity in the ipsilateral ROI compared to the contralateral one (Figure 64.E-F).

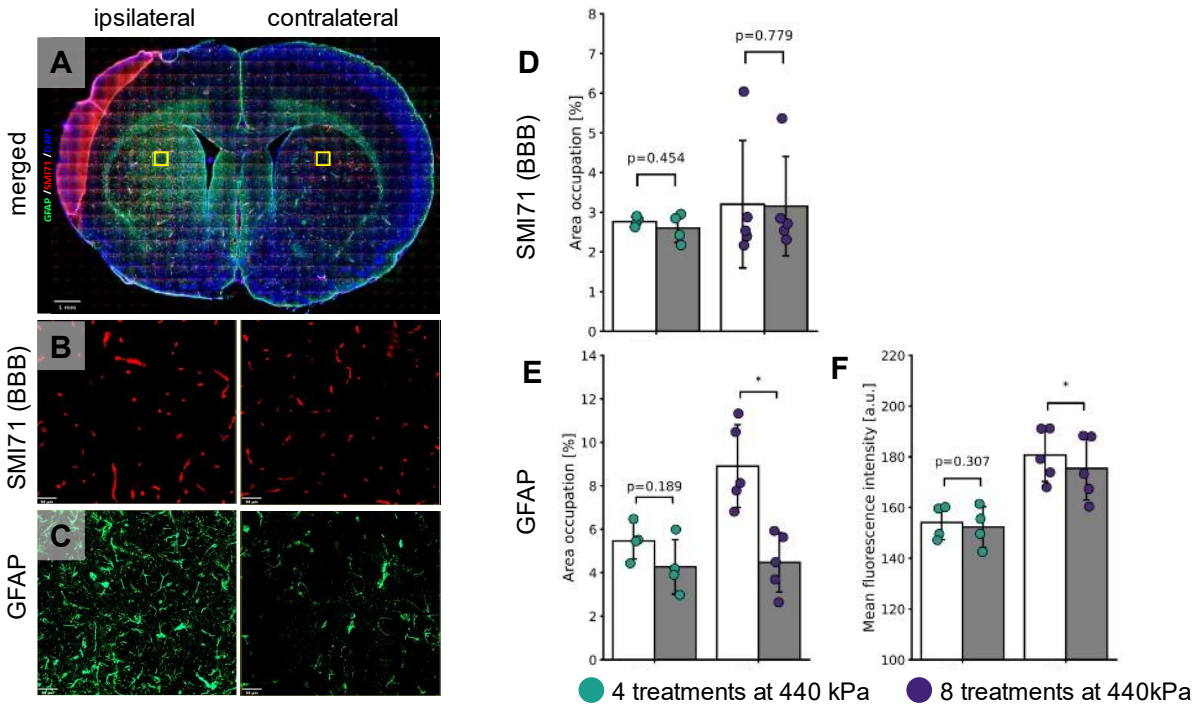


*Figure 64. Representative micrograph for an 8-FUS rat at 440 kPa one week after the last FUS treatment (**A**). Extracted zooms for SMI71 (**B**) and GFAP (**C**) markers at the level of ipsilateral and contralateral regions (extracted from the two yellow squares). Mean area of occupation for ipsilateral (white) and contralateral (grey) regions for SMI71 (**D**), GFAP (**E**) and mean fluorescence intensity for GFAP (**F**). The data were analysed using a two-sample parametric test (*p < 0.05). The results are expressed as mean ± S.D.*

6.3. Discussion

As there is a lack of studies that achieved repeated BBB opening with fine guidance of the BBB opening, we repeatedly applied FUS to permeabilise the BBB in a large area of the brain once or twice a week for 4 weeks. Two different acoustic pressures were used to evaluate the impact of the pressure increase (MI: 0.32 and 0.37). These MI are known to be sufficient to deliver therapeutic agents and low enough to not induce lesions [Chevaleyre *et al.*, 2023; Dréan *et al.*, 2019; McDannold *et al.*, 2019]. The repeatability and accuracy of the BBB opening across all treatment sessions was very good, thanks to the MR-guided FUS device. We did not observe any lesions (bleeding, oedema), whatever the group or the session.

We measured a significant increase in BBB permeability after 4 treatments in the 8-FUS group, suggesting an alteration of the BBB permeability in that group, while the FUS-induced BBB permeability was stable across sessions in the 4-FUS group. In addition, we measured, on average, a significant drop of perfusion in the FUS-irradiated area 30 min after FUS, as previously reported [Labriji *et al.*, 2023; Rigollet *et al.*, 2024c]. The same effect was observed at almost each session and was less pronounced or absent when the contralateral perfusion was low. Overall, the reduction in perfusion was slightly smaller for the lower acoustic pressure. Short-term longitudinal perfusion measurements showed that 90 minutes post-FUS the perfusion returned to baseline values, thus this modification seems to not impact long-term brain perfusion. Moreover, we estimated with an MR fingerprint approach different quantitative parameters: R, Vf and SO_2. Very minimal modifications were measured for all parameters

when animals received 4-FUS treatments. For the 8-FUS groups, we measured significant differences between ipsilateral and contralateral regions with a trend towards larger values of R and Vf and smaller SO_2 values. To the best of our knowledge, no one has measured these parameters in this context before. One week after the last FUS-session, histological staining showed that the vessels in the ipsilateral region were dilated compared to contralateral in the group that received 8-FUS treatments at 440 kPa. In this same group we also observed a strong astrogliosis.

Two studies from Frank's lab evaluated the effect of 6 repeated treatments over 6 weeks in Sprague-Dawley rats using histology, anatomical MRI and PET [Kovacs *et al.*, 2018; Sinharay *et al.*, 2019]. Two and 7 weeks after a single FUS session at 0.4 MI, they reported a substantial number of hypointense regions in T2*-w images acquired either at 3 or 9.4 T and it was accompanied by astrogliosis and inflammation markers. This suggests that despite the relatively low and safe MI used [Chu *et al.*, 2016], the BBB opening was not safe in their settings. This could be related to their use of a dose of Optison™ (460 µL/kg) that is 10-fold the dose used in previous studies [Bing *et al.*, 2018; McDannold *et al.*, 2007, 2006] in addition to the fact that it is known that Optison™ MB produce a larger effect that Definity MB [McDannold *et al.*, 2007]. Regarding the repeated FUS, with their settings, they measured a significant decrease in the T2* ratios (FUS-treated vs. non-FUS-treated) between a single FUS treatment and a 2-FUS treatment, as well as between a single FUS treatment and a 6-FUS treatment. In addition, they observed a significant ventricular enlargement after 6-FUS treatments in the ipsilateral hemisphere. Astrogliosis and inflammation were observed in the cortex one week after 6-FUS. In the other study [Sinharay *et al.*, 2019], with much the same FUS parameters, they did not observe significant differences in GFAP and Iba1 (although a slight increase was visible) 24 h after 1-FUS, 2 weeks after 2-FUS and 1 week after 6-FUS. These results are very surprising as evidence of neuroinflammation was visible on their PET images. Moreover, many studies report astrogliosis and microglial scars 24 h after 1-FUS [Kovacs *et al.*, 2017; McMahon *et al.*, 2017; Rigollet *et al.*, 2024c]. Yet, the comparison of different FUS treatments, performed using different settings and at very different timepoints is difficult. Interestingly, they observed in all conditions infiltrating systemic macrophages in the targeted cortex and hippocampus. Surprisingly, they also found significantly more newly born neurons in the cortex 1 week after 6-FUS. Finally, they observed increased expression of the phosphorylated Tau protein in the targeted cortex 1 week after 6-FUS treatments. Altogether, they highlighted the potential link between the repeated BBB opening and a sterile inflammation that could contribute to neurodegenerative processes [Bellucci *et al.*, 2011].

Regarding application of safer FUS parameters to repeatedly open the BBB, Blackmore *et al*. reported no metabolite alterations with *in* vivo ^{1}H-MRS, spatial learning memory differences, synaptic transmission and plasticity in the dentate gyrus and neuronal morphology in the dentate gyrus using electrophysiology recordings. Yet, significant differences were measured using diffusion MRI 4.5 months after 6 weekly FUS treatments in fractional anisotropy (increase), and radial diffusivity (decrease) parameters in various brain areas (hippocampus, prefrontal cortex, thalamus, corpus callosum), associated with reduced mean diffusivity values [Blackmore *et al.*, 2018]. These results suggest that a neuroprotective effect of a whole brain FUS treatment on the brain is triggered. Hatch *et al*. found no altered firing of CA1 pyramidal neurons after either a single FUS treatment or six repeated weekly FUS treatments in the whole brain [Hatch *et al.*, 2016]. Tsai *et al*., observed short-term effects of two repeated treatments and found that a FUS treatment every 2 days with 0.33 MI was efficient without causing tissue damage (no red blood cells and mild astrogliosis at 2 h) or

behavioural change [Tsai *et al.*, 2018]. All these studies suggest, *in fine*, that the repeated permeabilisation of the BBB is feasible and limited effects can be seen.

In line with these results, our study provides evidence of safety regarding weekly repeated MR-guided FUS treatments at two MI (0.32, 0.37). Astrogliosis remains limited when applying a single treatment per week, compared to two treatments per week, and very limited effects on the brain vascular function are observed across FUS sessions, except the strong and transient reduction in brain perfusion. Our study can be used to complete Tsai *et al*. findings and we suggest that applying a FUS treatment twice a week however may result in non-negligible secondary bioeffects such as chronic neuroinflammation, brain structure modifications and a reduction in the NVU functions. We also observed ventricular enlargement, a brain structure modification already observed in various studies [Kobus *et al.*, 2016; Kovacs *et al.*, 2018], and also found in female PVG rats after repeated sub-concussive impacts over 2 weeks [Hiles-Murison *et al.*, 2021]. Yet, the rat strain used in this study is naturally subject to spontaneous development of ventriculomegaly [Tu *et al.*, 2014], thus we cannot conclude on the origin of this modification in our study.

Several studies have already used multiple FUS-induced BBB openings to evaluate a therapeutic strategy. This was performed mainly in Alzheimer's disease (AD) mice models (from 4 to 15 weekly FUS treatments) [Karakatsani *et al.*, 2019; Pandit *et al.*, 2019; Shen *et al.*, 2020] and tumour models with three weekly sessions in 9L glioma model [Aryal *et al.*, 2015, 2013] or 2 FUS treatments 3 weeks apart in F98 glioma model [McDannold *et al.*, 2019]. In AD models, they demonstrated memory improvements, reduction of phosphorylated Tau, clearance of neuronal Tau and Aβ plaques. Aryal *et al*. succeeded in eradicating 9L brain tumours with 3 weekly treatments and the administration of doxorubicin in 3/8 rats [Aryal *et al.*, 2013], yet this tumour model is controversial due to its strong immunogenicity and poor infiltrative pattern [Sahu *et al.*, 2022]. McDannold *et al*. obtained a reduction in tumour growth and increased mean survival time of F98 rats using 2 consecutive sessions of FUS (3 weeks apart) along with intravascular carboplatin delivery [McDannold *et al.*, 2019]. Their results appear as one of the best treatments for glioblastoma so far. Different studies have proven the feasibility or repeated BBB opening in larger animals as in a canine model [Meaghan Anne O'Reilly *et al.*, 2017] and NHP models [Downs *et al.*, 2015; Horodyckid *et al.*, 2017; McDannold *et al.*, 2012], as well as in AD patients [Epelbaum *et al.*, 2022; Sonabend *et al.*, 2023] and glioblastoma patients [Carpentier *et al.*, 2024; Idbaih *et al.*, 2019; Park *et al.*, 2021]. For the latter studies, the time between two FUS treatments was longer than those found in preclinical studies, this is partly explained by the difference in disease progression. For the sake of comparison, a Fischer rat implanted with 10^3 F98 cells has a mean survival time of 26 days [Elleaume *et al.*, 2020] while glioblastoma patients have a median survival reported of 6 to 10 months [Brodbelt *et al.*, 2015; Ostrom *et al.*, 2015]. Thus, the treatment planning strategies need to be adapted in preclinical models to fit and mimic the potential future schedules implemented in clinics. Table 15 summarises the different FUS treatment plannings observed in literature.

	Study	Model and disease	Delay between two FUS sessions	Number of FUS sessions
Brain tumour	[Carpentier *et al.*, 2024; Park *et al.*, 2021]	Glioblastoma patient	1 month	6
	[Idbaih *et al.*, 2019]	Glioblastoma patient	1 month	10
	[Aryal *et al.*, 2013]	9L Fischer rat	1 week	3
	[McDannold *et al.*, 2019]	F98 Fischer rat	3 weeks	2
Alzheimer's disease	[Leinenga and Götz, 2018]	APP23 mice	2 weeks	4
	[Karakatsani *et al.*, 2019]	rTg4510 mice	1 week	4
	[Pandit *et al.*, 2019]	K369I tau mice	1 week	15
	[Shen *et al.*, 2020]	3×Tg-AD mice	1 week	6
	[Epelbaum *et al.*, 2022]	AD patient	3 weeks	6
	[Sonabend *et al.*, 2023]	AD patient	2 weeks	7

Table 15. Summary of repeated FUS treatment schedules for brain tumour and AD studies.

In this context, and given our results, it seems that the mild consequences observed after repeated BBB opening do not prevent their use in the context of glioblastoma, which exhibits a 15-month median survival duration, even if caution is of course required as we showed that FUS-induced BBB permeabilisation may cause a slight decrease in brain oxygenation, creating a favourable environment for disease progression. However, in the context of neurodegenerative diseases, the two faces of FUS shall be considered: on the one hand, application of repeated FUS sessions may induce neuroinflammation and on the other hand, application of repeated FUS sessions help clearing the waste, as previously reported. Elements already published and our study will guide the optimisation of FUS parameters to improve Tau protein clearance by immune cells [Karakatsani *et al.*, 2019], and Aβ internalisation by astrocytes and microglia [Burgess *et al.*, 2014; Jordão *et al.*, 2013; Leinenga and Götz, 2015]. Compared to single FUS treatments, it was demonstrated that repeated FUS-induced BBB opening broke down larger Aβ plaques into smaller pieces facilitating its capture and degradation by activated microglia [Leinenga and Götz, 2018]. The created neuroinflammation induced by FUS needs to be characterised more precisely to assess whether pro- and/or anti-inflammatory processes are triggered.

To date, a few articles have evaluated the repeated impact of FUS on a specific brain region in humans, for example in the limbic part of the cortex, a region implicated in the emotion management and emotional processing, and this type of treatment could have an impact on aggressiveness, humour. FUS-induced neuromodulation (without the use of MB) is one of the promising methods to improve obsessive-compulsive disorder patient outcome [Ranjan *et al.*, 2024]. Future studies could also evaluate the impact for psychiatric disorders of repeated BBB opening in specific regions where neuro-deficient circuits originate.

The translation of our preclinical results to the clinical level is not straightforward. First, we performed BBB opening under anaesthesia. In the current clinical setting, FUS application is applied in awake subjects. Therefore, the vascular response could be slightly different, as isoflurane increased CBF in our preclinical study. Isoflurane also reduces the $CMRO_2$ [Schoknecht *et al.*, 2024] and thus protected the brain from the transient mild hypoxia that might be associated to the transient CBF reduction that

we observed. In addition, as the study was performed in rodents, we did not observe if specific alterations occur in white matter.

Regarding the limitations of our study, a cognitive study would help assess whether the repetition of FUS-induced BBB opening impacts the social behaviour, locomotor activity and anxiety level of animals. Future studies could evaluate, for example, the impact of repeated opening of the BBB in the olfactory bulbs, as social interaction behaviour in rodents rely heavily on olfactory signals [Freeman and Young, 2016]. Finally, the use of cavitation monitoring, as detailed in 4.2.2.2 and in Chapter 5, could help ensure the BBB is safely opened. It would be of interest to evaluate whether the signals from cavitation monitoring, possibly combined with imaging cues, can be used to predict neuroinflammation.

In conclusion, a single FUS treatment per week in rats does not lead to undesirable effects at the microvascular and neuroinflammatory levels, expected in the hours following the application of FUS. However, two FUS treatments per week induce the expression of several factors, although these expressions are mild, indicating that repeated FUS treatment is not harmless. Acoustic pressure should be kept as low as possible.

Chapter 7. Study 3: Median survival time in an F98 rat model is improved by the combination of FUS, carboplatin and radiotherapy

Dr Hélène Elleaume from the STROBE laboratory has been developing therapeutic strategies involving radiotherapy for a few decades. 15 years ago, a study published by Dr Julia Rousseau demonstrated impressive survival outcomes in a preclinical model of glioblastoma combining an intracerebral delivery of carboplatin and a single radiotherapy dose. However, this treatment couldn't be transferred to clinics due to the invasiveness of the procedure. With the emergence of the MR-guided FUS, few studies have tested the efficacy of the carboplatin delivery in the brain with FUS in small animal models [Dréan *et al.*, 2019; McDannold *et al.*, 2019] and the Pr Carpentier's team conducted several studies in glioblastoma patients with the implantable Sonocloud device to deliver carboplatin [Carpentier *et al.*, 2024; Idbaih *et al.*, 2019]. In addition, the radiotherapy coupled with FUS has been used in different tumour models but did not show significant increase in the mean survival time [Stecia-Marie P. Fletcher *et al.*, 2024]. The combination of both methods, MR-guided FUS to deliver carboplatin followed by radiotherapy, has not yet been tested and holds great promise for the future to improve the outcome of glioblastoma patients, something that has not been done since the work of Pr Roger Stupp who combined the radiotherapy with a concomitant administration of temozolomide [Stupp *et al.*, 2005]. With the recent installation of a preclinical stereotactic irradiation platform at the IRMaGe facility, the project to conduct this trial has begun. This project involved many actors and was carried out mainly by Master 2 intern Sarra Dbira supervised by Dr Hélène Elleaume and me, Dr Hélène Elleaume and me. More specifically, Sarra Dbira took in charge the cell culture with the support of Dr Claire Rome, Nora Collomb and Dr Benjamin Lemasson, Dr Sarvenaz Keshmiri conducted the radiotherapy, Dr Jean-Luc Ravanat analysed the DNA damages induced by the therapeutic protocol and Dr Benoît Chovelon analysed with ICP-MS the biological samples. I performed with Sarra Dbira the BBB opening with FUS as well as the MRI acquisition and MRI analysis. Part of the figures presented in this chapter were realised by Sarra Dbira.

Glioblastoma (GBM) is the most common malignant brain tumour and its incidence is rising steadily worldwide, with 3 cases per 100,000 people in 2018, compared with 2.1 a decade earlier [Darlix *et al.*, 2017]. This tumour is characterised by its ability to infiltrate healthy tissue, with an extremely poor prognosis, with a median survival of no more than 15 months despite aggressive treatment. In the treatment of GBM, radiotherapy has been shown to improve overall survival of patients but does not provide sufficient control of GBM [Walker *et al.*, 1979]. Radiation therapy acts on cells through the energy deposited when X-rays interact with tissue. After a surgical resection in association with temozolomide, Stupp *et al*. demonstrated an increase in the mean survival time of GBM patients by delivering 60 Gy in 30 fractions of 2 Gy [Stupp *et al.*, 2005], and this protocol is up to now the standard procedure used in clinics. However, many tumour cells are radioresistant and are found scattered throughout the brain leading to the death of the patient. Combining this radiotherapy with the intravenous injection of chemotherapies such as carboplatin, an alkylating agent that binds to DNA and inhibits its replication, increases the control of many cancers while maintaining acceptable toxicity [Curran *et al.*, 2011; Lacas *et al.*, 2021]. Yet, these strategies have not proved to be very effective due to the BBB. GBM presents as an organised tumour within the brain, possibly with a necrotic centre,

associated with extremely diffuse infiltration around the tumour with isolated tumour cells. Tumour angiogenesis, due to an increase in proangiogenic factors [Jain, 2014], leads to the formation of blood vessels that lack a normal physiological structure known as the BTB. In contrast to the BBB, the BTB is partially permeable, allowing the extravasation of large molecules [Kodack et al., 2017]. However, this permeability is highly heterogeneous for small and large molecules, as is tissue perfusion, leading to sub-optimal accumulation of therapeutic agents within the tumour. To date, molecule delivery remains poorly controlled and inadequate [Arvanitis *et al.*, 2020, 2018].

Thus, the resistance to treatment of GBM is due to several unfavourable factors. Firstly, complete resection is impossible due to the infiltrative nature of GBM and its proximity to functional areas of the brain, leading to tumour recurrence in the months following surgery. Secondly, the effectiveness of radiotherapy is limited by its location and severely limits the dose of X-rays that can be delivered to the tumour because of the potential damage to the surrounding healthy brain tissue, which will be associated with side-effects ranging from simple headaches to major neurological deficits. Finally, the presence of the BBB and the BTB limits the passage of radiosensitising agents, which would increase the dose received in the tumour while preserving the surrounding healthy tissue.

Convection-enhanced delivery of carboplatin in association with osmotic pumps to infuse the chemotherapy, in combination with radiotherapy has demonstrated unprecedented results with 60% of survival rats in an F98 rat model [Elleaume *et al.*, 2020]. However, this method was very invasive, and in the current context could not be transferred to the clinic. As introduced previously, FUS technology can enable biological membranes such as the BBB but also the BTB to be permeabilised in a precise and controlled manner. In this study, we seek at evaluating the biodistribution of the carboplatin into the tumour core, peritumoral area and the healthy tissue in a F98 rat model after BBB and BTB opening with FUS and the intravenous injection of carboplatin. In this chapter, we will use BBB to designate the BBB and BTB. And evaluate the therapeutic potential of this innovative combination on the survival rate. To do so, we evaluated in a first group the biodistribution of the carboplatin 1 h and 24 h after permeabilising the BBB and the BTB with inductively coupled plasma mass spectrometry (ICP-MS). In a second group, we applied MR-guided FUS and MB coupled with a vascular injection of carboplatin and delivered stereotaxically 15 Gy 24 h after. We monitored longitudinally with MRI the cerebral blood flow (CBF), the water diffusion with the apparent diffusion coefficient (ADC), the tumour permeability with dynamic-contrast enhancement (DCE) in order to evaluate the tumour progression.

7.1. Methods

7.1.1. Cell culture and clonogenic assay

F98 cells (ATCC) were cultivated in monolayers of Dulbecco's modified Eagle's medium (DMEM) supplemented with 10% fetal bovine serum (FBS), 1% penicillin/streptomycin antibiotics, and maintained at 37°C and 5% CO_2 in Nuclon Delta surface treated flasks 4. Cells were used at passage 13 and tested negative for mycoplasma with a MycoAlert® mycoplasma detection kit. A clonogenic assay was performed to evaluate the impact of carboplatin on the survival of the F98 cells (see annexe A.5.1).

7.1.2. Animal care and tumour model

75 male Fischer 44 rats were housed according to the regulations of the French Ministry of Education and Research and the whole protocol was validated by the local ethic committee under the APAFIS

n°48225. The behaviour, according to a pre-established grid, and the weight of the rats were monitored after tumour implantation 3 times a week and every day after the FUS treatment and the injection of the chemotherapy. Every procedure was carried out under anaesthesia using 2% isoflurane in air and oxygen (80/20%). One week after their arrival, animals were implanted with 10^3 of F98 cells stereotaxically in the right caudate nucleus (bregma; AP, 0 mm; ML, +3.5 mm; DV, -5.5 mm) according to the previous protocol described by Bulin *et al*. [Bulin *et al.*, 2022]. Three rats died during the experiment for tumour implantation. Between 12 and 14 days after tumour implantation, rats were imaged using the MRI and an anatomical T2-w sequence to assess the tumour volume and the tumour location.

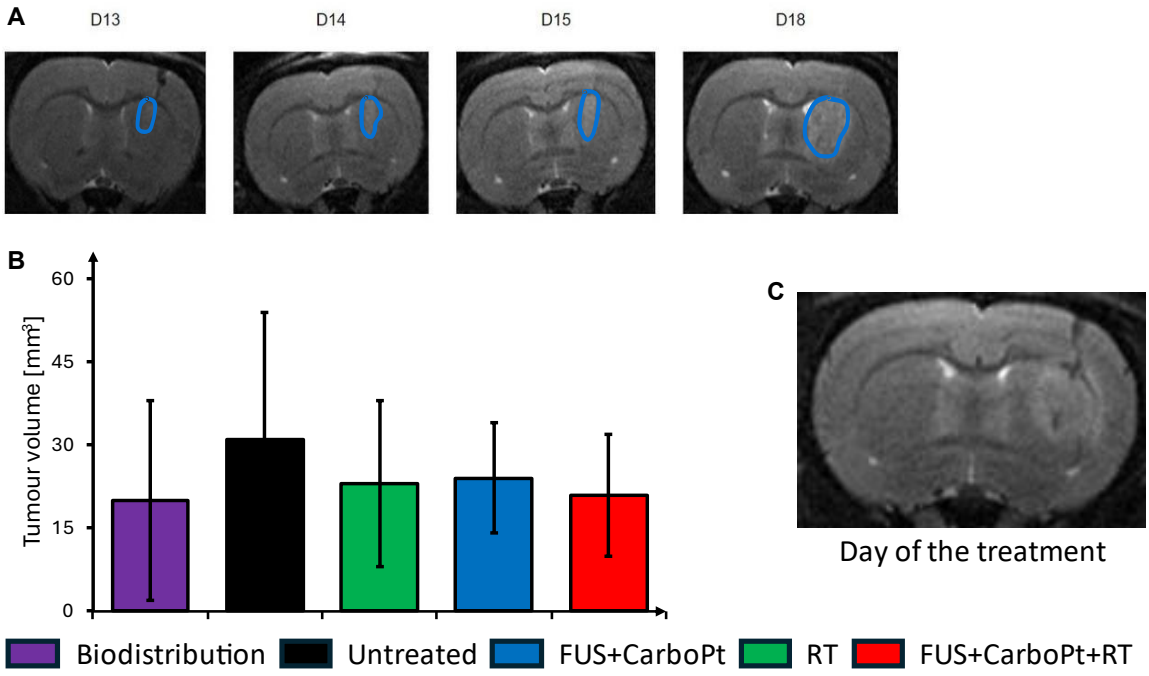


*Figure 65. F98 brain tumour evolution and volumes. **A**) Representative example of T2-w image to evaluate the tumour growth in a rat at days 13 to 18 after stereotaxic implantation. The hyperintense volume was delineated manually to evaluate the tumour volume. **B**) Tumour volume for each of the six groups at the day of the treatment. The results are expressed as mean ± S.D.*

This information was used to randomly assign animals to a group, while maintaining similar average tumour size (Figure 65). 1 rat did not show any evidence of tumour growth and was removed from the study. 36 rats were assigned to the survival study and 35 to the biodistribution study. Regarding the survival study, 4 groups were distinguished: the untreated group, which did not receive any treatment, the group which received a single stereotaxic radiotherapy dose 14 days after tumour implantation (named as RT), the group which received at day 14 the FUS and the injection of carboplatin in the vascular system (named as FUS+CarboPt), and the group which received the combination at day 14 of FUS and an injection of carboplatin and a 15 Gy dose of radiotherapy the next day (named as FUS+CarboPt+RT).

The detailed protocol of FUS and radiotherapy are respectively detailed in 7.1.3 and 7.1.4. We did not take into account the following groups: a group receiving only FUS with MB and a group receiving only carboplatin because of the different studies that have shown that the mean survival rate is not improved [Elleaume *et al.*, 2020; Stecia-Marie P. Fletcher *et al.*, 2024; McDannold *et al.*, 2019]. Animals

were closely monitored every day and put to death when the previously limited established points were reached.

Regarding the evaluation of the biodistribution of the carboplatin after the application of FUS in the brain, animals were divided in two groups: a control group, a group which received a dose of carboplatin intravenously and the latter received the combination of FUS and carboplatin. Animals were euthanised 1 h or 24 h after the injection of carboplatin. The brain, the liver, the heart, the spleen, the kidneys and a blood sample were recovered. Organs were frozen in isopentane and the plasma from the serum was separated after 10 min centrifugation at 1500 rotation per minute. Organs were analysed with ICP-MS.

A summary of the study and all groups are displayed in Figure 66 and Table 16.

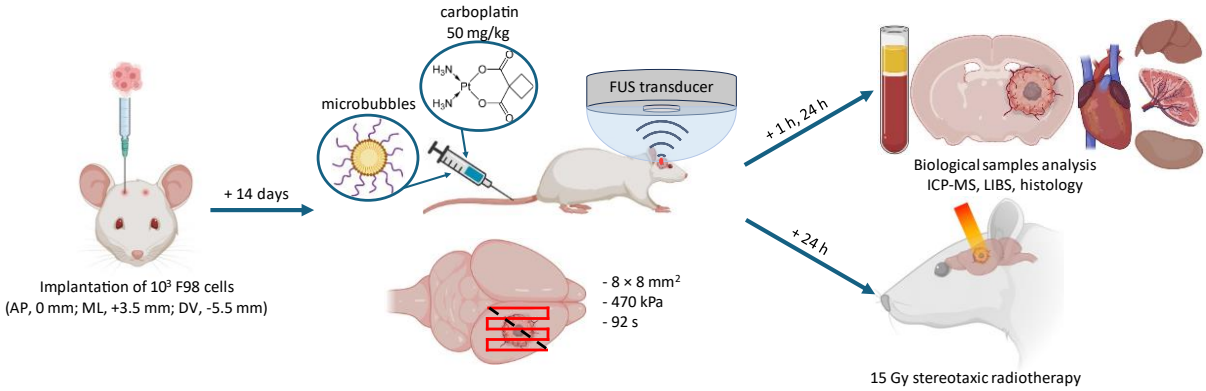


Figure 66. Overview of the experimental protocol with F98 cell implantation, MR-guided FUS with a raster scan and either the harvesting of brains and organs 1 h and 24 h post-FUS for carboplatin biodistribution evaluation or a radiotherapy session with a 15 Gy dose and MRI follow-up.

Study	Group	number of animals
Biodistribution	ICP-MS control	2
	ICP-MS 1 h	6
	ICP-MS 24 h	6
	Phase contrast control	2
	Phase contrast 1 h	3
	Phase contrast 24 h	3
	Fluo-X control	2
	Fluo-X 1 h	3
	Fluo-X 24 h	3
Efficacy	Untreated	6
	RT	5
	FUS + CarboPt	8
	FUS + CarboPt + RT	10
	Total	71

Table 16. Overview of the different groups of the study. Phase contrast and fluorescence X imaging data are not presented here due to time constraints (acquisition is planned at ESRF (Grenoble, France) in November 2024).

7.1.3. MR-guided FUS procedure

Animals were imaged with the 4.7 T preclinical scanner (see 4.5) and the BBB was permeabilised as described in 4.4 with an average pressure of 470 kPa *in situ* and the transducer followed a raster scan of 8 × 8 mm^2 (Figure 68) to permeabilise the whole hyperintensity signal visible on the T2-w image. The steering was adjusted per rat at the centre of the tumour location. Total FUS duration was equal to 90 seconds. BBB permeabilisation was assessed with the acquisition of two T1-w image before and after the injection of a 200µmol/kg Gd-DOTA bolus.

7.1.4. Radiotherapy protocol

Animals were treated using the small animal radiation research platform (SARRP, Xstrahl GmbH, Germany; IRMaGe), which is specifically designed for small animal studies and replicates clinical radiation therapy technologies. This platform integrates a motorised variable collimator, or a set of various fixed collimators, enabling the performance of conformal radiation therapy techniques commonly used in clinical settings (Figure 67.A). Treatment planning dosimetry was conducted using the MuriPlan software (Figure 67.B). The tumour was localised at the centre of the right caudate nucleus. Tissues were segmented semi-automatically to identify bone, air, and soft tissues for treatment planning. After contouring the irradiation region and defining the tumour isocentre, a 10 x 10 mm^2 irradiation field was applied using a fixed square collimator. A dose of 15 Gy was delivered in a volumetric 150° arc mode, with the animal positioned on the irradiation platform, while the collimated X-ray beam rotated from -75° to +75° relative to the vertical. Dose-volume histogram was plotted for each animal, as shown in Figure 67.B.c, to ensure that at least 70% of the delineated tumour received 14.5 Gy.

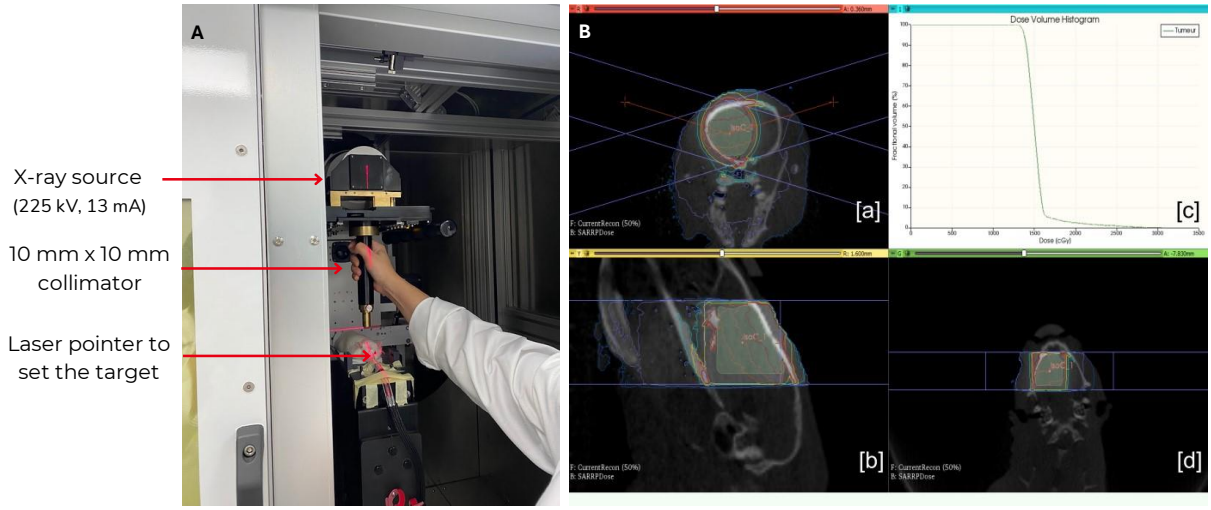


*Figure 67. Radiotherapy platform and software. **A**) SARRP system with X-ray source, the 10 × 10 mm^2 collimator, laser pointer to centre the subject of study and the subject of study positioned in the bed with anaesthesia mask. **B**) Treatment planning window on MuriPlan software (Xstrahl GmbH, Germany) with axial (**a**), sagittal (**b**) and coronal (**d**) 2D views. **B.c**) The dose-volume histogram simulation.*

7.1.5. MRI follow-up after treatment

Rats were monitored using MRI. The acquisition protocol of each MRI session included: anatomical T2-w image, CBF map (based on ASL), T1 map, mean diffusivity map (based on diffusion MRI) and a permeability map (based on a DCE sequence) (see 4.5). The whole MRI protocol lasted 35 min.

7.1.6. Carboplatin quantification

To quantify the carboplatin extravasation and biodistribution after the BBB permeabilisation, organs of control animals were harvested without any additional procedure except the tumour implantation 14 days earlier. We considered one group who received a unique injection of carboplatin through the tail vein and another group who received the carboplatin injection just after the FUS-induced BBB permeabilisation was confirmed by Gd-DOTA and MRI. For the latter groups, organs were harvested 1 h or 24 h after the carboplatin injection. The delay of 24 hours was chosen based on the fact that animals were irradiated 24 hours after the injection of carboplatin in the therapy study. Hence, it is interesting to study the biodistribution of carboplatin at the moment of radiotherapy treatment. Biopsies were obtained from the tumour region, the peritumoral region, and the healthy brain (contralateral cortex) as shown in Figure 69 and were precisely weighted. The kidney, heart, spleen and liver were also extracted and frozen at -80°C. Blood samples were also collected and centrifuged for 10 min at 1500 rpm to separate plasma and red blood cells.

The carboplatin was quantified with ICP-MS at the Institut de Biologie et Pathologie (CHU Grenoble Alpes, France). ICP-MS is an analytical technique used for detecting and quantifying trace elements and isotopes in a wide variety of samples. Only one sample for each group was analysed so far. Other imaging techniques were considered to evaluate the biodistribution of the carboplatin among them the LIBS and fluorescence X-ray spectroscopy. The samples for these techniques were recovered but due to time constraints, the imaging acquisition will be performed later, thus will not be presented here.

7.2. Results

7.2.1. Blood-brain barrier disruption

The FUS were delivered with a raster scan that covered the whole hyperintense region visible in T2-w image (Figure 68.C). The BBB was successfully permeabilised in all animals of the study and revealed with the acquisition of two T1-w images before and after the injection of Gd-DOTA (Figure 68.A-B). The average BBB opening volume across all animals was equal to 246 ± 165 mm^3. We did not observe significant differences between the groups and the BBB opening was consistent (Figure 68.C). We also observed a greater relative contrast enhancement compared to the contralateral in the tumour core (1750%) compared to the rest of the contrast enhancement region (700%), very likely due to the leaky BTB.

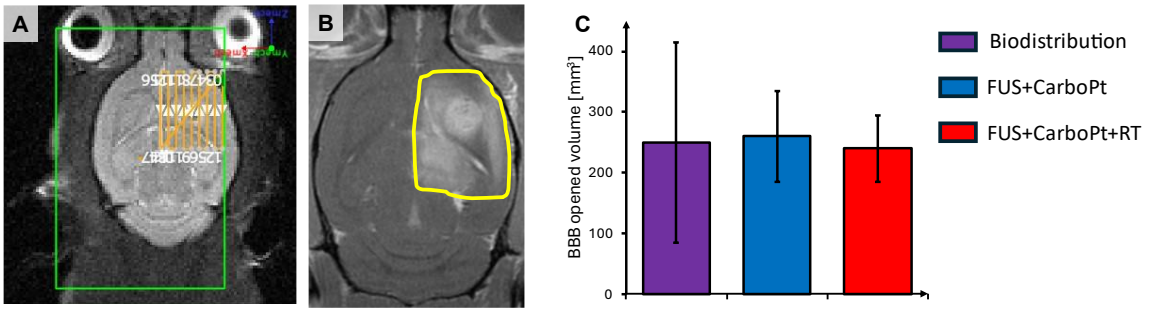


*Figure 68. FUS-induced BBB permeabilisation. **A**) MR-guided FUS procedure. **B**) Representative coronal T1-w image after Gd-DOTA injection with the permeabilised region highlighted in yellow. **C**) Average BBB opening volume across groups. The results are expressed as mean ± S.D.*

7.2.2. Biodistribution of carboplatin

We measured with ICP-MS the concentration of platinum in the tumour, the peritumoral region and the contralateral hemisphere 1 h and 24 h post-FUS to assess the quantity of carboplatin with and without the application of FUS. An important enhancement was measured in the tumour and peritumoral regions compared to control and to the contralateral regions. At 24 h, the peritumoral region had lower uptake of platinum compared to the tumour region, yet this was not significant. Regarding the other organs, the results are displayed in the annexe A.5.2 (Figure 88). For the groups that received an injection of carboplatin and harvested 1 h after, except for the heart that have comparable values found in the brain, in the kidney, spleen and liver the concentrations of carboplatin. At 24 h, the kidney is the organ with the highest concentrations of all. Only one animal per group was analysed, thus we cannot provide statistical analysis, yet FUS-induced BBB opening seems to induce a larger extravasation of carboplatin that persists 24 h after. Thus, at the time of the radiotherapy, there is still a strong presence of platinum and a potential increased radiosensitising effect.

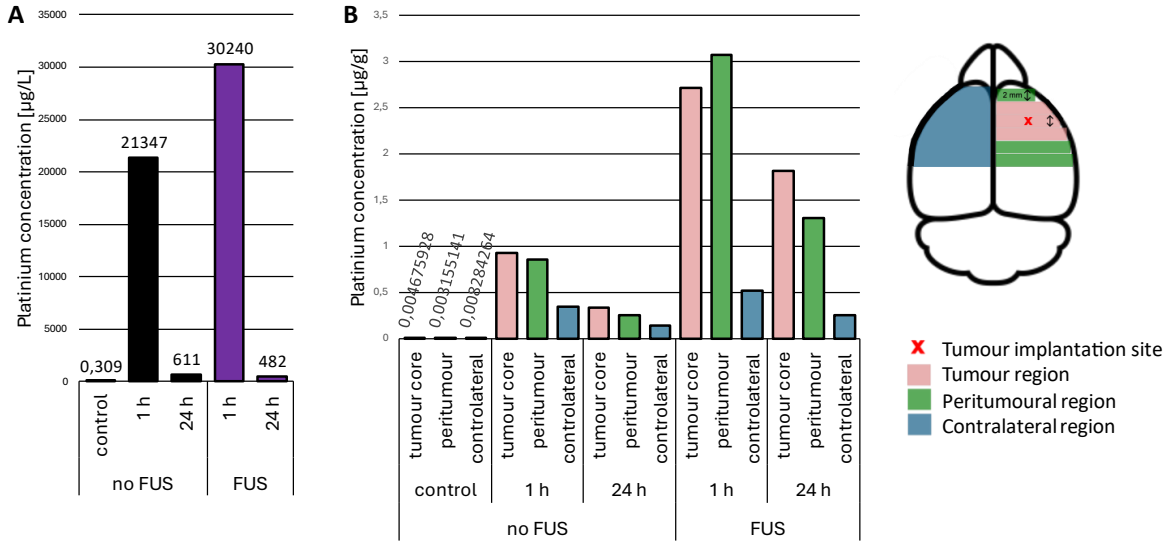


*Figure 69. Platinum biodistribution. **A**) Concentration of platinum in the tumour, **B**) peritumoral and **C**) contralateral regions for groups that did not receive carboplatin, that received carboplatin only and carboplatin coupled with FUS 1 h and 24 h post-FUS.*

7.2.3. Survival, weight

In terms of weight, rats gained weight normally after tumour implantation (data not shown). After the treatment, rats in the untreated and radiotherapy groups continued to gain weight until they were euthanised due to the ethical limits reached. On day 14 after treatment, a slowdown was observed in the radiotherapy group (Figure 70.A.i-ii). In the groups receiving carboplatin, most of the animals started to lose weight between 5 and 15 days after treatment in the most extreme case. They then started to regain weight before reaching a plateau or decreasing in the last days of their lives (Figure 70.A.iii-iv).

Regarding the survival rate, median survival time (MeST) for untreated, RT, FUS+CarboPt and FUS+CarboPt+RT were respectively 30.5, 41.5, 30 and 60 days. It corresponds to increased rate of 40% and 100% for RT and FUS+CarboPt+RT groups relative to the untreated. Significant increase in life span between RT and untreated groups was measured, as well as FUS+CarboPt+RT and untreated groups group and were found statistically significant ($p < 0.001$ and $p < 0.05$), respectively (Table 17). MeST was not found significant between RT and FUS+CarboPt+RT groups but we observed a 45% increase of MeST. No significant increase in the MeST between the untreated and FUS+CarboPt group that received carboplatin was observed. We also observed early deaths in groups that received a carboplatin injection (3 in the FUS+CarboPt group and 2 in the FUS+CarboPt+RT group) (Figure 70.B).

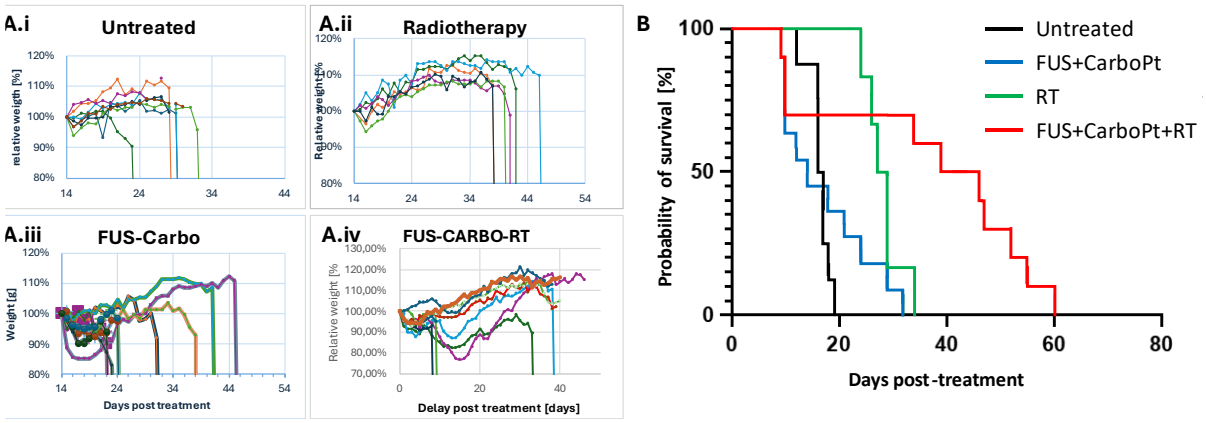


*Figure 70. Weight and survival rate evolutions. **A**) Relative weight evolution post-treatment for untreated (**i**), radiotherapy (**ii**), FUS+CarboPt (**iii**) and FUS+CarboPt+RT (**iv**). **B**) Kaplan-Meier survival curve after the treatment. The data were analysed with a Log-rank test and the results are displayed in Table 17.*

	***p*-value**	**Significant**	**%ILS**
Untreated vs FUS + CarboPt	0.4873	ns	0%
Untreated vs RT	0.0003	***	40%
Untreated vs FUS + CarboPt + RT	0.0207	*	100%
FUS + CarboPt vs FUS + CarboPt + RT	0.0038	**	100%
RT vs FUS + CarboPt + RT	0.0511	ns	45%

*Table 17. Summary of Kaplan-Meier survival survival curve statistical test. Results were analysed with a Log-rank test with PRISM software (ns, non-significant; *p < 0.05; **p < 0.01, ***p < 0.001). Percent increase in life span (%ILS).*

7.2.4. Tumour growth rate and MRI analysis

Tumour growth was followed by MRI with the acquisition of anatomical T2-w image, ADC and CBF parameters and DCE-MRI sequence to assess BBB permeability. An overview is displayed in Figure 71. Three different patterns can be distinguished within the hemisphere where the tumour was implanted. First the necrotic core of the tumour with low perfusion, high diffusivity, hyperintense on T2-w image without evidence of Gd-DOTA extravasation. Then, the region of the tumour growth with high perfusion, low diffusivity and high BBB permeability. This pattern is due to the angiogenesis phenomenon with tortuous and leaky vessels and is a typical pattern seen in high grade gliomas such as glioblastoma. As shown in panels A and B of the Figure 71 and in Figure 89 (annexe A.5.3), we observed that the tumour evolution was different between the groups. At 29 days after tumour implantation (15 days after the treatment), the tumour in the untreated group was very large (544 ± 236 mm^3, n = 3) and the left hemisphere was compressed by tumour the progression. In the FUS+CarboPt group, the tumour was growing slower than in the untreated group, but a necrotic part was already visible and the area of hyperintensity on the T2-w image was equal to 123 ± 15 mm^3 (n = 3). On day 29 after the implantation, brains from the RT and FUS+CarboPt+RT groups appeared similar with a reduced tumour growth and no necrotic part (T2-w hyperintensity volumes: 168 ± 63 mm^3 and 92 ± 44 mm^3, respectively). The large hyperintensity volume is probably residual oedema in the RT group. On day 35 after the implantation, we observed greater differences between brains from the RT and FUS+CarboPt+RT groups. In the RT group we observed a necrotic part with low permeability surrounded by a highly perfused region, indicating disease progression. For the FUS+CarboPt+RT group, tumour progression seemed to be slowed down without the presence of a necrotic part. However, this region appeared to be highly perfused, probably due to angiogenesis processes. Volumes from RT and FUS+CarboPt+RT at on day 35 were equal to 369 ± 159 mm^3 and 114 ± 38 mm^3 (Figure 71.C).

In conclusion, the combination of FUS and MB to permeabilise the BBB, coupled with the injection of carboplatin followed 24 hours later by a single 15 Gy dose of radiotherapy, appears to slow tumour progression compared to the radiotherapy, or the FUS and carboplatin alone as measured by weekly MRI follow-up, despite the highly invasive nature of this type of brain tumour. Further complete analysis of all MRI data should provide more accurate conclusions on tumour growth patterns, permeability of the tumour and treatment efficacy by applying previously published tumour characterisation algorithms [Arnaud *et al.*, 2018; Bouchet *et al.*, 2017; Galbán *et al.*, 2015; Lemasson *et al.*, 2011, 2010].

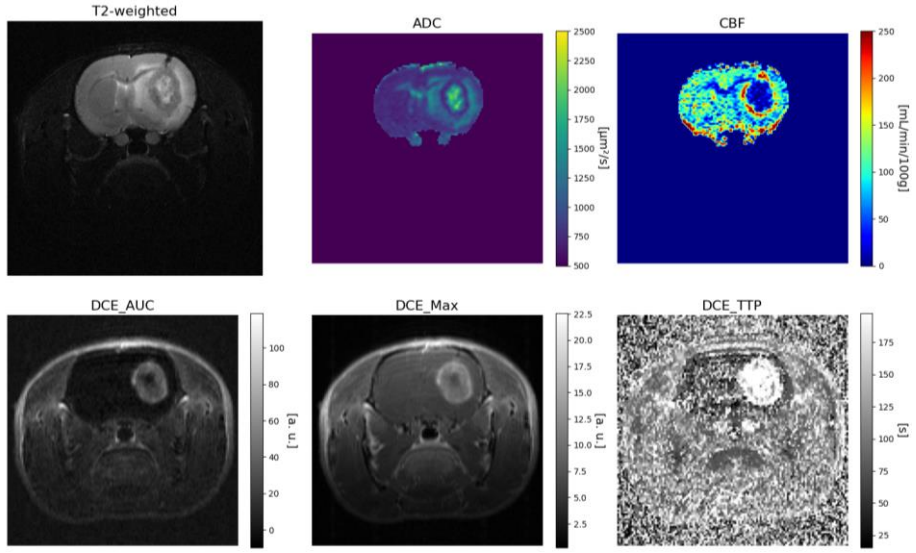


Figure 71. Representative example of the different parameters measured longitudinally following the treatment.

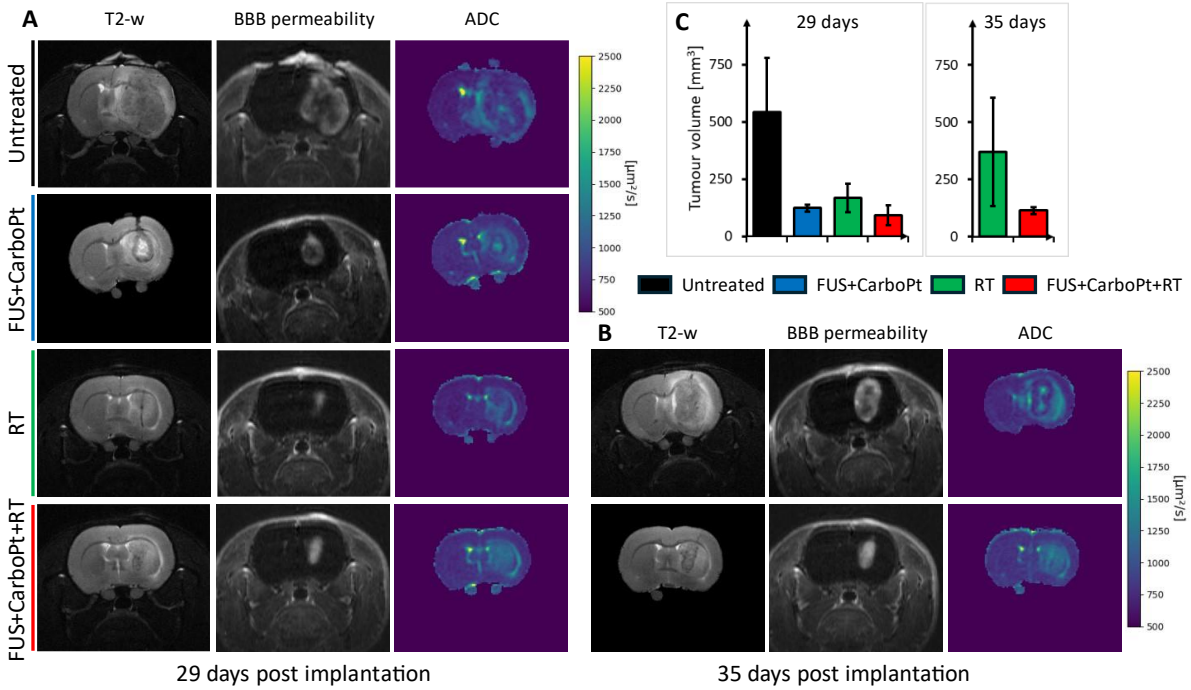


*Figure 72. Representative examples of T2-w, BBB permeability and ADC parameters 29 days (panel **A**) and 35 days (panel **B**) post implantation. Treatment was performed on the same day (day 14). CBF maps are shown in annexe A.5.3, Figure 89 for the sake of clarity. By 35 days post implantation, all rats in the untreated group had died and rats in the FUS+CarboPt groups were not imaged to avoid additional anaesthesia (only 3/8 were still alive). **C**) Average tumour size delineated on T2-w images 29 and 35 days after tumour implantation.*

7.3. Discussion and conclusion

This study presents the first attempt to apply the combination of FUS to permeabilise the BBB with an injection of carboplatin and followed by radiotherapy. We improved the delivery of carboplatin with a large BBB opening in the tumour core and in the peritumoral area. The enhanced concentration of carboplatin was found increased in the brain at the level of the open BBB 24 h, the timing of the radiotherapy. We observed an increase in the median survival time in the radiotherapy and the group treated with the combination of FUS, carboplatin and radiotherapy compared to the untreated group, with an increase in lifespan of 40% and 90%. The treated group showed a 36% increase in lifespan compared to the radiotherapy group. Animals tolerated quite well the treatment procedure, yet 5 rats in the two groups that received an intravascular injection of carboplatin showed early death. Potentially due to the carboplatin dose. The dose used in this study was similar to the dose used in previous studies [McDannold *et al.*, 2019].

We used the F98 model, which is a model largely accepted to mimic glioblastoma development in the human brain due to its infiltrative capacity as observed in the MRI with a strong increase in the ADC values in the white matter area. Many studies have already been conducted in this model as highlighted in Table 18 with the evaluation of a large range of chemotherapies and radiation therapy protocols. Except the studies from Rousseau *et al*. and Bobyk *et al*. that demonstrated unprecedented increases in survival lifespan with 17% of long-term survivors after convection-enhanced delivery and LINAC irradiation [Rousseau *et al.*, 2007] and 55% of long-term survivors with an infusion of carboplatin with Alzet® osmotic pumps followed by stereotaxic synchrotron radiotherapy or LINAC irradiation [Bobyk *et al.*, 2012; Rousseau *et al.*, 2009], no other studies demonstrated similar results in term of increase in lifespan. One can note that the use of convection-enhanced delivery is very invasive and will probably not be transferred into clinics in the following decades and the studies that used Alzet® osmotic pumps started the carboplatin infusion only 7 days after the tumour implantation. Consequently, the tumour was less developed, and the effect of the chemotherapy started earlier. McDannold *et al*. injected 2×10^4 F98 cells and started 8 days after the treatment of the rats with FUS and the injection of carboplatin [McDannold *et al.*, 2019], yet according to a recent study that compared different number of inoculated cells, the treated tumours can be found equivalent [Zoteva *et al.*, 2024]. We can see that a single application of FUS coupled with the injection of carboplatin did not improve the animal outcome, yet, with 2 sessions of treatment, a significant improvement in the lifespan was found [McDannold *et al.*, 2019].

In this study we did not monitor the acoustic cavitation, an important parameter for the safety of the BBB opening, but the pressure used has been evaluated as safe [Chu *et al.*, 2016] and the study presented in the Chapter 5 of this thesis with the same equipment demonstrated safe BBB opening with a pressure equal to 0.6 MPa and with the monitoring of the cavitation (5.1.2). In addition, the early death observed in some rats is probably due to the toxicity of the carboplatin, which is responsible for the important weight loss, a phenomenon previously reported [Siddik *et al.*, 1987]. We assume that the permeabilisation of the BBB increases the brain toxicity, observation not reported by McDannold *et al*. [McDannold *et al.*, 2019], but further studies need to take into account the dose of carboplatin and evaluate the potential effects of carboplatin delivered by FUS in more detail. In GBM patients who received repeated doses of carboplatin and repeated FUS-induced permeabilisation of the BBB, there was also no increase in toxicity [Carpentier *et al.*, 2024; Idbaih *et al.*, 2019].

Treatment	Animal model	Mean survival time [days]		%ILS (relative to untreated)	References
		Untreated	Treated		
CED	F98 rat	28	45	61%	[Rousseau *et al.*, 2007]
CED + 3 × 5 Gy$^{\$, €}$	F98 rat	23	58$^{€}$	15%	[Yang *et al.*, 2011]
CED + 3 × 8 Gy$^{\$, €}$	F98 rat	28	60$^{\$}$ / 79$^{€}$	114% / 182%	[Rousseau *et al.*, 2007]
OP + 15 Gy$^{\$, €}$	F98 rat	24	195$^{\$}$ *	713%	[Bobyk *et al.*, 2012; Rousseau *et al.*, 2009]
		33	180$^{€}$ *	445%	
4 × FUS	U87LN mice	24	35.5	48%	[Dréan *et al.*, 2019]
	6240LN mice	54	79	46%	
2 × FUS	F98 rat	25	41.5	66%	[McDannold *et al.*, 2019]
FUS + 15 Gy$^{¥}$	F98 rat	27	33	22%	[Stecia-Marie P. Fletcher *et al.*, 2024]
FUS	F98 rat	30.5	30	0%	This study
FUS + 15 Gy$^{¥}$	F98 rat	30.5	60	100%	This study

*Table 18. Summary of preclinical studies on F98 rats with different methods of carboplatin administration in combination with different radiotherapy methods and FUS. Radiotherapy delivered with stereotaxic synchrotron radiotherapy, linear accelerator and SARRP are highlighted with $^{\$}$, $^{€}$ and $^{¥}$ respectively. Osmotic pump, OP. *Biased, censored survival (end of study). In grey is highlighted the studies that did not involve carboplatin injection.*

In conclusion, this study showed encouraging results for the treatment of glioblastoma by combining BBB permeabilisation with FUS and MB, carboplatin injection and radiotherapy. These results pave the way for a future phase 1 clinical trial to improve the outcome of GBM patients. Future studies will have to combine the possible repetition of the BBB opening, the injection of carboplatin and the splitting of the radiotherapy dose, taking into account the toxicity and secondary bioeffects of all these components, which have already been highlighted in previous studies, as well as our study presented in the Chapter 6 with new insight into secondary bioeffects of repeated FUS-induced BBB opening.

Chapter 8. Study 4: Whole brain gene delivery in a *Fmr1^{KO}* mice model of fragile X syndrome

In this chapter, we will present part of the outcome from an ongoing study I was involved in during my thesis. The first step was the validation of the method for the permeabilisation of the BBB in the whole brain, already presented in 4.4.1 and presented at the 6th SFRMBM during my 2nd year of PhD [Rigollet *et al.*, 2023]. Then this protocol was applied in two knock-out mice models of the fragile X syndrome (FXS) and the Leigh syndrome. The project involving *Ndufs4KO* mice for the model of the Leigh syndrome with Dr Michael Decressac's team aimed to evaluate a gene therapy protocol using viral vectors delivered by FUS to target and restore mitochondrial function in this mouse model. The results will not be presented here.

The study on the fragile X syndrome was initiated in the laboratory of Pr Chantal Pichon and Dr Anthony Delalande in collaboration with Dr Anthony Laugeray from NBPHARMATOX (Orléans, France) and Dr Arnaud Menuet (INEM, Orléans, France). This study is one of the main projects from the Ph.D. thesis of Thomas Ador. In this section, I will briefly expose the methods and results from the experiments in which I took part. A lot of validation experiments, work on the gene expression and MB formulation was done earlier at Orléans by Thomas Ador and Mylène Fournié as well as many BBB opening and bioluminescence follow-up of the gene expression. In Grenoble, as we developed and validated the protocol to permeabilise the whole brain in mice (4.4.1), Thomas Ador came to realise the BBB opening in wild-type (WT) and in *Fmr1^{KO}* mice and the behavioural follow-up of these mice, using the facilities available at GIN. During this 4-months period, I realised with Thomas Ador the BBB opening and performed the MRI acquisitions. Thomas Ador performed the behavioural follow-up with the aid of Dr Anthony Laugeray, the immunohistological analysis with Mylène Fournié and Dr Arnaud Menuet.

FXS is the most common inherited form of intellectual disability and a leading genetic cause of autism spectrum disorder. It is caused by a mutation in the *Fmr1* gene, located on the X chromosome. In individuals with FXS, a segment of DNA known as a CGG trinucleotide repeat is expanded within the *Fmr1* gene, leading to its silencing. This methylation of the *Fmr1* promoter causes gene silencing and loss of expression of the protein product, fragile X mental retardation protein (FMRP). FMRP plays a crucial role in brain development and functioning. This disease affects approximately 1 in 4000 males and 1 in 8000 females [Crawford *et al.*, 2001; Visootsak *et al.*, 2005]. The manifestations of FXS are variable and depend on sex, age (Figure 73.A), background genetic effects, environmental influences and molecular variations. In the case of individuals with a premutation (50 to 200 CGG repeats), variations in methylation levels can lead to differences in FMRP production. This is due to reduced methylation compared to the full mutation, which typically has over 200 CGG repeats. It is important to note that in individuals with a full mutation, FMRP is absent. Additionally, in those with a premutation, there is often an overexpression of *Fmr1* mRNA, although FMRP levels are still downregulated by a mechanism that remains not fully understood [Dyer-Friedman *et al.*, 2002; Loesch *et al.*, 2004]. While some physical features of FXS can include prominent ears (Figure 73.B), a long face, flat feet, hyperextensible finger joints, double-jointed thumbs, soft skin and macroorchidism developing around puberty, these traits are not consistently present in all individuals [Hagerman *et al.*, 2017].

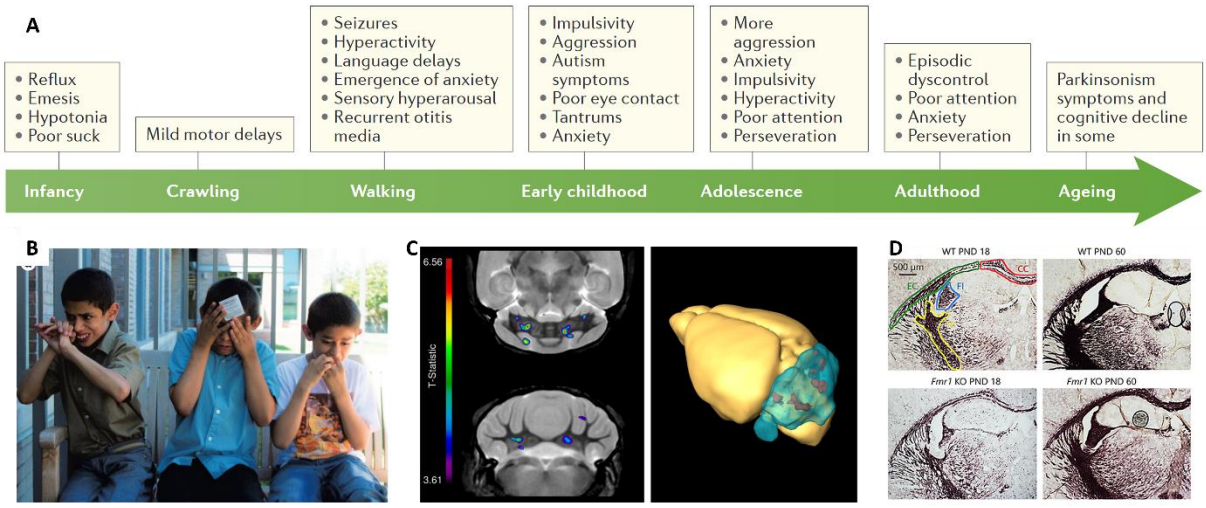


Figure 73. Overview of FXS features. ***A****) Clinical features of FXS during the infancy to adulthood [Hagerman* et al.*, 2017].* ***B****) Three brothers with FXS show prominent ears and have typical behaviour features such as stereotyped movements of the hands (the boy on the left), avoiding eye contact (the boy on the centre) and hand biting (the boy on the right) [Hagerman* et al.*, 2017].* ***C****) T2-w image and 3D representation of an Fmr1KO mice brain with significant volume decrease highlighted in the cerebellum [Ellegood* et al.*, 2010].* ***D****) Representative image of myelin staining with Black Gold II in wild-type and Fmr1^{KO} mice. Approximate ROIs are drawn with corpus callosum (CC) in red, external capsule (EC) in green, internal capsule (IC) in yellow, and fimbria (FI) in blue. One can note a significant decrease of density in the EC, IC and FI at postnatal days 18 (PND 18) and in the EC and IC at PND 60 [Shi* et al.*, 2019].*

FXS is the most common inherited form of intellectual disability and a leading genetic cause of autism spectrum disorder (ASD). It is caused by a mutation in the *Fmr1* gene, located on the X chromosome. In individuals with FXS, a segment of DNA known as a CGG trinucleotide repeat is expanded within the *Fmr1* gene, leading to its silencing. This methylation of the *Fmr1* promoter causes gene silencing and loss of expression of the protein product, fragile X mental retardation protein (FMRP). FMRP plays a crucial role in brain development and functioning. This disease affects approximately 1 in 4000 males and 1 in 8000 females [Crawford *et al.*, 2001; Visootsak *et al.*, 2005]. The manifestations of FXS are variable and depend on sex, age (Figure 73.A), background genetic effects, environmental influences and molecular variations. In the case of individuals with a premutation (50 to 200 CGG repeats), variations in methylation levels can lead to differences in FMRP production. This is due to reduced methylation compared to the full mutation, which typically has over 200 CGG repeats. It is important to note that in individuals with a full mutation, FMRP is absent. Additionally, in those with a premutation, there is often an overexpression of *Fmr1* mRNA, although FMRP levels are still downregulated by a mechanism that remains not fully understood [Dyer-Friedman *et al.*, 2002; Loesch *et al.*, 2004]. While some physical features of FXS can include prominent ears (Figure 73.B), a long face, flat feet, hyperextensible finger joints, double-jointed thumbs, soft skin and macroorchidism developing around puberty, these traits are not consistently present in all individuals [Hagerman *et al.*, 2017]. More commonly, FXS is considered an 'invisible' disability, as physical features are often subtle or absent. The primary manifestations of the syndrome are intellectual disability, often accompanied by behavioural traits such as autism spectrum disorder, hyperactivity, and attention deficits, as highlighted in Figure 73.A. There are still no treatments for FXS, but the emergence of an animal model in which the *Fmr1* gene is knocked out has made possible to develop and identify different therapeutic strategies. The introduction of the *Fmr1^{KO}* mice model by *The Dutch-Belgian Fragile X Consortium* in

1994 has since served as a valuable tool for the study of the physiological, behavioural, and biological mechanisms involved in mental retardation and more particularly in FXS [The Dutch-Belgian Fragile X Consortium, 1994]. Yet, the first generation of this model presented residual expression of truncated mRNA (thus not producing FMRP protein), with potential less reliable phenotype and behaviour among subjects. Thus, a second generation was developed to make up for these deficits [Mientjes *et al.*, 2006], and this was the model used in this study. *Fmr1*^{KO} mice show macroorchidism, cognitive and other behavioural deficits comparable to those of human FXS patients. In addition, the abnormally long and thin dendritic spines characteristic of FXS patients are also found in juvenile KOs. *Fmr1*^{KO} mice have been tested in several behavioural tasks relevant to FXS and these animals have therefore been validated as a model for the disease [Bernardet and Crusio, 2006]. In addition, from a more structural perspective, the *Fmr1*^{KO} mice brains have been extensively characterised and possess significant reduction of volume (Figure 73.C) [Ellegood *et al.*, 2010], white matter alteration (Figure 73.D) [Shi *et al.*, 2019], structural connectivity alterations [Haberl *et al.*, 2015] and functional MRI dysregulation [Kenkel *et al.*, 2016]. All the measured and characterised patterns seemed to mimic the human symptoms very well, making it an excellent model for studying this pathology. Different therapeutic approaches were developed and validated as reviewed by Hagerman *et al*. [Hagerman *et al.*, 2017]. In addition, an extensive review of the clinical trials derived from preclinical work was conducted by Watkins and colleagues [Watkins *et al.*, 2024]. Among all treatments, Phase I and II clinical trials targeting the mGluR1 signaling pathway (an essential molecular mechanism involved in synaptic plasticity, neuronal communication and cognitive functions such as learning and memory) initially demonstrated promising results [Berry-Kravis *et al.*, 2016, 2012; Jacquemont *et al.*, 2011]. However, later results were disappointing, with some trials revealing that the treatment performed no better, and in some cases, even worse than placebo. Progress with targeted and symptomatic treatments is still insufficient and etiological approaches for FXS treatment could be more effective by reversing epigenetic marks [Shitik *et al.*, 2020]. One of the most promising etiological approaches is gene therapy, a potential therapeutic strategy that aims to correct or compensate for the underlying genetic defect. Two studies have shown a reactivation of the *Fmr1* gene by CRISPR/Cas9 [C.-Y. Park *et al.*, 2015; Xie *et al.*, 2016]. In addition, Chadman *et al*. demonstrated efficient delivery of *Fmr1* through the BBB with an AAV-PHP.B construction [Chadman *et al.*, 2023] and Wong *et al*. showed a rescue in different phenotypes of *Fmr1*^{KO} mice by delivering with an intrathecal injection AAV [Wong *et al.*, 2023]. These studies are one of the most encouraging therapeutic approaches for treating FXS patients, yet their transfer to clinics will be very difficult but they paved the way to AAV-like therapeutic approaches. However, the AAV-PHP.B vector is not FDA approved and further investigations need to be performed in order to validate its use in clinics [Hordeaux *et al.*, 2018] (see 1.3). Yet, the use of other AAV vectors as the AAV type 9 vector was validated by the FDA in May 2019 for the treatment of type 1 spinal muscle atrophy after the concluding results from three clinical trials (NCT01839656, NCT02193074 and NCT02386553) [Finkel *et al.*, 2016] and offers solutions for gene therapy in rare diseases. However, the passage of AAV is prevented by the BBB. Recently, the combination of AAV delivery with FUS to permeabilise the BBB has shown promising results in mice models [Felix *et al.*, 2021; Owusu-Yaw *et al.*, 2024; Thévenot *et al.*, 2012] and in large animal model with limited secondary bioeffects [Blesa *et al.*, 2023].

Therefore, in this study, we aimed to evaluate a viral gene therapy protocol for FXS, a genetic disorder causing intellectual disability, by FUS-induced BBB opening on adult male *Fmr1*^{KO} mice.

8.1. Methods

57 *Fmr1*^{KO} mice over 8 weeks-old weighing approximately 26 ± 5 g at the beginning of the procedure were used in this study. All experimental procedures were validated by the French Ministry of Education and Research and by the local ethics committee under APAFIS n° 43777, n° 47771 and n° 47394. Two types of AAV produced by the viral vector production centre from the INSERM gene therapy laboratory (TaRGeT facility, UMR1089, Nantes, France) were used: AAV2/9.CMV.Luciferase encoding Luciferase gene under CMV promoter and AAV2/9.CMV.*Fmr1*-eGFP encoding Fmr1-GFP gene under CMV promoter at a dose of 1×10^7 vg. Two experiments were conducted, the first to assess the longitudinal expression of the *Fmr1* gene, and the second to perform experimental behaviour analysis from 3 to 8 weeks after the treatment. For the first experiment, one group of C57BL/6 mice underwent a FUS treatment and an injection of AAV2/9.CMV.Luciferase and the second only received an AAV2/9.CMV.Luciferase intravascular dose (Figure 74). They were followed longitudinally with the Luciferase reporter and bioluminescence imaging. Bioluminescence imaging was performed at the Optimal imaging facility (Grenoble, France) from 2 weeks to 8 weeks post AAV injection. For the second experiment, we distinguished 4 groups: untreated wild-type (WT) mice, untreated *Fmr1*^{KO} mice, FUS-only *Fmr1*^{KO} mice, and *Fmr1*^{KO} mice treated with FUS and AAV2/9.CMV.*Fmr1*-eGFP. The latter will be called the treated group. FUS-induced BBB opening was realised as described in 4.4.1 with a PNP estimated to 370 kPa *in situ*. We injected approximately 7.5×10^7 MB before applying FUS. Behavioural experiments were performed at the Animal housing facility of the GIN (Grenoble, France) and included a series of different tests. The open field, the social open field, the elevated plus maze and the direct interaction test were performed 3 weeks after the treatment. The novel recognition test was performed at 5 or 6 weeks, and the Marble and the Y-maze at 7 or 8 weeks. These tests enable us to monitor different behavioural phenotypes such as anxiety, obsessive-compulsive behaviour, sociability, locomotor activity (hyper- or hypoactivity), learning and memory skills. At the end of the procedures, brains and livers were harvested to perform histology and RT-qPCR. The results were analysed using a bilateral Mann-Whitney test with R studio (version 4.4.0).

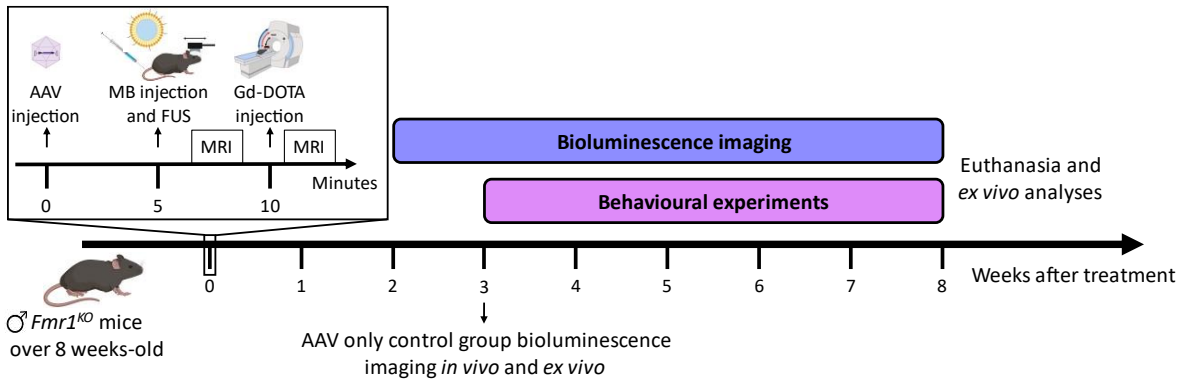


Figure 74. Summary of the experimental timeline.

8.2. Results

8.2.1. Blood-brain barrier opening and safety of the procedure

The BBB was permeabilised in all mice and assessed by the Gd-DOTA injection and T1-w images. An average of 62.9 ± 0.6 % of the total volume brain was permeabilised (Figure 75). No differences were found across the different groups (WT, FUs-only *Fmr1*^{KO} mice and treated *Fmr1*^{KO} mice).

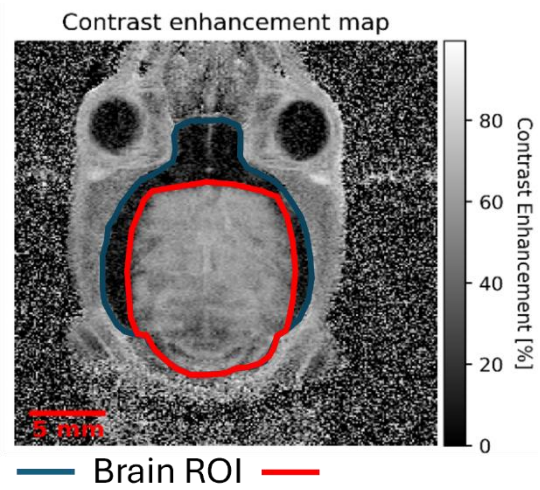


Figure 75. Representative contrast enhancement map. In red is highlighted the opened BBB area and in blue the brain contour. The dark area around the red area corresponds to brain tissue with closed BBB.

8.2.2. FUS-BBB opening enables stable gene expression

Histological analysis of the brains from untreated *Fmr1*^{KO} mice, untreated WT mice and the treatment combination of AAV and FUS in *Fmr1*^{KO} mice was performed 8 weeks after the treatment. We can see that the FMRP was successfully expressed in the brain of *Fmr1*^{KO} mice at different locations as in the hypothalamus (Figure 76.B) and the prefrontal cortex (Figure 76.C). RT-qPCR measurements 8 weeks after the injection of the AAV and the FUS treatment showed a significant expression of *Fmr1* in the brain of *Fmr1*^{KO} mice compared to untreated *Fmr1*^{KO} mice. Yet, expression level of WT mice remained significantly higher than treated mice (Figure 76.D).

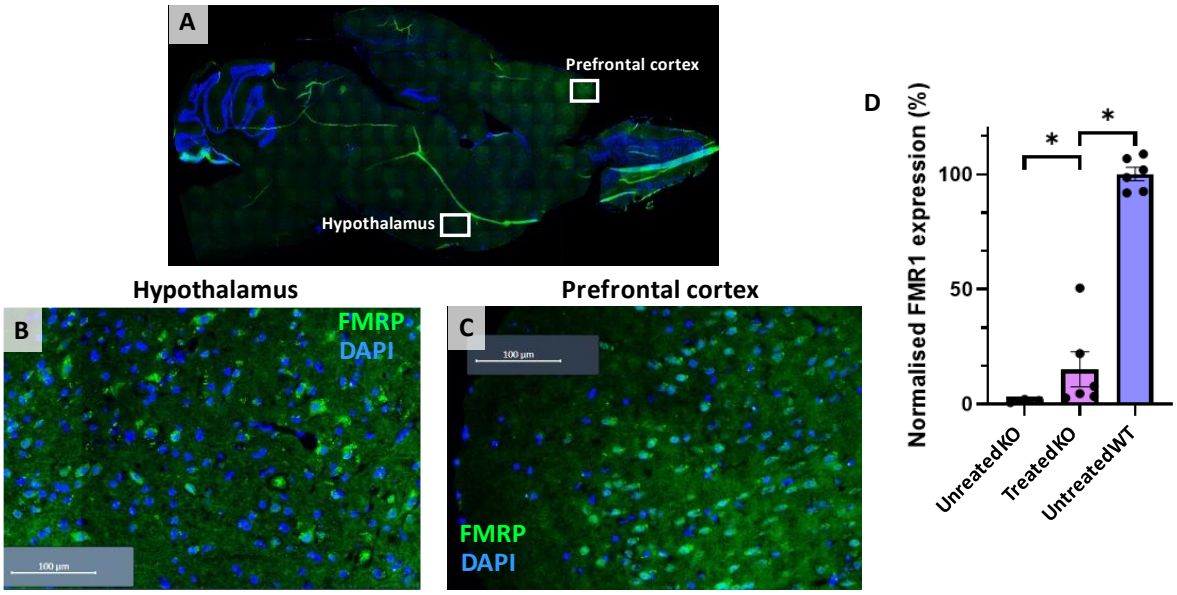


*Figure 76. Histological investigation of the brain in WT and Fmr1^{KO} mice. **A**) Scanning microscopy fluorescence image showing a sagittal brain section stained for FMRP (green) and DAPI (blue). **B**) and **C**) Enlargement of the hypothalamus and prefrontal cortex with a white square in the image above (**A**). **D**) Bar plot showing the changes in normalised Fmr1 expression for untreated Fmr1^{KO}, treated Fmr1^{KO} and untreated WT mice. The data were analysed using bilateral Mann-Whitney test (*p < 0.05). The results are expressed as mean ± SEM.*

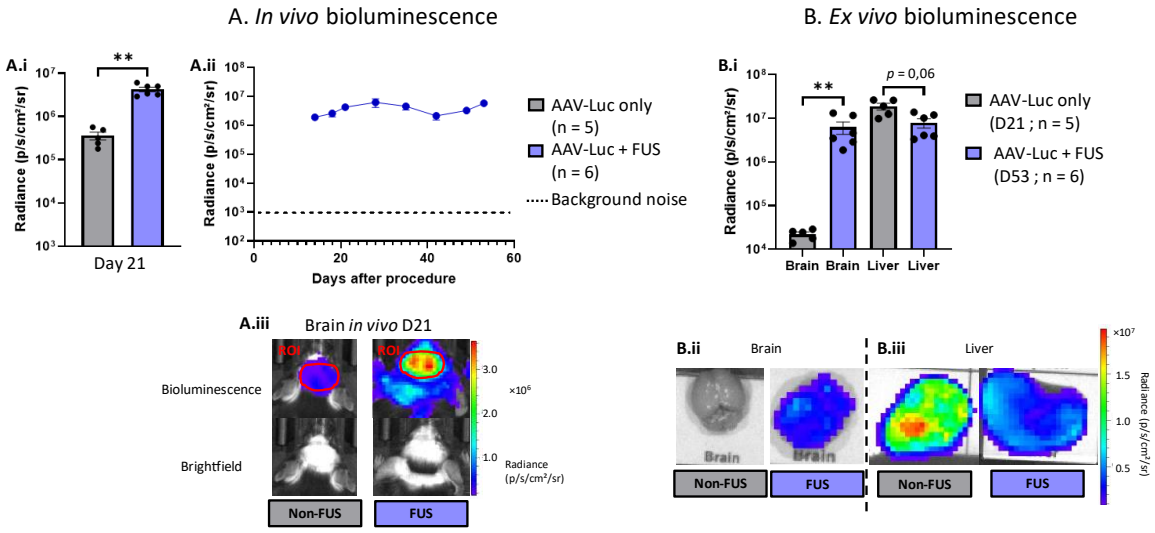


*Figure 77. Gene transfer is assessed by bioluminescence. **A**) In vivo and **B**) ex vivo bioluminescence measurements. **A.i**) Bar plot showing the average radiance 21 weeks after AAV injection for the FUS-treated mice and non-FUS-treated mice. **A.ii**) Longitudinal radiance for treated mice, the background noise corresponds to the ambient measured noise without any animal **A.iii**) Representative in vivo bioluminescence images 21 days post-treatment for FUS and non-FUS mice. **B.i**) Bar plot showing the average radiance in the brain and liver for FUS (day 53) and non-FUS (day 21) mice. **B.ii**) Representative ex vivo bioluminescence images of the brain for FUS (day 53) and non-FUS (day 21) mice. The data were analysed using bilateral Mann-Whitney test (**p < 0.01). The results are expressed as mean ± SEM.*

The longitudinal evaluation of the luciferase expression after the injection of the AAV2/9.CMV.Luciferase and FUS application was assessed with bioluminescence imaging every week for 6 weeks starting 2 weeks after AAV injection for the group that received FUS and an AAV injection.

Despite the background noise from the skin, we did see an increase in the bioluminescence signal in the FUS-treated mice compared to non-FUS-treated mice (Figure 77.A.iii). 21 days after the treatment procedure including FUS and AAV injection, we can see a significant increase in Luciferase expression (20-fold) compared to mice that only received the AAV injection (Figure 77.A.i).

The expression was stable from day 14 to day 53 when the mice were euthanised for histological and RT-qPCR analysis. No significant differences between day 14 and day 53 timepoints were measured. *Ex vivo* bioluminescence showed that 21 days post-AAV injection and FUS application, a 200-fold increase in bioluminescence signal was measured compared to the non-FUS-treated mice group (Figure 77.B.ii). 8 other organs were analysed (liver, testicles, heart, pancreas, kidney, lung, spleen and intestine), they did not show significant difference in expression. For the liver, we did not measure a significant difference between the signal from AAV-only mice at day 21 and treated mice at day 53 (Figure 77.B.i). Yet, we can see an increase in the signal at day 21 (AAV-only) compared to day 53 (treated) in the Figure 77.B.iii.

8.2.3. Gene therapy partially rescues FXS phenotypes

Regarding the behavioural tests, we will present the results from the most representative tests conducted for a more concise presentation. The marble test aims at measuring anxiety and obsessive-compulsive behaviour. It is heavily used in the evaluation of autism spectrum disorder models [Angoa-Pérez *et al.*, 2013] and consists in a number of glass or plastic marbles evenly spaced on the surface of bedding in a cage. This animal is placed in the cage and, every 5 minutes for 30 minutes the number of marbles buried (at least 3/4) by the mouse is counted. The direct interaction test aims at observing the sociability of the subject, that is to say the disposition to interact with one another [Kim *et al.*, 2019]. The open field test describes animal hyperactivity.

We observed that for the open field test, compared to the WT, a significant increase of the distance travelled was observed for *Fmr1*^{KO} mice. This is due to the hyperactivity of the *Fmr1*^{KO} mice. FUS coupled with AAV or not demonstrated a significant decrease in the distance travelled compared to untreated *Fmr1*^{KO} mice. No difference was observed between the two groups that received a FUS treatment (Figure 78.A). For the marble test, we calculated the area under the curve of the marbles buried as a function of time and these values were compared between groups. A significant difference was measured between WT and KO mice, showing the lowered anxiety-driven marbles burying phenotype of KO mice. No significant rescue was observed for the FUS-only group, but a significant rescue to WT value for the treated group was observed (Figure 78.B).

For the direct interaction test, a significant increase in the sniffing time was observed between WT and *Fmr1*^{KO} mice. A decrease, yet non-significant, was observed between the *Fmr1*^{KO} mice and treated *Fmr1*^{KO} mice either with FUS and AAV or FUS alone (Figure 78.C).

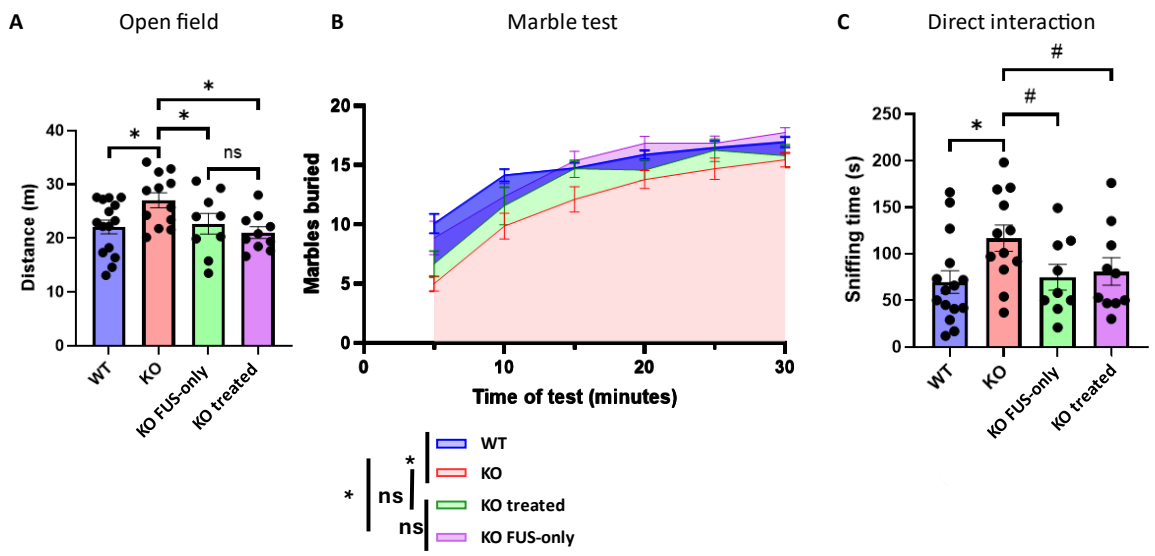


*Figure 78. Behavioural results. **A**) Bar plot showing the average distance travelled across the different groups for 5 minutes. **B**) Evolution of the number of marbles buried during the session of 30 minutes starting from 5 minutes. **C**) Bar plot showing the average sniffing time during 10 minutes between two mice in the direct interaction chamber. The data were analysed using a bilateral Mann-Whitney test (# non-significant difference, *p < 0.05). The results are expressed as mean ± SEM.*

To conclude, we observed that both treated groups have recovered from their hyperactivity and similar distance travelled from WT was measured after the treatment. Plus, only the FMRP re-expression associated with FUS treatment restores anxiety phenotypes to WT values (given the marble test results) and finally, both treated groups seem to rescue their social behaviour.

8.3. Discussion and conclusion

To conclude, we efficiently delivered AAV-like viral vectors with the permeabilisation of the whole brain by FUS and MB. The procedure was safe, and animals did not show any sign of haemorrhage or oedema after MRI monitoring. Transgene expression was followed in bioluminescence for 6 weeks, starting 2 weeks after the injection. The expression remained stable over time and was significantly higher with the use of FUS and MB to open the BBB. Immunohistological staining revealed that transgene expression in *FMR1*^{KO} mice was significant in the brain compared to untreated *FMR1*^{KO} mice. We could see a good distribution all over the brain. However, *Fmr1* gene expression in untreated WT mice was 7-fold higher than in Fmr1KO mice after BBB permeabilisation and injection of the gene therapy vector. Analysis of the behavioural results, and more specifically the open field test, the burying test and the direct interaction test, showed more or less good restoration of the phenotype. *Fmr1*^{KO} mice tended to cover significantly more distance in the open field test compared with WT mice and the use of FUS alone or FUS combined with injection of the viral vector showed a significant reduction in the distance covered. But no difference was observed between these two groups. The burying test showed a significant difference in the number of objects buried between Fmr1KO mice and mice treated with FUS, suggesting a reduction in anxiety. Finally, the direct interaction test did not show any significant differences between groups that received an AAV injection and FUS compared to FUS only, although shorter sniffing times were observed after treatment compared to FMR1^{KO} mice control. Thus, we observed that both treated groups recovered their hyperactivity and that a distance similar to that of the WT was measured after treatment. These results suggest that the effects of FUS

with or without the gene therapy vectors restored similarly the phenotypes of mice. In our study, we measured the overall expression levels of the transgene, and we are seeking to evaluate in detail the cell types that express this transgene.

Further studies should focus on improving the delivery of AAV-type vectors to enhance brain transduction. Since AAV treatments cannot be repeated, improving tissue delivery through nanobubbles that penetrate small capillaries could address this limitation. Repeated FUS delivery in non-viral gene therapy strategies may help overcome this issue. Moreover, replacing the ubiquitous CMV promoter used in this study with GFA2 or hSyn, which offer more physiological expression, could provide better regulation of FMR1 expression. A recent study by Li *et al*. has developed a new generation of AAV-type vectors that improve neuronal transduction in the brain while reducing unwanted transduction in peripheral organs [Li *et al*., 2024]. Future research could leverage this advancement to enhance protein re-expression and restore phenotypic function. Additionally, FUS-induced BBB opening may have already a therapeutic benefit by triggering the SIR and facilitating the clearance of Aβ plaques [Burgess *et al*., 2014; Jordão *et al*., 2013; Leinenga and Götz, 2015].

Currently, this technique has not yet been translated to clinical use, and no clinical trials have been conducted. A recent study using an NHP model of Parkinson's disease emphasised that viral vector expression following extensive BBB permeabilisation remains unsatisfactory and requires further optimisation [Blesa *et al*., 2023]. Despite these challenges, this therapeutic approach remains one of the most promising for improving outcomes in patients with rare genetic diseases, as demonstrated in small animal therapeutic trials.

General discussion and conclusion

The present work presents the first studies in relation to the use of FUS and MB to permeabilise the BBB conducted in the laboratory. At the interface between methodological developments, characterisation of phenomena after FUS-induced BBB opening and the development of new therapeutic strategies, we explored a broad range of aspects of therapeutic FUS. We proposed here the exploration of vascular and functional parameters after the permeabilisation of the BBB with FUS and evaluated new therapeutic strategies for the treatment of aggressive brain tumours as glioblastoma and neurodegenerative genetic diseases. This work paves the way for more targeted and efficient therapeutic approaches by refining treatment parameters in today's world of personalised precision medicine.

First, we presented a methodological validation of the FUS system provided by IGT. It involved the characterisation of the FUS system with the design and control of a 3-axis automated device, its validation using different MRI techniques that were not or partially developed in the team, the characterisation of different types of MB specifically designed for BBB opening purposes, and the development and validation of FUS sequence patterns to efficiently deliver different therapeutic compounds to the brain of preclinical mice and rats models. + MRI/QSM, data validation….

Second, we explored the transient modification of different parameters after the permeabilisation of the BBB. We monitored the cerebral blood flow and blood volume fraction as well as different neuroinflammation markers with MRI and histological methods. We observed that FUS treatment parameters can deeply but transiently influence CNS physiology, in particular brain perfusion. A close monitoring of the cavitation activity of the MB is necessary to ensure the best translation to clinics.

Third, regarding the precedent results, we naturally investigated different types of repeated FUS treatments supported by the fact that repeated FUS application to permeabilise the BBB is likely to become the benchmark treatment for several CNS diseases. We monitored a broad range of quantitative MRI parameters with an MR fingerprint approach developed in the laboratory and evaluated the subsequent astrogliosis. This study necessitated a substantial number of FUS treatment and MRI acquisition sessions. Several parameters investigated were not presented here, because of the lack of time for analysis. This includes other vascular and inflammatory markers and a metabolomic analysis of collected blood samples.

Additionally, the recent installation of a preclinical irradiator next to the MRI scanners and the FUS system improved the landscape of therapeutic strategies available in the laboratory. Considering the poor prognosis of glioblastoma patients, we evaluated a novel treatment planning involving the delivery of carboplatin with FUS followed 24 h after by a radiotherapy session in a preclinical model of glioblastoma. In this model, we evaluated the biodistribution of carboplatin using ICP-MS, the survival rate, and the tumour progression with MRI. We demonstrated an improved survival rate with this novel treatment strategy. Further analysis will be necessary to conclude this study with the evaluation of DNA strand breaks that could result from FUS, radiotherapy, carboplatin or an association of the three. The acquisition of fluorescence X-ray images at the synchrotron (ESRF, Grenoble, France) will help gain more insight into the 3D distribution of the carboplatin. The evaluation of histological markers, including vascular proteins, will be useful to assess the safety of the procedure. In addition, we have planned to acquire X-ray phase contrast computed tomography images that will provide data

from the whole organs at an unprecedent spatial resolution level. This study is the first to assess this new combination of treatments and further steps will be necessary to evaluate whether the repetition of this treatment improves animal outcome. In this case, this protocol could be transferred into a phase 1 clinical trial.

Finally, we showed in two preclinical models of genetic diseases of the CNS an improvement in animal outcome (behaviour phenotype, survival) after delivering AAV to the whole brain using FUS. The re-expression of the protein of interest was in both cases satisfying. The three application studies, performed on the IRMaGe facility, demonstrate that our preclinical FUS may readily be embarked into new preclinical trials: the system is robust and, overall, the success rate of BBB opening in the last year of this thesis was above 95%. Further optimisations are required to determine whether one set of FUS parameters is optimal for all brain applications or whether disease specific optimisations are required, depending on the targeted brain area and its characteristics (e.g. perfusion parameters).

This work is part of a broad and heterogeneous landscape of FUS devices, microbubble types and FUS treatment patterns. The system and parameters have been characterised in detail using a variety of methods, with the aim of ensuring the best possible translation to other animal models and future clinical trials. Considering the considerable number of studies in the field of therapeutic FUS, particularly those involving BBB permeabilisation, there is a pressing need for standardisation procedures to perform and to report FUS studies. The proliferation of FUS devices and high-impact journal publications has led to a situation where it is challenging to contextualise the vast array of results and develop reliable, valid and transferable therapeutic approaches for patients.

In addition, numerous studies have evaluated the effect of the BBB permeabilisation with FUS, yet the mechanisms are not fully understood and the role played by many components of the NVU is still not known as pericytes, astrocytes and tight junctions. It already has been demonstrated that at least two or three types of leakages may arise: a faster, a slower and a sustained one [Cho *et al.*, 2011; Raymond *et al.*, 2007]. Plus, the vasculature seems to play an important role in the targeted permeabilisation with the first observation of significant changes in BBB opening with FUS and microbubbles as a function of blood vessel diameter [Katz *et al.*, 2023] as well as an enhanced extravasation in small blood vessels using nanobubbles [Gattegno *et al.*, 2024].

It is certain that such a procedure is not without consequences and produces a high number of transient dysregulation (vascular, cellular, genetic), yet safe FUS parameters - possibly associated with real-time cavitation monitoring - do not produce irreversible lesions. Moreover, this method is intended to be applied in brain diseases with a poor prognosis such as glioblastoma or with dramatic consequences on the quality of life of these patients. In all cases, the benefit/risk ratio has to be considered. Future studies must focus on the use of treatment parameters safe for clinical applications and must take into account the differences between animal models and patients. Addressing all these issues will facilitate the transferability of the results and study the secondary effects that may arise in clinical trials.

In conclusion, the studies conducted from this Ph.D. project led to a better understanding of the consequences of single FUS and multiple FUS treatments in the brain. Furthermore, we put forward novel therapeutic strategies for three pathologies: glioblastoma, the most aggressive and prevalent brain tumour in adults; Leigh syndrome, a mitochondrial genetic disease; and Fragile X syndrome, the second most common intellectual impairment genetic disease. These approaches are promising, and

we hope to see them evaluated in clinical trials in the near future. In addition, the initial implementation of cavitation monitoring algorithm in Chapter 5 and the first development of a cavitation control algorithm for single spot and large BBB opening as stated in section 4.2.2.2 will benefit the IGT enterprise. Future work will validate these methods and their future integration into the MR-guided software with a cavitation monitoring and control algorithm to increase the safety and the reproducibility of the FUS-induced BBB opening.

Over the past three years, numerous collaborations have been established with researchers from the GIN and the Grenoble area: Dr Michael Decressac from GIN with a study involving the delivery of adeno-associated viruses in a mice model of the Leigh syndrome, and Dr. Clément Hébert from GIN, with whom we intend to validate our hypothesis regarding the cortical spread depression wave that forms subsequent to FUS application, as discussed in the Chapter 5, Dr Hélène Elleaume and Dr Alexandre Leboucher (and many other researchers) with whom the study presented in the Chapter 7 was conducted, Dr Pascale Perret and Dr Nicolas De Leiris from the Laboratory for Bioclinical Radiopharmaceuticals (LRB, Grenoble, France) with whom a project to improve the early diagnosis of Alzheimer's disease, and finally Dr Bastien Arnal from the Interdisciplinary Laboratory of Physics (LIPhy, Grenoble, France) with the idea to validate *in vivo* oxygenation imaging with multispectral photoacoustic fluctuation imaging and potentially validate the MRI measurements of the CBF conducted in the Chapter 5.

Annexes

A.1. *In vitro* cavitation

Influence of the frequency on the cavitation behaviour of biotin functionalised (Figure 79) and cationic (Figure 80) MB. Each data point was averaged from three measurements, accounting for acoustic intensity variations between 2 and 30% with a 0.1% footstep.

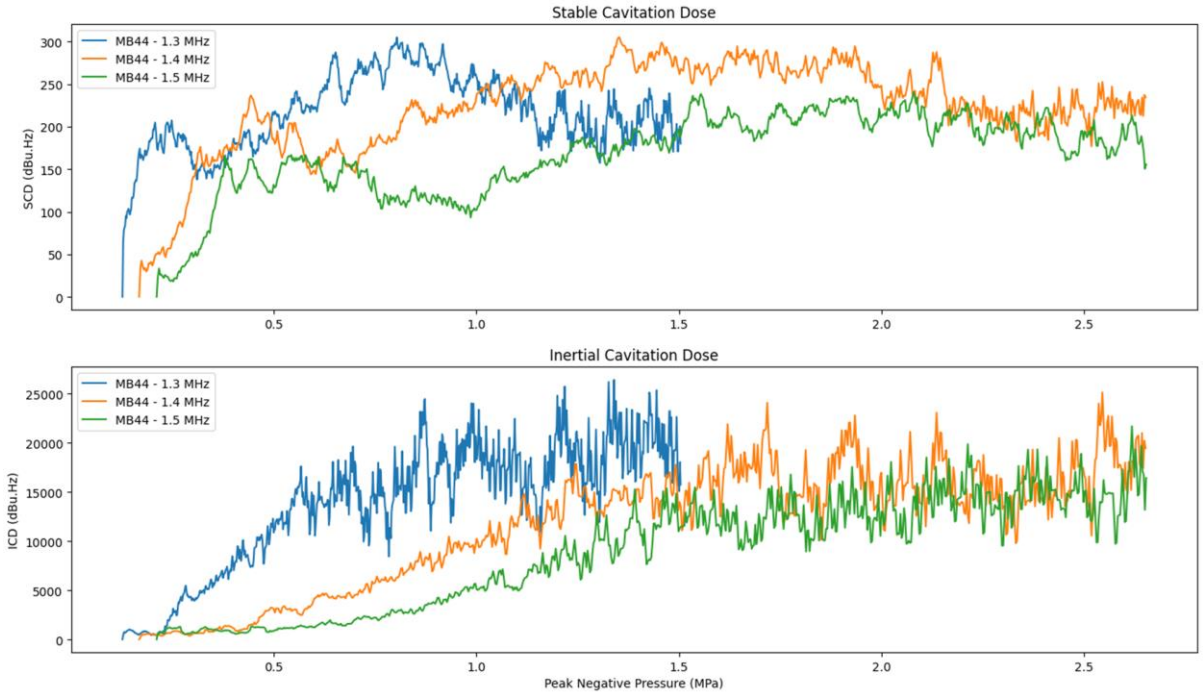


Figure 79. Stable (top) and inertial (bottom) cavitation dose for DSPC-DSPE-PEG2000-biotin MB in function of the applied PNP pressure and for different excitation frequencies. Each data point was averaged from three measurements, accounting for acoustic intensity variations between 2 and 30% with a 0.1% footstep.

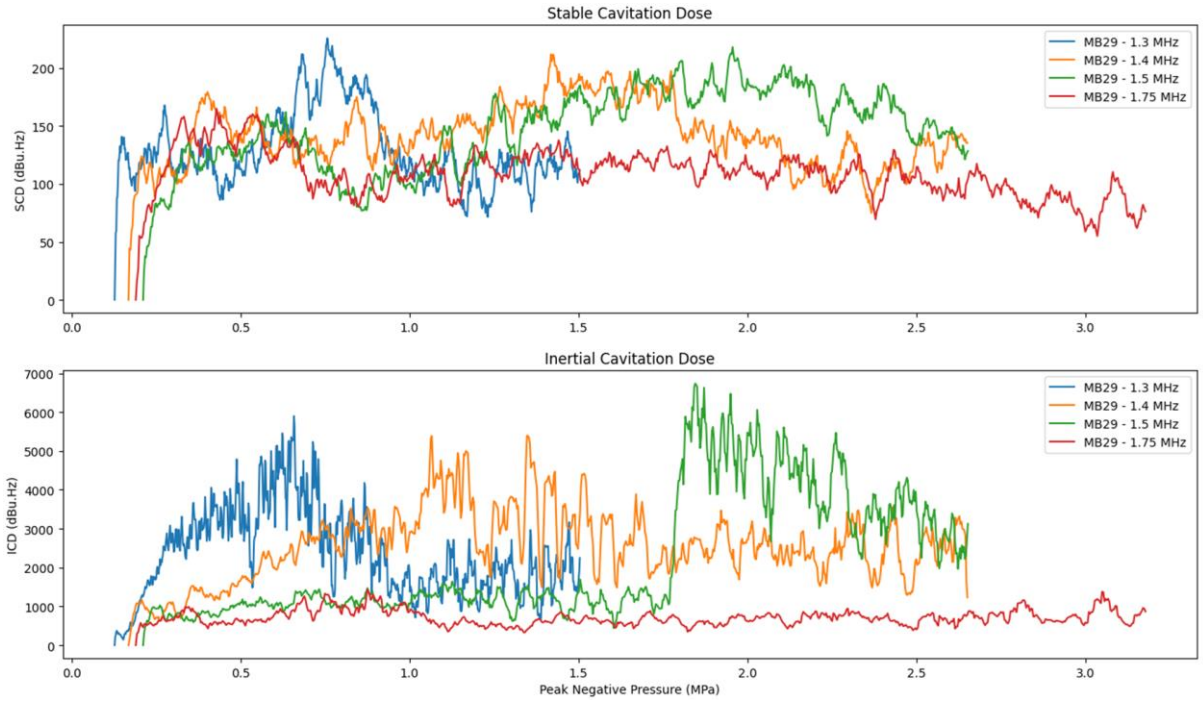


Figure 80. Stable (top) and inertial (bottom) cavitation dose for DMPC-DMPE-PEG2000 MB in function of the applied PNP pressure and for different excitation frequencies.

A.2. Overview of multiparametric MRI image processing

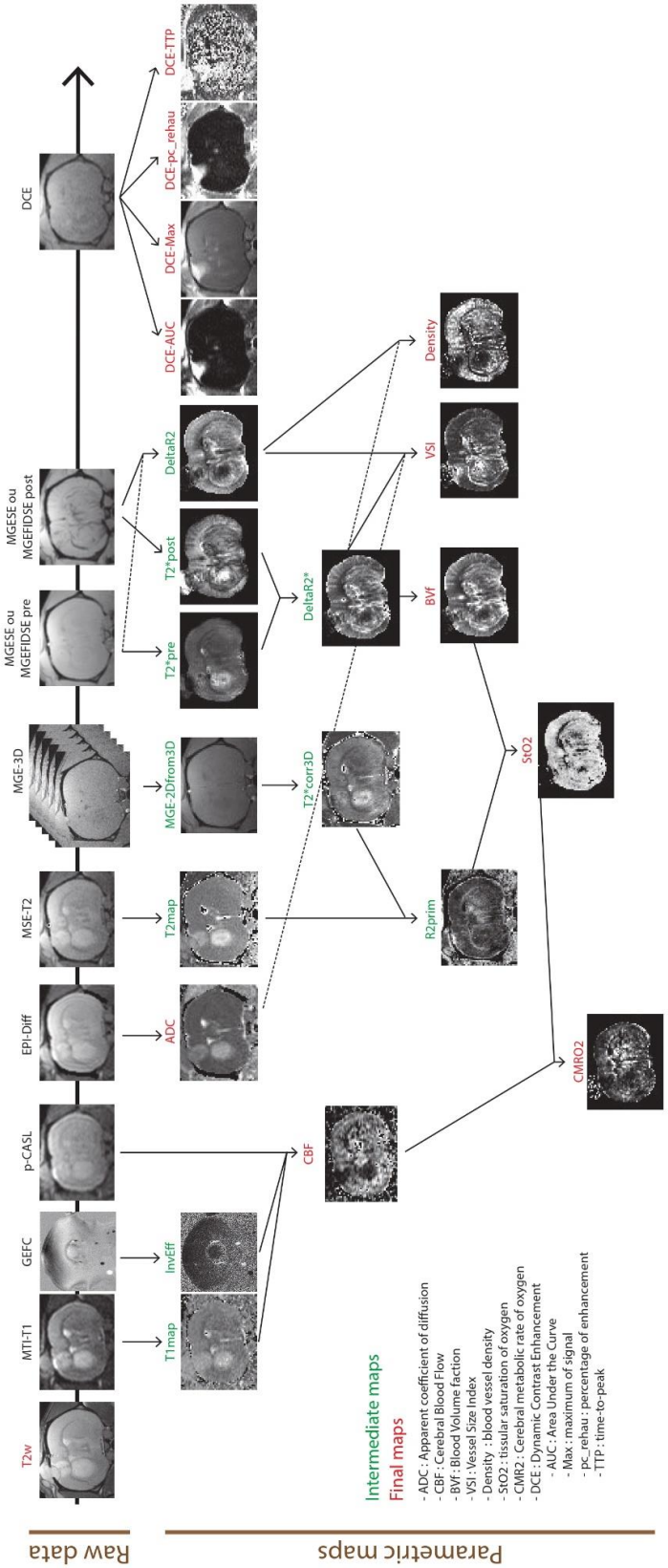


Figure 81. MRI processing pipeline to compute quantitative multiparametric MRI maps. Provided by Dr Benjamin Lemasson

A.3. Supplementary figures from Study 1

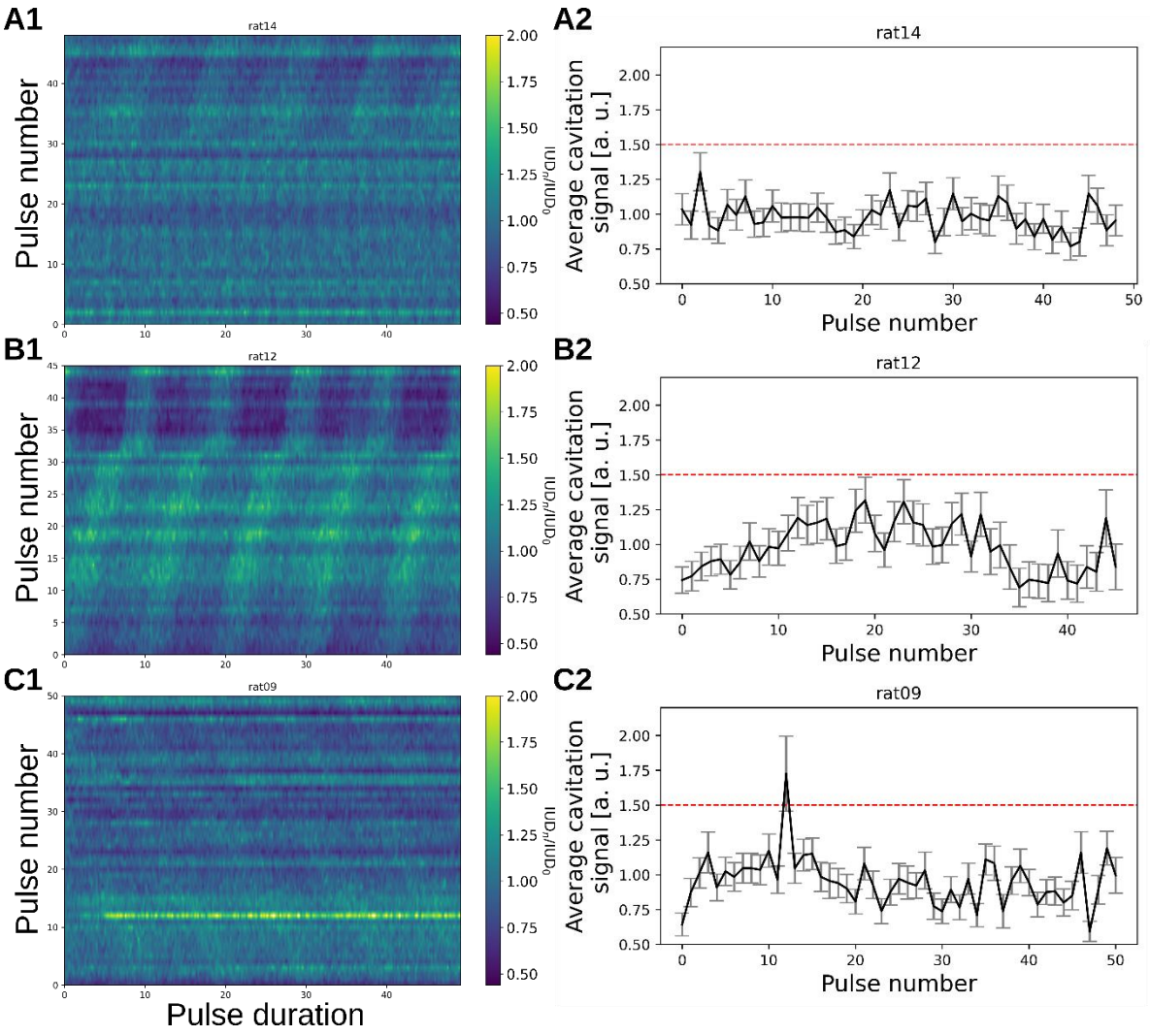


*Figure 82. Example of the evolution of the relative IUD over every pulse of the treatment for soft (**A1**), mild (**B1**) and hard (**C1**) classification treatment. The corresponding average and standard deviation cavitation signal for the three classification cases with the red dashed line representing the inertial threshold (**A2**, **B2**, **C2**).*

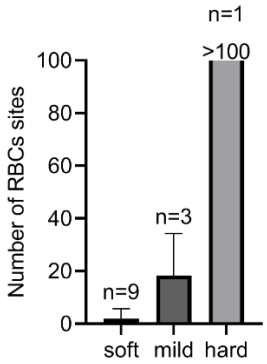


*Figure 83. number of **red blood cells** sites analysed on H&E images for each cavitation-based classification group. The results are expressed as mean ± S.D.*

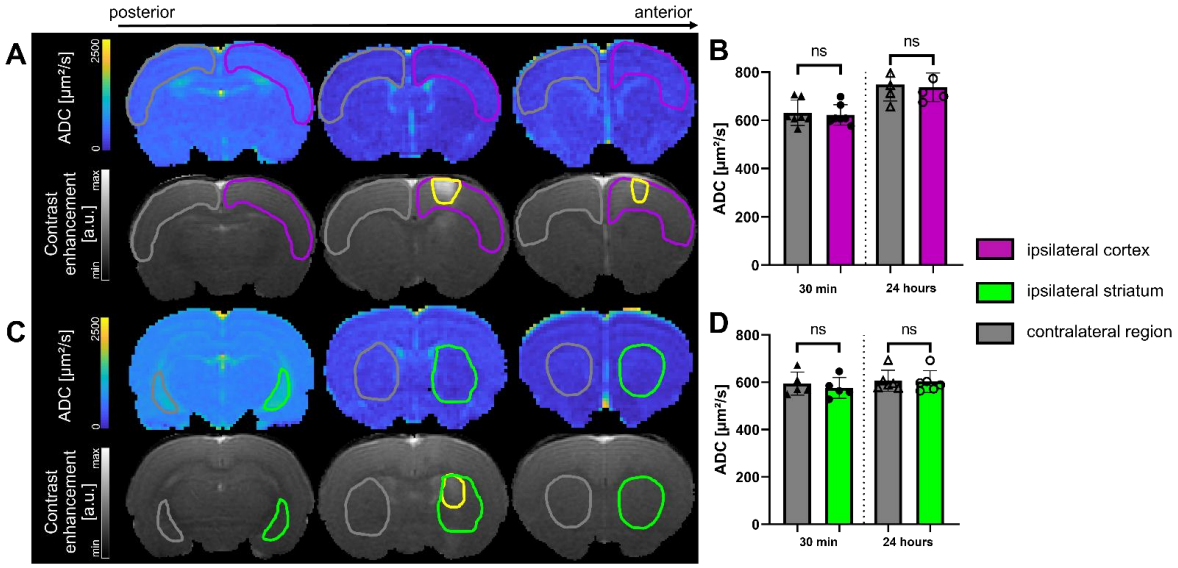


*Figure 84. Examples of ADC maps 30 minutes after BBB opening in the cortex (**A**) and striatum (**C**), and associated T1-w images after Gd-DOTA injection. The opened area is delineated in yellow. ADC 30 minutes and 24 hours after FUS in the cortex (**B**) and in the striatum (**D**). Data were analysed using a two-tailed non-parametric test (Wilcoxon) (*p < 0.05; **p < 0.01; ***p < 0,001; ns, non-significant). Results are expressed as mean ± S.D.*

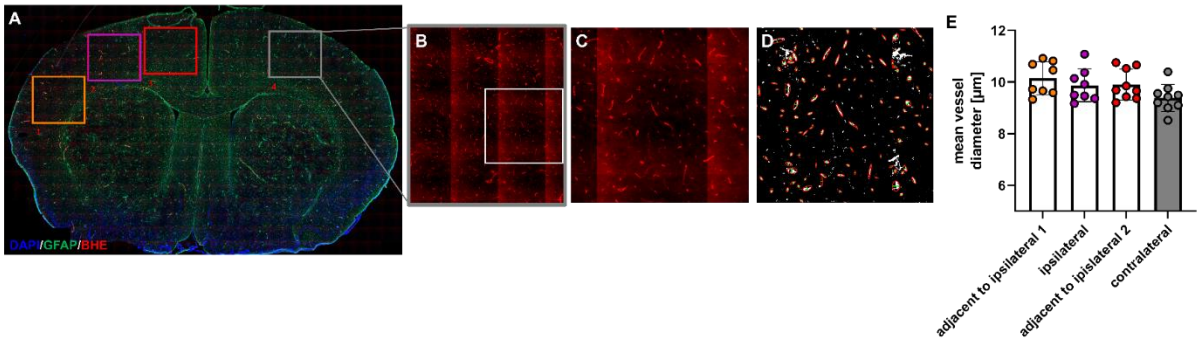


*Figure 85. **A**) representative micrograph of DAPI, GFAP and BBB markers with 2 adjacent ROI (orange and red). **B**) and **C**) zooms at different levels on the contralateral cortex. **D**) example from image segmentation and diameter analysis script. **E**) Mean vessel diameter of 2 adjacent ipsilateral ROI at the left and the right of the ipsilateral region. Results are expressed as mean± S.D.*

A.4. Supplementary figures from Study 2

A.4.1. Comparison of quantitative MRI maps between the classical and fingerprint approaches

A.4.2. Ventricular enlargements

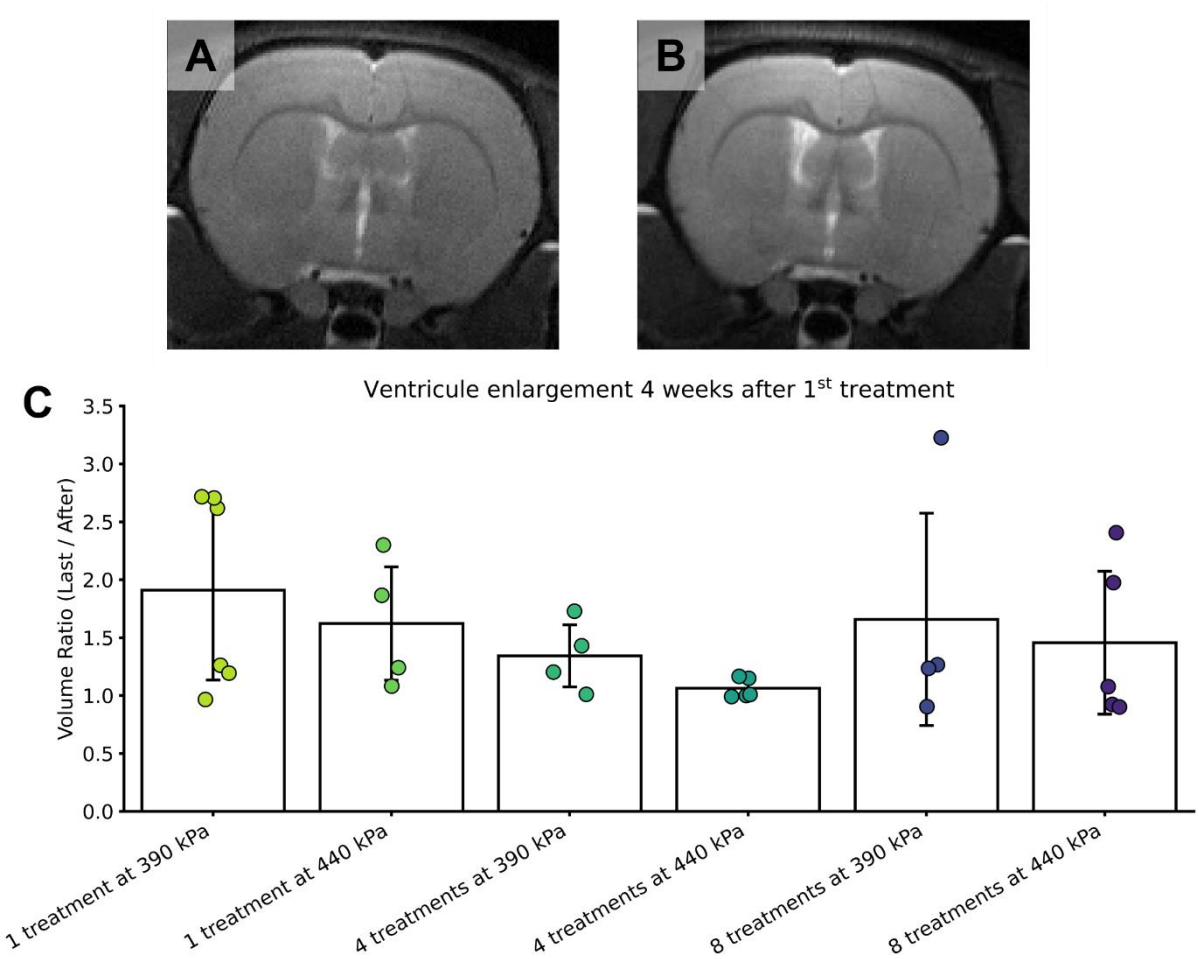


*Figure 86. Ventricular enlargement. Representative example of anatomical T2-w images after the first (**A**) and last (**B**) FUS treatment. (**C**) Volume ratio of the ventricle from the ipsilateral hemisphere between the first and last treatment for all groups. One can notice the large heterogeneity across the groups.*

A.5. Supplementary figures from Study 3

A.5.1. Clonogenic assay

A clonogenic assay study was performed to study the efficacy of the radiotherapy on F98 cells and quantify the radiosensitising effect of carboplatin. Cells were cultivated in T25 cm^2 flasks. At a confluence of 40-50%, carboplatin was introduced at a concentration of 2.5 µg/mL. Cells were incubated at 37°C and 5% CO_2 for 24 h. The flasks containing 5 mL of culture media were placed at 35 cm from the X-ray source and were irradiated in an open irradiation field without any collimator at doses of 0, 2, 4, 6, 8, and 10 Gy, using the SARRP preclinical irradiation system (see XX). The average energy given to cells was 67 keV. After irradiation, the treated cells were seeded at 3 different densities in triplicates and incubated for 9 days to allow the colonies to form. On day 10, colonies were fixed and coloured with crystal violet. Colonies were left to dry for 24 h and then counted semi-automatically using ImageJ. Only colonies of at least 50 cells were considered.

To interpret the results of cell survival assays quantitatively, it is important to delineate two quantities: the plating efficiency and the surviving fraction. The plating efficiency PE reflects the percentage of seeded cells that survive to form colonies under control conditions (0 Gy and no chemotherapy) and is defined as follows:

$$PE = \frac{Number\ of\ colonies\ counted\ at\ 0\ Gy}{Number\ of\ cells\ seeded\ at\ 0\ Gy} \tag{22}$$

Knowing this factor, one can normalise the surviving fraction to eliminate variables contributing to cell death unrelated to radiation.

The surviving fraction SF is defined as:

$$SF(x) = \frac{Number\ of\ colonies\ counted\ at\ x\ Gy}{Number\ of\ cells\ seeded\ at\ x\ Gy} \tag{23}$$

And the normalised surviving fraction S is defined as:

$$S(x) = \frac{SF(x)}{PE} \tag{24}$$

After irradiation the number of cells seeded is chosen to ensure that the number of colonies after treatment will be in the range 10 to 80.

A linear quadratic model with the following shape: $e^{-\alpha x-\beta x^2}$ is commonly used to fit the survival curves in radiotherapy. A linear relationship, characterised by the α-parameter (Gy−1), is observed at very low doses, while for higher doses the quadratic relationship is governed by the β (Gy−2) parameter becomes dominant. The ratio α/β is a common parameter to study in radiobiology. It assesses the radiosensitivity of cells. A high α/β ratio indicates a significant influence of the linear component; hence cells are killed at a constant rate with increasing the dose. Conversely, a low α/β ratio indicates that the quadratic component is more influential, resulting in a pronounced curvature. The ratio α/β is considered in clinical treatment to determine the optimal dose fractionation. The survival fraction curves were fit into a linear-quadratic model using PRISM and the ratios α/β were calculated.

Cells incubated for 24 hours with 2.5 µg/mL of carboplatin, without radiation dose, showed a marked decrease in the survival fraction compared to untreated cells, as can be seen in Figure 87.A.

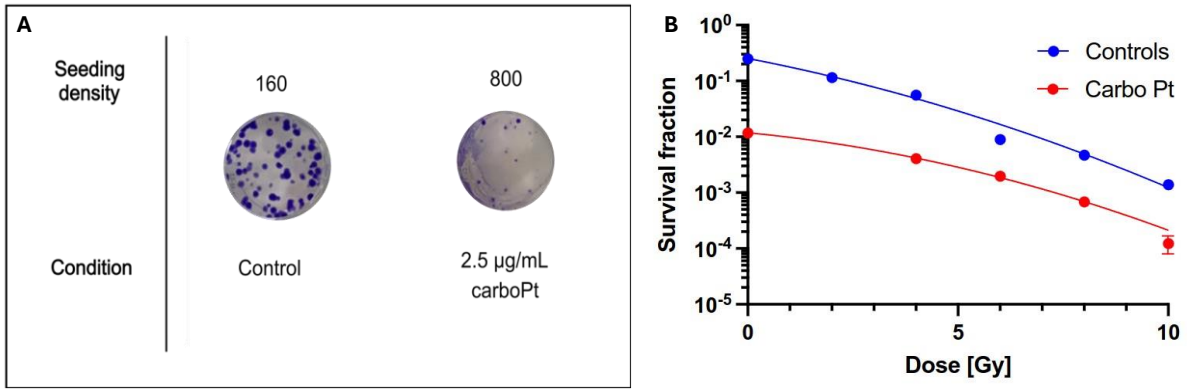


*Figure 87. Clonogenic assay results. **A**) Colonies formed for control cells (left) and cells treated with carboplatin (24 h incubation time and 2.5 µg/mL) (right), without exposure to any X-rays. **B**) Survival fraction comparison between cells subjected to irradiation alone (blue circles) and cells treated with 2.5 µg/mL carboplatin for 24 hours followed by irradiation (red circles).*

The survival and normalised survival fraction of F98 cells exposed to 0 or 2.5 µg/mL of carboplatin for 24 h and irradiated at increasing X-ray doses are shown in Figure 87.B. The corresponding survival at 0 Gy, α, β and α/β parameters are reported in Table 19 for the two treatment conditions.

Condition	α	β	α/β
Control	0.3339	0.01978	16.88
Pretreated with carboplatin	0.1663	0.02351	7.07

Table 19. α and β parameters for the two treatment conditions.

From the fits of the survival curves shown in Figure 87.B, the α/β was found to be equal to 16.88 in the control group compared to 7.076 the cells treated with carboplatin before irradiation. This suggests that pretreatment with carboplatin fosters the pronounced curvature in cell survival, implying that the rate of cell death in these treated cells changes more with increasing radiation dose compared to the control group.

The outcomes of the in vitro study demonstrated the effectiveness of combining carboplatin and radiotherapy. It was observed that carboplatin exhibits high cytotoxicity, with a survival fraction of less than 0.01 for cells exposed to a concentration of only 2.5 µg/mL for 24 hours. An important difference in the survival fraction was observed between cells receiving only irradiation and cells that were pretreated with carboplatin. These results are comparable to those obtained previously [Yang *et al.*, 2011].

A.5.2. Platinum concentrations in organs

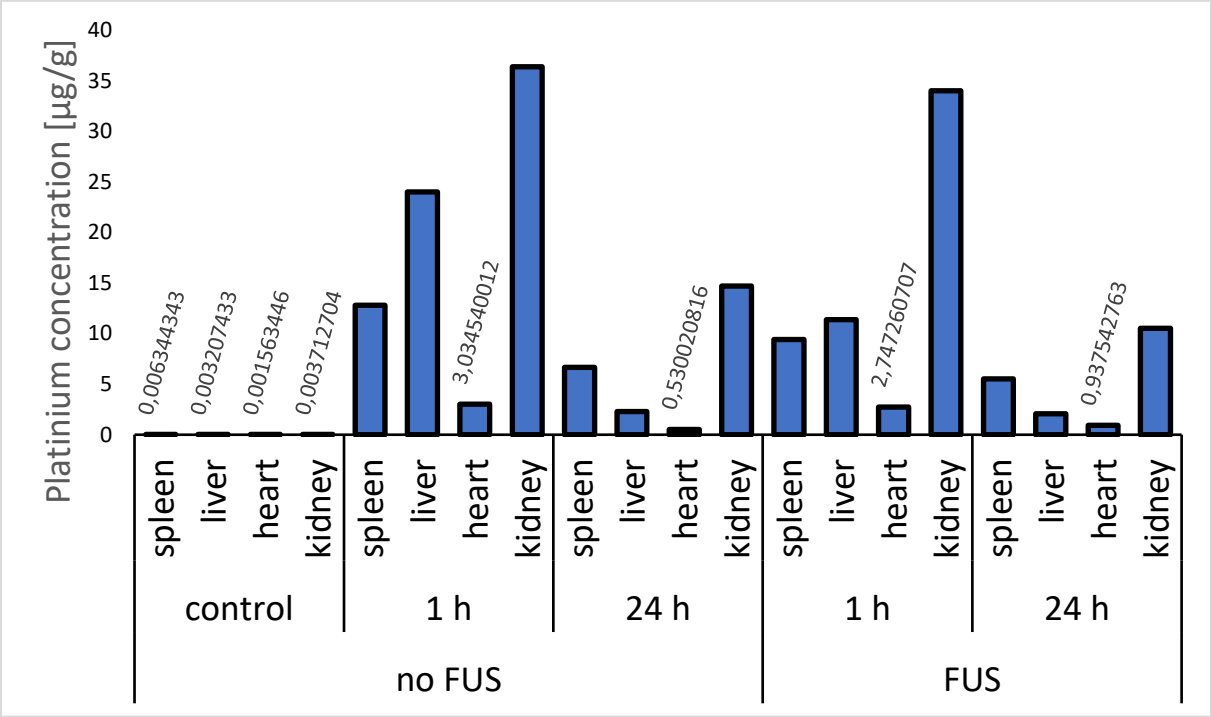


Figure 88. ICP-MS platinum concentrations measured in the spleen, liver, heart and kidney of control, carboplatin and FUS+CarboPt groups.

A.5.3. MRI follow-up

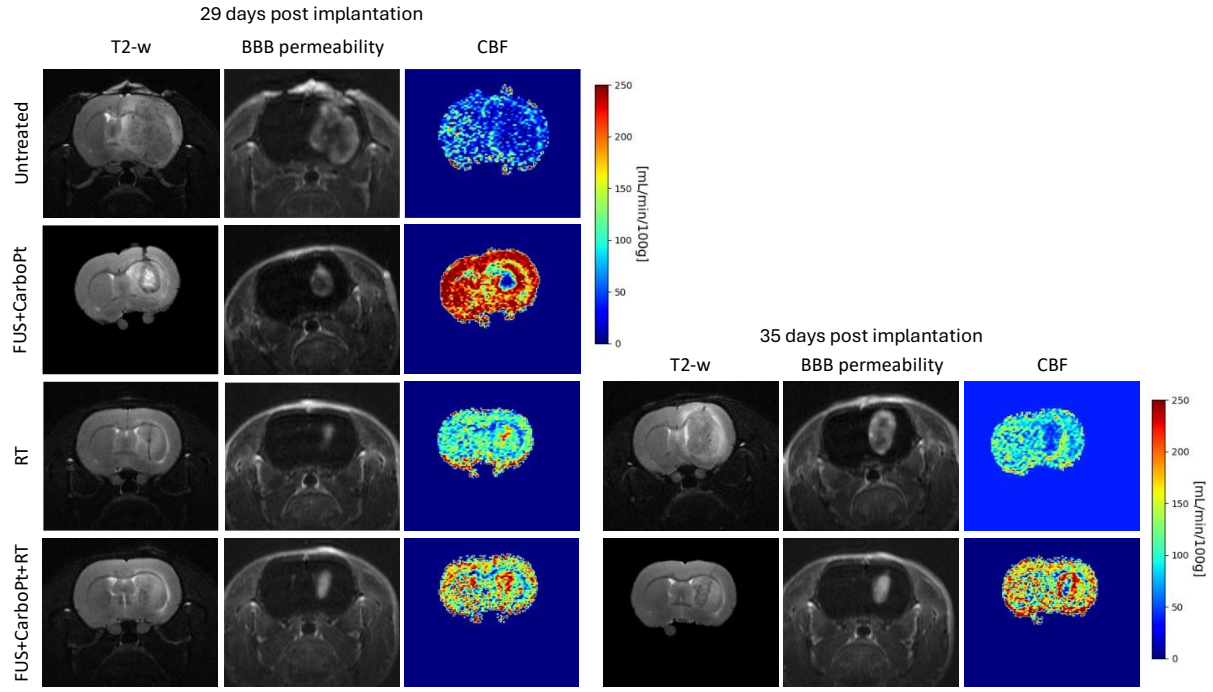


Figure 89. Representative examples of T2-w, BBB permeability and CBF parameters for all groups 29 and 35 days after implantation. Treatment was performed on the same day (day 14)

Curriculum vitae

Sébastien Rigollet

Grenoble Institut des Neurosciences, France
Sebastien.Rigollet@univ-grenoble-alpes.fr
+33 6 43 57 01 60



Education

Ph. D. candidate in physics, GIN, France (November 2021 – now)

Evaluation of secondary bioeffects of FUS induced BBB opening with quantitative MRI methods, funded by Image Guided Therapy (Pessac, France) and supervised by Emmanuel L. Barbier (GIN, Inserm, Grenoble, France) and Chantal Pichon (LIR^{2}SO, Orléans, France).

M. Sc. Biomedical Engineering (2018 – 2021)

Phelma, School of engineering in Physics, Applied Physics, Electronics & Materials Science, Grenoble Institute of Technology, France. Graduated in Sept 2021.

Intensive course in physics, mathematics and engineering (2015 – 2018)

Lycée Joffre, Montpellier, France

Experience

Supervision activities

- Master 2 student - Lucas Tachen-Migheli : ”In vitro acoustic cavitation evaluation for characterization of therapeutic microbubbles for BBB opening” (February – July 2024) co-supervised with Dr Vasile Stupar
- Master 2 student – Sarra Dbira : “Evaluation of carboplatin biodistribution after FUS induced BBB opening” (February – August 2024) co-supervised with Dr Hélène Elleaume
- Bachelor student – Qendresa Arifi : “Histological evaluation of FUS induced BBB opening” (January – June 2023)

Junior scientific council of CDP CerCoG@UGA (January 2023 – now)

Creating and developing collaborations between Grenoble’s laboratories among the Clinical neurosciences, Cognition and Brain axes. Social networks, podcast and conferences.

Teaching (2023 – now)

- Plenary about MR-guided FUS for Bachelor and Master 2 students
- Tutorials on innovative therapeutic projects for cancer diseases

Graduation Project – 6 months internship – Grenoble Institute of Neurosciences (2021)

Supervised by Vasile Stupar (Vasile.Stupar@univ-grenoble-alpes.fr).

iGEM competition : PyoBusters project – Phelma, Grenoble Institute of Technology & TIMC-IMAG (December 2019 – February 2021): https://2020.igem.org/Team:Grenoble_Alpes

Journal articles

Rigollet S, Rome C, Ador T, Dumont E, Pichon C, Delalande A, Barbier EL, Stupar V. FUS-mediated BBB opening leads to transient perfusion decrease and inflammation without acute or chronic brain lesion. Theranostics 2024; 14(10):4147-4160. Doi: https://doi.org/10.7150/thno.96721

Ador, T., Fournier, M., **Rigollet, S.**, Counil, C., Stupar, V., Barbier E. L., Pichon, C., Delalande, A., Ultrasound-Assisted Blood Brain Barrier Opening Monitoring by Photoacoustic and Fluorescence Imaging Using Indocyanine Green, 2024, *submitted to iScience*

Conference proceedings

Oral presentation

Rigollet, S., Ador, T., Dumont, E., Pichon, C., Barbier, E. L., Delalande, A., Stupar, V., (2024) Longitudinal study tracking physiological changes through multiparametric MRI during repeated MRgFUS-induced BBB opening, In *31st International Society for Magnetic Resonance in Medicine Annual Meeting* (*ISMRM*).

Ador, T., **Rigollet, S.**, Laugeray, A., Fournié, M., Stupar, V., Barbier, E. L., Pichon, C., Menuet, A., Delalande, A., (2024) Longitudinal MR vascular fingerprinting approach tracking physiological changes during repeated MR guided FUS mediated BBB opening on rats., In *23rd European Molecular Imaging Meeting* (*EMIM*).

Rigollet, S., Ador, T., Dumont, E., Pichon, C., Delalande, A., Barbier, E. L., Stupar, V., (2023) Cerebral perfusion monitoring after FUS mediated blood-brain barrier opening: a study to evaluate ultrasound bioeffect, In *23rd International Society for Therapeutic Ultrasound* (*ISTU*).

Rigollet, S., Ador, T., Dumont, E., Pichon, C., Delalande, A., Barbier, E. L., Stupar, V., (2023) Cerebral perfusion monitoring after FUS mediated blood-brain barrier opening: a study to evaluate ultrasound bioeffect, In *23rd International Society for Therapeutic Ultrasound* (*ISTU*).

Poster session

Rigollet, S., Clément, R., Decressac, M., Barbier, E. L., Delalande, A., Stupar, V., (2023) Optimisation de la barrière hémato-encéphalique contrôlé par IRM sur cerveau entier, In *6e congrès de la Société Française de Résonance Magnétique en Biologie et Médecine* (*SFRMBM*).

Ador, T., Fournie, M., **Rigollet, S.**, Stupar, V., Barbier, E. L., Pichon, C., Delalande, A., (2023) Production and characterisation of cationic microbubbles for gene delivery in vivo, In *23rd International Society of Therapeutic Ultrasound* (*ISTU*)

List Of Figures

Figure 1. Overview of the brain vascular structure and the neurovascular unit complex 19
Figure 2. Transmission electron microscopy of the BBB. 20
Figure 3. A schematic diagram of the endothelial cells and the perivascular end-feet of astrocytes that form the BBB. 21
Figure 4. Overview of BBB in pathological conditions 22
Figure 5. Overview of BBB drug delivery alternatives 25
Figure 6. Principle of the BBB opening with FUS and MB. 26
Figure 7. State of research and regulatory approvals for neurobiological and neurological applications 33
Figure 8. The cumulative number of clinical trials 35
Figure 9. Overview of the different cavitation mechanisms induced by FUS on a MB. 38
Figure 10. Scheme of the stable and inertial cavitation regimes 39
Figure 11. Typical example of regular (top) and “compression-only” oscillations of a SonoVue® MB. 40
Figure 12. Different cavitation regimes of the MB according to their spectral signature 41
Figure 13. Different in vitro cavitation monitoring setups 42
Figure 14. Microscopy images of three different MB (SonoVue, Definity, and USphere). 47
Figure 15. Influence of MB properties on cavitation 48
Figure 16. Example of a closed-loop cavitation controller 49
Figure 17. Overview of the techniques used to study the secondary effects of FUS 54
Figure 18. Focused ultrasound transducer pulse echo transfer function. 75
Figure 19. Transducer characterisation system and calibration curves. 76
Figure 20. Transducer characteristics as a function of frequency and steering. 76
Figure 21. Results of the simulation of the focal spot 77
Figure 22. In vitro cavitation experimental setup. 79
Figure 23. Cavitation spectrum for SCD (**A**) and ICD (**B**) 79
Figure 24. Evolution of ICD depending on the PNP for increasing MB concentrations 80
Figure 25. Evolution of the SCD (top) and ICD (bottom) in function of the PNP 81
Figure 26. Evolution of the SCD (top) and ICD (bottom) at 1.5 MHz for the three types of MB 81
Figure 27. In vivo cavitation monitoring 82
Figure 28. The MR-guided FUS system 85
Figure 29. Thermoguide® screenshots of target location 85
Figure 30. Thermometry results. 86
Figure 31. Time sequence diagram of the ARFI sequence. 87
Figure 32. Validation of Acoustic Radiation Force Imaging. 88
Figure 33. T2-w TurboRARE coronal images 89
Figure 34. BBB closure dynamics. 91

Figure 35. Optimisation parameters for whole brain BBB permeabilisation. 93
Figure 36. Validation of whole brain BBB permeabilisation..... 93
Figure 37. Preclinical 4.7 T MRI 94
Figure 38. T2-w images..... 94
Figure 39. Principle of DCE-MRI and example of DCE-computed images 95
Figure 40. Cerebral blood flow image processing pipeline. 97
Figure 41. Overview of computed MRI maps with the multiparametric MRI protocol. 99
Figure 42. Principle of the MRI fingerprint approach 99
Figure 43. Abstract caption 104
Figure 44. Workflow of the study, with the timeline for each group. 109
Figure 45. Outline of the different steps of the study..... 111
Figure 46. Representative T1-w images of the brain after the BBB has been opened 112
Figure 47. Number of events above the $1.5 \times IUD0$ threshold 113
Figure 48. Representative examples of soft (row **A**), mild (row **B**), and hard (row **C**) BBB opening... 113
Figure 49. Examples of CBF maps 30 min after BBB opening..... 115
Figure 50. CBF in ipsi- and contralateral cortices as a function of time following the opening of the BBB. 115
Figure 51. Examples of BVf maps 30 min after BBB opening 116
Figure 52. Activation of astrocytes (**A1**) and microglia (**B1**)..... 118
Figure 53. Raster scan planned on the T2-w MRI in Thermoguide® software 126
Figure 54. Relative mean weight evolutions of the different groups..... 127
Figure 55. **A**) Representative T2-w images covering the treated brain volume. 128
Figure 56. Relative contrast enhancement (top panel) and time to peak (bottom panel) values..... 128
Figure 57. Representative MRI T2-w (**A**), T2* (**B**) and ADC maps (**C**) images..... 129
Figure 58. Representative T2-w (**A**) and contrast enhancement (**B**) MRI images and H&E staining .. 129
Figure 59. Representative micrographs of H&E for 4-FUS and 8-FUS groups..... 130
Figure 60. Cerebral blood flow after repeated FUS..... 131
Figure 61. Ipsilateral (white) and contralateral (grey) values of R (**A**), Vf (**B**) and SO2 (**C**) 132
Figure 62. Representative T2-w images (**A**), QSM maps (**B**), the paramagnetic contribution (**C**) and diamagnetic contribution (**D**) 133
Figure 63. Ipsilateral (white) and contralateral (grey) QSM..... 134
Figure 64. Representative micrograph for an 8-FUS rat at 440 kPa..... 135
Figure 65. F98 brain tumour evolution and volumes. 143
Figure 66. Overview of the experimental protocol 144
Figure 67. Radiotherapy platform and software. 145
Figure 68. FUS-induced BBB permeabilisation. 147
Figure 69. Platinum biodistribution..... 147
Figure 70. Weight and survival rate evolutions..... 148

Figure 71. Representative example of the different parameters measured longitudinally following the treatment. 150
Figure 72. Representative examples of T2-w, BBB permeability and ADC parameters 150
Figure 73. Overview of FXS features. 156
Figure 74. Summary of the experimental timeline. 158
Figure 75. Representative contrast enhancement map. 159
Figure 76. Histological investigation of the brain in WT and $Fmr1^{KO}$ mice. 160
Figure 77. Gene transfer is assessed by bioluminescence. 160
Figure 78. Behavioural results. 162
Figure 79. Stable (top) and inertial (bottom) cavitation dose for DSPC-DSPE-PEG2000-biotin MB ... 169
Figure 80. Stable (top) and inertial (bottom) cavitation dose for DMPC-DMPE-PEG2000 MB 170
Figure 81. MRI processing pipeline to compute quantitative multiparametric MRI maps. 171
Figure 82. Example of the evolution of the relative IUD over every pulse of the treatment 172
Figure 83. number of red blood cells sites analysed on H&E images 172
Figure 84. Examples of ADC maps 30 minutes after BBB opening 173
Figure 85. **A**) representative micrograph of DAPI, GFAP and BBB 173
Figure 86. Ventricular enlargement. 174
Figure 87. Clonogenic assay results. 176
Figure 88. ICP-MS platinum concentrations 177
Figure 89. Representative examples of T2-w, BBB permeability and CBF parameters 177

List Of Tables

Table 1. Summary of the safe parameters necessary for efficient drug delivery 30
Table 2. Summary of preclinical studies for different chemotherapies in mice and rat models. 32
Table 3. Different studies using the SCD and ICD indexes..... 44
Table 4. Different MB cavitation properties..... 46
Table 5. Summary of extravasated compounds following FUS-induced BBB opening. 57
Table 6. Summary of neuroinflammatory response studies 62
Table 7. List of behaviour tests performed on mice after FUS..... 64
Table 8. Presentation of the full width at half maximum (FWHM) of the focal spot..... 77
Table 9. Microbubble formulations..... 78
Table 10. Acquisition parameters for the multiparametric MRI protocol. 98
Table 11. List of combinations of primary and secondary antibodies 101
Table 12. Summary of the number of animals per group 125
Table 13. CBF values after a single FUS treatment measured 30 min and 4 weeks post-FUS. 130
Table 14. Summary of relative differences (in %) between ipsilateral and contralateral regions 132
Table 15. Summary of repeated FUS treatment schedules for brain tumour and AD studies. 138
Table 16. Overview of the different groups of the study. 144
Table 17. Summary of Kaplan-Meier survival survival curve statistical test. 148
Table 18. Summary of preclinical studies on F98 rats..... 152
Table 19. α and β parameters for the two treatment conditions. 176

References

Abbott, N.J., Patabendige, A.A.K., Dolman, D.E.M., Yusof, S.R., Begley, D.J., 2010. Structure and function of the blood–brain barrier. Neurobiol Dis 37, 13–25. https://doi.org/10.1016/j.nbd.2009.07.030

Abbott, N.J., Rönnbäck, L., Hansson, E., 2006. Astrocyte–endothelial interactions at the blood–brain barrier. Nat Rev Neurosci 7, 41–53. https://doi.org/10.1038/nrn1824

Allen, J.S., Rashid, M.M., 2004. Dynamics of a Hyperelastic Gas-Filled Spherical Shell in a Viscous Fluid. Journal of Applied Mechanics 71, 195–200. https://doi.org/10.1115/1.1653722

Alonso, A., Reinz, E., Fatar, M., Hennerici, M.G., Meairs, S., 2011. Clearance of albumin following ultrasound-induced blood–brain barrier opening is mediated by glial but not neuronal cells. Brain Research 1411, 9–16. https://doi.org/10.1016/j.brainres.2011.07.006

Alonso, A., Reinz, E., Fatar, M., Jenne, J., Hennerici, M.G., Meairs, S., 2010. Neurons but not glial cells overexpress ubiquitin in the rat brain following focused ultrasound-induced opening of the blood-brain barrier. Neuroscience 169, 116–124. https://doi.org/10.1016/j.neuroscience.2010.04.001

Alsop, D.C., Detre, J.A., Golay, X., Günther, M., Hendrikse, J., Hernandez-Garcia, L., Lu, H., MacIntosh, B.J., Parkes, L.M., Smits, M., Van Osch, M.J.P., Wang, D.J.J., Wong, E.C., Zaharchuk, G., 2015. Recommended implementation of arterial spin-labeled perfusion MRI for clinical applications: A consensus of the ISMRM perfusion study group and the European consortium for ASL in dementia. Magnetic Resonance in Med 73, 102–116. https://doi.org/10.1002/mrm.25197

An, H., Lin, W., Celik, A., Lee, Y.Z., 2001. Quantitative measurements of cerebral metabolic rate of oxygen utilization using MRI: a volunteer study. NMR in Biomedicine 14, 441–447. https://doi.org/10.1002/nbm.717

Anastasiadis, P., Gandhi, D., Guo, Y., Ahmed, A.-K., Bentzen, S.M., Arvanitis, C., Woodworth, G.F., 2021. Localized blood–brain barrier opening in infiltrating gliomas with MRI-guided acoustic emissions–controlled focused ultrasound. Proc Natl Acad Sci U S A 118, e2103280118. https://doi.org/10.1073/pnas.2103280118

Angeli, E., Nguyen, T.T., Janin, A., Bousquet, G., 2019. How to Make Anticancer Drugs Cross the Blood–Brain Barrier to Treat Brain Metastases. IJMS 21, 22. https://doi.org/10.3390/ijms21010022

Angla, C., Larrat, B., Gennisson, J., Chatillon, S., 2023. Transcranial ultrasound simulations: A review. Medical Physics 50, 1051–1072. https://doi.org/10.1002/mp.15955

Angoa-Pérez, M., Kane, M.J., Briggs, D.I., Francescutti, D.M., Kuhn, D.M., 2013. Marble burying and nestlet shredding as tests of repetitive, compulsive-like behaviors in mice. J Vis Exp 50978. https://doi.org/10.3791/50978

Apfel, R.E., 1982. Acoustic cavitation: a possible consequence of biomedical uses of ultrasound. Br J Cancer Suppl 5, 140–146.

Argaw, A.T., Gurfein, B.T., Zhang, Y., Zameer, A., John, G.R., 2009. VEGF-mediated disruption of endothelial CLN-5 promotes blood-brain barrier breakdown. Proc Natl Acad Sci U S A 106, 1977–1982. https://doi.org/10.1073/pnas.0808698106

Armulik, A., Genové, G., Mäe, M., Nisancioglu, M.H., Wallgard, E., Niaudet, C., He, L., Norlin, J., Lindblom, P., Strittmatter, K., Johansson, B.R., Betsholtz, C., 2010. Pericytes regulate the blood-brain barrier. Nature 468, 557–561. https://doi.org/10.1038/nature09522

Arnaud, A., Forbes, F., Coquery, N., Collomb, N., Lemasson, B., Barbier, E.L., 2018. Fully Automatic Lesion Localization and Characterization: Application to Brain Tumors Using Multiparametric Quantitative MRI Data. IEEE Trans. Med. Imaging 37, 1678–1689. https://doi.org/10.1109/TMI.2018.2794918

Arnold, T.C., Freeman, C.W., Litt, B., Stein, J.M., 2023. Low-field MRI: Clinical promise and challenges. J Magn Reson Imaging 57, 25–44. https://doi.org/10.1002/jmri.28408

Arvanitis, C.D., Askoxylakis, V., Guo, Y., Datta, M., Kloepper, J., Ferraro, G.B., Bernabeu, M.O., Fukumura, D., McDannold, N., Jain, R.K., 2018. Mechanisms of enhanced drug delivery in brain metastases with focused ultrasound-induced blood–tumor barrier disruption. PNAS 115. https://doi.org/10.1073/pnas.1807105115

Arvanitis, C.D., Ferraro, G.B., Jain, R.K., 2020. The blood–brain barrier and blood–tumour barrier in brain tumours and metastases. Nat Rev Cancer 20, 26–41. https://doi.org/10.1038/s41568-019-0205-x

Arvanitis, C.D., Livingstone, M.S., Vykhodtseva, N., McDannold, N., 2012. Controlled Ultrasound-Induced Blood-Brain Barrier Disruption Using Passive Acoustic Emissions Monitoring. PLoS ONE 7, e45783. https://doi.org/10.1371/journal.pone.0045783

Aryal, M., Vykhodtseva, N., Zhang, Y.-Z., McDannold, N., 2015. Multiple sessions of liposomal doxorubicin delivery via focused ultrasound mediated blood–brain barrier disruption: A safety study. J Control Release 204, 60–69. https://doi.org/10.1016/j.jconrel.2015.02.033

Aryal, M., Vykhodtseva, N., Zhang, Y.-Z., Park, J., McDannold, N., 2013. Multiple treatments with liposomal doxorubicin and ultrasound-induced disruption of blood–tumor and blood–brain barriers improve outcomes in a rat glioma model. J Control Release 169, 103–111. https://doi.org/10.1016/j.jconrel.2013.04.007

Ashokkumar, M., Mason, T.J., 2007. Sonochemistry, in: John Wiley & Sons, Inc. (Ed.), Kirk-Othmer Encyclopedia of Chemical Technology. John Wiley & Sons, Inc., Hoboken, NJ, USA, p. 1915141519211912.a01.pub2. https://doi.org/10.1002/0471238961.1915141519211912.a01.pub2

Atchley, A.A., Frizzell, L.A., Apfel, R.E., Holland, C.K., Madanshetty, S.I., Roy, R.A., 1988. Thresholds for cavitation produced in water by pulsed ultrasound. Ultrasonics. https://doi.org/10.1016/0041-624x(88)90018-2

Bader, K.B., Holland, C.K., 2013. Gauging the likelihood of stable cavitation from ultrasound contrast agents. Phys Med Biol 58, 127–144. https://doi.org/10.1088/0031-9155/58/1/127

Bae, S., Liu, K., Pouliopoulos, A.N., Ji, R., Jiménez-Gambín, S., Yousefian, O., Kline-Schoder, A.R., Batts, A.J., Tsitsos, F.N., Kokossis, D., Mintz, A., Honig, L.S., Konofagou, E.E., 2024. Transcranial blood-brain barrier opening in Alzheimer's disease patients using a portable focused ultrasound system with real-time 2-D cavitation mapping. Theranostics 14, 4519–4535. https://doi.org/10.7150/thno.94206

Bankhead, P., Loughrey, M.B., Fernández, J.A., Dombrowski, Y., McArt, D.G., Dunne, P.D., McQuaid, S., Gray, R.T., Murray, L.J., Coleman, H.G., James, J.A., Salto-Tellez, M., Hamilton, P.W., 2017. QuPath: Open source software for digital pathology image analysis. Sci Rep 7, 16878. https://doi.org/10.1038/s41598-017-17204-5

Barbier, E.L., Lamalle, L., Décorps, M., 2001. Methodology of brain perfusion imaging: Methodology of Brain Perfusion Imaging. J. Magn. Reson. Imaging 13, 496–520. https://doi.org/10.1002/jmri.1073

Barrière, D.A., Magalhães, R., Novais, A., Marques, P., Selingue, E., Geffroy, F., Marques, F., Cerqueira, J., Sousa, J.C., Boumezbeur, F., Bottlaender, M., Jay, T.M., Cachia, A., Sousa, N., Mériaux, S., 2019. The SIGMA rat brain templates and atlases for multimodal MRI data analysis and visualization. Nat Commun 10, 5699. https://doi.org/10.1038/s41467-019-13575-7

Bauer, H., Zweimueller-Mayer, J., Steinbacher, P., Lametschwandtner, A., Bauer, H.C., 2010. The dual role of zonula occludens (ZO) proteins. J Biomed Biotechnol 2010, 402593. https://doi.org/10.1155/2010/402593

Beaumont, M., Lemasson, B., Farion, R., Segebarth, C., Rémy, C., Barbier, E.L., 2009. Characterization of Tumor Angiogenesis in Rat Brain Using Iron-Based Vessel Size Index MRI in Combination

with Gadolinium-Based Dynamic Contrast-Enhanced MRI. J Cereb Blood Flow Metab 29, 1714–1726. https://doi.org/10.1038/jcbfm.2009.86

Beisteiner, R., Matt, E., Fan, C., Baldysiak, H., Schönfeld, M., Philippi Novak, T., Amini, A., Aslan, T., Reinecke, R., Lehrner, J., Weber, A., Reime, U., Goldenstedt, C., Marlinghaus, E., Hallett, M., Lohse-Busch, H., 2020. Transcranial Pulse Stimulation with Ultrasound in Alzheimer's Disease-A New Navigated Focal Brain Therapy. Adv Sci (Weinh) 7, 1902583. https://doi.org/10.1002/advs.201902583

Bellucci, A., Bugiani, O., Ghetti, B., Spillantini, M.G., 2011. Presence of reactive microglia and neuroinflammatory mediators in a case of frontotemporal dementia with P301S mutation. Neurodegener Dis 8, 221–229. https://doi.org/10.1159/000322228

Berchel, M., Le Gall, T., Lozach, O., Haelters, J.-P., Montier, T., Jaffrès, P.-A., 2016. Lipophosphoramidate-based bipolar amphiphiles: their syntheses and transfection properties. Org. Biomol. Chem. 14, 2846–2853. https://doi.org/10.1039/C5OB02512E

Bernardet, M., Crusio, W.E., 2006. *Fmr1* KO Mice as a Possible Model of Autistic Features. The Scientific World JOURNAL 6, 1164–1176. https://doi.org/10.1100/tsw.2006.220

Berry-Kravis, E., Des Portes, V., Hagerman, R., Jacquemont, S., Charles, P., Visootsak, J., Brinkman, M., Rerat, K., Koumaras, B., Zhu, L., Barth, G.M., Jaecklin, T., Apostol, G., von Raison, F., 2016. Mavoglurant in fragile X syndrome: Results of two randomized, double-blind, placebo-controlled trials. Sci Transl Med 8, 321ra5. https://doi.org/10.1126/scitranslmed.aab4109

Berry-Kravis, E.M., Hessl, D., Rathmell, B., Zarevics, P., Cherubini, M., Walton-Bowen, K., Mu, Y., Nguyen, D.V., Gonzalez-Heydrich, J., Wang, P.P., Carpenter, R.L., Bear, M.F., Hagerman, R.J., 2012. Effects of STX209 (Arbaclofen) on Neurobehavioral Function in Children and Adults with Fragile X Syndrome: A Randomized, Controlled, Phase 2 Trial. Sci. Transl. Med. 4. https://doi.org/10.1126/scitranslmed.3004214

Bezer, J.H., Prentice, P., Kee Chang, W.L., Morse, S.V., Christensen-Jeffries, K., Rowlands, C.J., Kozlov, A.S., Choi, J.J., 2023. Microbubble dynamics in brain microvessels. https://doi.org/10.1101/2023.10.25.563941

Bing, C., Hong, Y., Hernandez, C., Rich, M., Cheng, B., Munaweera, I., Szczepanski, D., Xi, Y., Bolding, M., Exner, A., Chopra, R., 2018. Characterization of different bubble formulations for blood-brain barrier opening using a focused ultrasound system with acoustic feedback control. Sci Rep 8, 7986. https://doi.org/10.1038/s41598-018-26330-7

Bing, K.F., Howles, G.P., Qi, Y., Palmeri, M.L., Nightingale, K.R., 2009. Blood-Brain Barrier (BBB) Disruption Using a Diagnostic Ultrasound Scanner and Definity® in Mice. Ultrasound in Medicine & Biology 35, 1298–1308. https://doi.org/10.1016/j.ultrasmedbio.2009.03.012

Blackmore, D.G., Turpin, F., Mohamed, A.Z., Zong, F., Pandit, R., Pelekanos, M., Nasrallah, F., Sah, P., Bartlett, P.F., Götz, J., 2018. Multimodal analysis of aged wild-type mice exposed to repeated scanning ultrasound treatments demonstrates long-term safety. Theranostics 8, 6233–6247. https://doi.org/10.7150/thno.27941

Blackwell, J., Kraśny, M.J., O'Brien, A., Ashkan, K., Galligan, J., Destrade, M., Colgan, N., 2022. Proton Resonance Frequency Shift Thermometry: A Review of Modern Clinical Practices. Magnetic Resonance Imaging 55, 389–403. https://doi.org/10.1002/jmri.27446

Blesa, J., Pineda-Pardo, J.A., Inoue, K.-I., Gasca-Salas, C., Balzano, T., Del Rey, N.L.-G., Reinares-Sebastián, A., Esteban-García, N., Rodríguez-Rojas, R., Márquez, R., Ciorraga, M., Del Álamo, M., García-Cañamaque, L., Ruiz de Aguiar, S., Rachmilevitch, I., Trigo-Damas, I., Takada, M., Obeso, J.A., 2023. BBB opening with focused ultrasound in nonhuman primates and Parkinson's disease patients: Targeted AAV vector delivery and PET imaging. Sci Adv 9, eadf4888. https://doi.org/10.1126/sciadv.adf4888

Bobyk, L., Edouard, M., Deman, P., Rousseau, J., Adam, J.-F., Ravanat, J.-L., Estève, F., Balosso, J., Barth, R.F., Elleaume, H., 2012. Intracerebral delivery of Carboplatin in combination with either 6 MV

Photons or monoenergetic synchrotron X-rays are equally efficacious for treatment of the F98 rat glioma. J Exp Clin Cancer Res 31, 78. https://doi.org/10.1186/1756-9966-31-78

Boisserand, L.S.B., Lemasson, B., Hirschler, L., Moisan, A., Hubert, V., Barbier, E.L., Rémy, C., Detante, O., 2017. Multiparametric magnetic resonance imaging including oxygenation mapping of experimental ischaemic stroke. J Cereb Blood Flow Metab 37, 2196–2207. https://doi.org/10.1177/0271678X16662044

Bouchet, A., Potez, M., Coquery, N., Rome, C., Lemasson, B., Bräuer-Krisch, E., Rémy, C., Laissue, J., Barbier, E.L., Djonov, V., Serduc, R., 2017. Permeability of Brain Tumor Vessels Induced by Uniform or Spatially Microfractionated Synchrotron Radiation Therapies. International Journal of Radiation Oncology*Biology*Physics 98, 1174–1182. https://doi.org/10.1016/j.ijrobp.2017.03.025

Bouvier, J., Detante, O., Tahon, F., Attye, A., Perret, T., Chechin, D., Barbieux, M., Boubagra, K., Garambois, K., Tropres, I., Grand, S., Barbier, E.L., Krainik, A., 2015. Reduced CMRO $_2$ and cerebrovascular reserve in patients with severe intracranial arterial stenosis: A combined multiparametric qBOLD oxygenation and BOLD fMRI study. Human Brain Mapping 36, 695–706. https://doi.org/10.1002/hbm.22657

Boux, F., Forbes, F., Arbel, J., Lemasson, B., Barbier, E.L., 2021a. Bayesian Inverse Regression for Vascular Magnetic Resonance Fingerprinting. IEEE Trans Med Imaging 40, 1827–1837. https://doi.org/10.1109/TMI.2021.3066781

Boux, F., Forbes, F., Collomb, N., Zub, E., Mazière, L., De Bock, F., Blaquiere, M., Stupar, V., Depaulis, A., Marchi, N., Barbier, E.L., 2021b. Neurovascular multiparametric MRI defines epileptogenic and seizure propagation regions in experimental mesiotemporal lobe epilepsy. Epilepsia 62, 1244–1255. https://doi.org/10.1111/epi.16886

Brahmachari, S., Karuppagounder, S.S., Ge, P., Lee, S., Dawson, V.L., Dawson, T.M., Ko, H.S., 2017. c-Abl and Parkinson's Disease: Mechanisms and Therapeutic Potential. JPD 7, 589–601. https://doi.org/10.3233/JPD-171191

Brasnjevic, I., Steinbusch, H.W.M., Schmitz, C., Martinez-Martinez, P., European NanoBioPharmaceutics Research Initiative, 2009. Delivery of peptide and protein drugs over the blood-brain barrier. Prog Neurobiol 87, 212–251. https://doi.org/10.1016/j.pneurobio.2008.12.002

Brennen, C.E., 1995. Cavitation and bubble dynamics. Cambridge University Press, New York.

Brodbelt, A., Greenberg, D., Winters, T., Williams, M., Vernon, S., Collins, V.P., 2015. Glioblastoma in England: 2007–2011. European Journal of Cancer 51, 533–542. https://doi.org/10.1016/j.ejca.2014.12.014

Brossard, C., Montigon, O., Boux, F., Delphin, A., Christen, T., Barbier, E.L., Lemasson, B., 2020. MP3: Medical Software for Processing Multi-Parametric Images Pipelines. Front Neuroinform 14, 594799. https://doi.org/10.3389/fninf.2020.594799

Buck, J., Larkin, J.R., Simard, M.A., Khrapitchev, A.A., Chappell, M.A., Sibson, N.R., 2018. Sensitivity of Multiphase Pseudocontinuous Arterial Spin Labelling (MP pCASL) Magnetic Resonance Imaging for Measuring Brain and Tumour Blood Flow in Mice. Contrast Media Mol Imaging 2018, 4580919. https://doi.org/10.1155/2018/4580919

Bulin, A.-L., Adam, J.-F., Elleaume, H., 2022. Stereotaxic Implantation of F98 Cells in Fischer Rats: A Syngeneic Model to Investigate Photodynamic Therapy Response in Glioma. Methods Mol Biol 2451, 203–210. https://doi.org/10.1007/978-1-0716-2099-1_15

Burgess, A., Dubey, S., Yeung, S., Hough, O., Eterman, N., Aubert, I., Hynynen, K., 2014. Alzheimer Disease in a Mouse Model: MR Imaging–guided Focused Ultrasound Targeted to the Hippocampus Opens the Blood-Brain Barrier and Improves Pathologic Abnormalities and Behavior. Radiology 273, 736–745. https://doi.org/10.1148/radiol.14140245

Byrne, J.H., 1997. Chapter 11: Blood Brain Barrier and Cerebral Metabolism, in: Neuroscience Online: An Electronic Textbook for the Neurosciences. Department of Neurobiology and Anatomy; McGovern Medical School at The University of Texas Health Science Center at Houston (UTHealth).

Carpentier, A., Stupp, R., Sonabend, A.M., Dufour, H., Chinot, O., Mathon, B., Ducray, F., Guyotat, J., Baize, N., Menei, P., De Groot, J., Weinberg, J.S., Liu, B.P., Guemas, E., Desseaux, C., Schmitt, C., Bouchoux, G., Canney, M., Idbaih, A., 2024. Repeated blood–brain barrier opening with a nine-emitter implantable ultrasound device in combination with carboplatin in recurrent glioblastoma: a phase I/II clinical trial. Nat Commun 15, 1650. https://doi.org/10.1038/s41467-024-45818-7

Castro Dias, M., Coisne, C., Lazarevic, I., Baden, P., Hata, M., Iwamoto, N., Francisco, D.M.F., Vanlandewijck, M., He, L., Baier, F.A., Stroka, D., Bruggmann, R., Lyck, R., Enzmann, G., Deutsch, U., Betsholtz, C., Furuse, M., Tsukita, S., Engelhardt, B., 2019. Claudin-3-deficient C57BL/6J mice display intact brain barriers. Sci Rep 9, 203. https://doi.org/10.1038/s41598-018-36731-3

Çavuşoğlu, M., Zhang, J., Ielacqua, G.D., Pellegrini, G., Signorell, R.D., Papachristodoulou, A., Brambilla, D., Roth, P., Weller, M., Rudin, M., Martin, E., Leroux, J.-C., Werner, B., 2019. Closed-loop cavitation control for focused ultrasound-mediated blood-brain barrier opening by long-circulating microbubbles. Phys Med Biol 64, 045012. https://doi.org/10.1088/1361-6560/aafaa5

Chadman, K.K., Adayev, T., Udayan, A., Ahmed, R., Dai, C.-L., Goodman, J.H., Meeker, H., Dolzhanskaya, N., Velinov, M., 2023. Efficient Delivery of FMR1 across the Blood Brain Barrier Using AAVphp Construct in Adult FMR1 KO Mice Suggests the Feasibility of Gene Therapy for Fragile X Syndrome. Genes (Basel) 14, 505. https://doi.org/10.3390/genes14020505

Chai, W.-Y., Chu, P.-C., Tsai, M.-Y., Lin, Y.-C., Wang, J.-J., Wei, K.-C., Wai, Y.-Y., Liu, H.-L., 2014. Magnetic-resonance imaging for kinetic analysis of permeability changes during focused ultrasound-induced blood–brain barrier opening and brain drug delivery. J Control Release 192, 1–9. https://doi.org/10.1016/j.jconrel.2014.06.023

Chen, G.Y., Nuñez, G., 2010. Sterile inflammation: sensing and reacting to damage. Nat Rev Immunol 10, 826–837. https://doi.org/10.1038/nri2873

Chen, K.-T., Chai, W.-Y., Lin, Y.-J., Lin, C.-J., Chen, P.-Y., Tsai, H.-C., Huang, C.-Y., Kuo, J.S., Liu, H.-L., Wei, K.-C., 2021. Neuronavigation-guided focused ultrasound for transcranial blood-brain barrier opening and immunostimulation in brain tumors. Sci. Adv. 7, eabd0772. https://doi.org/10.1126/sciadv.abd0772

Chen, L., Sutharsan, R., Lee, J.L., Cruz, E., Asnicar, B., Palliyaguru, T., Wasielewska, J.M., Gaudin, A., Song, J., Leinenga, G., Götz, J., 2022. Claudin-5 binder enhances focused ultrasound-mediated opening in an *in vitro* blood-brain barrier model. Theranostics 12, 1952–1970. https://doi.org/10.7150/thno.65539

Chen, S., Nazeri, A., Baek, H., Ye, D., Yang, Y., Yuan, J., Rubin, J.B., Chen, H., 2021. A review of bioeffects induced by focused ultrasound combined with microbubbles on the neurovascular unit. J Cereb Blood Flow Metab 0271678X2110461. https://doi.org/10.1177/0271678X211046129

Chen, W., Chang, P.P., Matula, T.J., Crum, L.A., 2000. Correlations between UCA-destruction-induced bioeffects and inertial cavitation dose. J Acoust Soc Am 107, 2814–2814. https://doi.org/10.1121/1.429071

Chen, W.-S., Brayman, A.A., Matula, T.J., Crum, L.A., 2003a. Inertial cavitation dose and hemolysis produced in vitro with or without Optison®. Ultrasound Med Biol 29, 725–737. https://doi.org/10.1016/S0301-5629(03)00013-9

Chen, W.-S., Matula, T.J., Brayman, A.A., Crum, L.A., 2003b. A comparison of the fragmentation thresholds and inertial cavitation doses of different ultrasound contrast agents. J Acoust Soc Am 113, 643–651. https://doi.org/10.1121/1.1529667

Cheng, B., Bing, C., Xi, Y., Shah, B., Exner, A.A., Chopra, R., 2019. Influence of Nanobubble Concentration on Blood–Brain Barrier Opening Using Focused Ultrasound Under Real-Time Acoustic Feedback Control. Ultrasound Med Biol 45, 2174–2187. https://doi.org/10.1016/j.ultrasmedbio.2019.03.016

Chevaleyre, C., Novell, A., Tournier, N., Dauba, A., Dubois, S., Kereselidze, D., Selingue, E., Jego, B., Maillère, B., Larrat, B., Nozach, H., Truillet, C., 2023. Efficient PD-L1 imaging of murine glioblastoma with FUS-aided immunoPET by leveraging FcRn-antibody interaction. Theranostics 13, 5584–5596. https://doi.org/10.7150/thno.87168

Cho, E.E., Drazic, J., Ganguly, M., Stefanovic, B., Hynynen, K., 2011. Two-Photon Fluorescence Microscopy Study of Cerebrovascular Dynamics in Ultrasound-Induced Blood—Brain Barrier Opening. J Cereb Blood Flow Metab 31, 1852–1862. https://doi.org/10.1038/jcbfm.2011.59

Cho, H., Lee, H.-Y., Han, M., Choi, J., Ahn, S., Lee, T., Chang, Y., Park, J., 2016. Localized Down-regulation of P-glycoprotein by Focused Ultrasound and Microbubbles induced Blood-Brain Barrier Disruption in Rat Brain. Sci Rep 6, 31201. https://doi.org/10.1038/srep31201

Choi, H., Lee, E.-H., Han, M., An, S.-H., Park, J., 2019. Diminished Expression of P-glycoprotein Using Focused Ultrasound Is Associated With JNK-Dependent Signaling Pathway in Cerebral Blood Vessels. Front Neurosci 13, 1350. https://doi.org/10.3389/fnins.2019.01350

Choi, H.J., Han, M., Seo, H., Park, C.Y., Lee, E.-H., Park, J., 2022. The new insight into the inflammatory response following focused ultrasound-mediated blood–brain barrier disruption. Fluids Barriers CNS 19, 103. https://doi.org/10.1186/s12987-022-00402-3

Choi, J.J., Carlisle, R.C., Coviello, C., Seymour, L., Coussios, C.-C., 2014. Non-invasive and real-time passive acoustic mapping of ultrasound-mediated drug delivery. Phys Med Biol 59, 4861–4877. https://doi.org/10.1088/0031-9155/59/17/4861

Choi, J. J., Pernot, M., Brown, T.R., Small, S.A., Konofagou, E.E., 2007. Spatio-temporal analysis of molecular delivery through the blood-brain barrier using focused ultrasound. Phys Med Biol 52, 5509–5530. https://doi.org/10.1088/0031-9155/52/18/004

Choi, James J., Pernot, M., Small, S.A., Konofagou, E.E., 2007. Noninvasive, transcranial and localized opening of the blood-brain barrier using focused ultrasound in mice. Ultrasound Med Biol 33, 95–104. https://doi.org/10.1016/j.ultrasmedbio.2006.07.018

Choi, James J, Selert, K., Gao, Z., Samiotaki, G., Baseri, B., Konofagou, E.E., 2011. Noninvasive and Localized Blood—Brain Barrier Disruption using Focused Ultrasound can be Achieved at Short Pulse Lengths and Low Pulse Repetition Frequencies. J Cereb Blood Flow Metab 31, 725–737. https://doi.org/10.1038/jcbfm.2010.155

Choi, James J., Selert, K., Vlachos, F., Wong, A., Konofagou, E.E., 2011. Noninvasive and localized neuronal delivery using short ultrasonic pulses and microbubbles. Proc Natl Acad Sci U S A 108, 16539–16544. https://doi.org/10.1073/pnas.1105116108

Choi, M., Ku, T., Chong, K., Yoon, J., Choi, C., 2011. Minimally invasive molecular delivery into the brain using optical modulation of vascular permeability. Proc Natl Acad Sci U S A 108, 9256–9261. https://doi.org/10.1073/pnas.1018790108

Chopra, R., Vykhodtseva, N., Hynynen, K., 2010. Influence of Exposure Time and Pressure Amplitude on Blood−Brain-Barrier Opening Using Transcranial Ultrasound Exposures. ACS Chem. Neurosci. 1, 391–398. https://doi.org/10.1021/cn9000445

Chou, N., Jiarong Wu, Bai Bingren, J., Anqi Qiu, Kai-Hsiang Chuang, 2011. Robust Automatic Rodent Brain Extraction Using 3-D Pulse-Coupled Neural Networks (PCNN). IEEE Trans. on Image Process. 20, 2554–2564. https://doi.org/10.1109/TIP.2011.2126587

Christen, Thomas, Bouzat, P., Pannetier, N., Coquery, N., Moisan, A., Lemasson, B., Thomas, S., Grillon, E., Detante, O., Rémy, C., Payen, J.-F., Barbier, E.L., 2014. Tissue Oxygen Saturation Mapping with Magnetic Resonance Imaging. J Cereb Blood Flow Metab 34, 1550–1557. https://doi.org/10.1038/jcbfm.2014.116

Christen, T., Lemasson, B., Pannetier, N., Farion, R., Segebarth, C., Rémy, C., Barbier, E.L., 2010. Evaluation of a quantitative blood oxygenation level-dependent (qBOLD) approach to map local blood oxygen saturation. NMR Biomed n/a-n/a. https://doi.org/10.1002/nbm.1603

Christen, T., Pannetier, N.A., Ni, W.W., Qiu, D., Moseley, M.E., Schuff, N., Zaharchuk, G., 2014. MR vascular fingerprinting: A new approach to compute cerebral blood volume, mean vessel radius, and oxygenation maps in the human brain. NeuroImage 89, 262–270. https://doi.org/10.1016/j.neuroimage.2013.11.052

Chu, C., Jablonska, A., Gao, Y., Lan, X., Lesniak, W.G., Liang, Y., Liu, G., Li, S., Magnus, T., Pearl, M., Janowski, M., Walczak, P., 2022. Hyperosmolar blood–brain barrier opening using intra-arterial injection of hyperosmotic mannitol in mice under real-time MRI guidance. Nat Protoc 17, 76–94. https://doi.org/10.1038/s41596-021-00634-x

Chu, P.-C., Chai, W.-Y., Tsai, C.-H., Kang, S.-T., Yeh, C.-K., Liu, H.-L., 2016. Focused Ultrasound-Induced Blood-Brain Barrier Opening: Association with Mechanical Index and Cavitation Index Analyzed by Dynamic Contrast-Enhanced Magnetic-Resonance Imaging. Sci Rep 6, 33264. https://doi.org/10.1038/srep33264

Chu, P.-C., Liu, H.-L., Lai, H.-Y., Lin, C.-Y., Tsai, H.-C., Pei, Y.-C., 2015. Neuromodulation accompanying focused ultrasound-induced blood-brain barrier opening. Sci Rep 5, 15477. https://doi.org/10.1038/srep15477

Clément, A., Doyen, M., Fauvelle, F., Hossu, G., Chen, B., Barberi-Heyob, M., Hirtz, A., Stupar, V., Lamiral, Z., Pouget, C., Gauchotte, G., Karcher, G., Beaumont, M., Verger, A., Lemasson, B., 2021. In vivo characterization of physiological and metabolic changes related to isocitrate dehydrogenase 1 mutation expcression by multiparametric MRI and MRS in a rat model with orthotopically grafted human-derived glioblastoma cell lines. NMR in Biomedicine 34, e4490. https://doi.org/10.1002/nbm.4490

Coluccia, D., Fandino, J., Schwyzer, L., O'Gorman, R., Remonda, L., Anon, J., Martin, E., Werner, B., 2014. First noninvasive thermal ablation of a brain tumor with MR-guided focused ultrasound. J Ther Ultrasound 2, 17. https://doi.org/10.1186/2050-5736-2-17

Cooper, I., Last, D., Ravid, O., Rand, D., Matsree, E., Omesi, L., Shemesh, C., Liberman, M., Zach, L., Furman, O., Daniels, D., Liraz-Zaltsman, S., Mardor, Y., Sharabi, S., 2023. BBB opening by low pulsed electric fields, depicted by delayed-contrast MRI, enables efficient delivery of therapeutic doxorubicin doses into mice brains. Fluids Barriers CNS 20, 67. https://doi.org/10.1186/s12987-023-00468-7

Cornu, C., Guédra, M., Béra, J.-C., Liu, H.-L., Chen, W.-S., Inserra, C., 2018. Ultrafast monitoring and control of subharmonic emissions of an unseeded bubble cloud during pulsed sonication. Ultrasonics Sonochemistry 42, 697–703. https://doi.org/10.1016/j.ultsonch.2017.12.026

Crawford, D.C., Acuña, J.M., Sherman, S.L., 2001. FMR1 and the fragile X syndrome: human genome epidemiology review. Genet Med 3, 359–371. https://doi.org/10.1097/00125817-200109000-00006

Curran, W.J., Paulus, R., Langer, C.J., Komaki, R., Lee, J.S., Hauser, S., Movsas, B., Wasserman, T., Rosenthal, S.A., Gore, E., Machtay, M., Sause, W., Cox, J.D., 2011. Sequential vs Concurrent Chemoradiation for Stage III Non-Small Cell Lung Cancer: Randomized Phase III Trial RTOG 9410. JNCI 103, 1452–1460. https://doi.org/10.1093/jnci/djr325

Daneman, R., Zhou, L., Kebede, A.A., Barres, B.A., 2010. Pericytes are required for blood-brain barrier integrity during embryogenesis. Nature 468, 562–566. https://doi.org/10.1038/nature09513

Darlix, A., Zouaoui, S., Rigau, V., Bessaoud, F., Figarella-Branger, D., Mathieu-Daudé, H., Trétarre, B., Bauchet, F., Duffau, H., Taillandier, L., Bauchet, L., 2017. Epidemiology for primary brain tumors: a nationwide population-based study. J Neurooncol 131, 525–546. https://doi.org/10.1007/s11060-016-2318-3

Dauba, A., Delalande, A., Kamimura, H.A.S., Conti, A., Larrat, B., Tsapis, N., Novell, A., 2020. Recent Advances on Ultrasound Contrast Agents for Blood-Brain Barrier Opening with Focused Ultrasound. Pharmaceutics 12, 1125. https://doi.org/10.3390/pharmaceutics12111125

De Jong, N., Emmer, M., Chin, C.T., Bouakaz, A., Mastik, F., Lohse, D., Versluis, M., 2007. "Compression-Only" Behavior of Phospholipid-Coated Contrast Bubbles. Ultrasound in Medicine & Biology 33, 653–656. https://doi.org/10.1016/j.ultrasmedbio.2006.09.016

De Jong, N., Hoff, L., Skotland, T., Bom, N., 1992. Absorption and scatter of encapsulated gas filled microspheres: Theoretical considerations and some measurements. Ultrasonics 30, 95–103. https://doi.org/10.1016/0041-624X(92)90041-J

Debacker, C., 2014. Développement de l'imagerie de perfusion cérébrale par marquage des spins artériels.

Deckers, R., Rome, C., Moonen, C.T.W., 2008. The role of ultrasound and magnetic resonance in local drug delivery. J. Magn. Reson. Imaging 27, 400–409. https://doi.org/10.1002/jmri.21272

Deffieux, T., Konofagou, E.E., 2010. Numerical study of a simple transcranial focused ultrasound system applied to blood-brain barrier opening. IEEE Trans. Ultrason., Ferroelect., Freq. Contr. 57, 2637–2653. https://doi.org/10.1109/TUFFC.2010.1738

Delalande, A., Bastié, C., Pigeon, L., Manta, S., Lebertre, M., Mignet, N., Midoux, P., Pichon, C., 2017. Cationic gas-filled microbubbles for ultrasound-based nucleic acids delivery. Biosci Rep 37, BSR20160619. https://doi.org/10.1042/BSR20160619

Delalande, A., Postema, M., Mignet, N., Midoux, P., Pichon, C., 2012. Ultrasound and microbubble-assisted gene delivery: recent advances and ongoing challenges. Therapeutic Delivery 3, 1199–1215. https://doi.org/10.4155/tde.12.100

Delaney, L.J., Eisenbrey, J.R., Brown, D., Brody, J.R., Jimbo, M., Oeffinger, B.E., Stanczak, M., Forsberg, F., Liu, J.-B., Wheatley, M.A., 2021. Gemcitabine-loaded microbubble system for ultrasound imaging and therapy. Acta Biomaterialia 130, 385–394. https://doi.org/10.1016/j.actbio.2021.05.046

Delphin, A., Boux, F., Brossard, C., Coudert, T., Warnking, J.M., Lemasson, B., Barbier, E.L., Christen, T., 2024. Enhancing MR vascular Fingerprinting through realistic microvascular geometries. https://doi.org/10.48550/ARXIV.2305.17092

Deverman, B.E., Pravdo, P.L., Simpson, B.P., Kumar, S.R., Chan, K.Y., Banerjee, A., Wu, W.-L., Yang, B., Huber, N., Pasca, S.P., Gradinaru, V., 2016. Cre-dependent selection yields AAV variants for widespread gene transfer to the adult brain. Nat Biotechnol 34, 204–209. https://doi.org/10.1038/nbt.3440

Dobre, M.C., Uğurbil, K., Marjanska, M., 2007. Determination of blood longitudinal relaxation time (T1) at high magnetic field strengths. Magnetic Resonance Imaging 25, 733–735. https://doi.org/10.1016/j.mri.2006.10.020

Downs, M.E., Buch, A., Sierra, C., Karakatsani, M.E., Chen, S., Konofagou, E.E., Ferrera, V.P., 2015. Long-Term Safety of Repeated Blood-Brain Barrier Opening via Focused Ultrasound with Microbubbles in Non-Human Primates Performing a Cognitive Task. PLoS ONE 10, e0125911. https://doi.org/10.1371/journal.pone.0125911

Dréan, A., Lemaire, N., Bouchoux, G., Goldwirt, L., Canney, M., Goli, L., Bouzidi, A., Schmitt, C., Guehennec, J., Verreault, M., Sanson, M., Delattre, J.-Y., Mokhtari, K., Sottilini, F., Carpentier, A., Idbaih, A., 2019. Temporary blood–brain barrier disruption by low intensity pulsed ultrasound increases carboplatin delivery and efficacy in preclinical models of glioblastoma. J Neurooncol 144, 33–41. https://doi.org/10.1007/s11060-019-03204-0

Dubois, L.G., Campanati, L., Righy, C., D'Andrea-Meira, I., Spohr, T.C.L. de S.E., Porto-Carreiro, I., Pereira, C.M., Balça-Silva, J., Kahn, S.A., DosSantos, M.F., Oliveira, M. de A.R., Ximenes-da-Silva, A., Lopes, M.C., Faveret, E., Gasparetto, E.L., Moura-Neto, V., 2014. Gliomas and the vascular fragility of the blood brain barrier. Front Cell Neurosci 8, 418. https://doi.org/10.3389/fncel.2014.00418

Durham, P.G., Butnariu, A., Alghorazi, R., Pinton, G., Krishna, V., Dayton, P.A., 2024. Current clinical investigations of focused ultrasound blood-brain barrier disruption: A review. Neurotherapeutics 21, e00352. https://doi.org/10.1016/j.neurot.2024.e00352

Dyer-Friedman, J., Glaser, B., Hessl, D., Johnston, C., Huffman, L.C., Taylor, A., Wisbeck, J., Reiss, A.L., 2002. Genetic and environmental influences on the cognitive outcomes of children with fragile X syndrome. J Am Acad Child Adolesc Psychiatry 41, 237–244. https://doi.org/10.1097/00004583-200203000-00002

ElAli, A., Thériault, P., Rivest, S., 2014. The role of pericytes in neurovascular unit remodeling in brain disorders. Int J Mol Sci 15, 6453–6474. https://doi.org/10.3390/ijms15046453

Elias, W.J., Lipsman, N., Ondo, W.G., Ghanouni, P., Kim, Y.G., Lee, W., Schwartz, M., Hynynen, K., Lozano, A.M., Shah, B.B., Huss, D., Dallapiazza, R.F., Gwinn, R., Witt, J., Ro, S., Eisenberg, H.M., Fishman, P.S., Gandhi, D., Halpern, C.H., Chuang, R., Butts Pauly, K., Tierney, T.S., Hayes, M.T., Cosgrove, G.R., Yamaguchi, T., Abe, K., Taira, T., Chang, J.W., 2016. A Randomized Trial of Focused Ultrasound Thalamotomy for Essential Tremor. N Engl J Med 375, 730–739. https://doi.org/10.1056/NEJMoa1600159

Elleaume, H., Barth, R.F., Rousseau, J., Bobyk, L., Balosso, J., Yang, W., Huo, T., Nakkula, R., 2020. Radiation therapy combined with intracerebral convection-enhanced delivery of cisplatin or carboplatin for treatment of the F98 rat glioma. J Neurooncol 149, 193–208. https://doi.org/10.1007/s11060-020-03600-x

Ellegood, J., Pacey, L.K., Hampson, D.R., Lerch, J.P., Henkelman, R.M., 2010. Anatomical phenotyping in a mouse model of fragile X syndrome with magnetic resonance imaging. NeuroImage 53, 1023–1029. https://doi.org/10.1016/j.neuroimage.2010.03.038

Epelbaum, S., Burgos, N., Canney, M., Matthews, D., Houot, M., Santin, M.D., Desseaux, C., Bouchoux, G., Stroer, S., Martin, C., Habert, M.-O., Levy, M., Bah, A., Martin, K., Delatour, B., Riche, M., Dubois, B., Belin, L., Carpentier, A., 2022. Pilot study of repeated blood-brain barrier disruption in patients with mild Alzheimer's disease with an implantable ultrasound device. Alz Res Therapy 14, 40. https://doi.org/10.1186/s13195-022-00981-1

Errico, C., Pierre, J., Pezet, S., Desailly, Y., Lenkei, Z., Couture, O., Tanter, M., 2015. Ultrafast ultrasound localization microscopy for deep super-resolution vascular imaging. Nature 527, 499–502. https://doi.org/10.1038/nature16066

Esparza-Coss, E., Wosik, J., Narayana, P.A., 2010. Perfusion in rat brain at 7 T with arterial spin labeling using FAIR-TrueFISP and QUIPSS. Magnetic Resonance Imaging 28, 607–612. https://doi.org/10.1016/j.mri.2010.01.004

Ewing, J.R., Wei, L., Knight, R.A., Pawa, S., Nagaraja, T.N., Brusca, T., Divine, G.W., Fenstermacher, J.D., 2003. Direct comparison of local cerebral blood flow rates measured by MRI arterial spin-tagging and quantitative autoradiography in a rat model of experimental cerebral ischemia. J Cereb Blood Flow Metab 23, 198–209. https://doi.org/10.1097/01.WCB.0000046147.31247.E8

Fan, C.-H., Liu, H.-L., Huang, C.-Y., Ma, Y.-J., Yen, T.-C., Yeh, C.-K., 2012. Detection of Intracerebral Hemorrhage and Transient Blood-Supply Shortage in Focused-Ultrasound-Induced Blood–Brain Barrier Disruption by Ultrasound Imaging. Ultrasound Med Biol 38, 1372–1382. https://doi.org/10.1016/j.ultrasmedbio.2012.03.013

Fan, C.-H., Ting, C.-Y., Lin, H.-J., Wang, C.-H., Liu, H.-L., Yen, T.-C., Yeh, C.-K., 2013. SPIO-conjugated, doxorubicin-loaded microbubbles for concurrent MRI and focused-ultrasound enhanced

brain-tumor drug delivery. Biomaterials 34, 3706–3715. https://doi.org/10.1016/j.biomaterials.2013.01.099

Felix, M.-S., Borloz, E., Metwally, K., Dauba, A., Larrat, B., Matagne, V., Ehinger, Y., Villard, L., Novell, A., Mensah, S., Roux, J.-C., 2021. Ultrasound-Mediated Blood-Brain Barrier Opening Improves Whole Brain Gene Delivery in Mice. Pharmaceutics 13, 1245. https://doi.org/10.3390/pharmaceutics13081245

Finkel, R.S., Chiriboga, C.A., Vajsar, J., Day, J.W., Montes, J., De Vivo, D.C., Yamashita, M., Rigo, F., Hung, G., Schneider, E., Norris, D.A., Xia, S., Bennett, C.F., Bishop, K.M., 2016. Treatment of infantile-onset spinal muscular atrophy with nusinersen: a phase 2, open-label, dose-escalation study. Lancet 388, 3017–3026. https://doi.org/10.1016/S0140-6736(16)31408-8

Fischer, S., Wiesnet, M., Marti, H.H., Renz, D., Schaper, W., 2004. Simultaneous activation of several second messengers in hypoxia-induced hyperpermeability of brain derived endothelial cells. J Cell Physiol 198, 359–369. https://doi.org/10.1002/jcp.10417

Fisher, D.G., Sharifi, K.A., Shah, I.M., Gorick, C.M., Breza, V.R., Debski, A.C., Hoch, M.R., Cruz, T., Samuels, J.D., Sheehan, J.P., Schlesinger, D., Moore, D., Lukens, J.R., Miller, G.W., Tvrdik, P., Price, R.J., 2024. Focused Ultrasound Blood-Brain Barrier Opening Arrests the Growth and Formation of Cerebral Cavernous Malformations. bioRxiv 2024.01.31.577810. https://doi.org/10.1101/2024.01.31.577810

Fletcher, Stecia-Marie P., Chisholm, A., Lavelle, M., Guthier, R., Zhang, Y., Power, C., Berbeco, R., McDannold, N., 2024. A study combining microbubble-mediated focused ultrasound and radiation therapy in the healthy rat brain and a F98 glioma model. Sci Rep 14, 4831. https://doi.org/10.1038/s41598-024-55442-6

Fletcher, Stecia-Marie P, Zhang, Y.-Z., Chisholm, A., Martinez, S., McDannold, N.J., 2024. The impact of pulse repetition frequency on microbubble activity and drug delivery during focused ultrasound-mediated blood-brain barrier opening. Phys. Med. Biol. https://doi.org/10.1088/1361-6560/ad5b47

Freeman, S.M., Young, L.J., 2016. Comparative Perspectives on Oxytocin and Vasopressin Receptor Research in Rodents and Primates: Translational Implications. J Neuroendocrinol 28. https://doi.org/10.1111/jne.12382

Frinking, P., Segers, T., Luan, Y., Tranquart, F., 2020. Three Decades of Ultrasound Contrast Agents: A Review of the Past, Present and Future Improvements. Ultrasound Med Biol 46, 892–908. https://doi.org/10.1016/j.ultrasmedbio.2019.12.008

Gadani, S.P., Walsh, J.T., Lukens, J.R., Kipnis, J., 2015. Dealing with Danger in the CNS: The Response of the Immune System to Injury. Neuron 87, 47–62. https://doi.org/10.1016/j.neuron.2015.05.019

Galbán, C.J., Lemasson, B., Hoff, B.A., Johnson, T.D., Sundgren, P.C., Tsien, C., Chenevert, T.L., Ross, B.D., 2015. Development of a Multiparametric Voxel-Based Magnetic Resonance Imaging Biomarker for Early Cancer Therapeutic Response Assessment. Tomography 1, 44–52. https://doi.org/10.18383/j.tom.2015.00124

Gao, Y., Gao, S., Zhao, B., Zhao, Y., Hua, X., Tan, K., Liu, Z., 2012. Vascular Effects of Microbubble-Enhanced, Pulsed, Focused Ultrasound on Liver Blood Perfusion. Ultrasound Med Biol 38, 91–98. https://doi.org/10.1016/j.ultrasmedbio.2011.09.018

Gasca-Salas, C., Fernández-Rodríguez, B., Pineda-Pardo, J.A., Rodríguez-Rojas, R., Obeso, I., Hernández-Fernández, F., del Álamo, M., Mata, D., Guida, P., Ordás-Bandera, C., Montero-Roblas, J.I., Martínez-Fernández, R., Foffani, G., Rachmilevitch, I., Obeso, J.A., 2021. Blood-brain barrier opening with focused ultrasound in Parkinson's disease dementia. Nat Commun 12, 779. https://doi.org/10.1038/s41467-021-21022-9

Gasca-Salas, C., Pineda-Pardo, J.A., Del Álamo, M., Jiménez, T., Trompeta, C., Toltsis, G., Garcia-Cañamaque, L., Fernández-Rodríguez, B., Matarazzo, M., Plaza De Las Heras, I., Natera-Villalba,

E., Martínez-Fernández, R., Duque, A., Ruiz De Aguiar, S., Blesa, J., Rachmilevich, I., Obeso, J.A., 2024. Nigrostriatal blood-brain barrier opening in Parkinson's disease. J Neurol Neurosurg Psychiatry jnnp-2023-332967. https://doi.org/10.1136/jnnp-2023-332967

Gattegno, R., Arbel, L., Riess, N., Shinar, H., Katz, S., Ilovitsh, T., 2024. Enhanced capillary delivery with nanobubble-mediated blood-brain barrier opening and advanced high resolution vascular segmentation. Journal of Controlled Release 369, 506–516. https://doi.org/10.1016/j.jconrel.2024.04.001

German Mouse Clinic Consortium, Castro Dias, M., Coisne, C., Baden, P., Enzmann, G., Garrett, L., Becker, L., Hölter, S.M., Hrabě De Angelis, M., Deutsch, U., Engelhardt, B., 2019. Claudin-12 is not required for blood–brain barrier tight junction function. Fluids Barriers CNS 16, 30. https://doi.org/10.1186/s12987-019-0150-9

Gerstenmayer, M., Fellah, B., Magnin, R., Selingue, E., Larrat, B., 2018. Acoustic Transmission Factor through the Rat Skull as a Function of Body Mass, Frequency and Position. Ultrasound Med Biol 44, 2336–2344. https://doi.org/10.1016/j.ultrasmedbio.2018.06.005

Giesecke, T., Hynynen, K., 2003. Ultrasound-mediated cavitation thresholds of liquid perfluorocarbon droplets in vitro. Ultrasound Med Biol 29, 1359–1365. https://doi.org/10.1016/S0301-5629(03)00980-3

Gonçalves, C., Berchel, M., Gosselin, M.-P., Malard, V., Cheradame, H., Jaffrès, P.-A., Guégan, P., Pichon, C., Midoux, P., 2014. Lipopolyplexes comprising imidazole/imidazolium lipophosphoramidate, histidinylated polyethyleneimine and siRNA as efficient formulation for siRNA transfection. Int J Pharm 460, 264–272. https://doi.org/10.1016/j.ijpharm.2013.11.005

Gorick, C.M., Mathew, A.S., Garrison, W.J., Thim, E.A., Fisher, D.G., Copeland, C.A., Song, J., Klibanov, A.L., Miller, G.W., Price, R.J., 2020. Sonoselective transfection of cerebral vasculature without blood–brain barrier disruption. Proc Natl Acad Sci U S A 117, 5644–5654. https://doi.org/10.1073/pnas.1914595117

Goutal, S., Novell, A., Leterrier, S., Breuil, L., Selingue, E., Gerstenmayer, M., Marie, S., Saubaméa, B., Caillé, F., Langer, O., Truillet, C., Larrat, B., Tournier, N., 2023. Imaging the impact of blood-brain barrier disruption induced by focused ultrasound on P-glycoprotein function. J Control Release 361, 483–492. https://doi.org/10.1016/j.jconrel.2023.08.012

Gu, Y., Xue, Y., Wang, Y., Wang, J., Chen, X., ShangGuan, Q., Lian, Y., Zhong, L., Meng, Y., 2013. Minoxidil sulfate induced the increase in blood-brain tumor barrier permeability through ROS/RhoA/PI3K/PKB signaling pathway. Neuropharmacology 75, 407–415. https://doi.org/10.1016/j.neuropharm.2013.08.004

Guo, S., Wang, H., Yin, Y., 2022. Microglia Polarization From M1 to M2 in Neurodegenerative Diseases. Front Aging Neurosci 14, 815347. https://doi.org/10.3389/fnagi.2022.815347

Gyöngy, M., Coussios, C.-C., 2010a. Passive spatial mapping of inertial cavitation during HIFU exposure. IEEE Trans Biomed Eng 57, 48–56. https://doi.org/10.1109/TBME.2009.2026907

Gyöngy, M., Coussios, C.-C., 2010b. Passive cavitation mapping for localization and tracking of bubble dynamics. J Acoust Soc Am 128, EL175-180. https://doi.org/10.1121/1.3467491

Haberl, M.G., Zerbi, V., Veltien, A., Ginger, M., Heerschap, A., Frick, A., 2015. Structural-functional connectivity deficits of neocortical circuits in the *Fmr1* $^{-/y}$ mouse model of autism. Sci Adv 1, e1500775. https://doi.org/10.1126/sciadv.1500775

Hagerman, R.J., Berry-Kravis, E., Hazlett, H.C., Bailey, D.B., Moine, H., Kooy, R.F., Tassone, F., Gantois, I., Sonenberg, N., Mandel, J.L., Hagerman, P.J., 2017. Fragile X syndrome. Nat Rev Dis Primers 3, 17065. https://doi.org/10.1038/nrdp.2017.65

Han, L., Kong, D.K., Zheng, M.-Q., Murikinati, S., Ma, C., Yuan, P., Li, L., Tian, D., Cai, Q., Ye, C., Holden, D., Park, J.-H., Gao, X., Thomas, J.-L., Grutzendler, J., Carson, R.E., Huang, Y., Piepmeier, J.M., Zhou, J., 2016. Increased Nanoparticle Delivery to Brain Tumors by Autocatalytic Priming for

Improved Treatment and Imaging. ACS Nano 10, 4209–4218. https://doi.org/10.1021/acsnano.5b07573

Harris, F., J., 1978. On the Use of Windows for Harmonic Analysis with the Discrete Fourier Transform. Proceedings of the IEEE 66, 51–83. https://doi.org/10.1109/proc.1978.10837

Hartings, J.A., Bullock, M.R., Okonkwo, D.O., Murray, L.S., Murray, G.D., Fabricius, M., Maas, A.I., Woitzik, J., Sakowitz, O., Mathern, B., Roozenbeek, B., Lingsma, H., Dreier, J.P., Puccio, A.M., Shutter, L.A., Pahl, C., Strong, A.J., 2011. Spreading depolarisations and outcome after traumatic brain injury: a prospective observational study. The Lancet Neurology 10, 1058–1064. https://doi.org/10.1016/S1474-4422(11)70243-5

Hatch, R.J., Leinenga, G., Götz, J., 2016. Scanning Ultrasound (SUS) Causes No Changes to Neuronal Excitability and Prevents Age-Related Reductions in Hippocampal CA1 Dendritic Structure in Wild-Type Mice. PLoS ONE 11, e0164278. https://doi.org/10.1371/journal.pone.0164278

Herscovitch, P., Raichle, M.E., 1985. What is the Correct Value for the Brain-Blood Partition Coefficient for Water? J Cereb Blood Flow Metab 5, 65–69. https://doi.org/10.1038/jcbfm.1985.9

Hiles-Murison, B., Lavender, A.P., Hackett, M.J., Armstrong, J.J., Nesbit, M., Rawlings, S., McGonigle, T., Warnock, A., Lam, V., Mamo, J.C.L., Fitzgerald, M., Takechi, R., 2021. Blood–brain barrier disruption and ventricular enlargement are the earliest neuropathological changes in rats with repeated sub-concussive impacts over 2 weeks. Sci Rep 11, 9261. https://doi.org/10.1038/s41598-021-88854-9

Hirschler, L., Collomb, N., Voiron, J., Köhler, S., Barbier, E.L., Warnking, J.M., 2020. SAR comparison between CASL and pCASL at high magnetic field and evaluation of the benefit of a dedicated labeling coil. Magn Reson Med 83, 254–261. https://doi.org/10.1002/mrm.27931

Hirschler, L., Debacker, C.S., Voiron, J., Köhler, S., Warnking, J.M., Barbier, E.L., 2018. Interpulse phase corrections for unbalanced pseudo-continuous arterial spin labeling at high magnetic field: RF Phase Optimization for Unbalanced pCASL. Magn Reson Med 79, 1314–1324. https://doi.org/10.1002/mrm.26767

Hordeaux, J., Wang, Q., Katz, N., Buza, E.L., Bell, P., Wilson, J.M., 2018. The Neurotropic Properties of AAV-PHP.B Are Limited to C57BL/6J Mice. Mol Ther 26, 664–668. https://doi.org/10.1016/j.ymthe.2018.01.018

Horodyckid, C., Canney, M., Vignot, A., Boisgard, R., Drier, A., Huberfeld, G., François, C., Prigent, A., Santin, M.D., Adam, C., Willer, J.-C., Lafon, C., Chapelon, J.-Y., Carpentier, A., 2017. Safe long-term repeated disruption of the blood-brain barrier using an implantable ultrasound device: a multiparametric study in a primate model. JNS 126, 1351–1361. https://doi.org/10.3171/2016.3.JNS151635

Hossmann, K.A., 1996. Periinfarct depolarizations. Cerebrovasc Brain Metab Rev 8, 195–208.

Huang, Q., Deng, J., Wang, F., Chen, S., Liu, Y., Wang, Zhibiao, Wang, Zhigang, Cheng, Y., 2012. Targeted gene delivery to the mouse brain by MRI-guided focused ultrasound-induced blood–brain barrier disruption. Experimental Neurology 233, 350–356. https://doi.org/10.1016/j.expneurol.2011.10.027

Huang, Y., Meng, Y., Pople, C.B., Bethune, A., Jones, R.M., Abrahao, A., Hamani, C., Kalia, S.K., Kalia, L.V., Lipsman, N., Hynynen, K., 2022. Cavitation Feedback Control of Focused Ultrasound Blood-Brain Barrier Opening for Drug Delivery in Patients with Parkinson's Disease. Pharmaceutics 14. https://doi.org/10.3390/pharmaceutics14122607

Hugon, G., Goutal, S., Dauba, A., Breuil, L., Larrat, B., Winkeler, A., Novell, A., Tournier, N., 2021. [18F]2-Fluoro-2-deoxy-sorbitol PET Imaging for Quantitative Monitoring of Enhanced Blood-Brain Barrier Permeability Induced by Focused Ultrasound. Pharmaceutics 13, 1752. https://doi.org/10.3390/pharmaceutics13111752

Hwang, J.H., Tu, J., Brayman, A.A., Matula, T.J., Crum, L.A., 2006. Correlation between inertial cavitation dose and endothelial cell damage in vivo. Ultrasound Med Biol 32, 1611–1619. https://doi.org/10.1016/j.ultrasmedbio.2006.07.016

Hynynen, K., Chung, A.H., Colucci, V., Jolesz, F.A., 1996. Potential adverse effects of high-intensity focused ultrasound exposure on blood vessels in vivo. Ultrasound Med Biol 22, 193–201. https://doi.org/10.1016/0301-5629(95)02044-6

Hynynen, K., McDannold, N., Vykhodtseva, N., Jolesz, F.A., 2001. Noninvasive MR Imaging–guided Focal Opening of the Blood-Brain Barrier in Rabbits. Radiology 220, 640–646. https://doi.org/10.1148/radiol.2202001804

Hynynen, K., McDannold, N., Vykhodtseva, N., Raymond, S., Weissleder, R., Jolesz, F.A., Sheikov, N., 2006. Focal disruption of the blood–brain barrier due to 260-kHz ultrasound bursts: a method for molecular imaging and targeted drug delivery. JNS 105, 445–454. https://doi.org/10.3171/jns.2006.105.3.445

Iadecola, C., 2004. Neurovascular regulation in the normal brain and in Alzheimer's disease. Nat Rev Neurosci 5, 347–360. https://doi.org/10.1038/nrn1387

Idbaih, A., Canney, M., Belin, L., Desseaux, C., Vignot, A., Bouchoux, G., Asquier, N., Law-Ye, B., Leclercq, D., Bissery, A., De Rycke, Y., Trosch, C., Capelle, L., Sanson, M., Hoang-Xuan, K., Dehais, C., Houillier, C., Laigle-Donadey, F., Mathon, B., André, A., Lafon, C., Chapelon, J.-Y., Delattre, J.-Y., Carpentier, A., 2019. Safety and Feasibility of Repeated and Transient Blood–Brain Barrier Disruption by Pulsed Ultrasound in Patients with Recurrent Glioblastoma. Clin Cancer Res 25, 3793–3801. https://doi.org/10.1158/1078-0432.CCR-18-3643

Ilovitsh, A., Fite, B.Z., Ilovitsh, T., Ferrara, K.W., 2019. Acoustic radiation force imaging using a single-shot spiral readout. Phys Med Biol 64, 125004. https://doi.org/10.1088/1361-6560/ab1e21

Ilyichev, V.I., Koretz, V.L., Melnikov, N.P., 1989. Spectral characteristics of acoustic cavitation. Ultrasonics 27, 357–361. https://doi.org/10.1016/0041-624X(89)90034-6

Ishihara, Y., Calderon, A., Watanabe, H., Okamoto, K., Suzuki, Y., Kuroda, K., Suzuki, Y., 1995. A precise and fast temperature mapping using water proton chemical shift. Magn Reson Med 34, 814–823. https://doi.org/10.1002/mrm.1910340606

Itani, M., Mattrey, R.F., 2012. The effect of inhaled gases on ultrasound contrast agent longevity in vivo. Mol Imaging Biol 14, 40–46. https://doi.org/10.1007/s11307-011-0475-5

Jacobs, S., McCully, C.L., Murphy, R.F., Bacher, J., Balis, F.M., Fox, E., 2010. Extracellular fluid concentrations of cisplatin, carboplatin, and oxaliplatin in brain, muscle, and blood measured using microdialysis in nonhuman primates. Cancer Chemother Pharmacol 65, 817–824. https://doi.org/10.1007/s00280-009-1085-7

Jacquemont, S., Curie, A., des Portes, V., Torrioli, M.G., Berry-Kravis, E., Hagerman, R.J., Ramos, F.J., Cornish, K., He, Y., Paulding, C., Neri, G., Chen, F., Hadjikhani, N., Martinet, D., Meyer, J., Beckmann, J.S., Delange, K., Brun, A., Bussy, G., Gasparini, F., Hilse, T., Floesser, A., Branson, J., Bilbe, G., Johns, D., Gomez-Mancilla, B., 2011. Epigenetic modification of the FMR1 gene in fragile X syndrome is associated with differential response to the mGluR5 antagonist AFQ056. Sci Transl Med 3, 64ra1. https://doi.org/10.1126/scitranslmed.3001708

Jain, R.K., 2014. Antiangiogenesis strategies revisited: from starving tumors to alleviating hypoxia. Cancer Cell 26, 605–622. https://doi.org/10.1016/j.ccell.2014.10.006

Jalali, S., Huang, Y., Dumont, D.J., Hynynen, K., 2010. Focused ultrasound-mediated bbb disruption is associated with an increase in activation of AKT: experimental study in rats. BMC Neurol 10, 114. https://doi.org/10.1186/1471-2377-10-114

Jenkinson, M., Bannister, P., Brady, M., Smith, S., 2002. Improved optimization for the robust and accurate linear registration and motion correction of brain images. NeuroImage 17, 825–841. https://doi.org/10.1016/s1053-8119(02)91132-8

Ji, R., Karakatsani, M.E., Burgess, M., Smith, M., Murillo, M.F., Konofagou, E.E., 2021. Cavitation-modulated inflammatory response following focused ultrasound blood-brain barrier opening. J Control Release 337, 458–471. https://doi.org/10.1016/j.jconrel.2021.07.042

Johnston, K., Tapia-Siles, C., Gerold, B., Postema, M., Cochran, S., Cuschieri, A., Prentice, P., 2014. Periodic shock-emission from acoustically driven cavitation clouds: A source of the subharmonic signal. Ultrasonics 54, 2151–2158. https://doi.org/10.1016/j.ultras.2014.06.011

Jones, R.M., Deng, L., Leung, K., McMahon, D., O'Reilly, M.A., Hynynen, K., 2018. Three-dimensional transcranial microbubble imaging for guiding volumetric ultrasound-mediated blood-brain barrier opening. Theranostics 8, 2909–2926. https://doi.org/10.7150/thno.24911

Jordão, J.F., Ayala-Grosso, C.A., Markham, K., Huang, Y., Chopra, R., McLaurin, J., Hynynen, K., Aubert, I., 2010. Antibodies Targeted to the Brain with Image-Guided Focused Ultrasound Reduces Amyloid-β Plaque Load in the TgCRND8 Mouse Model of Alzheimer's Disease. PLoS ONE 5, e10549. https://doi.org/10.1371/journal.pone.0010549

Jordão, J.F., Thévenot, E., Markham-Coultes, K., Scarcelli, T., Weng, Y.-Q., Xhima, K., O'Reilly, M., Huang, Y., McLaurin, J., Hynynen, K., Aubert, I., 2013. Amyloid-β plaque reduction, endogenous antibody delivery and glial activation by brain-targeted, transcranial focused ultrasound. Experimental Neurology 248, 16–29. https://doi.org/10.1016/j.expneurol.2013.05.008

Kadry, H., Noorani, B., Cucullo, L., 2020. A blood-brain barrier overview on structure, function, impairment, and biomarkers of integrity. Fluids Barriers CNS 17, 69. https://doi.org/10.1186/s12987-020-00230-3

Kamimura, H.A., Flament, J., Valette, J., Cafarelli, A., Aron Badin, R., Hantraye, P., Larrat, B., 2019. Feedback control of microbubble cavitation for ultrasound-mediated blood-brain barrier disruption in non-human primates under magnetic resonance guidance. J Cereb Blood Flow Metab 39, 1191–1203. https://doi.org/10.1177/0271678X17753514

Kamimura, H.A.S., Wu, S.-Y., Grondin, J., Ji, R., Aurup, C., Zheng, W., Heidmann, M., Pouliopoulos, A.N., Konofagou, E.E., 2021. Real-Time Passive Acoustic Mapping Using Sparse Matrix Multiplication. IEEE Trans. Ultrason., Ferroelect., Freq. Contr. 68, 164–177. https://doi.org/10.1109/tuffc.2020.3001848

Kaplan, L., Chow, B.W., Gu, C., 2020. Neuronal regulation of the blood–brain barrier and neurovascular coupling. Nat Rev Neurosci 21, 416–432. https://doi.org/10.1038/s41583-020-0322-2

Karakatsani, M.E., Kugelman, T., Ji, R., Murillo, M., Wang, S., Niimi, Y., Small, S.A., Duff, K.E., Konofagou, E.E., 2019. Unilateral Focused Ultrasound-Induced Blood-Brain Barrier Opening Reduces Phosphorylated Tau from The rTg4510 Mouse Model. Theranostics 9, 5396–5411. https://doi.org/10.7150/thno.28717

Katiyar, A., Sarkar, K., 2011. Excitation threshold for subharmonic generation from contrast microbubbles. J Acoust Soc Am 130, 3137–3147. https://doi.org/10.1121/1.3641455

Katsuno, T., Umeda, K., Matsui, T., Hata, M., Tamura, A., Itoh, M., Takeuchi, K., Fujimori, T., Nabeshima, Y., Noda, T., Tsukita, Shoichiro, Tsukita, Sachiko, 2008. Deficiency of Zonula Occludens-1 Causes Embryonic Lethal Phenotype Associated with Defected Yolk Sac Angiogenesis and Apoptosis of Embryonic Cells. MBoC 19, 2465–2475. https://doi.org/10.1091/mbc.e07-12-1215

Katz, S., Gattegno, R., Peko, L., Zarik, R., Hagani, Y., Ilovitsh, T., 2023. Diameter-dependent assessment of microvascular leakage following ultrasound-mediated blood-brain barrier opening. iScience 26, 106965. https://doi.org/10.1016/j.isci.2023.106965

Kenkel, W.M., Yee, J.R., Moore, K., Madularu, D., Kulkarni, P., Gamber, K., Nedelman, M., Ferris, C.F., 2016. Functional magnetic resonance imaging in awake transgenic fragile X rats: evidence of dysregulation in reward processing in the mesolimbic/habenular neural circuit. Transl Psychiatry 6, e763. https://doi.org/10.1038/tp.2016.15

Khan, S., 2022. Improved Cavitation Monitoring and Detection Methods for Focused Ultrasound Blood-Brain Barrier Disruption. University of Calgary, Calgary, Canada.

Kilic, E., Kilic, U., Wang, Y., Bassetti, C.L., Marti, H.H., Hermann, D.M., 2006. The phosphatidylinositol-3 kinase/Akt pathway mediates VEGF's neuroprotective activity and induces blood brain barrier permeability after focal cerebral ischemia. FASEB J 20, 1185–1187. https://doi.org/10.1096/fj.05-4829fje

Kim, D.G., Gonzales, E.L., Kim, S., Kim, Y., Adil, K.J., Jeon, S.J., Cho, K.S., Kwon, K.J., Shin, C.Y., 2019. Social Interaction Test in Home Cage as a Novel and Ethological Measure of Social Behavior in Mice. Exp Neurobiol 28, 247–260. https://doi.org/10.5607/en.2019.28.2.247

Kim, T., Kim, S.-G., 2005. Quantification of cerebral arterial blood volume and cerebral blood flow using MRI with modulation of tissue and vessel (MOTIVE) signals. Magn Reson Med 54, 333–342. https://doi.org/10.1002/mrm.20550

Kisler, K., Nelson, A.R., Montagne, A., Zlokovic, B.V., 2017. Cerebral blood flow regulation and neurovascular dysfunction in Alzheimer disease. Nat Rev Neurosci 18, 419–434. https://doi.org/10.1038/nrn.2017.48

Kobus, T., Vykhodtseva, N., Pilatou, M., Zhang, Y., McDannold, N., 2016. Safety Validation of Repeated Blood–Brain Barrier Disruption Using Focused Ultrasound. Ultrasound Med Biol 42, 481–492. https://doi.org/10.1016/j.ultrasmedbio.2015.10.009

Kodack, D.P., Askoxylakis, V., Ferraro, G.B., Sheng, Q., Badeaux, M., Goel, S., Qi, X., Shankaraiah, R., Cao, Z.A., Ramjiawan, R.R., Bezwada, D., Patel, B., Song, Y., Costa, C., Naxerova, K., Wong, C.S.F., Kloepper, J., Das, R., Tam, A., Tanboon, J., Duda, D.G., Miller, C.R., Siegel, M.B., Anders, C.K., Sanders, M., Estrada, M.V., Schlegel, R., Arteaga, C.L., Brachtel, E., Huang, A., Fukumura, D., Engelman, J.A., Jain, R.K., 2017. The brain microenvironment mediates resistance in luminal breast cancer to PI3K inhibition through HER3 activation. Sci Transl Med 9, eaal4682. https://doi.org/10.1126/scitranslmed.aal4682

Kong, C., Ahn, J.W., Kim, S., Park, J.Y., Na, Y.C., Chang, J.W., Chung, S., Chang, W.S., 2023. Long-lasting restoration of memory function and hippocampal synaptic plasticity by focused ultrasound in Alzheimer's disease. Brain Stimulation 16, 857–866. https://doi.org/10.1016/j.brs.2023.05.014

Kong, C., Yang, E.-J., Shin, J., Park, J., Kim, S.-H., Park, S.-W., Chang, W.S., Lee, C.-H., Kim, H., Kim, H.-S., Chang, J.W., 2022. Enhanced delivery of a low dose of aducanumab via FUS in 5×FAD mice, an AD model. Transl Neurodegener 11, 57. https://doi.org/10.1186/s40035-022-00333-x

Kooiman, K., Van Rooij, T., Qin, B., Mastik, F., Vos, H.J., Versluis, M., Klibanov, A.L., De Jong, N., Villanueva, F.S., Chen, X., 2017. Focal areas of increased lipid concentration on the coating of microbubbles during short tone-burst ultrasound insonification. PLoS ONE 12, e0180747. https://doi.org/10.1371/journal.pone.0180747

Kovacs, Z.I., Kim, S., Jikaria, N., Qureshi, F., Milo, B., Lewis, B.K., Bresler, M., Burks, S.R., Frank, J.A., 2017. Disrupting the blood-brain barrier by focused ultrasound induces sterile inflammation. Proc Natl Acad Sci U S A 114, E75–E84. https://doi.org/10.1073/pnas.1614777114

Kovacs, Z.I., Tu, T.-W., Sundby, M., Qureshi, F., Lewis, B.K., Jikaria, N., Burks, S.R., Frank, J.A., 2018. MRI and histological evaluation of pulsed focused ultrasound and microbubbles treatment effects in the brain. Theranostics 8, 4837–4855. https://doi.org/10.7150/thno.24512

Krishna, P.D., Shankar, P.M., Newhouse, V.L., 1999. Subharmonic generation from ultrasonic contrast agents. Phys Med Biol 44, 681–694. https://doi.org/10.1088/0031-9155/44/3/004

Labriji, W., Clauzel, J., Mestas, J., Lafond, M., Lafon, C., Salabert, A., Hirschler, L., Warnking, J.M., Barbier, E.L., Loubinoux, I., Desmoulin, F., 2023. Evidence of cerebral hypoperfusion consecutive to ultrasound-mediated blood-brain barrier opening in rats. Magn Reson Med mrm.29596. https://doi.org/10.1002/mrm.29596

Lacas, B., *et al*., 2021. Meta-analysis of chemotherapy in head and neck cancer (MACH-NC): An update on 107 randomized trials and 19,805 patients, on behalf of MACH-NC Group. Radiother Oncol 156, 281–293. https://doi.org/10.1016/j.radonc.2021.01.013

Larrat, B., Pernot, M., Aubry, J.-F., Dervishi, E., Sinkus, R., Seilhean, D., Marie, Y., Boch, A.-L., Fink, M., Tanter, M., 2010. MR-guided transcranial brain HIFU in small animal models. Phys Med Biol 55, 365–388. https://doi.org/10.1088/0031-9155/55/2/003

Leao, A.A.P., 1944. SPREADING DEPRESSION OF ACTIVITY IN THE CEREBRAL CORTEX. Journal of Neurophysiology 7, 359–390. https://doi.org/10.1152/jn.1944.7.6.359

Lee, H., Guo, Y., Ross, J.L., Schoen, S., Degertekin, F.L., Arvanitis, C., 2022. Spatially targeted brain cancer immunotherapy with closed-loop controlled focused ultrasound and immune checkpoint blockade. Sci Adv 8, eadd2288. https://doi.org/10.1126/sciadv.add2288

Lehmann, J.F., Herrick, J.F., 1953. Biologic reactions to cavitation, a consideration for ultrasonic therapy. Arch Phys Med Rehabil 34, 86–98.

Leighton, T., 1994. The Acoustic Bubble. Elsevier Science, Saint Louis.

Leinenga, G., Götz, J., 2018. Safety and Efficacy of Scanning Ultrasound Treatment of Aged APP23 Mice. Front Neurosci 12, 55. https://doi.org/10.3389/fnins.2018.00055

Leinenga, G., Götz, J., 2015. Scanning ultrasound removes amyloid-β and restores memory in an Alzheimer's disease mouse model. Sci Transl Med 7, 278ra33. https://doi.org/10.1126/scitranslmed.aaa2512

Lemasson, B., Christen, T., Tizon, X., Farion, R., Fondraz, N., Provent, P., Segebarth, C., Barbier, E.L., Genne, P., Duchamp, O., Remy, C., 2011. Assessment of multiparametric MRI in a human glioma model to monitor cytotoxic and anti-angiogenic drug effects. NMR Biomed 24, 473–482. https://doi.org/10.1002/nbm.1611

Lemasson, B., Pannetier, N., Coquery, N., Boisserand, L.S.B., Collomb, N., Schuff, N., Moseley, M., Zaharchuk, G., Barbier, E.L., Christen, T., 2016. MR Vascular Fingerprinting in Stroke and Brain Tumors Models. Sci Rep 6, 37071. https://doi.org/10.1038/srep37071

Lemasson, B., Serduc, R., Maisin, C., Bouchet, A., Coquery, N., Robert, P., Le Duc, G., Troprès, I., Rémy, C., Barbier, E.L., 2010. Monitoring Blood-Brain Barrier Status in a Rat Model of Glioma Receiving Therapy: Dual Injection of Low-Molecular-Weight and Macromolecular MR Contrast Media. Radiology 257, 342–352. https://doi.org/10.1148/radiol.10092343

Lemasson, B., Valable, S., Farion, R., Krainik, A., Rémy, C., Barbier, E.L., 2013. In vivo imaging of vessel diameter, size, and density: A comparative study between MRI and histology: Vessel Diameter, Size, and Density: MRI vs. Histology. Magn Reson Med 69, 18–26. https://doi.org/10.1002/mrm.24218

Li, H.R., Harb, M., Heath, J.E., Trippett, J.S., Shapiro, M.G., Szablowski, J.O., 2024. Engineering viral vectors for acoustically targeted gene delivery. Nat Commun 15, 4924. https://doi.org/10.1038/s41467-024-48974-y

Liddelow, S.A., Guttenplan, K.A., Clarke, L.E., Bennett, F.C., Bohlen, C.J., Schirmer, L., Bennett, M.L., Münch, A.E., Chung, W.-S., Peterson, T.C., Wilton, D.K., Frouin, A., Napier, B.A., Panicker, N., Kumar, M., Buckwalter, M.S., Rowitch, D.H., Dawson, V.L., Dawson, T.M., Stevens, B., Barres, B.A., 2017. Neurotoxic reactive astrocytes are induced by activated microglia. Nature 541, 481–487. https://doi.org/10.1038/nature21029

Lidington, D., Kroetsch, J.T., Bolz, S.-S., 2018. Cerebral artery myogenic reactivity: The next frontier in developing effective interventions for subarachnoid hemorrhage. J Cereb Blood Flow Metab 38, 17–37. https://doi.org/10.1177/0271678X17742548

Lim Kee Chang, W., Chan, T.G., Raguseo, F., Mishra, A., Chattenton, D., De Rosales, R.T.M., Long, N.J., Morse, S.V., 2023. Rapid short-pulses of focused ultrasound and microbubbles deliver a range of agent sizes to the brain. Sci Rep 13, 6963. https://doi.org/10.1038/s41598-023-33671-5

Lin, C.-Y., Tsai, C.-H., Feng, L.-Y., Chai, W.-Y., Lin, C.-J., Huang, C.-Y., Wei, K.-C., Yeh, C.-K., Chen, C.-M., Liu, H.-L., 2019. Focused ultrasound-induced blood brain-barrier opening enhanced vascular permeability for GDNF delivery in Huntington's disease mouse model. Brain Stimulation 12, 1143–1150. https://doi.org/10.1016/j.brs.2019.04.011

Lin, Y., Lin, L., Cheng, M., Jin, L., Du, L., Han, T., Xu, L., Yu, A.C.H., Qin, P., 2017. Effect of acoustic parameters on the cavitation behavior of SonoVue microbubbles induced by pulsed ultrasound. Ultrasonics Sonochemistry 35, 176–184. https://doi.org/10.1016/j.ultsonch.2016.09.016

Lipsman, N., Meng, Y., Bethune, A.J., Huang, Y., Lam, B., Masellis, M., Herrmann, N., Heyn, C., Aubert, I., Boutet, A., Smith, G.S., Hynynen, K., Black, S.E., 2018. Blood–brain barrier opening in Alzheimer's disease using MR-guided focused ultrasound. Nat Commun 9, 2336. https://doi.org/10.1038/s41467-018-04529-6

Liu, H., Hsu, P., Chu, P., Wai, Y., Chen, J., Shen, C., Yen, T., Wang, J., 2009. Magnetic resonance imaging enhanced by superparamagnetic iron oxide particles: Usefulness for distinguishing between focused ultrasound-induced blood–brain barrier disruption and brain hemorrhage. Magnetic Resonance Imaging 29, 31–38. https://doi.org/10.1002/jmri.21599

Liu, H.-L., Chen, P.-Y., Yang, H.-W., Wu, J.-S., Tseng, I.-C., Ma, Y.-J., Huang, Chih-Ying, Tsai, H.-C., Chen, S.-M., Lu, Y.-J., Huang, Chiung-Yin, Hua, M.-Y., Ma, Y.-H., Yen, T.-C., Wei, K.-C., 2011. In vivo MR quantification of superparamagnetic iron oxide nanoparticle leakage during low-frequency-ultrasound-induced blood-brain barrier opening in swine. J Magn Reson Imaging 34, 1313–1324. https://doi.org/10.1002/jmri.22697

Liu, H.-L., Fan, C.-H., Ting, C.-Y., Yeh, C.-K., 2014a. Combining Microbubbles and Ultrasound for Drug Delivery to Brain Tumors: Current Progress and Overview. Theranostics 4, 432–444. https://doi.org/10.7150/thno.8074

Liu, H.-L., Huang, C.-Y., Chen, J.-Y., Wang, H.-Y.J., Chen, P.-Y., Wei, K.-C., 2014b. Pharmacodynamic and Therapeutic Investigation of Focused Ultrasound-Induced Blood-Brain Barrier Opening for Enhanced Temozolomide Delivery in Glioma Treatment. PLoS ONE 9, e114311. https://doi.org/10.1371/journal.pone.0114311

Liu, T., Wisnieff, C., Lou, M., Chen, W., Spincemaille, P., Wang, Y., 2013. Nonlinear formulation of the magnetic field to source relationship for robust quantitative susceptibility mapping. Magnetic Resonance in Med 69, 467–476. https://doi.org/10.1002/mrm.24272

Loesch, D.Z., Huggins, R.M., Hagerman, R.J., 2004. Phenotypic variation and FMRP levels in fragile X. Ment Retard Dev Disabil Res Rev 10, 31–41. https://doi.org/10.1002/mrdd.20006

Lv, J., Hu, W., Yang, Z., Li, T., Jiang, S., Ma, Z., Chen, F., Yang, Y., 2018. Focusing on claudin-5: A promising candidate in the regulation of BBB to treat ischemic stroke. Prog Neurobiol 161, 79–96. https://doi.org/10.1016/j.pneurobio.2017.12.001

Ma, D., Gulani, V., Seiberlich, N., Liu, K., Sunshine, J.L., Duerk, J.L., Griswold, M.A., 2013. Magnetic resonance fingerprinting. Nature 495, 187–192. https://doi.org/10.1038/nature11971

Madanshetty, S.I., Roy, R.A., Apfel, R.E., 1991. Acoustic microcavitation: its active and passive acoustic detection. J Acoust Soc Am 90, 1515–1526. https://doi.org/10.1121/1.401891

Magnin, R., Rabusseau, F., Salabartan, F., Mériaux, S., Aubry, J.-F., Le Bihan, D., Dumont, E., Larrat, B., 2015. Magnetic resonance-guided motorized transcranial ultrasound system for blood-brain barrier permeabilization along arbitrary trajectories in rodents. J Ther Ultrasound 3, 22. https://doi.org/10.1186/s40349-015-0044-5

Maimbourg, G., Houdouin, A., Santin, M., Lehericy, S., Tanter, M., Aubry, J.-F., 2018. Inside/outside the brain binary cavitation localization based on the lowpass filter effect of the skull on the harmonic content: a proof of concept study. Phys Med Biol 63, 135012. https://doi.org/10.1088/1361-6560/aaca21

Marchetti, L., Engelhardt, B., 2020. Immune cell trafficking across the blood-brain barrier in the absence and presence of neuroinflammation. Vascular Biology 2, H1–H18. https://doi.org/10.1530/VB-19-0033

Marmottant, P., Van Der Meer, S., Emmer, M., Versluis, M., De Jong, N., Hilgenfeldt, S., Lohse, D., 2005. A model for large amplitude oscillations of coated bubbles accounting for buckling and rupture. The Journal of the Acoustical Society of America 118, 3499–3505. https://doi.org/10.1121/1.2109427

Marquet, F., Teichert, T., Ferrera, V., Konofagou, E.E., Tung, Y.-S., 2011. Feasibility of noninvasive cavitation-guided blood-brain barrier opening using focused ultrasound and microbubbles in nonhuman primates. Appl. Phys. Lett. 98, 163704. https://doi.org/10.1063/1.3580763

Marquet, F., Teichert, T., Wu, S.-Y., Tung, Y.-S., Downs, M., Wang, S., Chen, C., Ferrera, V., Konofagou, E.E., 2014. Real-time, transcranial monitoring of safe blood-brain barrier opening in non-human primates. PLoS One 9, e84310. https://doi.org/10.1371/journal.pone.0084310

Marsac, L., Chauvet, D., Larrat, B., Pernot, M., Robert, B., Fink, M., Boch, A.L., Aubry, J.F., Tanter, M., 2012. MR-guided adaptive focusing of therapeutic ultrasound beams in the human head. Med Phys 39, 1141–1149. https://doi.org/10.1118/1.3678988

Martinez, P.J., Song, J.J., Garay, F.G., Song, K.-H., Mufford, T., Steiner, J., DeSisto, J., Ellens, N., Serkova, N.J., Green, A.L., Borden, M., 2024. Comprehensive assessment of blood–brain barrier opening and sterile inflammatory response: unraveling the therapeutic window. Sci Rep 14, 17036. https://doi.org/10.1038/s41598-024-67916-8

Marty, B., Larrat, B., Van Landeghem, M., Robic, C., Robert, P., Port, M., Le Bihan, D., Pernot, M., Tanter, M., Lethimonnier, F., Mériaux, S., 2012. Dynamic Study of Blood–Brain Barrier Closure after its Disruption using Ultrasound: A Quantitative Analysis. J Cereb Blood Flow Metab 32, 1948–1958. https://doi.org/10.1038/jcbfm.2012.100

Masvidal-Codina, E., Illa, X., Dasilva, M., Calia, A.B., Dragojević, T., Vidal-Rosas, E.E., Prats-Alfonso, E., Martínez-Aguilar, J., De La Cruz, J.M., Garcia-Cortadella, R., Godignon, P., Rius, G., Camassa, A., Del Corro, E., Bousquet, J., Hébert, C., Durduran, T., Villa, R., Sanchez-Vives, M.V., Garrido, J.A., Guimerà-Brunet, A., 2019. High-resolution mapping of infraslow cortical brain activity enabled by graphene microtransistors. Nature Mater 18, 280–288. https://doi.org/10.1038/s41563-018-0249-4

Mayo, F., González-Vinceiro, L., Hiraldo-González, L., Calle-Castillejo, C., Morales-Alvarez, S., Ramírez-Lorca, R., Echevarría, M., 2023. Aquaporin-4 Expression Switches from White to Gray Matter Regions during Postnatal Development of the Central Nervous System. IJMS 24, 3048. https://doi.org/10.3390/ijms24033048

Mazumder, A.G., Julé, A.M., Cullen, P.F., Sun, D., 2022. Astrocyte heterogeneity within white matter tracts and a unique subpopulation of optic nerve head astrocytes. iScience 25, 105568. https://doi.org/10.1016/j.isci.2022.105568

McDannold, N., Arvanitis, C.D., Vykhodtseva, N., Livingstone, M.S., 2012. Temporary Disruption of the Blood–Brain Barrier by Use of Ultrasound and Microbubbles: Safety and Efficacy Evaluation in Rhesus Macaques. Cancer Res 72, 3652–3663. https://doi.org/10.1158/0008-5472.CAN-12-0128

McDannold, N., Maier, S.E., 2008. Magnetic resonance acoustic radiation force imaging. Medical physics 35, 3748–3758.

McDannold, N., Vykhodtseva, N., Hynynen, K., 2008. Effects of Acoustic Parameters and Ultrasound Contrast Agent Dose on Focused-Ultrasound Induced Blood-Brain Barrier Disruption. Ultrasound Med Biol 34, 930–937. https://doi.org/10.1016/j.ultrasmedbio.2007.11.009

McDannold, N., Vykhodtseva, N., Hynynen, K., 2007. Use of ultrasound pulses combined with Definity for targeted blood-brain barrier disruption: a feasibility study. Ultrasound Med Biol 33, 584–590. https://doi.org/10.1016/j.ultrasmedbio.2006.10.004

McDannold, N., Vykhodtseva, N., Hynynen, K., 2006. Targeted disruption of the blood–brain barrier with focused ultrasound: association with cavitation activity. Phys Med Biol 51, 793–807. https://doi.org/10.1088/0031-9155/51/4/003

McDannold, N., Vykhodtseva, N., Raymond, S., Jolesz, F.A., Hynynen, K., 2005. MRI-guided targeted blood-brain barrier disruption with focused ultrasound: Histological findings in rabbits. Ultrasound Med Biol 31, 1527–1537. https://doi.org/10.1016/j.ultrasmedbio.2005.07.010

McDannold, N., Wen, P.Y., Reardon, D.A., Fletcher, S.-M., Golby, A.J., 2024. Cavitation monitoring, treatment strategy, and acoustic simulations of focused ultrasound blood-brain barrier disruption in patients with glioblastoma. Journal of Controlled Release 372, 194–208. https://doi.org/10.1016/j.jconrel.2024.06.036

McDannold, N., Zhang, Y., Supko, J.G., Power, C., Sun, T., Peng, C., Vykhodtseva, N., Golby, A.J., Reardon, D.A., 2019. Acoustic feedback enables safe and reliable carboplatin delivery across the blood-brain barrier with a clinical focused ultrasound system and improves survival in a rat glioma model. Theranostics 9, 6284–6299. https://doi.org/10.7150/thno.35892

McDannold, N., Zhang, Y., Supko, J.G., Power, C., Sun, T., Vykhodtseva, N., Golby, A.J., Reardon, D.A., 2020. Blood-brain barrier disruption and delivery of irinotecan in a rat model using a clinical transcranial MRI-guided focused ultrasound system. Sci Rep 10, 8766. https://doi.org/10.1038/s41598-020-65617-6

McDannold, N., Zhang, Y., Vykhodtseva, N., 2017. The Effects of Oxygen on Ultrasound-Induced Blood–Brain Barrier Disruption in Mice. Ultrasound Med Biol 43, 469–475. https://doi.org/10.1016/j.ultrasmedbio.2016.09.019

McDannold, N., Zhang, Y., Vykhodtseva, N., 2011. Blood-Brain Barrier Disruption and Vascular Damage Induced by Ultrasound Bursts Combined with Microbubbles can be Influenced by Choice of Anesthesia Protocol. Ultrasound Med Biol 37, 1259–1270. https://doi.org/10.1016/j.ultrasmedbio.2011.04.019

McMahon, D., Bendayan, R., Hynynen, K., 2017. Acute effects of focused ultrasound-induced increases in blood-brain barrier permeability on rat microvascular transcriptome. Sci Rep 7, 45657. https://doi.org/10.1038/srep45657

McMahon, D., Hynynen, K., 2017. Acute Inflammatory Response Following Increased Blood-Brain Barrier Permeability Induced by Focused Ultrasound is Dependent on Microbubble Dose. Theranostics 7, 3989–4000. https://doi.org/10.7150/thno.21630

McMahon, D., Lassus, A., Gaud, E., Jeannot, V., Hynynen, K., 2020a. Microbubble formulation influences inflammatory response to focused ultrasound exposure in the brain. Sci Rep 10, 21534. https://doi.org/10.1038/s41598-020-78657-9

McMahon, D., Mah, E., Hynynen, K., 2018. Angiogenic response of rat hippocampal vasculature to focused ultrasound-mediated increases in blood-brain barrier permeability. Sci Rep 8, 12178. https://doi.org/10.1038/s41598-018-30825-8

McMahon, D., Oakden, W., Hynynen, K., 2020b. Investigating the effects of dexamethasone on blood-brain barrier permeability and inflammatory response following focused ultrasound and microbubble exposure. Theranostics 10, 1604–1618. https://doi.org/10.7150/thno.40908

Mehta, Rashi I., Carpenter, J.S., Mehta, Rupal I., Haut, M.W., Ranjan, M., Najib, U., Lockman, P., Wang, P., D'haese, P.-F., Rezai, A.R., 2021. Blood-Brain Barrier Opening with MRI-guided Focused Ultrasound Elicits Meningeal Venous Permeability in Humans with Early Alzheimer Disease. Radiology 298, 654–662. https://doi.org/10.1148/radiol.2021200643

Mehta, Rashi I., Carpenter, J.S., Mehta, Rupal I., Haut, M.W., Wang, P., Ranjan, M., Najib, U., D'Haese, P.-F., Rezai, A.R., 2023. Ultrasound-mediated blood–brain barrier opening uncovers an intracerebral perivenous fluid network in persons with Alzheimer's disease. Fluids Barriers CNS 20, 46. https://doi.org/10.1186/s12987-023-00447-y

Meng, Y., Pople, C.B., Suppiah, S., Llinas, M., Huang, Y., Sahgal, A., Perry, J., Keith, J., Davidson, B., Hamani, C., Amemiya, Y., Seth, A., Leong, H., Heyn, C.C., Aubert, I., Hynynen, K., Lipsman, N., 2021a. MR-guided focused ultrasound liquid biopsy enriches circulating biomarkers in patients with brain tumors. Neuro-Oncology 23, 1789–1797. https://doi.org/10.1093/neuonc/noab057

Meng, Y., Reilly, R.M., Pezo, R.C., Trudeau, M., Sahgal, A., Singnurkar, A., Perry, J., Myrehaug, S., Pople, C.B., Davidson, B., Llinas, M., Hyen, C., Huang, Y., Hamani, C., Suppiah, S., Hynynen, K., Lipsman, N., 2021b. MR-guided focused ultrasound enhances delivery of trastuzumab to Her2-positive brain metastases. Sci Transl Med 13, eabj4011. https://doi.org/10.1126/scitranslmed.abj4011

Meng, Y., Volpini, M., Black, S., Lozano, A.M., Hynynen, K., Lipsman, N., 2017. Focused ultrasound as a novel strategy for Alzheimer disease therapeutics. Annals of Neurology 81, 611–617. https://doi.org/10.1002/ana.24933

Miao, T., Ju, X., Zhu, Q., Wang, Y., Guo, Q., Sun, T., Lu, C., Han, L., 2019. Nanoparticles Surmounting Blood–Brain Tumor Barrier Through Both Transcellular and Paracellular Pathways to Target Brain Metastases. Adv Funct Materials 29, 1900259. https://doi.org/10.1002/adfm.201900259

Mientjes, E.J., Nieuwenhuizen, I., Kirkpatrick, L., Zu, T., Hoogeveen-Westerveld, M., Severijnen, L., Rifé, M., Willemsen, R., Nelson, D.L., Oostra, B.A., 2006. The generation of a conditional Fmr1 knock out mouse model to study Fmrp function in vivo. Neurobiol Dis 21, 549–555. https://doi.org/10.1016/j.nbd.2005.08.019

Miller, D.L., Thomas, R.M., 1995. Ultrasound contrast agents nucleate inertial cavitation in vitro. Ultrasound Med Biol 21, 1059–1065. https://doi.org/10.1016/0301-5629(95)93252-U

Miller, F., Fenart, L., Landry, V., Coisne, C., Cecchelli, R., Dehouck, M.-P., Buée-Scherrer, V., 2005. The MAP kinase pathway mediates transcytosis induced by TNF-alpha in an in vitro blood-brain barrier model. Eur J Neurosci 22, 835–844. https://doi.org/10.1111/j.1460-9568.2005.04273.x

Mishra, A., Reynolds, J.P., Chen, Y., Gourine, A.V., Rusakov, D.A., Attwell, D., 2016. Astrocytes mediate neurovascular signaling to capillary pericytes but not to arterioles. Nat Neurosci 19, 1619–1627. https://doi.org/10.1038/nn.4428

Mitchell, M.J., Billingsley, M.M., Haley, R.M., Wechsler, M.E., Peppas, N.A., Langer, R., 2021. Engineering precision nanoparticles for drug delivery. Nat Rev Drug Discov 20, 101–124. https://doi.org/10.1038/s41573-020-0090-8

Møllgård, K., Dziegielewska, K.M., Holst, C.B., Habgood, M.D., Saunders, N.R., 2017. Brain barriers and functional interfaces with sequential appearance of ABC efflux transporters during human development. Sci Rep 7, 11603. https://doi.org/10.1038/s41598-017-11596-0

Mondou, P., Mériaux, S., Nageotte, F., Vappou, J., Novell, A., Larrat, B., 2023. State of the art on microbubble cavitation monitoring and feedback control for blood-brain-barrier opening using focused ultrasound. Phys. Med. Biol. 68, 18TR03. https://doi.org/10.1088/1361-6560/ace23e

Montero, A.-S., Bielle, F., Goldwirt, L., Lalot, A., Bouchoux, G., Canney, M., Belin, F., Beccaria, K., Pradat, P.-F., Salachas, F., Boillée, S., Lobsiger, C., Lafon, C., Chapelon, J.-Y., Carpentier, A., 2019. Ultrasound-Induced Blood–Spinal Cord Barrier Opening in Rabbits. Ultrasound Med Biol 45, 2417–2426. https://doi.org/10.1016/j.ultrasmedbio.2019.05.022

Mullin, L., Gessner, R., Kwan, J., Kaya, M., Borden, M.A., Dayton, P.A., 2011. Effect of anesthesia carrier gas on in vivo circulation times of ultrasound microbubble contrast agents in rats. Contrast Media Mol Imaging 6, 126–131. https://doi.org/10.1002/cmmi.414

Nance, E., Pun, S.H., Saigal, R., Sellers, D.L., 2022. Drug delivery to the central nervous system. Nat Rev Mater 7, 314–331. https://doi.org/10.1038/s41578-021-00394-w

Neuwelt, E.A., Bauer, B., Fahlke, C., Fricker, G., Iadecola, C., Janigro, D., Leybaert, L., Molnár, Z., O'Donnell, M.E., Povlishock, J.T., Saunders, N.R., Sharp, F., Stanimirovic, D., Watts, R.J., Drewes, L.R., 2011. Engaging neuroscience to advance translational research in brain barrier biology. Nat Rev Neurosci 12, 169–182. https://doi.org/10.1038/nrn2995

Neuwelt, E.A., Frenkel, E.P., Diehl, J., Vu, L.H., Rapoport, S., Hill, S., 1980. Reversible osmotic blood-brain barrier disruption in humans: implications for the chemotherapy of malignant brain tumors. Neurosurgery 7, 44–52. https://doi.org/10.1227/00006123-198007000-00007

Noble, W., Hanger, D.P., Miller, C.C.J., Lovestone, S., 2013. The importance of tau phosphorylation for neurodegenerative diseases. Front Neurol 4, 83. https://doi.org/10.3389/fneur.2013.00083

Noltingk, B.E., Neppiras, E.A., 1950. Cavitation produced by Ultrasonics. Proc. Phys. Soc. B 63, 674–685. https://doi.org/10.1088/0370-1301/63/9/305

Nonnenmacher, M., Wang, W., Child, M.A., Ren, X.-Q., Huang, C., Ren, A.Z., Tocci, J., Chen, Q., Bittner, K., Tyson, K., Pande, N., Chung, C.H.-Y., Paul, S.M., Hou, J., 2021. Rapid evolution of blood-brain-barrier-penetrating AAV capsids by RNA-driven biopanning. Mol Ther Methods Clin Dev 20, 366–378. https://doi.org/10.1016/j.omtm.2020.12.006

Novell, A., Kamimura, H.A.S., Cafarelli, A., Gerstenmayer, M., Flament, J., Valette, J., Agou, P., Conti, A., Selingue, E., Aron Badin, R., Hantraye, P., Larrat, B., 2020. A new safety index based on intrapulse monitoring of ultra-harmonic cavitation during ultrasound-induced blood-brain barrier opening procedures. Sci Rep 10, 10088. https://doi.org/10.1038/s41598-020-66994-8

Olumolade, O.O., Wang, S., Samiotaki, G., Konofagou, E.E., 2016. Longitudinal Motor and Behavioral Assessment of Blood–Brain Barrier Opening with Transcranial Focused Ultrasound. Ultrasound Med Biol 42, 2270–2282. https://doi.org/10.1016/j.ultrasmedbio.2016.05.004

O'Reilly, Meaghan A., Hough, O., Hynynen, K., 2017. Blood-Brain Barrier Closure Time After Controlled Ultrasound-Induced Opening Is Independent of Opening Volume: Blood-Brain Barrier Closure Time After Ultrasound-Induced Opening. J Ultrasound Med 36, 475–483. https://doi.org/10.7863/ultra.16.02005

O'Reilly, M.A., Huang, Y., Hynynen, K., 2010. The impact of standing wave effects on transcranial focused ultrasound disruption of the blood–brain barrier in a rat model. Phys Med Biol 55, 5251–5267. https://doi.org/10.1088/0031-9155/55/18/001

O'Reilly, M.A., Hynynen, K., 2012. Blood-brain barrier: real-time feedback-controlled focused ultrasound disruption by using an acoustic emissions-based controller. Radiology 263, 96–106. https://doi.org/10.1148/radiol.11111417

O'Reilly, M.A., Hynynen, K., 2010. A PVDF receiver for ultrasound monitoring of transcranial focused ultrasound therapy. IEEE Trans Biomed Eng 57, 2286–2294. https://doi.org/10.1109/TBME.2010.2050483

O'Reilly, Meaghan Anne, Jones, R.M., Barrett, E., Schwab, A., Head, E., Hynynen, K., 2017. Investigation of the Safety of Focused Ultrasound-Induced Blood-Brain Barrier Opening in a Natural Canine Model of Aging. Theranostics 7, 3573–3584. https://doi.org/10.7150/thno.20621

O'Reilly, M.A., Waspe, A.C., Ganguly, M., Hynynen, K., 2011. Focused-Ultrasound Disruption of the Blood-Brain Barrier Using Closely-Timed Short Pulses: Influence of Sonication Parameters and Injection Rate. Ultrasound Med Biol 37, 587–594. https://doi.org/10.1016/j.ultrasmedbio.2011.01.008

Ostrom, Q.T., Gittleman, H., Fulop, J., Liu, M., Blanda, R., Kromer, C., Wolinsky, Y., Kruchko, C., Barnholtz-Sloan, J.S., 2015. CBTRUS Statistical Report: Primary Brain and Central Nervous System Tumors Diagnosed in the United States in 2008-2012. Neuro Oncol 17, iv1–iv62. https://doi.org/10.1093/neuonc/nov189

Owusu-Yaw, B.S., Zhang, Y., Garrett, L., Yao, A., Shing, K., Batista, A.R., Sena-Esteves, M., Upadhyay, J., Kegel-Gleason, K., Todd, N., 2024. Focused Ultrasound-Mediated Disruption of the Blood–Brain Barrier for AAV9 Delivery in a Mouse Model of Huntington's Disease. Pharmaceutics 16, 710. https://doi.org/10.3390/pharmaceutics16060710

Pandit, R., Koh, W.K., Sullivan, R.K.P., Palliyaguru, T., Parton, R.G., Götz, J., 2020. Role for caveolin-mediated transcytosis in facilitating transport of large cargoes into the brain via ultrasound. J Control Release 327, 667–675. https://doi.org/10.1016/j.jconrel.2020.09.015

Pandit, R., Leinenga, G., Götz, J., 2019. Repeated ultrasound treatment of tau transgenic mice clears neuronal tau by autophagy and improves behavioral functions. Theranostics 9, 3754–3767. https://doi.org/10.7150/thno.34388

Pannetier, N.A., Debacker, C.S., Mauconduit, F., Christen, T., Barbier, E.L., 2013. A Simulation Tool for Dynamic Contrast Enhanced MRI. PLoS ONE 8, e57636. https://doi.org/10.1371/journal.pone.0057636

Pardridge, W.M., 2019. Alzheimer's disease: future drug development and the blood-brain barrier. Expert Opinion on Investigational Drugs 28, 569–572. https://doi.org/10.1080/13543784.2019.1627325

Pardridge, W.M., 2005. The blood-brain barrier: bottleneck in brain drug development. NeuroRx 2, 3–14.

Park, C.-Y., Halevy, T., Lee, D.R., Sung, J.J., Lee, J.S., Yanuka, O., Benvenisty, N., Kim, D.-W., 2015. Reversion of FMR1 Methylation and Silencing by Editing the Triplet Repeats in Fragile X iPSC-Derived Neurons. Cell Reports 13, 234–241. https://doi.org/10.1016/j.celrep.2015.08.084

Park, H.S., Han, J.K., Lee, J.M., Kim, Y.I., Woo, S., Yoon, J.H., Choi, J.-Y., Choi, B.I., 2015. Dynamic Contrast-Enhanced MRI Using a Macromolecular MR Contrast Agent (P792): Evaluation of Antivascular Drug Effect in a Rabbit VX2 Liver Tumor Model. Korean J Radiol 16, 1029–1037. https://doi.org/10.3348/kjr.2015.16.5.1029

Park, S.H., Kim, M.J., Jung, H.H., Chang, W.S., Choi, H.S., Rachmilevitch, I., Zadicario, E., Chang, J.W., 2021. Safety and feasibility of multiple blood-brain barrier disruptions for the treatment of glioblastoma in patients undergoing standard adjuvant chemotherapy. Journal of Neurosurgery 134, 475–483. https://doi.org/10.3171/2019.10.JNS192206

Pascal, A., Li, N., Lechtenberg, K.J., Rosenberg, J., Airan, R.D., James, M.L., Bouley, D.M., Pauly, K.B., 2020. Histologic evaluation of activation of acute inflammatory response in a mouse model following ultrasound-mediated blood-brain barrier using different acoustic pressures and microbubble doses. Nanotheranostics 4, 210–223. https://doi.org/10.7150/ntno.49898

Patel, A., Schoen, S.J., Arvanitis, C.D., 2019. Closed-Loop Spatial and Temporal Control of Cavitation Activity With Passive Acoustic Mapping. IEEE Trans. Biomed. Eng. 66, 2022–2031. https://doi.org/10.1109/TBME.2018.2882337

Peeters, T.H., Kobus, T., Breukels, V., Lenting, K., Veltien, A., Heerschap, A., Scheenen, T.W.J., 2019. Imaging Hyperpolarized Pyruvate and Lactate after Blood–Brain Barrier Disruption with Focused Ultrasound. ACS Chem. Neurosci. 10, 2591–2601. https://doi.org/10.1021/acschemneuro.9b00085

Pei, M., Nguyen, T.D., Thimmappa, N.D., Salustri, C., Dong, F., Cooper, M.A., Li, J., Prince, M.R., Wang, Y., 2015. Algorithm for fast monoexponential fitting based on Auto-Regression on Linear Operations (ARLO) of data. Magnetic Resonance in Med 73, 843–850. https://doi.org/10.1002/mrm.25137

Pernet-Gallay, K., Jouneau, P.-H., Bertrand, A., Delaroche, J., Farion, R., Rémy, C., Barbier, E.L., 2017. Vascular permeability in the RG2 glioma model can be mediated by macropinocytosis and be independent of the opening of the tight junction. J Cereb Blood Flow Metab 37, 1264–1275. https://doi.org/10.1177/0271678X16654157

Plesset, M.S., 1949. The Dynamics of Cavitation Bubbles. Journal of Applied Mechanics 16, 277–282. https://doi.org/10.1115/1.4009975

Poewe, W., Seppi, K., Tanner, C.M., Halliday, G.M., Brundin, P., Volkmann, J., Schrag, A.-E., Lang, A.E., 2017. Parkinson disease. Nat Rev Dis Primers 3, 17013. https://doi.org/10.1038/nrdp.2017.13

Poon, C., Pellow, C., Hynynen, K., 2021. Neutrophil recruitment and leukocyte response following focused ultrasound and microbubble mediated blood-brain barrier treatments. Theranostics 11, 1655–1671. https://doi.org/10.7150/thno.52710

Porcu, E.P., Salis, A., Gavini, E., Rassu, G., Maestri, M., Giunchedi, P., 2016. Indocyanine green delivery systems for tumour detection and treatments. Biotechnology Advances 34, 768–789. https://doi.org/10.1016/j.biotechadv.2016.04.001

Poritsky, H., 1951. The collapse or growth of a spherical bubble or cavity in a viscous fluid, in: Journal of Applied Mechanics-Transactions of the ASME. ASME-AMER SOC MECHANICAL ENG 345 E 47TH ST, NEW YORK, NY 10017, pp. 332–333.

Porret, E., Kereselidze, D., Dauba, A., Schweitzer-Chaput, A., Jegot, B., Selingue, E., Tournier, N., Larrat, B., Novell, A., Truillet, C., 2023. Refining the delivery and therapeutic efficacy of cetuximab using focused ultrasound in a mouse model of glioblastoma: An 89Zr-cetuximab immunoPET study. Eur J Pharm Biopharm 182, 141–151. https://doi.org/10.1016/j.ejpb.2022.12.006

Postema, M., Marmottant, P., Lancée, C.T., Hilgenfeldt, S., Jong, N.D., 2004a. Ultrasound-induced microbubble coalescence. Ultrasound in Medicine & Biology 30, 1337–1344. https://doi.org/10.1016/j.ultrasmedbio.2004.08.008

Postema, M., van Wamel, A., Lancée, C.T., de Jong, N., 2004b. Ultrasound-induced encapsulated microbubble phenomena. Ultrasound Med Biol 30, 827–840. https://doi.org/10.1016/j.ultrasmedbio.2004.02.010

Pouliopoulos, A.N., Wu, S.-Y., Burgess, M.T., Karakatsani, M.E., Kamimura, H.A.S., Konofagou, E.E., 2020. A Clinical System for Non-invasive Blood-Brain Barrier Opening Using a Neuronavigation-Guided Single-Element Focused Ultrasound Transducer. Ultrasound Med Biol 46, 73–89. https://doi.org/10.1016/j.ultrasmedbio.2019.09.010

Presset, A., Bodard, S., Lefèvre, A., Millet, A., Oujagir, E., Dupuy, C., Iazourène, T., Bouakaz, A., Emond, P., Escoffre, J.-M., Nadal-Desbarats, L., 2022. First Metabolomic Signature of Blood-Brain Barrier Opening Induced by Microbubble-Assisted Ultrasound. Front Mol Neurosci 15, 888318. https://doi.org/10.3389/fnmol.2022.888318

QSM Consensus Organization Committee, Bilgic, B., Costagli, M., Chan, K., Duyn, J., Langkammer, C., Lee, J., Li, X., Liu, C., Marques, J.P., Milovic, C., Robinson, S.D., Schweser, F., Shmueli, K., Spincemaille, P., Straub, S., Van Zijl, P., Wang, Y., ISMRM Electro-Magnetic Tissue Properties Study Group, 2024. Recommended implementation of quantitative susceptibility mapping for clinical research in the brain: A consensus of the ISMRM electro-magnetic tissue properties study group. Magnetic Resonance in Med 91, 1834–1862. https://doi.org/10.1002/mrm.30006

Quail, D.F., Joyce, J.A., 2017. The Microenvironmental Landscape of Brain Tumors. Cancer Cell 31, 326–341. https://doi.org/10.1016/j.ccell.2017.02.009

Querfurth, H.W., LaFerla, F.M., 2010. Alzheimer's Disease. N Engl J Med 362, 329–344. https://doi.org/10.1056/NEJMra0909142

Ranjan, M., Mahoney, J.J., Rezai, A.R., 2024. Neurosurgical neuromodulation therapy for psychiatric disorders. Neurotherapeutics 21, e00366. https://doi.org/10.1016/j.neurot.2024.e00366

Rapoport, S.I., 2000. Osmotic opening of the blood-brain barrier: principles, mechanism, and therapeutic applications. Cell Mol Neurobiol 20, 217–230. https://doi.org/10.1023/a:1007049806660

Rapoport, S.I., Thompson, H.K., 1973. Osmotic opening of the blood-brain barrier in the monkey without associated neurological deficits. Science 180, 971. https://doi.org/10.1126/science.180.4089.971

Rayleigh, Lord, 1917. VIII. *On the pressure developed in a liquid during the collapse of a spherical cavity*. The London, Edinburgh, and Dublin Philosophical Magazine and Journal of Science 34, 94–98. https://doi.org/10.1080/14786440808635681

Raymond, S.B., Skoch, J., Hynynen, K., Bacskai, B.J., 2007. Multiphoton Imaging of Ultrasound/Optison Mediated Cerebrovascular Effects *in vivo*. J Cereb Blood Flow Metab 27, 393–403. https://doi.org/10.1038/sj.jcbfm.9600336

Raymond, S.B., Treat, L.H., Dewey, J.D., McDannold, N.J., Hynynen, K., Bacskai, B.J., 2008. Ultrasound Enhanced Delivery of Molecular Imaging and Therapeutic Agents in Alzheimer's Disease Mouse Models. PLoS ONE 3, e2175. https://doi.org/10.1371/journal.pone.0002175

Reese, T.S., Karnovsky, M.J., 1967. FINE STRUCTURAL LOCALIZATION OF A BLOOD-BRAIN BARRIER TO EXOGENOUS PEROXIDASE. Journal of Cell Biology 34, 207–217. https://doi.org/10.1083/jcb.34.1.207

Reynaud-Dulaurier, R., Benegiamo, G., Marrocco, E., Al-Tannir, R., Surace, E.M., Auwerx, J., Decressac, M., 2020. Gene replacement therapy provides benefit in an adult mouse model of Leigh syndrome. Brain 143, 1686–1696. https://doi.org/10.1093/brain/awaa105

Rezai, A.R., D'Haese, P.-F., Finomore, V., Carpenter, J., Ranjan, M., Wilhelmsen, K., Mehta, R.I., Wang, P., Najib, U., Vieira Ligo Teixeira, C., Arsiwala, T., Tarabishy, A., Tirumalai, P., Claassen, D.O., Hodder, S., Haut, M.W., 2024. Ultrasound Blood–Brain Barrier Opening and Aducanumab in Alzheimer's Disease. N Engl J Med 390, 55–62. https://doi.org/10.1056/NEJMoa2308719

Rezai, A.R., Ranjan, M., D'Haese, P.-F., Haut, M.W., Carpenter, J., Najib, U., Mehta, R.I., Chazen, J.L., Zibly, Z., Yates, J.R., Hodder, S.L., Kaplitt, M., 2020. Noninvasive hippocampal blood−brain barrier opening in Alzheimer's disease with focused ultrasound. Proc. Natl. Acad. Sci. U.S.A. 117, 9180–9182. https://doi.org/10.1073/pnas.2002571117

Rezai, A.R., Ranjan, M., Haut, M.W., Carpenter, J., D'Haese, P.-F., Mehta, R.I., Najib, U., Wang, P., Claassen, D.O., Chazen, J.L., Krishna, V., Deib, G., Zibly, Z., Hodder, S.L., Wilhelmsen, K.C., Finomore, V., Konrad, P.E., Kaplitt, M., __, 2022. Focused ultrasound–mediated blood-brain barrier opening in Alzheimer's disease: long-term safety, imaging, and cognitive outcomes. Journal of Neurosurgery 1–9. https://doi.org/10.3171/2022.9.JNS221565

Rigollet, S., Ador, T., Dumont, E., Pichon, C., Barbier, E.L., Delalande, A., Stupar, V., 2024a. Longitudinal study tracking physiological changes through multiparametric MRI during repeated MRgFUS-induced BBB opening, in: ISMRM 31st Annual Meeting & Exhibition. Presented at the ISMRM 31st Annual Meeting & Exhibition, Singapour.

Rigollet, S., Cresson, C., Barbier, E.L., Delalande, A., Decressac, M., Stupar, V., 2023. Optimisation de l'ouverture de la barrière hémato-encéphalique contrôlé par IRM sur cerveau entier, in: 6e Congrès Scientifique de La Société Française de Résonance Magnétique En Biologie et Médecine. Presented at the 6e Congrès scientifique de la Société Française de Résonance Magnétique en Biologie et Médecine, Paris, France.

Rigollet, S., Delphin, A., Ador, T., Dumont, E., Pichon, C., Barbier, E.L., Delalande, A., Stupar, V., 2024b. Longitudinal MR vascular fingerprinting approach tracking physiological changes during repeated MR guided focused ultrasound mediated BBB opening on rats, in: 19th European Molecular Imaging Meeting (EMIM 2024). Presented at the 19th European Molecular Imaging Meeting (EMIM 2024), Porto, Portugal.

Rigollet, S., Rome, C., Ador, T., Dumont, E., Pichon, C., Delalande, A., Barbier, E.L., Stupar, V., 2024c. FUS-mediated BBB opening leads to transient perfusion decrease and inflammation without acute or chronic brain lesion. Theranostics.

Rome, C., Couillaud, F., Moonen, C.T.W., 2005. Spatial and temporal control of expression of therapeutic genes using heat shock protein promoters. Methods 35, 188–198. https://doi.org/10.1016/j.ymeth.2004.08.011

Rosenberg, G.A., 2012. Neurological diseases in relation to the blood-brain barrier. J Cereb Blood Flow Metab 32, 1139–1151. https://doi.org/10.1038/jcbfm.2011.197

Rousseau, J., Barth, R.F., Moeschberger, M.L., Elleaume, H., 2009. Efficacy of Intracerebral Delivery of Carboplatin in Combination With Photon Irradiation for Treatment of F98 Glioma-Bearing Rats. International Journal of Radiation Oncology*Biology*Physics 73, 530–536. https://doi.org/10.1016/j.ijrobp.2008.09.018

Rousseau, J., Boudou, C., Barth, R.F., Balosso, J., Estève, F., Elleaume, H., 2007. Enhanced Survival and Cure of F98 Glioma–Bearing Rats following Intracerebral Delivery of Carboplatin in Combination with Photon Irradiation. Clin Cancer Res 13, 5195–5201. https://doi.org/10.1158/1078-0432.CCR-07-1002

Roy, R.A., Madanshetty, S.I., Apfel, R.E., 1990. An acoustic backscattering technique for the detection of transient cavitation produced by microsecond pulses of ultrasound. The Journal of the Acoustical Society of America 87, 2451–2458. https://doi.org/10.1121/1.399091

Ruan, S., Qin, L., Xiao, W., Hu, C., Zhou, Y., Wang, R., Sun, X., Yu, W., He, Q., Gao, H., 2018. Acid-Responsive Transferrin Dissociation and GLUT Mediated Exocytosis for Increased Blood–Brain Barrier Transcytosis and Programmed Glioma Targeting Delivery. Adv Funct Materials 28, 1802227. https://doi.org/10.1002/adfm.201802227

Sabbagh, A., Beccaria, K., Ling, X., Marisetty, A., Ott, M., Caruso, H., Barton, E., Kong, L.-Y., Fang, D., Latha, K., Zhang, D.Y., Wei, J., DeGroot, J., Curran, M.A., Rao, G., Hu, J., Desseaux, C., Bouchoux, G., Canney, M., Carpentier, A., Heimberger, A.B., 2021. Opening of the Blood-Brain Barrier Using Low-Intensity Pulsed Ultrasound Enhances Responses to Immunotherapy in Preclinical Glioma Models. Clin Cancer Res 27, 4325–4337. https://doi.org/10.1158/1078-0432.CCR-20-3760

Sabraoui, A., Inserra, C., Gilles, B., Béra, J.-C., Mestas, J.-L., 2011. Feedback loop process to control acoustic cavitation. Ultrasonics Sonochemistry 18, 589–594. https://doi.org/10.1016/j.ultsonch.2010.07.011

Sahu, U., Barth, R.F., Otani, Y., McCormack, R., Kaur, B., 2022. Rat and Mouse Brain Tumor Models for Experimental Neuro-Oncology Research. Journal of Neuropathology & Experimental Neurology 81, 312–329. https://doi.org/10.1093/jnen/nlac021

Saitou, M., Fujimoto, K., Doi, Y., Itoh, M., Fujimoto, T., Furuse, M., Takano, H., Noda, T., Tsukita, S., 1998. Occludin-deficient embryonic stem cells can differentiate into polarized epithelial cells bearing tight junctions. J Cell Biol 141, 397–408. https://doi.org/10.1083/jcb.141.2.397

Saitou, M., Furuse, M., Sasaki, H., Schulzke, J.-D., Fromm, M., Takano, H., Noda, T., Tsukita, S., 2000. Complex Phenotype of Mice Lacking Occludin, a Component of Tight Junction Strands. MBoC 11, 4131–4142. https://doi.org/10.1091/mbc.11.12.4131

Samiotaki, G., Konofagou, E.E., 2013. Dependence of the reversibility of focused- ultrasound-induced blood-brain barrier opening on pressure and pulse length in vivo. IEEE Trans Ultrason Ferroelectr Freq Control 60, 2257–2265. https://doi.org/10.1109/TUFFC.2013.6644731

Samuel, S., Fowlkes, J., Miller, D., 2009. An in vitro study of the correlation between bubble distribution, acoustic emission, and cell damage by contrast ultrasound. IEEE Trans. Ultrason., Ferroelect., Freq. Contr. 56, 589–599. https://doi.org/10.1109/TUFFC.2009.1075

Santin, M.D., King, D.A., Foiret, J., Haak, A., O'Brien, W.D., Bridal, S.L., 2010. Encapsulated contrast microbubble radial oscillation associated with postexcitation pressure peaks. J Acoust Soc Am 127, 1156–1164. https://doi.org/10.1121/1.3277216

Schaeffer, S., Iadecola, C., 2021. Revisiting the neurovascular unit. Nat Neurosci 24, 1198–1209. https://doi.org/10.1038/s41593-021-00904-7

Schoen, S., Dash, P., Arvanitis, C.D., 2022. Experimental Demonstration of Trans-Skull Volumetric Passive Acoustic Mapping With the Heterogeneous Angular Spectrum Approach. IEEE Trans Ultrason Ferroelectr Freq Control 69, 534–542. https://doi.org/10.1109/TUFFC.2021.3125670

Schoknecht, K., Maechler, M., Wallach, I., Dreier, J.P., Liotta, A., Berndt, N., 2024. Isoflurane lowers the cerebral metabolic rate of oxygen and prevents hypoxia during cortical spreading depolarization in vitro: An integrative experimental and modeling study. J Cereb Blood Flow Metab 44, 1000–1012. https://doi.org/10.1177/0271678X231222306

Schoknecht, K., Maechler, M., Wallach, I., Dreier, J.P., Liotta, A., Berndt, N., 2023. Isoflurane lowers the cerebral metabolic rate of oxygen and prevents hypoxia during cortical spreading

depolarization *in vitro* : An integrative experimental and modeling study. J Cereb Blood Flow Metab 0271678X231222306. https://doi.org/10.1177/0271678X231222306

Sheikov, N., McDannold, N., Vykhodtseva, N., Jolesz, F., Hynynen, K., 2004. Cellular mechanisms of the blood-brain barrier opening induced by ultrasound in presence of microbubbles. Ultrasound Med Biol 30, 979–989. https://doi.org/10.1016/j.ultrasmedbio.2004.04.010

Shekhar, H., Awuor, I., Thomas, K., Rychak, J.J., Doyley, M.M., 2014. The Delayed Onset of Subharmonic and Ultraharmonic Emissions from a Phospholipid-Shelled Microbubble Contrast Agent. Ultrasound Med Biol 40, 727–738. https://doi.org/10.1016/j.ultrasmedbio.2014.01.002

Shemer, A., Erny, D., Jung, S., Prinz, M., 2015. Microglia Plasticity During Health and Disease: An Immunological Perspective. Trends Immunol 36, 614–624. https://doi.org/10.1016/j.it.2015.08.003

Shen, Y., Hua, L., Yeh, C.-K., Shen, L., Ying, M., Zhang, Z., Liu, G., Li, S., Chen, S., Chen, X., Yang, X., 2020. Ultrasound with microbubbles improves memory, ameliorates pathology and modulates hippocampal proteomic changes in a triple transgenic mouse model of Alzheimer's disease. Theranostics 10, 11794–11819. https://doi.org/10.7150/thno.44152

Shi, D., Xu, S., Zhuo, J., McKenna, M.C., Gullapalli, R.P., 2019. White Matter Alterations in Fmr1 KO mice during Early Postnatal Brain Development. Dev Neurosci 41, 274–289. https://doi.org/10.1159/000506679

Shin, H.-G., Lee, Jingu, Yun, Y.H., Yoo, S.H., Jang, J., Oh, S.-H., Nam, Y., Jung, S., Kim, S., Fukunaga, M., Kim, W., Choi, H.J., Lee, Jongho, 2021. χ-separation: Magnetic susceptibility source separation toward iron and myelin mapping in the brain. NeuroImage 240, 118371. https://doi.org/10.1016/j.neuroimage.2021.118371

Shin, J., Kong, C., Cho, J.S., Lee, J., Koh, C.S., Yoon, M.-S., Na, Y.C., Chang, W.S., Chang, J.W., 2018. Focused ultrasound–mediated noninvasive blood-brain barrier modulation: preclinical examination of efficacy and safety in various sonication parameters. Neurosurgical Focus 44, E15. https://doi.org/10.3171/2017.11.FOCUS17627

Shinozaki, Y., Shibata, K., Yoshida, K., Shigetomi, E., Gachet, C., Ikenaka, K., Tanaka, K.F., Koizumi, S., 2017. Transformation of Astrocytes to a Neuroprotective Phenotype by Microglia via P2Y1 Receptor Downregulation. Cell Rep 19, 1151–1164. https://doi.org/10.1016/j.celrep.2017.04.047

Shitik, E.M., Velmiskina, A.A., Dolskiy, A.A., Yudkin, D.V., 2020. Reactivation of FMR1 gene expression is a promising strategy for fragile X syndrome therapy. Gene Ther 27, 247–253. https://doi.org/10.1038/s41434-020-0141-0

Siddik, Z., Boxall, F., Harrap, K., 1987. Haematological toxicity of carboplatin in rats. Br J Cancer 55, 375–379. https://doi.org/10.1038/bjc.1987.75

Sigrist, R.M.S., Liau, J., Kaffas, A.E., Chammas, M.C., Willmann, J.K., 2017. Ultrasound Elastography: Review of Techniques and Clinical Applications. Theranostics 7, 1303–1329. https://doi.org/10.7150/thno.18650

Singh, A., Kusunose, J., Phipps, M.A., Wang, F., Chen, L.M., Caskey, C.F., 2022. Guiding and monitoring focused ultrasound mediated blood–brain barrier opening in rats using power Doppler imaging and passive acoustic mapping. Sci Rep 12, 14758. https://doi.org/10.1038/s41598-022-18328-z

Sinharay, S., Tu, T.-W., Kovacs, Z.I., Schreiber-Stainthorp, W., Sundby, M., Zhang, X., Papadakis, G.Z., Reid, W.C., Frank, J.A., Hammoud, D.A., 2019. In vivo imaging of sterile microglial activation in rat brain after disrupting the blood-brain barrier with pulsed focused ultrasound: [18F]DPA-714 PET study. J Neuroinflammation 16, 155. https://doi.org/10.1186/s12974-019-1543-z

Sirsi, S.R., Hernandez, S.L., Zielinski, L., Blomback, H., Koubaa, A., Synder, M., Homma, S., Kandel, J.J., Yamashiro, D.J., Borden, M.A., 2012. Polyplex-microbubble hybrids for ultrasound-guided

plasmid DNA delivery to solid tumors. J Control Release 157, 224–234. https://doi.org/10.1016/j.jconrel.2011.09.071

Sofroniew, M.V., Vinters, H.V., 2010. Astrocytes: biology and pathology. Acta Neuropathol 119, 7–35. https://doi.org/10.1007/s00401-009-0619-8

Sonabend, A.M., Gould, A., Amidei, C., Ward, R., Schmidt, K.A., Zhang, D.Y., Gomez, C., Bebawy, J.F., Liu, B.P., Bouchoux, G., Desseaux, C., Helenowski, I.B., Lukas, R.V., Dixit, K., Kumthekar, P., Arrieta, V.A., Lesniak, M.S., Carpentier, A., Zhang, H., Muzzio, M., Canney, M., Stupp, R., 2023. Repeated blood–brain barrier opening with an implantable ultrasound device for delivery of albumin-bound paclitaxel in patients with recurrent glioblastoma: a phase 1 trial. The Lancet Oncology 24, 509–522. https://doi.org/10.1016/S1470-2045(23)00112-2

Song, R., Pekrun, K., Khan, T.A., Zhang, F., Paşca, S.P., Kay, M.A., 2022. Selection of rAAV vectors that cross the human blood-brain barrier and target the central nervous system using a transwell model. Mol Ther Methods Clin Dev 27, 73–88. https://doi.org/10.1016/j.omtm.2022.09.002

Spottiswoode, B., 2022. 2D phase unwrapping algorithms.

Steeg, P.S., 2021. The blood–tumour barrier in cancer biology and therapy. Nat Rev Clin Oncol 18, 696–714. https://doi.org/10.1038/s41571-021-00529-6

Steinmetz, J.D., *et al*., 2024. Global, regional, and national burden of disorders affecting the nervous system, 1990–2021: a systematic analysis for the Global Burden of Disease Study 2021. The Lancet Neurology 23, 344–381. https://doi.org/10.1016/S1474-4422(24)00038-3

Strong, A.J., Fabricius, M., Boutelle, M.G., Hibbins, S.J., Hopwood, S.E., Jones, R., Parkin, M.C., Lauritzen, M., 2002. Spreading and Synchronous Depressions of Cortical Activity in Acutely Injured Human Brain. Stroke 33, 2738–2743. https://doi.org/10.1161/01.STR.0000043073.69602.09

Stupar, V., Delalande, A., Collomb, N., Rome, C., Barbier, E.L., 2018. Impact of focused ultrasound on cerebral blood flow [abstract].

Stupp, R., Mason, W.P., Van Den Bent, M.J., Weller, M., Fisher, B., Taphoorn, M.J.B., Belanger, K., Brandes, A.A., Marosi, C., Bogdahn, U., Curschmann, J., Janzer, R.C., Ludwin, S.K., Gorlia, T., Allgeier, A., Lacombe, D., Cairncross, J.G., Eisenhauer, E., Mirimanoff, R.O., 2005. Radiotherapy plus Concomitant and Adjuvant Temozolomide for Glioblastoma. N Engl J Med 352, 987–996. https://doi.org/10.1056/NEJMoa043330

Su, W.-S., Wu, C.-H., Chen, S.-F., Yang, F.-Y., 2017. Low-intensity pulsed ultrasound improves behavioral and histological outcomes after experimental traumatic brain injury. Sci Rep 7, 15524. https://doi.org/10.1038/s41598-017-15916-2

Sun, T., Krishnan, V., Pan, D.C., Filippov, S.K., Ravid, S., Sarode, A., Kim, J., Zhang, Y., Power, C., Aday, S., Guo, J., Karp, J.M., McDannold, N.J., Mitragotri, S.S., 2023. Ultrasound-mediated delivery of flexibility-tunable polymer drug conjugates for treating glioblastoma. Bioengineering & Transla Med 8. https://doi.org/10.1002/btm2.10408

Sun, T., Samiotaki, G., Wang, S., Acosta, C., Chen, C.C., Konofagou, E.E., 2015. Acoustic cavitation-based monitoring of the reversibility and permeability of ultrasound-induced blood-brain barrier opening. Phys Med Biol 60, 9079–9094. https://doi.org/10.1088/0031-9155/60/23/9079

Sun, T., Zhang, Y., Power, C., Alexander, P.M., Sutton, J.T., Aryal, M., Vykhodtseva, N., Miller, E.L., McDannold, N.J., 2017. Closed-loop control of targeted ultrasound drug delivery across the blood-brain/tumor barriers in a rat glioma model. Proc Natl Acad Sci U S A 114, E10281–E10290. https://doi.org/10.1073/pnas.1713328114

Sweeney, M.D., Ayyadurai, S., Zlokovic, B.V., 2016. Pericytes of the neurovascular unit: key functions and signaling pathways. Nat Neurosci 19, 771–783. https://doi.org/10.1038/nn.4288

Swift, T.J., Connick, R.E., 1962. NMR-Relaxation Mechanisms of O17 in Aqueous Solutions of Paramagnetic Cations and the Lifetime of Water Molecules in the First Coordination Sphere. The Journal of Chemical Physics 37, 307–320. https://doi.org/10.1063/1.1701321

Takano, T., Tian, G.-F., Peng, W., Lou, N., Libionka, W., Han, X., Nedergaard, M., 2006. Astrocyte-mediated control of cerebral blood flow. Nat Neurosci 9, 260–267. https://doi.org/10.1038/nn1623

Tanaka, Y., Nagaoka, T., Nair, G., Ohno, K., Duong, T.Q., 2011. Arterial spin labeling and dynamic susceptibility contrast CBF MRI in postischemic hyperperfusion, hypercapnia, and after mannitol injection. J Cereb Blood Flow Metab 31, 1403–1411. https://doi.org/10.1038/jcbfm.2010.228

The Dutch-Belgian Fragile X Consortium, 1994. Fmr1 knockout mice: a model to study fragile X mental retardation. Cell 78, 23–33.

Thévenot, E., Jordão, J.F., O'Reilly, M.A., Markham, K., Weng, Y.-Q., Foust, K.D., Kaspar, B.K., Hynynen, K., Aubert, I., 2012. Targeted Delivery of Self-Complementary Adeno-Associated Virus Serotype 9 to the Brain, Using Magnetic Resonance Imaging-Guided Focused Ultrasound. Human Gene Therapy 23, 1144–1155. https://doi.org/10.1089/hum.2012.013

Tho, P., Manasseh, R., Ooi, A., 2007. Cavitation microstreaming patterns in single and multiple bubble systems. J. Fluid Mech. 576, 191–233. https://doi.org/10.1017/S0022112006004393

Thorne, R.G., Pronk, G.J., Padmanabhan, V., Frey, W.H., 2004. Delivery of insulin-like growth factor-I to the rat brain and spinal cord along olfactory and trigeminal pathways following intranasal administration. Neuroscience 127, 481–496. https://doi.org/10.1016/j.neuroscience.2004.05.029

Tinkov, S., Winter, G., Coester, C., Bekeredjian, R., 2010. New doxorubicin-loaded phospholipid microbubbles for targeted tumor therapy: Part I — Formulation development and in-vitro characterization. J Control Release 143, 143–150. https://doi.org/10.1016/j.jconrel.2009.12.026

Todd, N., Angolano, C., Ferran, C., Devor, A., Borsook, D., McDannold, N., 2020. Secondary effects on brain physiology caused by focused ultrasound-mediated disruption of the blood–brain barrier. J Control Release 324, 450–459. https://doi.org/10.1016/j.jconrel.2020.05.040

Todd, N., Zhang, Y., Arcaro, M., Becerra, L., Borsook, D., Livingstone, M., McDannold, N., 2018. Focused ultrasound induced opening of the blood-brain barrier disrupts inter-hemispheric resting state functional connectivity in the rat brain. NeuroImage 178, 414–422. https://doi.org/10.1016/j.neuroimage.2018.05.063

Todd, N., Zhang, Y., Livingstone, M., Borsook, D., McDannold, N., 2019. The neurovascular response is attenuated by focused ultrasound-mediated disruption of the blood-brain barrier. NeuroImage 201, 116010. https://doi.org/10.1016/j.neuroimage.2019.116010

Treat, L.H., McDannold, N., Vykhodtseva, N., Hynynen, K., 2004. Transcranial MRI-guided focused ultrasound-induced blood-brain barrier opening in rats, in: IEEE Ultrasonics Symposium, 2004. Presented at the IEEE Ultrasonics Symposium, 2004, IEEE, Montreal, Canada, pp. 998–1000. https://doi.org/10.1109/ULTSYM.2004.1417932

Treeby, B.E., Cox, B.T., 2010. k-Wave: MATLAB toolbox for the simulation and reconstruction of photoacoustic wave fields. J Biomed Opt 15, 021314. https://doi.org/10.1117/1.3360308

Troprès, I., Grimault, S., Vaeth, A., Grillon, E., Julien, C., Payen, J.F., Lamalle, L., Décorps, M., 2001. Vessel size imaging. Magn Reson Med 45, 397–408. https://doi.org/10.1002/1522-2594(200103)45:3<397::aid-mrm1052>3.0.co;2-3

Troprès, I., Pannetier, N., Grand, S., Lemasson, B., Moisan, A., Péoc'h, M., Rémy, C., Barbier, E.L., 2015. Imaging the microvessel caliber and density: Principles and applications of microvascular MRI: MRI of the Microvessel Caliber and Density. Magn Reson Med 73, 325–341. https://doi.org/10.1002/mrm.25396

Tsai, C.-H., Zhang, J.-W., Liao, Y.-Y., Liu, H.-L., 2016. Real-time monitoring of focused ultrasound blood-brain barrier opening via subharmonic acoustic emission detection: implementation of confocal dual-frequency piezoelectric transducers. Phys Med Biol 61, 2926–2946. https://doi.org/10.1088/0031-9155/61/7/2926

Tsai, H.-C., Tsai, C.-H., Chen, W.-S., Inserra, C., Wei, K.-C., Liu, H.-L., 2018. Safety evaluation of frequent application of microbubble-enhanced focused ultrasound blood-brain-barrier opening. Sci Rep 8, 17720. https://doi.org/10.1038/s41598-018-35677-w

Tu, T.-W., Turtzo, L.C., Williams, R.A., Lescher, J.D., Dean, D.D., Frank, J.A., 2014. Imaging of Spontaneous Ventriculomegaly and Vascular Malformations in Wistar Rats: Implications for Preclinical Research. J Neuropathol Exp Neurol 73, 1152–1165. https://doi.org/10.1097/NEN.0000000000000140

Tung, Y.-S., Choi, J.J., Baseri, B., Konofagou, E.E., 2010a. Identifying the Inertial Cavitation Threshold and Skull Effects in a Vessel Phantom Using Focused Ultrasound and Microbubbles. Ultrasound Med Biol 36, 840–852. https://doi.org/10.1016/j.ultrasmedbio.2010.02.009

Tung, Y.-S., Vlachos, F., Choi, J.J., Deffieux, T., Selert, K., Konofagou, E.E., 2010b. *In vivo* transcranial cavitation threshold detection during ultrasound-induced blood–brain barrier opening in mice. Phys Med Biol 55, 6141–6155. https://doi.org/10.1088/0031-9155/55/20/007

Tung, Y.-S., Vlachos, F., Feshitan, J.A., Borden, M.A., Konofagou, E.E., 2011. The mechanism of interaction between focused ultrasound and microbubbles in blood-brain barrier opening in mice. J Acoust Soc Am 130, 3059–3067. https://doi.org/10.1121/1.3646905

Turner, M.D., Nedjai, B., Hurst, T., Pennington, D.J., 2014. Cytokines and chemokines: At the crossroads of cell signalling and inflammatory disease. Biochimica et Biophysica Acta (BBA) - Molecular Cell Research 1843, 2563–2582. https://doi.org/10.1016/j.bbamcr.2014.05.014

Umeda, K., Ikenouchi, J., Katahira-Tayama, S., Furuse, K., Sasaki, H., Nakayama, M., Matsui, T., Tsukita, Sachiko, Furuse, M., Tsukita, Shoichiro, 2006. ZO-1 and ZO-2 Independently Determine Where Claudins Are Polymerized in Tight-Junction Strand Formation. Cell 126, 741–754. https://doi.org/10.1016/j.cell.2006.06.043

Valable, S., Lemasson, B., Farion, R., Beaumont, M., Segebarth, C., Remy, C., Barbier, E.L., 2008. Assessment of blood volume, vessel size, and the expression of angiogenic factors in two rat glioma models: a longitudinal *in vivo* and *ex vivo* study. NMR Biomed 21, 1043–1056. https://doi.org/10.1002/nbm.1278

Valdés-Hernández, P.A., 2011. An in vivo MRI template set for morphometry, tissue segmentation, and fMRI localization in rats. Front Neuroinform 5. https://doi.org/10.3389/fninf.2011.00026

van Wamel, A., Kooiman, K., Harteveld, M., Emmer, M., ten Cate, F.J., Versluis, M., de Jong, N., 2006. Vibrating microbubbles poking individual cells: Drug transfer into cells via sonoporation. J Control Release 112, 149–155. https://doi.org/10.1016/j.jconrel.2006.02.007

Visootsak, J., Warren, S.T., Anido, A., Graham, J.M., 2005. Fragile X syndrome: an update and review for the primary pediatrician. Clin Pediatr (Phila) 44, 371–381. https://doi.org/10.1177/000992280504400501

Vlachos, F., Tung, Y.-S., Konofagou, E., 2011. Permeability dependence study of the focused ultrasound-induced blood-brain barrier opening at distinct pressures and microbubble diameters using DCE-MRI. Magn Reson Med 66, 821–830. https://doi.org/10.1002/mrm.22848

Vlachos, F., Tung, Y.-S., Konofagou, E.E., 2010. Permeability assessment of the focused ultrasound-induced blood–brain barrier opening using dynamic contrast-enhanced MRI. Phys Med Biol 55, 5451–5466. https://doi.org/10.1088/0031-9155/55/18/012

Vykhodtseva, N., Sorrentino, V., Jolesz, F.A., Bronson, R.T., Hynynen, K., 2000. MRI detection of the thermal effects of focused ultrasound on the brain. Ultrasound Med Biol 26, 871–880. https://doi.org/10.1016/S0301-5629(00)00216-7

Walker, M.D., Strike, T.A., Sheline, G.E., 1979. An analysis of dose-effect relationship in the radiotherapy of malignant gliomas. IJROBP 5, 1725–1731. https://doi.org/10.1016/0360-3016(79)90553-4

Wang, J., Xie, L., Shi, Y., Ao, L., Cai, F., Yan, F., 2021. Early Detection and Reversal of Cell Apoptosis Induced by Focused Ultrasound-Mediated Blood-Brain Barrier Opening. ACS Nano 15, 14509–14521. https://doi.org/10.1021/acsnano.1c04029

Wang, Y., Liu, T., 2015. Quantitative susceptibility mapping (QSM): Decoding MRI data for a tissue magnetic biomarker. Magnetic Resonance in Med 73, 82–101. https://doi.org/10.1002/mrm.25358

Watkins, L.V., Moon, S., Burrows, L., Tromans, S., Barwell, J., Shankar, R., 2024. Pharmacological management of fragile X syndrome: a systematic review and narrative summary of the current evidence. Expert Opin Pharmacother 25, 301–313. https://doi.org/10.1080/14656566.2024.2323605

Wegener, S., Wu, W.-C., Perthen, J.E., Wong, E.C., 2007. Quantification of rodent cerebral blood flow (CBF) in normal and high flow states using pulsed arterial spin labeling magnetic resonance imaging. J Magn Reson Imaging 26, 855–862. https://doi.org/10.1002/jmri.21045

Wei, H., Dibb, R., Zhou, Y., Sun, Y., Xu, J., Wang, N., Liu, C., 2015. Streaking artifact reduction for quantitative susceptibility mapping of sources with large dynamic range: Streaking Artifact Reduction for QSM. NMR Biomed. 28, 1294–1303. https://doi.org/10.1002/nbm.3383

Wei, H.-J., Upadhyayula, P.S., Pouliopoulos, A.N., Englander, Z.K., Zhang, X., Jan, C.-I., Guo, J., Mela, A., Zhang, Z., Wang, T.J.C., Bruce, J.N., Canoll, P.D., Feldstein, N.A., Zacharoulis, S., Konofagou, E.E., Wu, C.-C., 2021. Focused Ultrasound-Mediated Blood-Brain Barrier Opening Increases Delivery and Efficacy of Etoposide for Glioblastoma Treatment. Int J Radiat Oncol Biol Phys 110, 539–550. https://doi.org/10.1016/j.ijrobp.2020.12.019

Wei, K.-C., Chu, P.-C., Wang, H.-Y.J., Huang, C.-Y., Chen, P.-Y., Tsai, H.-C., Lu, Y.-J., Lee, P.-Y., Tseng, I.-C., Feng, L.-Y., Hsu, P.-W., Yen, T.-C., Liu, H.-L., 2013. Focused Ultrasound-Induced Blood–Brain Barrier Opening to Enhance Temozolomide Delivery for Glioblastoma Treatment: A Preclinical Study. PLoS ONE 8, e58995. https://doi.org/10.1371/journal.pone.0058995

Weng, J., Wu, S., Lin, W., Tseng, W.I., 2011. Detecting blood–brain barrier disruption within minimal hemorrhage following transcranial focused ultrasound: A correlation study with contrast-enhanced MRI. Magnetic Resonance in Med 65, 802–811. https://doi.org/10.1002/mrm.22643

West, J.B., 2007. Pulmonary physiology and pathophysiology: an integrated, case-based approach., Philadelphia, PA: Lippincott Williams & Wilkins. Philadelphia, PA: Lippincott Williams & Wilkins.

Westergaard, E., Brightman, M.W., 1973. Transport of proteins across normal cerebral arterioles. J of Comparative Neurology 152, 17–44. https://doi.org/10.1002/cne.901520103

Wong, H., Hooper, A.W., Kang, H.R., Lee, S.J., Zhao, J., Sadhu, C., Rawat, S., Gray, S.J., Hampson, D.R., 2023. CNS-dominant human FMRP isoform rescues seizures, fear, and sleep abnormalities in Fmr1-KO mice. JCI Insight 8, e169650. https://doi.org/10.1172/jci.insight.169650

Wu, B., Li, W., Guidon, A., Liu, C., 2012. Whole brain susceptibility mapping using compressed sensing. Magnetic Resonance in Med 67, 137–147. https://doi.org/10.1002/mrm.23000

Wu, D., Chen, Q., Chen, X., Han, F., Chen, Z., Wang, Y., 2023. The blood–brain barrier: structure, regulation, and drug delivery. Sig Transduct Target Ther 8, 217. https://doi.org/10.1038/s41392-023-01481-w

Wu, S.-K., Chu, P.-C., Chai, W.-Y., Kang, S.-T., Tsai, C.-H., Fan, C.-H., Yeh, C.-K., Liu, H.-L., 2017. Characterization of Different Microbubbles in Assisting Focused Ultrasound-Induced Blood-Brain Barrier Opening. Sci Rep 7, 46689. https://doi.org/10.1038/srep46689

Wu, S.-Y., Aurup, C., Sanchez, C.S., Grondin, J., Zheng, W., Kamimura, H., Ferrera, V.P., Konofagou, E.E., 2018. Efficient Blood-Brain Barrier Opening in Primates with Neuronavigation-Guided

Ultrasound and Real-Time Acoustic Mapping. Sci Rep 8, 7978. https://doi.org/10.1038/s41598-018-25904-9

Wu, S.-Y., Tung, Y.-S., Marquet, F., Downs, M., Sanchez, C., Chen, C., Ferrera, V., Konofagou, E., 2014. Transcranial cavitation detection in primates during blood-brain barrier opening--a performance assessment study. IEEE Trans Ultrason Ferroelectr Freq Control 61, 966–978. https://doi.org/10.1109/TUFFC.2014.2992

Xie, N., Gong, H., Suhl, J.A., Chopra, P., Wang, T., Warren, S.T., 2016. Reactivation of FMR1 by CRISPR/Cas9-Mediated Deletion of the Expanded CGG-Repeat of the Fragile X Chromosome. PLoS ONE 11, e0165499. https://doi.org/10.1371/journal.pone.0165499

Xu, J., Kausalya, P.J., Phua, D.C.Y., Ali, S.M., Hossain, Z., Hunziker, W., 2008. Early Embryonic Lethality of Mice Lacking ZO-2, but Not ZO-3, Reveals Critical and Nonredundant Roles for Individual Zonula Occludens Proteins in Mammalian Development. Molecular and Cellular Biology 28, 1669–1678. https://doi.org/10.1128/MCB.00891-07

Yang, F., Horng, S., Lin, Y., Kao, Y., 2010. Association between contrast-enhanced MR images and blood–brain barrier disruption following transcranial focused ultrasound. Magnetic Resonance Imaging 32, 593–599. https://doi.org/10.1002/jmri.22297

Yang, F.-Y., Chang, W.-Y., Chen, J.-C., Lee, L.-C., Hung, Y.-S., 2014. Quantitative assessment of cerebral glucose metabolic rates after blood-brain barrier disruption induced by focused ultrasound using FDG-MicroPET. Neuroimage 90, 93–98. https://doi.org/10.1016/j.neuroimage.2013.12.033

Yang, G., Zhang, Y., Ross, M.E., Iadecola, C., 2003. Attenuation of activity-induced increases in cerebellar blood flow in mice lacking neuronal nitric oxide synthase. American Journal of Physiology-Heart and Circulatory Physiology 285, H298–H304. https://doi.org/10.1152/ajpheart.00043.2003

Yang, W., Huo, T., Barth, R.F., Gupta, N., Weldon, M., Grecula, J.C., Ross, B.D., Hoff, B.A., Chou, T.-C., Rousseau, J., Elleaume, H., 2011. Convection enhanced delivery of carboplatin in combination with radiotherapy for the treatment of brain tumors. J Neurooncol 101, 379–390. https://doi.org/10.1007/s11060-010-0272-z

Yasui, K., 2023. Origin of the broad-band noise in acoustic cavitation. Ultrasonics Sonochemistry 93, 106276. https://doi.org/10.1016/j.ultsonch.2022.106276

Yasui, K., 2018. Acoustic Cavitation and Bubble Dynamics, SpringerBriefs in Molecular Science. Springer International Publishing, Cham. https://doi.org/10.1007/978-3-319-68237-2

Yonemori, K., Tsuta, K., Ono, M., Shimizu, C., Hirakawa, A., Hasegawa, T., Hatanaka, Y., Narita, Y., Shibui, S., Fujiwara, Y., 2010. Disruption of the blood brain barrier by brain metastases of triple-negative and basal-type breast cancer but not HER2/neu-positive breast cancer. Cancer 116, 302–308. https://doi.org/10.1002/cncr.24735

Yoon, K., Lee, W., Chen, E., Lee, J.E., Croce, P., Cammalleri, A., Foley, L., Tsao, A.L., Yoo, S.-S., 2019. Localized Blood-Brain Barrier Opening in Ovine Model Using Image-Guided Transcranial Focused Ultrasound. Ultrasound Med Biol 45, 2391–2404. https://doi.org/10.1016/j.ultrasmedbio.2019.05.023

Zhang, D., Ruan, J., Peng, S., Li, J., Hu, X., Zhang, Y., Zhang, T., Ge, Y., Zhu, Z., Xiao, X., Zhu, Yunxu, Li, Xuzhao, Li, T., Zhou, L., Gao, Q., Zheng, G., Zhao, B., Li, Xiangqing, Zhu, Yanming, Wu, J., Li, W., Zhao, J., Ge, W., Xu, T., Jia, J.-M., 2024. Synaptic-like transmission between neural axons and arteriolar smooth muscle cells drives cerebral neurovascular coupling. Nat Neurosci 27, 232–248. https://doi.org/10.1038/s41593-023-01515-0

Zhao, Z., Nelson, A.R., Betsholtz, C., Zlokovic, B.V., 2015. Establishment and Dysfunction of the Blood-Brain Barrier. Cell 163, 1064–1078. https://doi.org/10.1016/j.cell.2015.10.067

Zhou, Y., Yang, K., Cui, J., Ye, J.Y., Deng, C.X., 2012. Controlled permeation of cell membrane by single bubble acoustic cavitation. Journal of Controlled Release 157, 103–111. https://doi.org/10.1016/j.jconrel.2011.09.068

Zhu, X., Guo, J., He, C., Geng, H., Yu, G., Li, J., Zheng, H., Ji, X., Yan, F., 2016. Ultrasound triggered image-guided drug delivery to inhibit vascular reconstruction via paclitaxel-loaded microbubbles. Sci Rep 6, 21683. https://doi.org/10.1038/srep21683

Zoteva, V., De Meulenaere, V., De Boeck, M., Vanhove, C., Leybaert, L., Raedt, R., Pieters, L., Vral, A., Boterberg, T., Deblaere, K., 2024. An improved F98 glioblastoma rat model to evaluate novel treatment strategies incorporating the standard of care. PLoS ONE 19, e0296360. https://doi.org/10.1371/journal.pone.0296360

Résumé français - French Summary

1. Introduction

En 2021, les maladies du système nerveux central ont touché plus d'une personne sur trois, comme le rapporte la prestigieuse revue The Lancet Neurology. Parmi celles-ci, la maladie de Parkinson, la maladie d'Alzheimer et les tumeurs cérébrales représentent les trois maladies les plus répandues, avec une augmentation respective de leur prévalence de 100 %, 110 % et 210 % depuis 1990 [Steinmetz *et al*., 2024]. Une multitude d'essais cliniques n'ont pas réussi à démontrer une amélioration des résultats, malgré le fait que de nombreuses molécules thérapeutiques aient montré une efficacité in vitro ou dans des modèles précliniques [Angeli *et al*., 2019 ; Brahmachari *et al*., 2017 ; Rousseau *et al*., 2007]. L'un des principaux facteurs contribuant à cela est la barrière très imperméable que représente la barrière hémato-encéphalique (BHE) qui empêche le passage des médicaments dans le cerveau. Le système nerveux central est efficacement protégé par cette BHE qui sert de frontière pour maintenir l'homéostasie cérébrale et empêcher le cerveau d'être atteint par des agents pathogènes nocifs. Il a été démontré que plus de 98 % des grosses molécules (d'un poids moléculaire supérieur à 500 Da) ne peuvent pénétrer dans le système nerveux central par la BHE [Pardridge, 2005].

Par conséquent, la majorité des composés thérapeutiques qui ont été développés, y compris l'anticorps aducanumab pour la maladie d'Alzheimer ou encore le carboplatine pour le glioblastome (le type de tumeur cérébrale le plus agressif avec un très mauvais pronostic) sont incapables de traverser la BHE [Jacobs *et al*., 2010 ; Pardridge, 2019]. La combinaison des ultrasons focalisés (FUS) et de microbulles de gaz, dont l'utilisation clinique est approuvée en tant qu'agent de contraste pour l'imagerie ultrasonore, a récemment montré des résultats encourageants en termes de perméabilisation de la BHE chez les patients. Plus récemment, la délivrance de l'aducanumab chez des patients atteints de la maladie d'Alzheimer, du trastuzumab dans le cadre d'une étude chez des patients présentant des métastases cérébrales du cancer du sein et du carboplatine chez des patients en récidive de glioblastome a été permis grâce aux progrès de cette technologie [Carpentier *et al*, 2024 ; Lipsman *et al*., 2018 ; Meng *et al*., 2021b ; Rezai *et al*., 2024]. Les FUS ont la capacité de cibler n'importe quelle structure cérébrale avec une précision millimétrique, permettant ainsi l'administration contrôlée et sûre de médicaments dans les régions cérébrales ciblées. Cependant, cette technologie en est encore à ses débuts, avec moins de 100 articles publiés sur la perméabilisation de la BHE chez les patients (mots-clés de la recherche PubMed : "human" AND ("fus" OR "focused ultrasound") AND "bbb" AND ("opening" OR "permeabilised" OR "delivery"), n = 97, 01/08/2024).

Une grande partie des récentes études précliniques ont été menée pour évaluer l'efficacité de l'ouverture de la BHE par FUS et l'administration d'une série de médicaments, incluant les chimiothérapies et des vecteurs de thérapie génique [Felix *et al*., 2021 ; Wei *et al*., 2021]. Quelques articles ont aussi évalué les effets secondaires biologiques des paramètres FUS démontrant des dommages significatifs après la procédure. Les paramètres alors utilisés se sont avérés dangereux par la suite [Weng *et al*., 2011 ; Yang *et al*., 2010]. Ces études illustrent les effets indésirables potentiels qui peuvent survenir si la technique n'est pas totalement maîtrisée. Plus récemment, d'autres chercheurs ont mis en lumière des dérégulations biologiques à la suite de l'application des FUS, même en l'absence de dommages importants évidents, tels que des hémorragies [Ji *et al*., 2021 ; McMahon et Hynynen, 2017]. Le nombre de caractéristiques évaluées après l'ouverture de la BHE est encore

relativement faible, compte tenu de l'intérêt récent pour cette technologie. De plus, il est raisonnable de supposer que la FUS combinés aux microbulles a un impact direct sur le fonctionnement de l'unité neurovasculaire par le biais du système vasculaire, lieu des modifications induites par le phénomène de cavitation des microbulles sous l'influence des FUS.

Pour apporter des premières réponses, différentes études ont évalué les effets cellulaires de l'ouverture de la BHE induite par FUS avec la MB dans le cerveau [S. Chen *et al*., 2021], tenté de décrypter les variations vasculaires et les altérations fonctionnelles à l'aide de l'imagerie par résonance magnétique (IRM) [Todd *et al*., 2019, 2018], et mesuré l'évolution temporelle de ces changements à l'aide de l'imagerie à bi photonique et/ou de l'IRM [Labriji *et al*., 2023 ; Raymond *et al*., 2007]. L'IRM est la modalité d'imagerie de choix à la fois pour l'imagerie à échelle fine des structures cérébrales et pour la mesure de paramètres quantitatifs au niveau du système nerveux central. Les récents travaux menés pour améliorer la mesure de la perfusion cérébrale sans agent de contraste [Hirschler *et al*., 2018] et des paramètres vasculaires quantitatifs [Troprès *et al*., 2015] avec de nouvelles méthodes d'IRM rapide telles que l'approche IRM dite "fingerprint" [T. Christen *et al*., 2014 ; Lemasson *et al*., 2016 ; Ma *et al*., 2013] permettent aujourd'hui de caractériser avec précision le réseau microvasculaire cérébral de manière non invasive. Aujourd'hui, il existe un manque cruel de connaissances concernant la modification potentielle de ces paramètres microvasculaires à la suite de la perméabilisation de la BHE.

Pour combler ces lacunes, dans cette thèse, nous avons d'abord évalué et quantifié la dynamique d'une série de paramètres microvasculaires, y compris la perfusion cérébrale, les niveaux d'oxygène et les propriétés vasculaires, en utilisant des approches innovantes d'IRM quantitative. Nous avons également utilisé des techniques histologiques pour étudier les effets cellulaires associés. Nous avons ainsi pu mettre en lumière plusieurs effets secondaires et modifications consécutives à la perméabilisation de la BHE induite par les FUS, qui n'ont pas encore été élucidés jusqu'à présent. Deuxièmement, nous avons appliqué les FUS dans plusieurs modèles animaux dans le but d'améliorer l'administration d'agents thérapeutiques dans l'espoir d'améliorer la condition des patients atteints du Syndrome de l'X fragile et de glioblastome.

Cette thèse a été réalisée dans un environnement interdisciplinaire et stimulant, qui fait partie d'un projet collaboratif tripartite impliquant la société Image Guided Therapy (Pessac, France), le laboratoire Grenoble Institut des Neurosciences (Grenoble, France) et le laboratoire LI²RSO (Orléans, France).

Le présent manuscrit est organisé en huit chapitres principaux résumés ci-dessous.

2. Résumé de l'introduction aux ultrasons focalisés pour perméabiliser la barrière hémato-encéphalique

Le développement et l'utilisation des ultrasons dans le domaine médical ont une riche histoire qui s'étend sur plusieurs décennies. Dans les années 1920, les bases théoriques ont été établies par Paul Langevin et les principes de l'échographie sonore [Langevin, 1924]. Les ultrasons ont rapidement été utilisés à des fins de diagnostic par imagerie médicale. Les nombreux développements méthodologiques de l'imagerie ultrasonore permettent aujourd'hui d'imager quantitativement le cerveau avec une résolution spatiale sans précédent [Errico *et al*., 2015] mais aussi de modifier l'élasticité des tissus et permettant par exemple le diagnostic des nodules thyroïdiens [Sigrist *et al*., 2017]. Contrairement à l'imagerie par ultrasons, qui utilise généralement de grands réseaux non focalisés de transducteurs à ultrasons, l'avènement des réseaux d'ultrasons focalisés (FUS) permet de faire converger vers un point focal désigné l'énergie ultrasonore. Pour focaliser les ondes ultrasonores, un réseau de transducteurs peut être contrôlé électroniquement afin d'ajuster la phase et l'amplitude des ondes ultrasonores qu'ils émettent. Le contrôle susmentionné permet une interférence constructive des ondes au point focal, créant ainsi un point à haute énergie. Cette capacité permet un ciblage précis à l'intérieur du corps sans affecter de manière significative les tissus environnants. Les FUS ont aujourd'hui diverses applications médicales en raison de leur capacité à fournir une énergie ciblée de manière non invasive: ablation de tumeurs en chauffant localement les tissus cancéreux [Coluccia *et al*., 2014], création de lésions dans le noyau intermédiaire ventral du thalamus pour traiter le tremblement essentiel [Elias *et al*., 2016], activation de protéines thermosensibles [Rome *et al*., 2005] et modification de l'activité neuronale pour obtenir des effets thérapeutiques [Beisteiner *et al*., 2020].

La BHE, associée à l'unité neurovasculaire est un complexe se situant à l'interface entre les vaisseaux sanguins cérébraux et le système nerveux central. L'unité neurovasculaire régule la perfusion cérébrale, l'homéostasie cérébrale et protège le système nerveux central contre les potentiels agents pathogènes et toxiques. Au niveau des capillaires, la BHE composée de cellules endothéliales maintenues par des jonctions serrées, de pieds astrocytaires et de péricytes assure les échanges physico-chimiques entre le système nerveux central et les vaisseaux sanguins via des mécanismes paracellulaires et transcellulaires. Cependant, plus de 98% des molécules thérapeutiques actuellement développées ne peuvent pas traverser cette barrière et ainsi rend les traitements inefficaces. Cette barrière est directement atteinte par les maladies du système nerveux central comme dans la maladie d'Alzheimer, de Parkinson ou dans les tumeurs. Elle devient alors plus ou moins perméable, et une restructuration de la vascularisation est parfois possible, notamment avec les mécanismes d'angiogenèse induit par la croissance tumorale. Cette augmentation de la perméabilité peut être diagnostiquée avec des méthodes d'imagerie comme l'IRM et l'injection d'agent de contraste de type gadolinium. Cependant bien que lésée, la BHE ne permet pas d'augmenter drastiquement le passage vers le système nerveux central de molécules thérapeutique, leur distribution est alors bien souvent trop hétérogène. C'est pourquoi les FUS couplés aux microbulles de gaz est aujourd'hui l'une des méthodes les plus prometteuse pour délivrer localement, de façon homogène et durablement des molécules thérapeutiques vers le système nerveux central. Bien que d'autres stratégies pour s'affranchir de la BHE aient été développées comme l'injection intracérébrale directe, l'administration par voie intranasale, l'utilisation de transporteur spécifiques de la BHE à des fins thérapeutiques, les vasodilatateurs tels que le mannitol ou bien des liposomes fonctionnalisés pouvant se lier à des

récepteurs spécifiques, la grande majorité de ceux-ci comportent des inconvénients (invasive, non spécifique, toxicité accrue, faible concentration déposée). La perméabilisation de la BHE par FUS est une méthode qui a aujourd'hui démontré une importante fiabilité et actuellement, bon nombre de transferts en clinique sont réalisés.

L'ouverture de la BHE par FUS est basée sur l'injection de microbulles de gaz dans le système vasculaire, qui sous l'influence du champ acoustique focalisé dans une région précise du cerveau entraine la vibration de ces microbulles. Ce phénomène de vibration appelé cavitation acoustique, induit un stress mécanique important au niveau des parois des cellules endothéliales et ainsi déstabilise celles-ci tout comme les jonctions serrées favorisant ainsi les mécanismes paracellulaires et transcellulaires et permettant aux molécules thérapeutiques circulantes de s'accumuler dans le système nerveux central. Cependant les mécanismes sous-jacents à la perméabilisation de la BHE ne sont pas encore totalement connus.

Afin de contrôler la perméabilisation de la BHE, de nombreux outils ont été développés pour vérifier et caractériser l'ouverture de la BHE. L'outils le plus utilisé à ce jour reste l'IRM en association à des agents de contraste. De nombreuses études ont ainsi caractérisé la dynamique de fermeture de la BHE, mais aussi l'influence des paramètres acoustiques et des microbulles sur la perméabilisation de la BHE. Une séquence FUS pour l'ouverture de la BHE est constituée d'une succession d'impulsion ultrasonore pendant une durée déterminée. La perméabilisation dépend donc de la pression acoustique, de la durée des impulsions ultrasonores, de la fréquence de répétition des impulsions, de la durée totale de la séquence FUS et de la fréquence d'excitation des microbulles de gaz. Celle-ci dépend donc aussi de la concentration et du type de microbulles utilisées. Tous ces paramètres sont aujourd'hui bien documentés et sont spécifiques à chaque modèle animal étudié.

Les essais thérapeutiques précliniques représentent aujourd'hui un grand nombre des études menées avec principalement l'étude de la maladie d'Alzheimer et des tumeurs du système nerveux central. Dans le cas de la maladie d'Alzheimer, caractérisée par une perte de la mémoire, un déclin cognitif due à l'accumulation de plaques amyloïde-β et d'enchevêtrements neurofibrillaires Tau dans le cerveau, plusieurs études ont démontré des améliorations cognitives suite à la perméabilisation de la BHE [Burgess *et al.*, 2014 ; Pandit *et al.*, 2019 ; Shen *et al.*, 2020]. La réduction en nombre et taille de plaques amyloïde-β, associé à l'augmentation du nombre de nouveaux neurones mais aussi la plasticité synaptique permet aujourd'hui d'affirmer que l'utilisation des FUS dans le cadre de cette pathologie est très prometteuse. De plus, de nombreuses molécules chimio-thérapeutiques ont été testées (témozolomide, carboplatine, doxorubicine, …) sans démontrer de grandes améliorations sur la survie bien que le carboplatine semble être aujourd'hui, délivrée par FUS, la molécule la plus performante avec des augmentations de survie significative dans des modèles murins [Dréan *et al.*, 2019 ; McDannold *et al.*, 2019].

En clinique, des essais prometteurs dans le cadre de la maladie d'Alzheimer, de Parkinson et des tumeurs du système nerveux central sont possible grâce au développement d'équipements adaptés. La faisabilité de cette opération a été démontrée tout comme la délivrance de molécules thérapeutiques prometteuses [Carpentier *et al*., 2024 ; Epelbaum *et al*., 2022 ; Rezai *et* al., 2024 ; Sonabend *et al*., 2023].

3. Effets secondaires de la perméabilisation de la barrière hémato-encéphalique par ultrasons focalisés

Les FUS sont connus pour produire à très haute intensité des effets secondaires irréversibles tels que l'apoptose cellulaire et/ou l'hémorragie. A moindre intensité, il a été démontré qu'une succession de phénomènes se produit après la perméabilisation de la BHE impliquant des processus neuroinflammatoires, des modifications vasculaires, métaboliques et sur le comportement.

Dans ce chapitre, nous avons réalisé une revue de la littérature afin d'établir dans le détail une synthèse des différents effets macroscopiques, fonctionnels, moléculaires et physiologiques qui surviennent après la perméabilisation de la BHE par FUS.

Pour évaluer les effets résultant de la perméabilisation de la BHE par FUS couplés aux microbulles de gaz, diverses techniques ont été employées. Ces différentes techniques permettent d'entreprendre une série d'approches complémentaires à différents niveaux d'observation, de l'échelle microscopique à l'échelle macroscopique. Les principales utilisées sont l'IRM, la tomographie par émission de positons, l'imagerie multi-photonique, l'imagerie par ultrasons avec contraste, l'analyse histologique avec coloration à l'hématoxyline et à l'éosine et coloration par immunofluorescence, ainsi que des analyses protéiques et génétiques avec diverses méthodes biologiques.

Au niveau vasculaire, des modifications physiologiques et fonctionnelles ont été observées avec l'altération du signal BOLD et la diminution transitoire de la perfusion en IRM et la vasoconstriction plus ou moins conséquente des vaisseaux perméabilisés [Labriji *et al*., 2023 ; Raymond *et al*., 2007 ; Todd *et al*., 2019]. Ceci est associé à des modifications de la perméabilité des cellules endothéliales avec l'augmentation des phénomènes de transcytose due à la dérégulation des transporteurs situés à ce niveau [Chen *et al*., 2021 ; Pandit *et al*., 2020 ; Sheikov *et al*., 2004]. De plus, des analyses transcriptomiques ont révélé une augmentation de facteurs liés à l'angiogenèse comme VEGFA [McMahon *et al*., 2018]. Ceci pourrait être un facteur encourageant dans le cas des ischémies cérébrale ou des traumatismes crâniens. Aussi, les jonctions serrées qui maintiennent les cellules endothéliales vasculaires de la BHE semblent fortement déstabilisées augmentant alors la perméabilité paracellulaire. Les études sur les jonctions serrées dans le cadre de la perméabilisation de la BHE sont encore peu nombreuses, de plus il n'existe pas aujourd'hui de consensus sur la liste et les fonctions des jonctions serrées présentes au niveau de la BHE, ce qui ne facilite pas la détermination de leur rôle et l'impact des FUS sur celles-ci. Des mécanismes de compensations sont très fortement susceptible d'être mis en place afin de balancer les dérèglements produits par les FUS.

La perméabilisation de la BHE permet à des grosses protéines telles que l'albumine de s'extravaser dans le système nerveux central [Alonso *et al.*, 2011 ; Kovacs *et al*., 2017]. L'albumine est connue pour possiblement déclencher de l'épilepsie et être à l'origine de processus neurodégénératif. Cependant, celle-ci semblerait être nettoyée par les cellules gliales au bout de 24 h, suggérant qu'une présence de courte durée [Alonso *et al*., 2011].

La caractérisation de la réponse neuroinflammatoire à la suite de la perméabilisation a été réalisée de manière extensive depuis la publication des travaux de Kovacs *et al*. Cette étude montre qu'une réponse stérile inflammatoire se produit dans les minutes qui suit la perméabilisation de la BHE et se poursuit pendant au moins 2 jours [Kovacs *et al*., 2017]. D'après les nombreux travaux qui ont succédé, il est aujourd'hui admis qu'une forte activité d'abord microgliale, puis astrocytaire se produit.

Cependant la durée et l'intensité restent encore floues du fait de la large gamme des paramètres FUS utilisés dans ces études dû au manque d'harmonisation des types de microbulles et dispositifs aujourd'hui développés. Ainsi, des résultats très contradictoires ont été montré avec pour certains une activation astrocytaire se poursuivant sur plusieurs semaines [Kovacs *et al*., 2018], ou bien qui se résorbe au bout de quelques jours [Jordão *et al.*, 2013]. La production de cytokines pro- et anti-inflammatoire a été largement quantifiées et les dérégulations sont nombreuses. Cependant, elles apparaissent n'être que très brèves et sont directement liées à l'intensité des paramètres FUS utilisés [Martinez *et al*., 2024 ; Pandit *et al*., 2019]. Le recrutement microglial semble aussi très important [Gorick *et al*., 2020 ; Kovacs *et al*., 2017). Pour les astrocytes et la microglie, les modifications cellulaires qui surviennent pouvant dériver vers des sous-types pro- ou anti-inflammatoire reste encore a prouver et une balance entre les deux semble être le plus plausible car dépendant des paramètres FUS. Il a cependant été démontré que l'augmentation de cette inflammation locale grâce aux FUS permet l'internalisation des plaques amyloïdes-β dans le cadre de la maladie d'Alzheimer. Les effets au niveau des neurones semblent être minimes avec l'absence de dégénération généralisée, bien qu'une étude ait observé des réactions d'ubiquitinylation de protéines neuronales mais pas gliales [Alonso *et al*., 2010]. Cependant la pression acoustique utilisée dans cette étude était très élevée et probablement pas compatible avec une utilisation clinique.

De façon plus générale, peu de modifications au niveau du comportement et de la cognition chez les rongeurs et les primates ont été observées notamment après la perméabilisation répétée de la BHE. Ceci suggère que les processus cognitifs ne sont pas ou que très peu impactés sur le long terme [Downs *et al.*, 2015 ; Horodyckid *et al*., 2017 ; McDannold *et al.*, 2012]. Ceci a aussi été observé en clinique avec peu d'effets secondaires direct liés au traitement par FUS et ce sur le long terme avec le suivi de patients atteints de la maladie d'Alzheimer sur plus de 15 mois ne démontrant pas de baisse cognitive significative grâce à l'évaluation de différents scores cliniques [Epelbaum *et al*., 2022 ; Rezai *et* al., 2024 ; Sonabend *et al*., 2023].

En conclusion, les effets secondaires de la perméabilisation de la BHE semblent être surtout au niveau vasculaire dans les premiers instants après l'application des FUS, puis au niveau cellulaire avec l'apparition d'un processus transitoire neuroinflammatoire. La neuroinflammation semble avoir des effets bénéfiques avec l'internalisation de molécules pathogènes, cependant celle-ci reste encore à définir précisément pour éviter par exemple le déclenchement d'une inflammation chronique. Enfin la perméabilisation de la BHE semble prendre différentes formes du fait des modifications au niveau paracellulaire mais aussi transcellulaire. La compréhension des mécanismes sous-jacents reste encore à élucider complètement et peu d'études à ce jour ont par exemple étudié de façon longitudinale les processus neuroinflammatoires jusqu'à leur disparition ou encore les liens entre les différentes perméabilités vasculaires (lente, rapide et soutenue [Cho *et al.*, 2011 ; Poon *et al.*, 2021 ; Raymond *et al.*, 2007]) et les processus moléculaires mis en jeu au niveau transcellulaire et paracellulaire.

4. Résumé des éléments de méthodes et développements méthodologiques

Dans cette section, un résumé des méthodes générales utilisées pendant les expériences et la caractérisation des aspects du contexte général. Nous avons notamment évalué : le transducteur focalisé, les microbulles, le système FUS guidé par IRM, l'ouverture de la BHE avec la cinétique de la perméabilisation, la méthode de suivi de la cavitation et enfin les séquences et le traitement IRM appliqués tout au long de cette thèse. Chaque étape d'évaluation comprend une description spécifique de ces méthodes.

Le transducteur ultrasonore est un transducteur piézoélectrique concave disposant de 7 éléments concentriques permettant ainsi de modifier la profondeur de la focalisation du champ ultrasonore. Ce transducteur a été caractérisé à l'aide d'un hydrophone monté sur un système de pilotage 3D commandé par un logiciel permettant l'automatisation de cette tâche.

Les microbulles utilisées dans cette thèse ont été fabriquées à Orléans par l'équipe du Pr Chantal Pichon, Dr Anthony Delalande et Thomas Ador. Trois types de microbulles ont été caractérisés, des microbulles avec une couche lipidique neutre, une couche biotinylée permettant une fonctionnalisation des microbulles et une couche cationique. Grâce au détecteur passif de cavitation (PCD) et à un système de mesure de la cavitation acoustique qui a été développé. Nous avons pu caractériser la réponse acoustique des différents types de microbulles en fonction de la pression ultrasonore, des durées d'applications, de leur concentration, ainsi que des différences entre les couches des trois types de microbulles.

Un premier algorithme a aussi été mis en place afin de caractériser la cavitation acoustique lors d'une perméabilisation large de la barrière hémato-encéphalique. Cette méthode a été testée sur plusieurs animaux implantés au préalable avec une tumeur F98. La corrélation entre les index SCD et ICD n'a pas encore démontré de résultats satisfaisants et une étude plus approfondie permettra de mettre en place complètement ce protocole afin par la suite de contrôler le temps d'application des FUS ainsi que les pressions ultrasonores.

L'utilisation du transducteur ultrasonore dans le système de guidage IRM des FUS fournit par l'entreprise IGT avec l'utilisation des microbulles de gaz a permis de valider l'ouverture de la BHE et le bon guidage par IRM des FUS. En ce sens nous avons donc implémenté et utilisé différentes méthodes IRM (IRM de température, IRM-ARFI (acoustic radiation force imaging)) permettant de conforter le bon guidage des FUS. De plus, la sensibilité de l'antenne IRM actuellement placée dans le système FUS possède une mauvaise sensibilité, ainsi nous avons réalisé les premiers tests avec une nouvelle antenne pour améliorer le guidage des FUS en réduisant le temps d'acquisition et augmentant la résolution des images. Cette antenne reste à être intégrée complètement afin que son usage soit facilité pour les prochaines expériences.

La cinétique d'ouverture de la BHE a été caractérisée sur des souris Balb/cJR de 6 semaines et 18 g en réalisant l'acquisition de séquences IRM permettant la mesure du paramètre T1 et l'injection d'un agent de contraste de type gadolinium à différents temps après application des FUS (0, 30, 60 et 120 minutes). Afin de calculer la concentration apparente de gadolinium extravasé, nous avons repris la méthode d'une étude de Marty *et al*. [Marty *et al.*, 2012]. Des mesures similaires ont été réalisées avec un agent de contraste photo-acoustique et bioluminescent : le vert d'indocyanine. Cela a permis de

finaliser une étude présentant cet agent de contraste comme un rapporteur de la perméabilisation de la BHE en utilisant ou bien l'imagerie photo-acoustique ou bien la bioluminescence. Nous avons ainsi comparé cette nouvelle modalité d'agent de contraste à l'IRM et au gadolinium, aujourd'hui la méthode référence pour la caractérisation de l'ouverture de la BHE. Ainsi, nous avons pu mesurer que la durée après laquelle la concentration de gadolinium et l'intensité du vert d'indocyanine étaient divisées par 2. Ces durées s'élevaient à 33 minutes pour les 2 agents de contraste. Ces durées sont en accord avec la littérature, bien que plus basses. En effet des pressions ultrasonores moins importantes ont été utilisées ce qui induit une perméabilisation moins longue de la BHE. Ces derniers résultats font partie d'une publication soumise dans le journal *iScience*.

Au cours de cette thèse, plusieurs types d'ouverture de la BHE ont été réalisés : une perméabilisation restreinte de la BHE permettant de viser des structures précises et une perméabilisation plus large sur plusieurs régions du cerveau ou sur le cerveau entier. Ces deux protocoles ont été validés chez le rat et la souris en optimisant les paramètres de la séquence ultrasonore et les pressions acoustiques. Ces travaux ont été présentés avec un poster à la 6^{e} SFRMBM.

L'IRM a été largement utilisée tout au long de la thèse afin de caractériser les effets de la perméabilisation de la BHE par FUS. Plusieurs méthodes IRM ont été utilisées et le traitement de ces images a été majoritairement réalisé sur le logiciel MP3 [Brossard *et al.*, 2020]. Parmi celles-ci, des images pondérées T2 pour évaluer la sécurité de l'ouverture (présence d'œdème et/ou d'hémorrhagies), plusieurs méthodes pour évaluer la perméabilité de la BHE (images pondérées T1, carte T1, suivi de bolus de gadolinium), une méthode pCASL (pseudo-continuous arterial spin labelling) permettant l'acquisition de carte de perfusion sans agent de contraste [Hirschler *et al.*, 2018], un protocole d'IRM multiparamétrique permettant de reconstruire des cartes de fraction de volume sanguin, de diffusion, de rayon moyen des vaisseaux sanguins, de saturation en oxygène des tissus et de taux métabolique d'oxygène cérébral. Enfin, l'utilisation d'une approche en IRM dite "fingerprint" permettant de réduire drastiquement le temps d'acquisition pour reconstruire notamment des cartes d'estimation de l'oxygénation cérébrale a permis de caractériser les effets à long-terme de la perméabilisation répétée de la BHE par FUS.

Enfin, de nombreux marquages histologiques (hématoxyline et éosine) et immunohistologiques ont été réalisés afin de caractériser l'inflammation et la vascularisation cérébrale. Les images acquises au microscope ont nécessité le développement d'outils de traitement d'image.

5. Résumé de l'étude 1 : La perméabilisation de la BHE par FUS entraîne une diminution transitoire de la perfusion et une inflammation sans lésion cérébrale aiguë ou chronique

Cette étude avait pour objectif d'étudier les modifications vasculaires qui survenaient à la suite de la perméabilisation de la BHE par FUS. La perméabilisation de la BHE a été réalisée avec un contrôle de la cavitation après traitement des signaux acoustiques ultérieurement. Nous avons mesuré en IRM, après perméabilisation de la BHE, avec une méthode sans agent de contraste appelée pCASL et développée récemment au laboratoire la perfusion cérébrale et avec un agent de contraste à base de fer la fraction de volume sanguin, représentant la quantité de sang présent dans chaque voxel. Des analyses *post mortem* sur le cerveau des rats ont été réalisée afin d'évaluer l'impact cellulaire de cette ouverture. Les résultats préliminaires de cette étude ont été présentés dans le congrès international ISTU puis l'étude a été publiée dans le journal *Theranostics* [Rigollet *et al.*, 2024c].

Les FUS combinés à une injection intravasculaire de microbulles de gaz permet une ouverture contrôlée et réversible de la BHE. Cependant, les effets précis sur les tissus cérébraux et la vascularisation après la perméabilisation de la BHE n'ont pas été pleinement explorés, ce qui limite la translation de ces méthodes en clinique en toute sécurité. Les premières études de Hynynen *et al*. [Hynynen *et al*., 1996] à la fin des années 1990 ont démontré que des FUS à haute puissance (6000 à 7000 W/cm²) sans l'utilisation de microbulles contractaient substantiellement l'artère fémorale, réduisant le flux sanguin de 50%. Un retour à l'état initial s'est produit en une semaine, bien que parfois accompagné de saignements localisés. Gao *et al*. ont étudié les effets vasculaires des microbulles couplées à des FUS de haute intensité à 4,6 MPa sur le foie avec une échographie de contraste. Ils ont conclu que cela pouvait temporairement bloquer ou réduire la perfusion hépatique chez les lapins, avec un retour à une perfusion normale en une heure [Gao *et al*., 2012]. Cho *et al*. ont surveillé la dynamique cérébro-vasculaire dans le cortex en utilisant la microscopie intra-vitale après la perméabilisation de la BHE avec des pressions allant de 0,071 MPa à 0,25 MPa, révélant une vasoconstriction ou une vasodilatation dans un petit nombre de cas [Cho *et al*., 2011]. En résumé, ces résultats suggèrent que la perméabilisation de la BHE par FUS pourrait affecter le flux sanguin cérébral (CBF).

D'autres rapports corroborent cette hypothèse. Après la stimulation de la patte arrière et la perméabilisation de la BHE dans le cortex somato-sensoriel droit, des mesures d'IRM en marquage de spin artériel (ASL) ont révélé une diminution significative des changements de CBF dans le cortex somato-sensoriel droit par rapport au gauche [Todd *et al*., 2019]. Plus récemment, Stupar *et al*. [Stupar *et al*., 2018] et Labriji *et al*. [Labriji *et al*., 2023] ont rapporté une diminution du CBF à la suite de la perméabilisation de la BHE, respectivement par FUS et par ultrasons non focalisés, en utilisant des microbulles à environ 0,38 MPa. Il est donc pertinent de se demander si la réduction du CBF se produit également lorsque la perméabilisation de la BHE est effectuée pour l'administration de médicaments au cerveau.

Nous avons émis l'hypothèse que l'ouverture de la BHE médiée par FUS pourrait entraîner des modifications significatives de la perfusion cérébrale, déclenchant ainsi des mécanismes cellulaires pour réparer la BHE.

L'objectif principal de cette étude était de mesurer et de comparer les changements de perfusion cérébrale à différents moments après la perméabilisation de la BHE par FUS. La cavitation acoustique a été surveillée pour évaluer la sécurité de la procédure et évaluer l'énergie déposée dans le cerveau. L'IRM a été utilisée pour quantifier le CBF et la fraction de volume sanguin (BVf) dans les régions cérébrales ciblées à 30, 60, 90 minutes et 24 heures après les FUS. Les changements histologiques dans le tissu cérébral ont été examinés en se concentrant sur les marqueurs de neuroinflammation, l'intégrité des vaisseaux et les signes d'hémorragies ou d'œdèmes. Cette analyse a été réalisée pour détecter toute altération structurelle ou cellulaire résultant de la perméabilisation de la BHE.

5.1. Eléments de méthode

Le protocole expérimental a été validé par le comité éthique local ainsi que le Ministère français de l'enseignement supérieur et de la recherche sous le numéro APAFIS #43777. Cette étude a été réalisée sur 37 rats mâle de la souche Wistar Han avec un âge moyen de 7 semaines et un poids situé entre 270 et 350 grammes au moment de la perméabilisation de la BHE. La perméabilisation de la BHE a été réalisée avec les microbulles neutres et sous guidage IRM afin de focaliser l'énergie des FUS précisément dans des régions précises du cerveau. Le guidage IRM sur le logiciel Thermoguide® (IGT, Pessac, France) inclut l'acquisition de 2 séquences pondérées T1 et d'une séquence plus haute résolution pondérée T2. Des impulsions ultrasonores de 50 ms à une pression de 0.6 MPa (estimée *in situ*) suivies de pauses de 950 ms ont été appliquées 60 fois. Pour délivrer la même pression ultrasonore pour chaque animal, celle-ci a été ajustée à chaque fois grâce à l'étape de calibration réalisée au préalable et la prise en compte de l'atténuation du crâne en fonction du poids de l'animal [Gerstenmayer *et al.*, 2018].

Le contrôle *a posteriori* de la cavitation a été réalisé avec le PCD situé au centre du transducteur (4). Basé sur la méthode publiée par Novell *et al*. [Novell *et al.*, 2020], nous l'avons adaptée pour notre application. L'IUD et l'IHD ont été calculés en considérant les fréquences suivantes, respectivement : $1.5 \times f_0$, $2.5 \times f_0$, $3.5 \times f_0$, et $2 \times f_0$, $3 \times f_0$, $4 \times f_0$ avec une bande passante de 50 kHz. Chaque impulsion ultrasonore de 50 ms a été découpée en 247 fenêtres de 200 µs sans tenir compte des 200 premières et 400 dernières microsecondes. Une transformée de Fourier rapide a été réalisée séparément pour chaque fenêtre avant de calculer les index IUD et IHD. Nous avons défini de façon empirique un seuil égale à 1,5 fois la valeur du premier index IUD nommé IUD_0 et avons à partir de celui-ci compté le nombre d'occurrences qui dépassait ce seuil pendant la totalité de la séquence FUS et avons discriminé trois niveaux de cavitation acoustique : léger, moyen et intense. Le cas léger a été considéré lorsqu'aucun événement ne dépassait le seuil de cavitation établi, le cas moyen lorsque la plupart des événements se situaient entre le seuil de bruit et que certains événements dépassaient le seuil, et le cas intense lorsque les événements dépassaient le seuil et que beaucoup d'entre eux étaient consécutifs et ce dernier était associé à de nombreuses extravasations de globules rouges.

Nous avons constitué 3 groupes différents : le premier pour étudier le CBF et le paramètre ADC à 30 minutes et 24 h après perméabilisation de la BHE, le second pour étudier l'évolution à court terme du CBF après perméabilisation de la BHE et le dernier pour étudier à 30 minutes le BVf. Toutes ces mesures ont été réalisées en IRM à 4.7 T. La perméabilisation de la BHE a été contrôlée avec l'injection d'un agent de contraste de type gadolinium entre 40 et 50 minutes après la fin de la séquence FUS. Les cerveaux ont été récupérés entre 24 h et 7 jours après perméabilisation de la BHE afin d'évaluer avec des marquages histologiques le développement de l'inflammation cérébrale avec les marqueurs

astrocytaires GFAP et microgliaux Iba1, ainsi qu'un marqueur de la BHE SMI71. La sécurité des ouvertures a été observée avec des marquages H&E.

5.2. Principaux résultats

La perméabilisation de la BHE a été effective chez tous les animaux. Seuls les animaux pour lesquels nous avons suivi l'évolution du CBF n'ont pas reçu une injection d'agent de contraste car la BHE était déjà refermée à la fin des mesures de CBF. L'augmentation du contraste dans la zone traitée a été en moyenne égale à 19%. Pour les animaux perméabilisés dans le cortex, 5% de ce dernier a été perméabilisé tandis que pour les animaux ayant reçu les FUS au niveau du striatum, 30% de ce dernier a été perméabilisé. Sur les 20 animaux suivis en cavitation, un seul a reçu une dose ultrasonore trop importante caractérisée par de nombreux saignements et des valeurs d'IUD dépassant très largement le seuil fixé. Une corrélation entre le pourcentage d'évènements dits inertiels et d'évènements inertiels consécutifs a été faite avec un $R^2 = 0.92$.

30 minutes après ouverture de la BHE par FUS, nous n'avons pas mesuré de différences dans les valeurs d'ADC. Pour le CBF, une baisse significative de 54% a été mesurée dans le cortex perméabilisé (ipsilatéral) en comparaison au cortex controlatéral et une basse significative de 38% a été mesurée dans le striatum ipsilatéral en comparaison au controlatéral. 24 h après, aucune différence significative n'a été observée entre les hémisphères ipsilatéraux et controlatéraux.

Dans le deuxième groupe, nous avons mesuré l'évolution à court terme à 30, 60 et 90 minutes du CBF après une perméabilisation dans le cortex. Des différences significatives à 30 et 60 minutes ont été mesurées. A 90 minutes, le test statistique ne donne plus de différence significative mais le CBF est encore légèrement diminué dans le cortex ipsilatéral ($p = 0.0547$, $CBF_{ipsi} = 117.2 \pm 44.9$ and $CBF_{contro} = 164.2 \pm 36.2$ mL/min/100g). 24 h après, plus aucune différence n'est visible et nous avons comparé les valeurs trouvées dans la littérature sans différence non plus. La mesure du BVf 30 minutes après perméabilisation de la BHE dans le cortex a montré des différences avec un diminution significative dans le cortex ipsilatéral comparé au controlatéral. Pour le striatum, seuls trois animaux ont été utilisés et nous observons aussi une tendance à la baisse de ce paramètre dans le striatum ipsilatéral.

L'expression de GFAP et Iba1 a été analysée en immunohistologie entre 1 et 7 jours au niveau de la zone ipsilatérale comparée à la zone controlatérale. Des différences significatives à 2 et 3 jours après perméabilisation de la BHE ont été mesurées démontrant une forte activation astrocytaire dans la zone perméabilisée. Plus aucune différence n'était observée 7 jours après. Pour le marqueur de la microglie, Iba1, une différence significative a été observée 24 h après la perméabilisation de la BHE. 2 et 3 jours après, plus aucune différence n'était observée. Ainsi nous avons observé une activation astrocytaire et microgliale transitoire au niveau de la zone perméabilisée.

5.3. Conclusion

Comprendre les effets secondaires associés à l'ouverture de la BHE induite par FUS est crucial pour développer des stratégies thérapeutiques efficaces qui reposent sur une administration localisée de médicaments au cerveau. Dans notre étude, nous avons observé que, malgré l'absence de dommages tissulaires importants, le flux sanguin et le volume sanguin étaient significativement réduits pendant au moins une heure dans une région étendue entourant la zone d'ouverture de la BHE. Bien que la perfusion se soit normalisée dans les 24 heures suivant le traitement par FUS, une inflammation

transitoire a persisté pendant plusieurs jours dans le tissu ciblé. De plus, nous avons introduit une méthode pour surveiller l'état de cavitation des microbulles pendant le traitement FUS, renforçant ainsi la robustesse de nos expériences.

L'ouverture de la BHE a été réalisée avec une surveillance en temps réel de la cavitation et des microbulles lipidiques faites maison. Nous avons choisi une configuration expérimentale avec des microbulles et un indice mécanique similaire à ceux utilisés dans des études précédentes [Chu *et al*., 2016 ; Wu *et al*., 2018], et toutes les procédures ont abouti à une ouverture de la BHE. Avec cette configuration, 95 % des procédures d'ouverture de la BHE n'ont entraîné ni œdème ni saignement, comme évalué par IRM. Il est à noter que la quantification des événements de cavitation inertielle à l'aide de l'IUD a permis de différencier les animaux ayant subi un traitement FUS excessif et développé des lésions de ceux qui n'en ont pas eu. Bien que ce ne fût pas l'objectif principal de l'étude, ces résultats sont encourageants et méritent d'être approfondis, notamment avec un plus grand nombre d'animaux pour démontrer le potentiel de cette approche. Des développements futurs devraient inclure un contrôle en boucle fermée de la cavitation pour prévenir les lésions. Par conséquent, la sécurité de la procédure d'ouverture de la BHE pourrait être améliorée, améliorant ainsi les résultats chez les animaux [Kamimura *et al*., 2019].

Pour mieux comprendre l'origine de cette réduction du CBF, nous avons également mesuré le volume sanguin fractionnaire (BVf) 30 minutes après le FUS. Le BVf a été réduit de seulement 15 % par rapport à 50 % dans le modèle d'AVC. Une réduction du diamètre des vaisseaux après le FUS, en ligne avec une réduction du BVf, a déjà été observée à l'aide de la microscopie bi-photon [Raymond *et al*., 2007]. Une réduction plus importante du flux sanguin que du volume sanguin peut s'expliquer par une réduction du flux entrant dans la zone observée. Fait intéressant, les réductions de CBF et de BVf étaient spatialement homogènes, suggérant que tous les vaisseaux de la zone ont subi une vasoconstriction, qui pourrait avoir été plus prononcée au niveau des plus grandes artères nourricières. De plus, la zone dans laquelle les paramètres de perfusion étaient réduits s'étendait au-delà de la cible du FUS, comme en témoignent l'extravasation de l'agent de contraste. Cela s'est produit lorsque la cible était dans le cortex (l'ensemble du cortex présentait une perfusion réduite) et lorsqu'elle se trouvait dans le striatum (l'ensemble du striatum est devenu hypo-perfusé). Ce décalage spatial entre l'extension de la cible ultrasonore et celle de la réduction de la perfusion a déjà été rapporté dans la littérature, sans utilisation d'un transducteur focalisé ou de surveillance de la cavitation [Labriji *et al*., 2023].

L'origine de cette divergence pourrait être attribuée à une vasoconstriction rétroactive, basée sur le mécanisme de vasodilatation rétroactive décrit par Schaeffer et Iadecola [Schaeffer et Iadecola, 2021]. Un autre mécanisme pourrait être les dépressions corticales propagées lentement décrites par Leaõ [Leao, 1944], qui ont été rapportées après un traumatisme crânien (TBI) [Strong *et al*., 2002] et un AVC [Hossmann, 1996 ; Hartings *et al*., 2011]. En résumé, même en l'absence de cavitation des microbulles et d'utilisation d'un transducteur focalisé, une réduction transitoire de la perfusion se produit et s'étend au-delà de la cible du FUS. Cette réduction ne conduit pas à un œdème tissulaire, comme contrôlé à l'aide de l'ADC. Des expériences supplémentaires, telles que la microscopie de localisation ultrasonore transcrânienne [Errico *et al*., 2015] ou l'enregistrement de l'activité électrique corticale [Masvidal-Codina *et al*., 2019], pourraient être menées pour mieux caractériser la réduction de la perfusion cérébrale qui survient après le FUS.

Au niveau cellulaire, certains changements sont survenus au cours des trois premiers jours suivant le FUS. Nous avons quantifié un pic d'activation astrocytaire au troisième jour après l'ouverture de la

BHE, un résultat très similaire à celui rapporté par Jordão *et al*. [Jordão *et al*., 2013]. De plus, une augmentation significative du recrutement des microglies a été observée, suggérant que le rôle neuroprotecteur du système nerveux central a été déclenché. Le pic d'activation a été observé au premier jour après le FUS. En revanche, plusieurs études passées en revue par Todd *et al*. [Todd *et al*., 2020] ont rapporté des activations à 1, 6 et 24 heures après l'ouverture de la BHE. Tant les astrocytes que les microglies sont revenus à des niveaux normaux une semaine après le FUS. Il est important de noter que cette neuroinflammation n'a été observée que dans la cible du FUS et n'a pas été observée dans la zone étendue où la perfusion était réduite. Cela suggère que l'inflammation est déclenchée par l'ouverture de la BHE. Cependant, il ne peut être exclu que la réduction de la perfusion contribue également à cet effet.

En extrapolant nos résultats aux humains, une différence clé réside dans le fait que notre étude a été menée sous anesthésie, ce qui réduit le taux métabolique cérébral de l'oxygène [Schoknecht *et al*., 2023]. De plus, l'anesthésie à l'isoflurane tend à augmenter le CBF. Étant donné qu'une diminution de la demande en oxygène et une augmentation de l'apport en oxygène peuvent conférer une certaine protection contre une réduction de la perfusion, notre étude pourrait sous-estimer les conséquences de la réduction de perfusion induite par le FUS. À l'inverse, il a été rapporté que l'ouverture de la BHE induite par FUS entrave temporairement la conduction axonale, réduisant ainsi l'activité neuronale et protégeant potentiellement le tissu contre une diminution de la perfusion [Chu *et al*., 2015]. D'autres investigations pourraient impliquer des études sur des animaux éveillés ou employer des protocoles d'anesthésie qui fournissent des valeurs de CBF similaires à celles observées dans l'état éveillé. Compte tenu de la réduction du flux sanguin et de l'absence d'altération des vaisseaux sanguins, il serait également intéressant d'explorer si des processus angiogéniques sont déclenchés, comme suggéré par Kovacs *et al*. [Kovacs *et al*., 2017]. Cela pourrait également impliquer une évaluation de l'expression de HIF-1a ou VEGF, peu de temps après le FUS.

En résumé, l'ouverture de la BHE induite par FUS provoque une vasoconstriction diffuse au-delà de la zone ciblée, entraînant une réduction transitoire du CBF et du BVf. Cependant, cette réduction est insuffisante pour causer des lésions tissulaires dans notre configuration expérimentale. Bien que des marqueurs transitoires d'inflammation tissulaire puissent être observés au niveau de la zone ciblée par le FUS, ils ne sont pas observés en dehors de cette zone. Ces résultats soulignent la nécessité de prendre en compte avec prudence la perfusion tissulaire lors de la transposition de l'ouverture de la BHE induite par FUS à des applications humaines.

6. Résumé de l'étude 2 : Suivi longitudinal en IRM vasculaire Fingerprint pour un suivi des changements physiologiques au cours de l'ouverture répétée de la BHE par FUS guidés par RM chez le rat

Dans la première étude, nous avons démontré qu'un seul traitement par FUS entraînait des modifications transitoires et significatives de la perfusion, ainsi qu'un processus neuroinflammatoire transitoire avec l'activation des astrocytes et de la microglie. Ces modifications transitoires n'ont pas provoqué d'effets secondaires dans le cerveau ni de perturbations comportementales chez les animaux.

Cependant, en tant qu'application unique des FUS, l'utilisation répétée des FUS pour perturber la BHE est associée à des mécanismes secondaires et à des effets secondaires potentiels. Le stress mécanique et la rupture subséquente de la BHE peuvent déclencher une cascade de réponses biologiques au sein de l'UNV, notamment des mécanismes de réparation, une inflammation et des modifications vasculaires, comme développé dans la section **Error! Reference source not found.**.

Des études récentes ont commencé à approfondir ces effets biologiques en étudiant les effets cumulatifs sur le tissu cérébral et la santé neurovasculaire [Kovacs *et al*., 2018 ; Sinharay *et al*., 2019], avec l'étude de la neuroinflammation associée à une perméabilisation répétée de la BHE par FUS. En outre, Olumolade *et al*. ont analysé les changements comportementaux potentiels liés à la répétition du BBB et n'ont constaté aucun effet négatif sur l'activité locomotrice des animaux traités [Olumolade *et al*., 2016]. Les limites de ces études récentes sont au nombre de trois : premièrement, les pressions utilisées dans les études de Kovacs *et al*. et de Sinharay *et al*. ne semblent pas très adaptées pour délivrer des molécules thérapeutiques en raison des zones hypo-intenses visible IRM après la perméabilisation ; deuxièmement, les temps auxquels les analyses histologiques ont été réalisées fournit peu d'explications, ce qui rend difficile la comparaison avec d'autres études ; enfin, Olumolade *et al*. ont administré des FUS toutes les deux semaines ou tous les mois, ce qui semble être un planning adapté pour les applications cliniques [Carpentier *et al*, 2024 ; Epelbaum *et al*., 2022 ; Idbaih *et al*., 2019 ; Sonabend *et al*., 2023], mais pour les études précliniques, cela peut être trop long compte tenu de la propagation de certains modèles de maladie (par exemple, la survie médiane dans le modèle de glioblastome de rat F98 est d'environ 20 à 30 jours après l'implantation, contre 15 mois chez l'homme), de sorte que nous devons étudier l'utilisation de calendriers plus condensés.

Ainsi, les mécanismes sous-jacents de l'ouverture répétée de la BHE ne sont pas entièrement compris, car il existe très peu de littérature sur le sujet, et les effets à long terme de cette nouvelle thérapie restent un sujet de recherche en cours, en particulier en ce qui concerne la microvascularisation du cerveau, qui n'a pas encore été étudiée.

Sur la base de cette littérature, nous avons émis l'hypothèse que l'ouverture répétée de la BHE par FUS pourrait conduire à des changements significatifs dans différents systèmes, tels que le système microvasculaire et le processus de neuroinflammation.

Pour combler ces lacunes, nous proposons dans cette étude d'évaluer longitudinalement les effets de l'ouverture répétée de la BHE induite par FUS sur le système vasculaire cérébral de rats sains. La perméabilisation de la BHE a été réalisée à l'aide de paramètres FUS connus pour être sûrs [Chu *et al*.,

2016] et pour délivrer efficacement des agents thérapeutiques tels que l'aducanumab, le carboplatine ou des polymères encapsulant la camptothécine et la doxorubicine [Kong *et al*., 2022 ; McDannold *et al*., 2019 ; Sun *et al*., 2023]. Les traitements FUS ont été administrés soit une fois, soit une fois par semaine, soit deux fois par semaine pendant quatre semaines. Deux pressions différentes ont été utilisées pour évaluer les effets de l'augmentation de la pression acoustique sur le système microvasculaire. Nous avons utilisé l'IRM pour mesurer la perfusion cérébrale, la diffusion de l'eau avec le paramètre ADC, la perméabilité de la BHE et une approche d'empreinte IRM pour évaluer quantitativement le rayon moyen des vaisseaux, la saturation en oxygène et la fraction de volume dans le cerveau du rat. Après le dernier traitement FUS guidé par RM, les cerveaux ont été analysés pour évaluer les effets cellulaires à l'aide de marqueurs de la barrière hémato-encéphalique et des cellules environnantes.

6.1. Éléments de méthode

Le protocole expérimental a été validé par le comité éthique local ainsi que le Ministère français de l'enseignement supérieur et de la recherche sous le numéro APAFIS #43777. Cette étude a nécessité l'utilisation de 50 rats mâles de la souche Wistar Han répartis en 3 groupes principaux : un groupe ne recevant qu'un seul traitement par FUS et microbulles, un groupe recevant 4 traitements FUS sur 4 semaines et un dernier groupe recevant 8 traitements FUS sur 4 semaines. Deux pressions ultrasonores différentes ont été testé pour chacun des groupes afin d'en évaluer l'impact à long terme. Un protocole d'IRM multiparamétrique permettant de mesurer les paramètres présentés précédemment dans le résumé général des méthodes (4) a été acquis à la suite de la perméabilisation de la BHE par FUS. Le protocole d'ouverture de BHE comprenait un guidage IRM, l'injection de microbulles avec une couche neutre et l'application d'un balayage sur 4 mm par 3.8 mm du transducteur ultrasonore afin de perméabiliser la BHE au niveau du striatum et de l'hippocampe. Une zone assez large a été choisie afin d'étudier l'effet de la perméabilisation répétée de la BHE sur le tissu sain. Les cerveaux ont été récupérés une semaine après les traitements répétés pour des analyses histologiques.

6.2. Résultats

Aucun des animaux utilisés pendant cette étude n'a vu son comportement atteindre les points limites au préalable établi et validés par le comité éthique. Le poids des animaux a été en constante augmentation et aucune lésion n'a été décelée après la perméabilisation de la BHE chez tous les animaux étudiés sur les images pondérées T2. Les analyses histologiques n'ont pas non plus montré de microhémorragies, en particulier un groupe de 4 animaux qui a été analysé 3 h après la perméabilisation de la BHE en marquage H&E n'a pas montré de signe de microhémorragies.

La perméabilisation répétée de la BHE a été très bien maîtrisée avec un volume conséquent perméabilisé. La répétabilité du traitement a été très bonne grâce au guidage IRM des FUS. Concernant la perméabilité vasculaire, grâce au suivi de bolus de gadolinium en IRM, nous avons pu mesurer les paramètres d'augmentation du contraste et de temps pour atteindre le maximum de contraste. Une diminution significative de ce dernier paramètre a été mesurée après 4 perméabilisations de la BHE pour le groupe ayant reçu deux traitements par semaine pendant 4 semaines, et ceci pour les deux pressions testées. Ceci démontre une BHE plus perméable du fait de la répétition du traitement.

Concernant les modifications vasculaires, une baisse significative du CBF a été observée dans l'hémisphère traité en comparaison à l'hémisphère controlatéral 30 minutes après une

perméabilisation de la BHE. Pour les groupes qui ont reçu plusieurs traitements successifs, une baisse a été observée après chaque traitement FUS. Les cartes reconstruites avec l'approche en IRM fingerprint nous ont permis de mesurer une augmentation significative du rayon moyen des vaisseaux après 2 et 6 traitements pour le groupe ayant reçu 8 traitements à la pression la plus élevée (440 kPa). Aucune modification de la fraction de volume sanguin n'a été mesurée mais une diminution significative de l'oxygénation a été observée dans la région traitée après 6 et 8 traitements FUS à la pression de 390 kPa.

La reconstruction de carte de susceptibilité magnétique a permis aussi de vérifier que l'ouverture répétée de la BHE par FUS en combinaison à l'injection d'agent de contraste à base de fer n'a pas induit des dépôts importants au niveau de la zone perméabilisée. Nous n'avons pas mesuré de différences significatives dans les régions traitées en comparaison aux régions controlatérales sur les cartes de susceptibilité magnétique, ni en séparant les contributions dia- et paramagnétiques de ces cartes.

Les résultats en immunohistologie ont démontré qu'une semaine après le dernier traitement FUS pour le groupe ayant reçu 4 traitements à 440 kPa aucune différence significative au niveau de l'expression du marqueur astrocytaire GFAP et d'un marqueur de la BHE dans la zone traitée. Pour le groupe ayant reçu 8 traitements à 440 kPa, une augmentation significative dans l'expression de GFAP est toujours visible au niveau de la zone traitée. De même nous avons observé une augmentation de la taille des vaisseaux sanguins dans la zone traitée, suggérant que l'augmentation du rayon moyen des vaisseaux dans la zone traitée mesurée en IRM une semaine auparavant se confirme en histologie. Ceci suggère que les vaisseaux ont subi des modifications qui ne se sont pas résorbées une semaine après le denier traitement.

6.3. Discussion et conclusion

Comme il existe un manque d'études ayant réalisé des ouvertures répétées de la BHE avec un contrôle précis de l'ouverture, nous avons appliqué à plusieurs reprises des FUS pour perméabiliser la BHE dans une grande zone du cerveau une ou deux fois par semaine pendant 4 semaines. Deux pressions acoustiques différentes ont été utilisées pour évaluer l'impact de l'augmentation de la pression (MI : 0,32 et 0,37). Ces indices mécaniques sont connus pour être suffisants pour délivrer des agents thérapeutiques tout en étant suffisamment faibles pour ne pas induire de lésions [Chevaleyre *et al.*, 2023 ; Dréan *et al.*, 2019 ; McDannold *et al.*, 2019]. La répétabilité et la précision de l'ouverture de la BHE ont été très bonnes tout au long des sessions de traitement, grâce au dispositif FUS guidé par IRM. Nous n'avons observé aucune lésion (saignement, œdème) dans aucun des groupes ni durant aucune des sessions.

7. Résumé de l'étude 3 : Amélioration de la survie dans un modèle rat F98 en associant les FUS, le carboplatine et la radiothérapie

Le glioblastome est la tumeur cérébrale maligne la plus fréquente et son incidence mondiale est en constante augmentation, avec 3 cas pour 100 000 personnes en 2018, alors qu'elle était de 2,1 dix ans plus tôt [Darlix *et al.*, 2017]. Cette tumeur est caractérisée par sa capacité d'infiltration des tissus sains, et son pronostic est extrêmement sombre puisque la survie médiane des patients n'excède pas 15 mois malgré des traitements agressifs. Le GBM se présente comme une tumeur organisée à l'intérieur du cerveau dont le centre est éventuellement nécrotique et associé à une infiltration extrêmement diffuse autour de la tumeur avec des cellules tumorales isolées. L'angiogenèse tumorale, due à l'augmentation de facteurs pro-angiogéniques [Jain, 2014], entraîne la formation de vaisseaux sanguins dépourvus d'une structure physiologique normale nommée la barrière hémato-tumorale (BHT).

Le protocole de soin comprend généralement une résection chirurgicale maximale de la tumeur, suivie par des sessions de radiothérapie et de chimiothérapie concomitante et adjuvante par témozolomide [Stupp *et al.*, 2005]. La radiothérapie a apporté un bénéfice sur la survie globale [Walker *et al.*, 1979] des patients mais ne permet pas un contrôle suffisant du glioblastome. Celle-ci agit sur les cellules grâce à l'énergie déposée lors des interactions entre les rayons X et les tissus. Cependant, bon nombre de cellules tumorales sont radio-résistantes et se trouvent disséminées au sein du cerveau. Coupler cette radiothérapie à l'injection intraveineuse de chimiothérapies telles que le carboplatine, agent alkylant se fixant sur l'ADN et inhibant sa réplication, permet d'augmenter le contrôle de nombreux cancers tout en conservant une toxicité acceptable [Curran *et al.*, 2011 ; Lacas *et al.*, 2021]. La BHT permet l'extravasation de larges molécules [Kodack *et al.*, 2017]. Cependant cette perméabilité est très hétérogène aux petites et larges molécules tout comme la perfusion ce qui mène à une accumulation sous-optimale des agents thérapeutiques au sein de la tumeur. La délivrance de molécules reste à ce jour peu contrôlée et insuffisante [Arvanitis *et al.*, 2020, 2018]. Au cours des dernières années, plusieurs études menées par Elleaume *et al*., ont démontré des résultats spectaculaires, avec jusqu'à 60% de rats long survivants après une administration intra-cérébrale de carboplatine couplée à la radiothérapie, sur un modèle de GBM (F98) implanté chez le rat [Bobyk *et al.*, 2012 ; Elleaume *et al.*, 2020]. Du fait du caractère invasif de cette procédure, cette approche n'a pas pu être amenée en clinique.

Plusieurs facteurs limitent aujourd'hui la progression des traitements du GBM. Premièrement, la résection complète est impossible à cause du caractère infiltrant du GBM et de la proximité d'aires fonctionnelles du cerveau, ce qui conduit à la récidive de la tumeur dans les mois suivant la chirurgie. Deuxièmement, l'efficacité de la radiothérapie est limitée par sa localisation et limite fortement la dose de rayons X délivrable à la tumeur en raison des potentiels dommages au tissu cérébral sain environnant qui s'associeront à des effets secondaires allant de simples céphalées aux déficits neurologiques majeurs. Finalement, la BHE et la BHT limitent le passage d'agents radio-sensibilisants qui permettraient d'augmenter la dose de rayons X reçue dans la tumeur tout en préservant les tissus sains environnant.

En ce sens, l'utilisation des FUS guidés par IRM pour la perméabilisation de la BHE associé à l'injection intravasculaire de carboplatine et à la radiothérapie permettrait d'améliorer de manière significative la survie des patients et le contrôle de la croissance tumorale. Plusieurs études ont déjà évalué la

faisabilité et l'efficacité de la délivrance de carboplatine dans des modèles murins [Dréan *et* al., 2019 ; McDannold *et al*., 2019] et chez l'homme avec les travaux du Pr Carpentier [Carpentier *et al*., 2024 ; Idbaih *et al*., 2019].

Nous nous proposons donc d'évaluer cette nouvelle combinaison de traitement dans un modèle de glioblastome chez le rat afin d'évaluer la biodistribution du carboplatine et l'efficacité sur la survie des rongeurs. Un suivi en IRM a été réalisé afin d'étudier au mieux l'impact de ce traitement sur la croissance tumorale.

7.1. Éléments de méthode

Le protocole expérimental a été validé par le comité éthique local ainsi que le Ministère français de l'enseignement supérieur et de la recherche sous le numéro APAFIS #48225. Pour cette étude, 75 rats mâles Fischer 44 ont été implanté de façon stéréotaxique dans le noyau caudé droit avec 1000 cellules F98 (passage n°13). Entre 12 et 15 jours après l'implantation, le passage en IRM des animaux a permis de créer des groupes de traitements homogène en termes de taille de tumeur. Le volume de la tumeur était en moyenne au moment du traitement égal à 23 mm^3. Deux études en parallèle ont été réalisées, la première visant à évaluer la biodistribution du carboplatine 1 h et 24 h après la perméabilisation de la BHE, et la deuxième pour évaluer le potentiel thérapeutique sur la survie et la croissance tumorale. Plusieurs techniques ont été utilisées pour évaluer la biodistribution : la méthode de laser ablation ICP-MS pour mesurer précisément la concentration de platine dans les tissus et des méthodes d'imagerie avec la spectrométrie d'émission atomique de plasma induit par laser (LIBS) pour obtenir des informations spatiales. Avec la tomographie à contraste de phase et l'histologie nous évaluerons les effets du traitement sur les tissus. Pour le groupe en survie, 4 groupes ont été considérés (groupe contrôle, groupe ne recevant que la radiothérapie, groupe recevant les FUS et le carboplatine et un groupe recevant la combinaison FUS, carboplatine et radiothérapie). Le CBF, l'ADC et la perméabilité vasculaire ont été mesuré en IRM de manière hebdomadaire afin de contrôler l'évolution tumorale.

La perméabilisation de la BHE a été réalisée sous guidage IRM en appliquant un balayage sur 8 × 8 mm^2 du transducteur ultrasonore afin de perméabiliser la BHE largement autour de la tumeur (définie comme les pixels hyper-intense en imagerie pondérée T2). Une pression de 470 kPa *in situ* a été délivrée en association aux microbulles à couche neutre. Le contrôle de la perméabilisation a été fait en IRM avec une injection de gadolinium. Le carboplatine a été injecté par la veine de la queue à une dose de 50 mg/kg. La radiothérapie a été délivrée 24 h après la perméabilisation de la BHE en délivrant 15 Gy sur une zone de 10 × 10 mm^2. Un guidage stéréotaxique après acquisition d'un scanner a permis un bon contrôle spatial de la dose délivrée.

7.2. Résultats

La BHE a été perméabilisée de façon reproductible pour chacun des animaux et le volume moyen perméabilisé était égal à 248 mm^3 entre les différents groupes sans différence significative. Une différence de contraste a été observée entre le cœur de la tumeur et la zone périphérique non tumorale. La quantification de l'extravasation du carboplatine en ICP-MS a montré que les FUS guidés par IRM ont permis une augmentation significative de la concentration de platine dans le cœur de la tumeur mais aussi dans la zone péri-tumorale en comparaison à l'hémisphère controlatéral et aux animaux contrôle n'ayant reçu que la dose de carboplatine sans FUS. Une diminution de la concentration en platine a été mesurée 24 h après l'injection de carboplatine et des FUS, cependant

grâce aux FUS la concentration de carboplatine reste plus élevée dans la zone perméabilisée en comparaison aux animaux sans BHE perméabilisée. Ceci suggère donc une bonne extravasation du carboplatine dans le cœur de tumeur qui persiste au moins 24 h, *i.e.* le moment de la séance de radiothérapie. L'acquisition des données en histologie, LIBS et contraste de phase sont encore à réaliser afin d'évaluer au mieux la distribution du platine dans le cerveau et les potentiels dommages tissulaires au niveau microscopique après la perméabilisation de la BHE.

Pour le groupe de survie, après l'implantation tous les rats ont pris régulièrement du poids. L'évolution a ensuite été différente d'un groupe à l'autre. Le groupe contrôle a rapidement vu la prise de poids s'atténuer et se stabiliser, la médiane de survie pour ce groupe était de 30 jours après implantation. Le groupe ayant reçu une dose de radiothérapie ont continué à prendre du poids avant que celui-ci se stabilise vers le 24^{e} jour après implantation. Ce groupe avait une médiane de survie de 42 jours. L'association des FUS au carboplatine ainsi que des FUS, du carboplatine et de la radiothérapie a induit une perte de poids plus ou moins importante en fonction des individus pendant une durée de 5 à 15 jours. Cette perte de poids a ensuite été compensée pour 4 des 8 rats du groupe ayant reçu les FUS et le carboplatine et pour 8 des 10 rats ayant reçu le traitement complet. La médiane de survie de ces groupes était de 30 et 60 jours, respectivement. Ainsi le pourcentage d'augmentation de la médiane de survie était de 40 et 100% pour les groupes ayant reçu une dose de radiothérapie et le traitement complet, contrairement à la combinaison FUS et carboplatine qui n'a pas permis d'améliorer leur survie. De plus le suivi longitudinal en IRM nous a permis de constater une importante diminution de la vitesse de la croissance tumorale après l'administration du traitement complet en comparaison aux contrôles et aux autres traitements.

7.3. Conclusion

Pour conclure, notre étude a démontré une survie accrue grâce à l'utilisation des FUS pour délivrer du carboplatine avant une séance de radiothérapie en comparaison aux contrôles, à la radiothérapie unique et l'association des FUS et du carboplatine sans radiothérapie. Aucune étude n'avait à ce jour étudié cette combinaison de traitement et seule une précédente étude combinant l'administration de carboplatine avec 2 sessions FUS avait démontré une augmentation significative dans ce modèle de tumeur murin très agressif. Ces résultats démontrent que l'association des FUS à la radiothérapie avec l'administration d'agent radio-sensibilisant pourrait devenir le traitement le plus efficace pour traiter les glioblastomes. L'utilisation d'algorithme de contrôle de la cavitation pour améliorer la perméabilisation de la BHE, augmenter la concentration locale de carboplatine et la sécurité de l'opération n'ont pas été utilisé ici mais serait important de mettre en place. De plus la perméabilisation répétée de la BHE n'a pas démontrée d'effets secondaires majeurs lorsque celle-ci est réalisée à une semaine d'intervalle chez le rat comme démontré dans l'étude 2 réalisée au préalable. Coupler l'ouverture répétée de la BHE avec un fractionnement de la dose de radiothérapie dans ce modèle devra être étudié afin de déceler si ce traitement est viable, améliore la survie des sujets sans augmenter la toxicité (qui semble accrue car nous avons observé de nombreux décès précoces) du traitement. Cette combinaison innovante pourrait complètement s'intégrer dans un planning de traitement en clinique et ainsi améliorer drastiquement le pronostic et le devenir des patients atteints par un glioblastome.

8. Résumé de l'étude 4 : Administration d'une thérapie génique dans le cerveau dans un modèle murin du syndrome de l'X-fragile

Cette étude a été initiée par l'équipe du Pr Chantal Pichon avec le Dr Anthony Delalande, le Dr Arnaud Menuet, le Dr Anthony Laugeray, Mylène Fournié et Thomas Ador, doctorant à Orléans. Ces travaux ont été réalisés en grande partie à Grenoble grâce au protocole développé pour la perméabilisation de la BHE sur le cerveau entier (voir 4). Ces travaux seront présentés plus largement dans la thèse de Thomas Ador, qui a majoritairement mené à bien ce projet.

Le syndrome de l'X fragile (FXS) est la forme héréditaire la plus courante de déficience intellectuelle et une des principales causes génétiques de troubles du spectre autistique. Il est causé par une mutation du gène *Fmr1*, situé sur le chromosome X. Chez les personnes atteintes de FXS, un segment d'ADN appelé répétition de tri-nucléotides CGG est étendu dans le gène *Fmr1*, ce qui conduit à son inhibition. Cette méthylation du promoteur *Fmr1* provoque l'inhibition du gène et la perte d'expression de son produit protéique, la protéine FMRP (fragile X mental retardation protein). FMRP joue un rôle crucial dans le développement et le fonctionnement du cerveau. Cette maladie touche environ 1 garçon sur 4000 et 1 fille sur 8000 [Crawford *et al.*, 2001 ; Visootsak *et al.*, 2005]. Les manifestations du FXS sont variables et dépendent du sexe, de l'âge, des effets génétiques de fond, des influences environnementales et des variations moléculaires. Plus couramment, le FXS est considéré comme un handicap "invisible", car les caractéristiques physiques sont souvent subtiles ou absentes. Il n'existe toujours pas de traitements pour le FXS, mais l'émergence d'un modèle animal dans lequel le gène *Fmr1* est inactivé a permis de développer et d'identifier différentes stratégies thérapeutiques.

Différentes approches thérapeutiques pour le FXS ont été développées et validées [Hagerman *et al.*, 2017] notamment par des essais cliniques [Watkins *et al.*, 2024]. L'une des approches les plus prometteuses est la thérapie génique, une stratégie thérapeutique potentielle visant à corriger ou à compenser le défaut génétique sous-jacent. Deux études ont montré une réactivation du gène *Fmr1* grâce à CRISPR/Cas9 [C.-Y. Park *et al.*, 2015 ; Xie *et al.*, 2016]. En outre, Chadman *et al*. ont démontré un passage efficace de *Fmr1* à travers la BHE avec une construction AAV-PHP.B [Chadman *et al.*, 2023] et Wong *et al*. ont montré une amélioration de différents phénotypes dommageables des souris $Fmr1^{KO}$, le modèle présentant les meilleures caractéristiques phénotypiques du FXS, en administrant une injection intrathécale de vecteurs viraux de type AAV [Wong *et al.*, 2023]. Ces études représentent l'une des approches thérapeutiques les plus encourageantes pour le traitement du FXS, bien que leur transfert en clinique reste très difficile. Cependant, le vecteur AAV-PHP.B n'est toujours pas approuvé par la FDA et des recherches supplémentaires doivent être menées afin de valider son utilisation en clinique [Hordeaux *et al.*, 2018]. Toutefois, l'utilisation d'autres vecteurs AAV, comme le vecteur AAV de type 9, a été validée par la FDA en mai 2019 pour le traitement de l'amyotrophie spinale de type 1 après les résultats concluants de trois essais cliniques (NCT01839656, NCT02193074 and NCT02386553) [Finkel *et al.*, 2016], et offre des solutions pour la thérapie génique dans les maladies rares. Cependant, la BHE empêche son passage. Récemment, la combinaison d'une injection d'AAV avec les FUS pour perméabiliser la BHE a montré des résultats prometteurs dans des modèles murins [Felix *et al.*, 2021 ; Owusu-Yaw *et al.*, 2024 ; Thévenot *et al.*, 2012] et dans un modèle de primate non-humain avec des effets secondaires limités [Blesa *et al.*, 2023].

Dans cette étude, nous nous proposons donc d'évaluer un protocole de thérapie génique virale pour le FXS par l'ouverture de la BHE par FUS sur des souris mâles adultes $Fmr1^{KO}$.

8.1. Éléments de méthode

Toutes les procédures expérimentales ont été validées par le Ministère français de la recherche et de l'éducation et par le comité d'éthique local sous les numéros APAFIS #43777, #47771 et #47394. 57 souris *Fmr1*^{KO} ont été utilisées dans cette étude et divisées en deux groupes. Le premier pour réaliser un suivi longitudinal de l'expression du transgène en bioluminescence et le second pour réaliser une étude comportementale. Deux vecteurs de thérapie génique ont été utilisés : AAV2/9.CMV.Luciferase codant pour le gène de la luciférase sous le promoteur CMV pour le suivi longitudinal de l'expression du transgène et AAV2/9.CMV.*Fmr1*-eGFP codant pour le gène *Fmr1*-GFP sous le promoteur CMV pour la réexpression du transgène et la restauration du phénotype comportemental. Le suivi en bioluminescence des souris ayant reçu uniquement le vecteur viral et de souris ayant reçu le vecteur viral après perméabilisation de la BHE a été réalisé de 2 à 8 semaines après l'injection du vecteur viral. Un suivi comportemental avec différents tests a été réalisé entre 3 et 8 semaines après l'administration du vecteur viral. Ces tests visaient à étudier l'impact de la thérapie sur l'hyperactivité, l'anxiété, les troubles obsessionnels-compulsifs, la sociabilité, l'apprentissage et la mémoire. Des analyses *ex vivo* ont été réalisées afin de quantifier l'expression du transgène dans le cerveau mais aussi d'autres organes (foie, reins, cœur, …) et d'examiner la distribution spatiale du transgène dans le cerveau en immunohistochimie. La BHE a été perméabilisée en utilisant un balayage du transducteur ultrasonore sur tout le cerveau afin d'en perméabiliser une large partie. La pression acoustique utilisée était de 370 kPa *in situ* et la séquence ultrasonore avait une durée égale à 90 secondes. Après perméabilisation, une imagerie pondérée T2 et T1 avec l'injection de gadolinium a permis de vérifier les potentiels dommages et la bonne perméabilisation de la BHE.

8.2. Résultats et conclusion

La BHE a été perméabilisée en moyenne sur 63% de la totalité du volume cérébral. L'ouverture de la BHE n'a pas entraîné de lésions visibles en IRM pondérée T2 et aucune différence n'a été mesurée entre les différents groupes étudiés. L'expression du transgène 8 semaines après l'injection du vecteur viral est significative dans les souris *Fmr1*^{KO} et sa distribution est assez homogène dans tout le cerveau. Néanmoins, l'expression du gène *Fmr1* dans les souris non traitées WT est 7 fois plus importante que dans les souris *Fmr1*^{KO} après perméabilisation de la BHE et injection du vecteur de thérapie génique. L'expression du transgène a montré une bonne stabilité entre 2 et 8 semaines après FUS grâce au suivi longitudinal en bioluminescence. Une différence significative a été mesurée 3 semaines après *in vivo* et *ex vivo* entre le groupe ayant reçu des FUS et le groupes sans FUS démontrant une expression du transgène dans le cerveau accrue grâce aux FUS. Dans les autres organes analysés, aucune différence n'a été observée.

L'analyse des résultats comportementaux, et plus particulièrement des tests de champ ouvert (activité motrice), d'enfouissement (anxiété) et d'interaction directe, ont démontré une restauration plus ou moins bonne du phénotype. Les souris *Fmr1*^{KO} ont tendance à parcourir significativement plus de distance lors du test de champ ouvert en comparaison aux souris WT et l'utilisation des FUS seuls ou des FUS combinés à l'injection du vecteur viral ont démontré une diminution significative de la distance parcourue. Cependant entre ces deux groupes aucune différence n'a été observée. Le test de l'enfouissement a démontré une différence significative du nombre d'objets enfouis entre les souris *Fmr1*^{KO} et les souris traitées avec les FUS suggérant une réduction de l'anxiété. Et enfin le test d'interaction directe n'a pas démontré de résultats significatifs bien que des durées de temps de

reniflement inférieures ont été observées après le traitement. Ainsi, nous avons observé que les deux groupes traités ont diminué leur hyperactivité et qu'une distance similaire à celle de la WT a été mesurée après le traitement. Ces résultats suggèrent que les effets du FUS avec ou sans les vecteurs de thérapie génique ont restauré de façon similaire une majeure partie du phénotype dommageable des souris *Fmr1*^{KO}. Dans notre étude, nous avons mesuré les niveaux d'expression globaux du transgène et il reste à évaluer en détail les types cellulaires qui expriment ce transgène.

D'autres études devraient se concentrer sur l'amélioration de l'administration des vecteurs de type AAV afin d'améliorer la transduction cérébrale. Comme un traitement à base d'AAV ne peut être répétés, l'amélioration de l'administration de cette thérapie grâce à des nanobulles qui pénètrent dans les petits capillaires pourrait remédier à cette limitation. L'administration répétée de FUS dans le cadre de stratégies de thérapie génique non virale pourrait contribuer à résoudre ce problème. En outre, le remplacement du promoteur CMV omniprésent utilisé dans cette étude par GFA2 ou hSyn, qui offrent une expression plus physiologique, pourrait permettre une meilleure régulation de l'expression du FMR1. Une étude récente de Li *et al*. a développé une nouvelle génération de vecteurs de type AAV qui améliorent la transduction neuronale dans le cerveau tout en réduisant la transduction indésirable dans les organes périphériques [Li *et al*., 2024]. Les recherches futures pourraient tirer parti de cette avancée pour améliorer la réexpression des protéines et restaurer la fonction phénotypique. En outre, l'ouverture de la BHE induite par les FUS pourrait déjà avoir un avantage thérapeutique en déclenchant le SIR et en facilitant la clairance des plaques Aβ [Burgess *et al*., 2014 ; Jordão *et al*., 2013 ; Leinenga et Götz, 2015].

À l'heure actuelle, aucun essai clinique combinant l'utilisation des FUS avec des AAV n'a été réalisé. Une étude récente utilisant un modèle de primate non-humain de la maladie de Parkinson a souligné que l'expression du vecteur viral après une perméabilisation importante de la BHE reste insatisfaisante et nécessite des optimisations supplémentaires [Blesa *et al*., 2023]. Malgré ces difficultés, cette approche thérapeutique reste l'une des plus prometteuses pour améliorer les résultats chez les patients atteints de maladies génétiques rares, comme l'ont démontré les essais thérapeutiques sur de petits animaux.

8.3. Discussion et conclusion générale

Ce travail présente les premières études menées au laboratoire concernant l'utilisation des FUS et des microbulles pour perméabiliser la BHE. À l'interface entre développements méthodologiques, caractérisation des phénomènes après l'ouverture de la BHE induite par FUS et développement de nouvelles stratégies thérapeutiques, nous avons exploré divers aspects des FUS thérapeutiques. Nous avons proposé l'exploration des paramètres vasculaires et fonctionnels après la perméabilisation de la BHE avec FUS, et évalué de nouvelles stratégies thérapeutiques pour traiter des tumeurs cérébrales agressives comme le glioblastome et des maladies neurodégénératives génétiques. Ce travail ouvre la voie à des approches thérapeutiques plus ciblées et efficaces en affinant les paramètres de traitement dans le contexte actuel de la médecine de précision personnalisée.

Premièrement, nous avons validé méthodologiquement le système FUS fourni par IGT. Cela a impliqué la caractérisation du transducteur, sa validation par différentes techniques IRM, la caractérisation de divers types de microbulles conçus spécifiquement pour l'ouverture de la BHE, ainsi que le développement et la validation de séquences FUS pour administrer efficacement différents composés thérapeutiques au cerveau de modèles murins et de rats précliniques.

Deuxièmement, nous avons exploré la modification transitoire de différents paramètres après la perméabilisation de la BHE. Le flux sanguin cérébral, la fraction de volume sanguin ainsi que différents marqueurs de neuroinflammation via des méthodes IRM et histologiques ont été quantifiés. Nous avons constaté que les FUS peuvent significativement, mais temporairement, influencer la physiologie du système nerveux central, en particulier la perfusion cérébrale. Le suivi étroit de l'activité de cavitation des microbulles est nécessaire pour garantir une meilleure traduction en clinique.

Troisièmement, nous avons étudié différents types de traitements FUS répétés, soutenus par le fait que l'application répétée des FUS pour perméabiliser la BHE pourrait devenir un traitement de référence pour plusieurs maladies du système nerveux central. Une large gamme de paramètres ont été mesurés en IRM quantitative avec une approche IRM fingerprint développée au laboratoire. Cette étude a nécessité un nombre important de sessions de traitement FUS et d'acquisition IRM. Plusieurs paramètres étudiés n'ont pas été présentés ici, faute de temps pour leur analyse. Cela inclut entre autres des marqueurs immunohistologiques vasculaires et inflammatoires, ainsi qu'une analyse métabolomique d'échantillons sanguins collectés.

De plus, l'installation récente d'un irradiateur stéréotaxique destiné au rongeur au sein de la plateforme préclinique a amélioré l'éventail des stratégies thérapeutiques disponibles au laboratoire. Compte tenu du pronostic défavorable des patients atteints de glioblastome, nous avons évalué une nouvelle planification de traitement impliquant l'administration de carboplatine avec FUS, suivie 24 heures plus tard d'une session de radiothérapie dans un modèle préclinique de glioblastome. Dans ce modèle, nous avons évalué la biodistribution du carboplatine, le taux de survie et la progression tumorale en IRM. Nous avons démontré une amélioration du taux de survie avec cette nouvelle stratégie de traitement. Des analyses supplémentaires seront nécessaires pour conclure cette étude, notamment l'évaluation des dommages sur l'ADN pouvant résulter de FUS, de la radiothérapie, du carboplatine ou de leur association et la formation potentielle d'adduit du platine. L'acquisition d'images en fluorescence X au synchrotron (ESRF, Grenoble, France) permettra de mieux comprendre la distribution 3D du carboplatine. L'évaluation de marqueurs histologiques, notamment des protéines vasculaires, sera utile pour évaluer la sécurité de la procédure. Cette étude est la première à évaluer

cette nouvelle combinaison de traitements et a démontré à ce jour les meilleurs résultats dans le modèle de glioblastome F98 en utilisant les FUS. D'autres étapes seront nécessaires pour déterminer si la répétition de ce traitement prolonge encore la survie des sujets ou bien induit une toxicité trop importante. Dans ce cas, ce protocole pourrait être transféré en un essai clinique de phase 1.

Enfin, nous avons montré dans un modèle préclinique de maladie génétique du système nerveux central une amélioration du phénotype comportemental après l'administration de virus AAV dans tout le cerveau à l'aide de FUS. Pour des raisons de confidentialité, seule l'étude sur la délivrance de thérapie génique dans le cerveau d'un modèle du syndrome de l'X-fragile a été présentée. Les trois études d'application, réalisées sur la plateforme IRMaGe, démontrent que notre système FUS préclinique peut être utilisé dans de nouveaux essais précliniques : le système est robuste et, dans l'ensemble, le taux de réussite de l'ouverture de la BHE au cours de cette thèse était supérieur à 95%. Des optimisations supplémentaires sont nécessaires pour déterminer si un ensemble de paramètres FUS est optimal pour toutes les applications cérébrales ou si des optimisations spécifiques à la maladie sont nécessaires, selon la région cérébrale ciblée et ses caractéristiques (par exemple les paramètres de perfusion).

Ce travail s'inscrit dans un paysage vaste et hétérogène de dispositifs FUS, de types de microbulles et de schémas de traitement FUS. Le système et les paramètres ont été caractérisés en détail à l'aide de diverses méthodes, dans le but d'assurer la meilleure translation possible vers d'autres modèles animaux et futurs essais cliniques. Étant donné le nombre considérable d'études dans le domaine des FUS thérapeutiques, en particulier celles impliquant la perméabilisation de la BHE, il y a un besoin pressant de procédures de standardisation pour la réalisation et la communication des études FUS. La prolifération des dispositifs FUS et des publications dans des revues à fort impact a conduit à une situation où il est difficile de contextualiser la vaste gamme de résultats et de développer des approches thérapeutiques fiables, valides et transférables pour les patients.

En outre, de nombreuses études ont évalué l'effet de la perméabilisation de la BHE avec les FUS, mais les mécanismes ne sont pas entièrement compris et le rôle joué par de nombreux composants de l'unité neurovasculaire n'est toujours pas connu, comme les péricytes, les astrocytes et les jonctions serrées. Il a déjà été démontré qu'au moins deux ou trois types de fuites peuvent se produire : une rapide, une plus lente et une prolongée [Cho *et al*., 2011 ; Poon *et al*., 2022 ; Raymond *et al*., 2007]. De plus, le réseau microvasculaire semble jouer un rôle important dans la perméabilisation ciblée, avec les premières observations de changements significatifs de l'ouverture de la BHE avec FUS et microbulles en fonction du diamètre des vaisseaux sanguins [Katz *et al*., 2023], ainsi qu'une extravasation accrue dans les petits vaisseaux sanguins avec l'utilisation de nanobulles [Gattegno *et al*., 2024].

Il est certain qu'une telle procédure n'est pas sans conséquences et produit un grand nombre de dysrégulations transitoires (vasculaires, cellulaires, génétiques), mais des paramètres FUS sûrs – possiblement associés à une surveillance en temps réel de la cavitation – ne produisent pas de lésions irréversibles. De plus, cette méthode est destinée à être appliquée dans des maladies cérébrales avec un pronostic défavorable, comme le glioblastome, ou ayant des conséquences dramatiques sur la qualité de vie des patients. Dans tous les cas, le rapport bénéfice/risque doit être pris en compte et les études précliniques futures doivent se concentrer sur l'utilisation de paramètres de traitement sûrs pour les applications cliniques et doivent tenir compte des différences entre les modèles animaux et

les patients. Résoudre toutes ces questions facilitera le transfert des résultats et permettra d'étudier les effets secondaires pouvant survenir dans les essais cliniques.

En conclusion, les études menées dans le cadre de ce projet de thèse ont permis de mieux comprendre les conséquences des traitements FUS simples et multiples dans le cerveau. De plus, nous avons proposé de nouvelles stratégies thérapeutiques pour trois pathologies : le glioblastome, la tumeur cérébrale la plus agressive et la plus fréquente chez les adultes ; le syndrome de Leigh, une maladie génétique mitochondriale ; et le syndrome de l'X fragile, la deuxième cause la plus courante de déficience intellectuelle d'origine génétique. Ces approches sont prometteuses, et nous espérons les voir évaluées dans des essais cliniques dans un avenir proche.

Au cours des trois dernières années, de nombreuses collaborations ont été établies avec des chercheurs du GIN et de la région de Grenoble : le Dr Michael Decressac du GIN pour une étude impliquant des virus adéno-associés dans un modèle murin du syndrome de Leigh, et le Dr Clément Hébert du GIN, avec qui nous avons l'intention de valider notre hypothèse concernant la vague de dépression corticale qui se forme suite à l'application de FUS; le Dr Hélène Elleaume et le Dr Alexandre Leboucher (et de nombreux autres chercheurs) avec qui l'étude sur le glioblastome a été menée ; le Dr Pascale Perret et le Dr Nicolas De Leiris du Laboratoire de Radiopharmaceutiques Biocliniques (LRB, Grenoble, France) avec lesquels un projet d'amélioration du diagnostic précoce de la maladie d'Alzheimer est en cours ; et enfin le Dr Bastien Arnal du Laboratoire Interdisciplinaire de Physique (LIPhy, Grenoble, France), avec l'idée de valider l'imagerie de l'oxygénation in vivo par imagerie multispectrale des fluctuations photo-acoustiques, et potentiellement valider les mesures d'IRM du débit sanguin cérébral (CBF) effectuées dans la première étude.

Le présent travail expose les premières études menées au laboratoire sur l'utilisation des ultrasons focalisés (FUS) et des microbulles pour perméabiliser la barrière hémato-encéphalique (BHE). Situé à l'interface des développements méthodologiques, de la caractérisation des phénomènes après l'ouverture de la BHE et du développement de nouvelles stratégies thérapeutiques, ce projet explore diverses facettes des ultrasons focalisés thérapeutiques. L'étude a permis de caractériser et comprendre en partie les modifications des paramètres vasculaires et fonctionnels après perméabilisation de la BHE et d'évaluer des stratégies de traitement pour des pathologies telles que le glioblastome et des maladies neurodéveloppementales génétiques, dans un contexte de médecine de précision.

Tout d'abord, la validation méthodologique du système FUS fourni par IGT a impliqué la caractérisation de divers types de microbulles, l'élaboration de séquences FUS, et leur validation par IRM pour l'administration ciblée de thérapies dans des modèles murins. Ensuite, l'impact transitoire de la perméabilisation de la BHE sur le flux sanguin cérébral et les marqueurs de neuroinflammation a été étudié, révélant que les paramètres FUS influencent temporairement la perfusion cérébrale, nécessitant une surveillance rigoureuse de l'activité de cavitation des microbulles pour une meilleure application clinique.

Une seconde étude a également exploré l'utilisation de différents plannings de perméabilisation répétées de la BHE par FUS, qui pourraient devenir le traitement de référence pour des maladies du système nerveux central comme la maladie d'Alzheimer et le glioblastome. Les nombreuses sessions FUS et acquisitions IRM nécessaire pour mener à bien ce projet ont permis d'analyser en IRM quantitative et histologie de nombreux paramètres, et plusieurs données restent à analyser, notamment histologiques et métabolomiques.

L'installation récente d'un irradiateur stéréotaxique a permis d'explorer une nouvelle approche combinée utilisant les FUS pour délivrer du carboplatine et la radiothérapie dans un modèle de glioblastome. Cette approche a montré une amélioration significative de la survie des animaux, bien que des analyses supplémentaires soient nécessaires pour évaluer la sécurité et l'efficacité à long terme. De plus, des études sur les maladies génétiques du système nerveux central, comme le syndrome de Leigh et le syndrome de l'X fragile, ont montré des améliorations comportementales et de survie après l'administration de thérapies géniques via FUS ainsi qu'une expression dans la durée du transgène signifiant en partie la restauration de l'expression du gène au préalable inhibé.

Le projet se situe dans un contexte plus large de dispositifs FUS, de types de microbulles et de traitements variés. Bien que des progrès significatifs aient été réalisés, une normalisation des procédures est nécessaire pour faciliter la traduction clinique. Les mécanismes d'action, notamment le rôle du système vasculaire et des cellules de l'unité neurovasculaire, restent à mieux comprendre.

En conclusion, les études menées dans le cadre de ce projet de thèse ont permis de mieux comprendre les conséquences des traitements FUS simples et multiples dans le cerveau. De plus, nous avons proposé de nouvelles stratégies thérapeutiques pour trois pathologies : le glioblastome, la tumeur cérébrale la plus agressive et la plus fréquente chez les adultes ; le syndrome de Leigh, une maladie génétique mitochondriale ; et le syndrome de l'X fragile, la deuxième cause la plus courante de déficience intellectuelle d'origine génétique. Ces approches sont prometteuses, et nous espérons les voir évaluées dans des essais cliniques dans un avenir proche. De nombreuses collaborations avec des chercheurs de Grenoble ont enrichi ce projet, notamment sur des études d'amélioration des

diagnostics de maladies neurodégénératives et de la compréhension des mécanismes sous-jacents qui surviennent après la perméabilisation de la BHE par FUS.

Impact of blood-brain barrier permeabilisation by focused ultrasound on the brain: a quantitative MRI approach

The blood-brain barrier (BBB) hinders efficient delivery of therapeutic compounds to the central nervous system (CNS) due to a structure gathering endothelial cells maintained by tight junctions, astrocytes and pericytes. The prevalence of neurological diseases is constantly increasing. The effectiveness of therapeutic agents that are already on the market or have been validated in pre-clinical trials is largely limited because the BBB prevents them from working. Recently, the use of focused ultrasound (FUS) coupled with a systemic vascular injection of gas microbubbles and guided by magnetic resonance imaging (MRI) has demonstrated excellent efficacy in reversibly permeabilising the BBB and thus locally increasing drug deposits. The mechanical action exerted by the gas microbubbles on the endothelial walls triggers a cascade of secondary effects that remain little studied to date, particularly at the level of cerebral microvascularisation.

The aim of this thesis was to characterise the impact of FUS on cerebral microvascularisation using innovative quantitative MRI methods and at microscopic level with histological analyses of neuroinflammation markers.

First, we characterised changes in cerebral perfusion and neuroinflammation after BBB permeabilisation and then changes during repeated BBB permeabilisation longitudinally using an MRI fingerprint approach. We then applied different FUS treatment regimens, firstly in an orthotopic model of glioblastoma to deliver chemotherapy in combination with radiotherapy, and in a transgenic model of Fragile X syndrome to deliver a gene therapy.

From the characterisation and understanding of the side effects of BBB permeabilisation by FUS to the application of this innovative method to deliver therapies, this work provides a better understanding of the use of FUS in the brain and enables us to rethink treatment parameters to ensure the best possible transfer to the clinic.

Keywords: Focused ultrasound, Secondary bioeffects, Quantitative MRI, Glioblastoma

Impact de la perméabilisation de la barrière hémato-encéphalique par ultrasons focalisés sur le cerveau : une approche quantitative en IRM

La barrière hémato-encéphalique (BHE) protège le système nerveux central des potentiels agents pathogène circulant grâce à une structure comprenant des cellules endothéliales maintenues par des jonctions serrées, des astrocytes et péricytes. La prévalence des maladies neurologiques est en constante augmentation. L'efficacité des agents thérapeutiques déjà disponible sur le marché ou bien validés en préclinique est en grande partie limitée car la BHE les en empêche. Récemment, l'utilisation des ultrasons focalisés (FUS) couplés à une injection systémique vasculaire de microbulles de gaz et guidés par imagerie de résonance magnétique (IRM) a démontré une excellente efficacité pour perméabiliser de façon réversible la BHE et ainsi augmenter localement les dépôts de médicament. L'action mécanique exercée par les microbulles de gaz sur les parois endothéliales déclenche une cascade d'effets secondaires qui restent à ce jour peu étudiés et plus particulièrement au niveau de la microvascularisation cérébrale. L'objectif de ce travail de thèse était de caractériser l'impact des FUS sur la microvascularisation cérébrale en utilisant des méthodes IRM quantitatives innovantes mais aussi au niveau microscopique avec des analyses histologiques de marqueurs de la neuroinflammation et de la vascularisation.

Tout d'abord, nous avons caractérisé les modifications de perfusion cérébrale et la neuroinflammation après la perméabilisation de la BHE puis les modifications au cours de la perméabilisation répétée de la BHE de manière longitudinale avec une approche en IRM fingerprint. Puis nous avons appliqué différents schémas de traitement par FUS, premièrement dans un modèle orthotopique de glioblastome pour délivrer une chimiothérapie en association à de la radiothérapie, puis dans un modèle transgénique du syndrome de l'X-fragile pour délivrer un vecteur de thérapie génique.

Ainsi, de la caractérisation et la compréhension des effets secondaires de la perméabilisation de la BHE par FUS à l'application de cette méthode innovante pour délivrer des thérapies, ce travail apporte une meilleure compréhension de l'utilisation des FUS dans le cerveau et permet de repenser les paramètres de traitement pour assurer le meilleur transfert possible en clinique.

Mots-clés : Ultrasons focalisés, Effets secondaires, IRM quantitative, Glioblastome